THE UNIVERSITY *of* EDINBURGH

Spectroscopic analysis of apoptotic tumour cell-derived extracellular vesicles

Catherine Lynch

Doctor of Philosophy with Integrated Study

Optical Medical Imaging with Healthcare Innovation and Entrepreneurship

The University of Edinburgh and The University of Strathclyde

2019

Declaration of authorship

I confirm that this thesis presented for the degree of Doctor of Philosophy with Integrated Study, has

i) been composed entirely by myself

ii) been solely the result of my own work except where explicitly stated otherwise in the text

iii) not been submitted for any other degree or professional qualification

Signed:

Date: 29/08/2019

Acknowledgements

I would like to thank both of my supervisors, Prof Chris Gregory and Prof Karen Faulds, for their excellent and patient support over the past 5 years.

I would also like to thank all of the members of the Gregory group, past and present, for their help throughout my time in the lab. In particular, Maggie Paterson for always being willing to share her lab-based wisdom, and Lynsey Melville for always being free for help and chats.

I need to thank all of the members of the BioNano group who have put up with me traipsing in occasionally and needing to be shown where everything is and how everything works, and for always being so welcoming. I would especially like to thank Lauren Jamieson for her extensive help with data processing.

I would like to thank Prof Colin Campbell, for all of his help throughout my PhD, and for allowing me to use his spectrometer so I didn't have to travel to Glasgow. Thanks also to Sarah McAughtrie, for her assistance in using the spectrometer.

Thank you to Prof Tom Freeman and Ajit Nirmal for their instruction and advice on how to use the BioLayout Express^{3D} software.

The support of the OPTIMA CDT has been invaluable throughout my PhD, in particular Jean O'Donoghue and Sam Brown for keeping all of us on track.

Joe, Alisia, and Holly…I definitely wouldn't have made it through without team JACH, thanks for making it a fun journey.

Last but by no means least, I could not have done any of this without the emotional, and more importantly financial, support of my loving family throughout all of life's upheavals.

This work is dedicated to my parents.

Abstract

Extracellular vesicles (EVs) are small, membrane delimited particles which are released from cells of all types and disease status. When EVs were first discovered they were thought to be a mechanism to remove waste from cells, but it has since been shown that EVs are important intercellular messengers. EVs contain biomolecules such as proteins and nucleic acids, including mRNA and miRNA, which reflect the status of the parental cell. EVs can be found in almost every bodily fluid, including blood, urine, saliva, and ascites. They are released into the extracellular milieu where they can be endocytosed by neighbouring cells. As EVs are enclosed with a lipid membrane their cargo is protected from degradation in circulation, so they can also travel to distal parts of the body and retain activity. Because of this EVs have been implicated in the pathogenesis of many diseases by transferral of biomolecules from diseased cells to healthy cells, for example transfer of oncogenes to induce oncogenic transformation in healthy cells. EVs have the potential to be used as non-invasive disease biomarkers, if suitable detection and characterisation methods were available.

Currently, the gold standard method of EV isolation is a process of differential centrifugation followed by ultracentrifugation. There is no current gold standard method of EV characterisation. Quantification and size determination of EVs can be done by methods such as nanoparticle tracking analysis (NTA), tunable resistive pulse sensing (TRPS), or dynamic light scattering (DLS). Size and morphology can be analysed by electron microscopy. Flow cytometry, invaluable for cell phenotyping, cannot be used on EVs because their small diameter does not sufficiently scatter the laser light in order to be detected. Protein analysis can be done by Western blot; however, this is a bulk technique and cannot distinguish rare subpopulations. Similarly, proteomic studies have been carried out on EV populations, but this is also a bulk technique and requires a large, highly purified sample and the results are not inherently quantitative. New methods of EV characterisation are required which are sensitive, high-throughput, and can analyse individual EVs.

In this work, EVs were isolated from Burkitt lymphoma (BL) cells, a type of high-grade non-Hodgkin lymphoma. *In vivo* these tumours have a high rate of constitutive apoptosis, which promotes the accumulation and activation of tumour associated macrophages (TAMs). TAMs have been shown to have pro-tumour phenotype, including the promoting tumour cell growth and angiogenesis, and may even play a role in metastasis due to their ability to remodel the extracellular matrix. It could be that the EVs released from the apoptotic tumour

cells (apoEVs) are impacting the microenvironment to promote the growth of the tumour. To determine if this could be the case, apoEVs and EVs derived from viable cancer cells were analysed to determine if there are any distinguishable biochemical differences between these EV groups which may imply a functional difference.

Raman spectroscopy was used to characterise both apoEVs and EVs released from viable tumour cells. This is a vibrational spectroscopy technique which can produce a molecular fingerprint of the analyte. By comparing the spectra of EVs and apoEVs using principal component analysis (PCA), a difference could be seen between the apoEVs and EVs. Differences could also be seen between EVs derived from cells of different lineages (HeLa cervical epithelial cells and BL cells). This implies that EVs derived from different sources have different chemical constituents, and Raman spectroscopy could be a useful tool for characterising and distinguishing different types of EVs.

A more targeted approach of detecting EVs would be to use surface enhanced Raman spectroscopy (SERS). Incubating EVs with gold nanoparticles functionalised with Raman reporter molecules and antibodies would allow for sensitive detection of EV subpopulations.

In order to identify target proteins for SERS analysis, a non-biased bioinformatic approach was carried out. First, gene expression profile data were obtained from the online repository gene expression omnibus (GEO). Gene expression levels in B cell samples were compared to levels in lymphoma samples. Genes with a higher expression in lymphoma samples were identified, with the view that these would preferentially identify lymphoma EVs in a blood sample, which would contain a mixed population of EVs deriving from both lymphoma and healthy B cells, as well as epithelial cells and other sources. The proteins identified by this analysis did not appear to be transferred onto the EV surface. Proteomics had been carried out on the BL apoEVs and viable BL cell EVs, so the results from this analysis were used to identify membrane proteins which were common to both EV subgroups, and proteins which were only found on the apoEVs in order to selectively detect this population. The pan-B cell marker CD20 was identified in both populations, while the lymphocyte receptor CD53 was found only on the apoEVs, so these proteins were used as targets for detection with SERS.

A nitrocellulose membrane was used to non-specifically capture EVs by hydrophobic interactions with proteins. A pilot study with BL cells showed that SERS signal of anti-CD20 functionalised gold nanoparticles increased with an increasing number of cells captured, with low levels of non-specific binding. However, when the assay was repeated with apoEVs and

EVs, the signals obtained from both anti-CD20 functionalised nanoparticles and anti-CD53 functionalised nanoparticles were at a similar level or lower than the signal obtained from the EV-free controls. Western blots of the EV populations showed that there was no detectable CD20 or CD53 in either population, despite showing up in the proteomic analysis.

This work shows that Raman spectroscopy can be used to differentiate between EVs of different types. SERS also has great potential in detecting EV sub-populations, however the target proteins chosen for this study were not present on the surface of the EV. Other markers could be used as targets for EV detection by SERS, such as proteins identified by proteomics which have been experimentally validated to be present on the EV surface, or lipid markers such as phosphatidylserine.

Lay summary

Extracellular vesicles are small particles which can be released from all cell types throughout the body. They are many times smaller than the cells from which they come, which makes them extremely difficult to study. However, in the past few decades research has shown that these tiny cell fragments can have some profound effects. They can carry messages all around the body and are found in every bodily fluid, from blood, to saliva, to tears, and even milk. These tiny messengers are often found to play a role in diseases. In particular, cancer cells release a lot of these particles, which can be taken up by nearby healthy cells to transform them into cancer cells, or travel to distant parts of the body to sow the seeds for cancer to spread.

In many types of cancer, a lot of cells dying within the tumour can actually release messages the cause the tumour to grow faster. These messages may be packaged up into the extracellular vesicles, as dying cells release many of these particles.

In my work, I have been studying the particles released from dying cancer cells to see whether they contain different messages to the particles from cancer cells which are not dying. To do this, I have used lasers to cause the atoms in the extracellular vesicles to vibrate. The vibrations of the atoms can change the colour of the light being shone on them, and the colour of the light emitted can indicate the type of atoms that are present. Using tiny particles of gold can make the light emitted brighter and easier for the instruments to see. This method has shown that the extracellular vesicles being released from dying cancer cells do appear to be different to the particles being released from cancer cells which are not dying. Finding out exactly what these vesicles have inside them could indicate why these dying cancer cells are able to make the tumour around them grow so rapidly.

Abbreviations

AFM	Atomic force microscopy
AgNP(s)	Silver nanoparticle(s)
ApoEV(s)	Apoptotic cell-derived extracellular vesicles
AuNP(s)	Gold nanoparticle(s)
AuNRs	Gold nanorods
AxV	Annexin V
AxV BB	Annexin V binding buffer
BL	Burkitt's lymphoma
BSA	Bovine serum albumin
BSA/PBT	0.1% BSA/0.05% Tween 20 in 10 mM phosphate buffer
CHOP	cyclophosphamide, doxorubicin, vincristine, and prednisolone
CLS	Classical least squares
DLBCL	Diffuse large B cell lymphoma
DLS	Dynamic light scattering
EBV	Epstein-Barr virus
ECL	Enhanced chemiluminescence
EDC	1-Ethyl-3-(3-dimethylaminopropyl) carbodiimide HCL
EDTA	Ethylenediaminetetraacetic acid
EGFR	Epidermal growth factor receptor
ELISA	Enzyme-linked immunosorbent assay
EM	Electron microscopy
EpCAM	Epithelial cell adhesion molecule
EV(s)	Extracellular vesicle(s)
FBS	Foetal bovine serum
FCS	Foetal calf serum
FL	Follicular lymphoma
FSC	Forward scatter
FWHM	Full width at half maximum
GC	Germinal centre
GEO	Gene Expression Omnibus
GEP	Gene expression profile
GO	Gene ontology

H&E	Haematoxylin and eosin
HBSS	Hank's balanced salt solution
HEPES	4-(2-Hyrdroxyethyl)piperazine-1-ethanesulfonic acid
HRP	Horse radish peroxidase
LDA	Linear discriminant analysis
L-glu	L-glutamine
LOD	Limit of detection
LSPR	Local surface plasmon resonance
LTRS	Laser tweezers Raman spectroscopy
mAb	Monoclonal antibody
MCL	Markov clustering algorithm
MEM	Minimum Essential Medium Eagle
MGITC	Malachite green isothiocyanate
MVB	Multivesicular bodies
NBF	Neutral buffered formalin
NEAA	Non-essential amino acids
NHL	Non-Hodgkin's lymphoma
NHS	*N*-Hydroxysuccinimide
NP(s)	Nanoparticle(s)
NTA	Nanoparticle tracking analysis
PB	Phosphate buffer
PBLs	Peripheral blood lymphocytes
PBS	Phosphate buffered saline
PBST	Phosphate buffered saline with 0.1% Tween 20
PBT	0.05% Tween 20 in 10 mM phosphate buffer
PCA	Principal component analysis
PdI	Polydispersity index
PEG	Polyethylene glycol
Phe	Phenylalanine
PS	Phosphatidylserine
PVDF	Polyvinylidene difluoride
RES	Reticuloendothelial system
SB	Sytox Blue

SD	Standard deviation
SEC	Size exclusion chromatography
SERRS	Surface enhanced resonance Raman scattering
SERS	Surface enhanced Raman spectroscopy
SSC	Side scatter
SVM	Support vector machine
TAM(s)	Tumour-associated macrophage(s)
TEM	Transmission electron microscopy
TNF	Tumour necrosis factor
TRPS	Tunable resistive pulse sensing
Tyr	Tyrosine
UC	Ultracentrifugation
UVB	Ultraviolet-B

Table of Contents

Declaration of authorship 1
Acknowledgements 2
Abstract 3
Lay summary 6
Abbreviations 7
Table of Contents 10
1 Introduction 14
1.1 Non-Hodgkin's Lymphoma 14
1.1.1 Burkitt's lymphoma 14
1.1.2 Follicular lymphoma 16
1.1.3 Diffuse large B cell lymphoma 17
1.2 Apoptosis 18
1.2.1 Hallmarks of apoptosis 18
1.2.2 Mechanisms of apoptosis 19
1.2.3 Apoptotic cell clearance 21
1.2.4 Oncoregenerative niche 22
1.3 Extracellular vesicles 24
1.3.1 Definition and characteristics 24
1.3.2 EV separation methods 26
1.3.3 EV analysis techniques 28
1.4 Raman spectroscopy 37
1.4.1 Application of Raman spectroscopy in biological analysis 39
1.5 Surface-enhanced Raman spectroscopy 48
1.5.1 Applications of SERS 51
1.6 Aims 55
2 Materials and Methods 57
2.1 Cell line maintenance 57
2.1.1 BL2 and BL2-bcl2 57
2.1.2 HeLa 57
2.2 Bioinformatic analysis of gene expression profiles 57
2.2.1 Selection of datasets 57
2.2.2 Data pre-processing 58
2.2.3 Network generation and analysis 58

2.3 EV generation and separation 59
2.3.1 Induction of apoptosis in cells 59
2.3.2 Separation procedure for EVs 60
2.3.3 Characterisation of EVs 61
2.4 Western blot 62
2.5 Flow cytometry 64
2.5.1 Cells – evaluation of apoptosis 64
2.5.2 Cell phenotyping 64
2.5.3 EV phenotyping 64
2.6 Raman spectroscopy of EVs and cells 65
2.6.1 Acquisition of Raman spectra from cells 65
2.6.2 Acquisition of Raman spectra from EVs 67
2.6.3 Data-processing of Raman spectra 67
2.7 Synthesis of nanoparticles for surface enhanced Raman spectroscopy 68
2.7.1 Gold nanoparticle synthesis 68
2.7.2 Functionalisation of AuNPs with Raman reporter 68
2.7.3 Conjugation of antibodies to nanoparticles 68
2.8 SERS of MGITC- and antibody-functionalised AuNPs 69
2.8.1 SERS of functionalised AuNPs in solution 69
2.8.2 SERS of MGITC-AuNPs on nitrocellulose 69
2.9 SERS MGITC-AuNP detection of biological samples 70
2.9.1 SERS measurements of cells 70
2.9.2 SERS measurements of EVs 71
2.10 Chemicals and reagents 72
2.11 Equipment and instrumentation 74
2.11.1 UV-Vis 74
2.11.2 DLS 74
2.11.3 Snowy 785 74
2.11.4 InVia 74
2.11.5 MATLAB 74
2.11.6 Flow cytometry 74
2.11.7 Plate reader 74
2.11.8 NanoSight 75
2.11.9 UV light source 75

2.11.10 IncuCyte 75
2.11.11 ImageJ 75
2.11.12 X-ray developer 75
2.11.13 Centrifuge 75
2.12 Tissue culture 75
2.13 Antibodies 75
3 Raman spectroscopy of cells and tumour cell-derived extracellular vesicles 77
3.1 Introduction 77
3.1.1 Raman spectroscopy of EVs 77
3.2 Aims of the chapter 78
3.3 Raman maps of whole cells 80
3.3.1 Viable and apoptotic BL2 and BL2-bcl2 cells 80
3.3.2 Viable and apoptotic HeLa cells 86
3.3.3 BL2 cells, BL2-bcl2 cells, and HeLa cells 92
3.4 Separation of EVs from apoptotic and non-apoptotic cells 96
3.4.1 Separation of EVs from BL2 and BL2-bcl2 cells 96
3.4.2 Separation of EVs from HeLa cells 97
3.5 Raman spectroscopy of EVs 100
3.5.1 Raman spectroscopy of BL2 and BL2-bcl2 EVs 100
3.5.2 Raman spectroscopy of HeLa and UVHeLa EVs 106
3.5.3 Comparison of Raman spectra for BL2 EVs, BL2-bcl2 EVs, HeLa EVs, and UVHeLa EVs 109
3.6 Discussion 113
4 Bioinformatics and proteomics to identify plasma membrane proteins present on extracellular vesicles 115
4.1 Introduction 115
4.1.1 Affymetrix gene expression microarrays and BioLayout *Express*^{3D} 115
4.1.2 Aims of the chapter 117
4.2 Datasets chosen 118
4.3 Evaluation of gene expression in datasets 120
4.4 Validation of protein targets 125
4.4.1 Detection of proteins on cells 125
4.4.2 Detection of proteins on EVs 126
4.5 Proteomics analysis of BL2 and BL2-bcl2 EVs 130
4.6 Discussion 133

5 Detection of extracellular vesicles by surface enhanced Raman spectroscopy 135
5.1 Introduction 135
5.1.1 EV characterisation using SERS 135
5.1.2 EV detection using SERS 137
5.1.3 SERS on nitrocellulose 139
5.2 Aims of chapter 140
5.3 Synthesis of SERS nanoparticles 141
5.3.1 Synthesis of gold nanoparticle colloid 141
5.3.2 Functionalisation of gold nanoparticles 142
5.4 Detection of BL2 cells using SERS nanoparticles 151
5.5 Detection of BL2 and BL2-bcl2 EVs with SERS nanoparticles 156
5.6 Western blot analysis of EVs 159
5.7 Discussion 160
6 Conclusion and perspectives 162
6.1 Conclusions 162
6.2 Perspectives 165
References 167
Appendix 180

1 Introduction

1.1 Non-Hodgkin's Lymphoma

Lymphoma is a cancer occurring in the lymph system. There are two main types of lymphoma: Hodgkin's lymphoma which makes up 10% of lymphoma cases, and non-Hodgkin's lymphoma (NHL) which accounts for the remaining 90% of cases. NHL has many different subclassifications, but taken together NHL is the fifth most commonly occurring cancer in the UK.[1] However, the survival rates for NHL have greatly increased since the 1970s with the development of new treatment methods.

The diagnosis of lymphoma is carried out by obtaining a tissue biopsy from the tumour, with analysis by both flow cytometry and immunohistochemistry on formalin-fixed paraffin-embedded tissue sections. Each NHL subtype has a specific set of markers used to identify it defined by WHO guidelines,[2] and some of these are outlined in Table 1.1**.**

Table 1.1: Diagnostic classifications of non-Hodgkin's lymphoma subtypes, according to WHO guidelines

Lymphoma type	**Immunophenotype**
Follicular lymphoma	CD19+, CD20+, IgM ± IgD, CD10+, Bcl-6+, Bcl-2±,
Diffuse large B cell lymphoma	CD19+, CD20+, Bcl-2±, Myc+
Burkitt's lymphoma	CD19+, CD20+, CD10+, Bcl-6+, Bcl-2-, CD5-, Myc+, Ki67>95%, (monotypic sIg+, MUM1-)

NHL can be fast-growing and aggressive, such as diffuse large B cell lymphoma (DLBCL), or a slow-growing indolent form such as follicular lymphoma (FL).

1.1.1 Burkitt's lymphoma

Burkitt's lymphoma (BL) was first reported as an aggressive sarcoma of the jaw observed in children in Uganda.[3] Along with the facial tumours, patients presented with tumours in the kidneys, liver, the thyroid, testis, heart, stomach, pancreas, salivary gland, cranium, and femur, with no tumours observed in the liver or spleen[3,4] and only minor involvement of the lymph nodes.[5] This lymphoma was the dominant form of childhood cancer in Uganda, accounting for 50% of cases compared to 6-10% of childhood cancer cases in other parts of the world.[4] However, incidence elsewhere did not occur with the jaw infiltration, only the abdominal tumours.[5] The high incidence of this lymphoma in certain geographic locations

implied an environmental factor. A herpes virus was found to be present in these BL cases, called the Epstein-Barr virus (EBV),[6] which was found to transfer to peripheral blood lymphocytes and promoted the growth of these cells.[7] High levels of antibody against EBV were found in both African and American patients.[8] The cases found predominantly in children in subequatorial Africa with presentation in the jaw, as described by Burkitt, are almost always EBV-positive and are known as endemic BL. Cases in the rest of the world rarely display EBV involvement and are called sporadic BL, and cases may also be associated with immunodeficiency or immunosuppression.[9]

Although only 5% of adult cases of NHL are BL, this is the most common form of lymphoma in children, accounting for 40% of childhood NHL.[10] BL is also the most aggressive form of lymphoma, displaying high rates of both proliferation and cell death which in turn promotes the accumulation and proliferation of macrophages, giving the tumours the characteristic 'starry-sky' appearance in haematoxylin and eosin (H&E) stained tissue sections.[3,5,11]

BL malignancies are derived from the highly proliferative germinal centre (GC) B cells and are positive for the GC markers CD10 and CD77.[12] BL is BCL-6+ but negative for BCL-2 (B cell lymphoma 2). However, analysis of BCL-6 for the diagnosis of BL does not improve classification above using CD10. The characteristic genetic mutation in BL is the t(8;14)(q24;q32) translocation of *c-MYC* from its locus on chromosome 8 to the immunoglobulin heavy chain in chromosome 14.[13–15] Translocations of t(8;22) and t(2;8) were also observed, corresponding to translocations with the κ- and λ-immunoglobulin light chain loci.[14] MYC is a transcription factor which can promote transition from the G_0 to S phase of proliferation by controlling pathways such as protein synthesis, DNA replication, and metabolism. High grade lymphomas such as BL showed *c-MYC* translocations from chromosome 8, whereas indolent lymphoma showed translocations of *BCL-2* from chromosome 18.[15] This translocation of *MYC* is not an oncogenic event in itself, although cells appeared to remain proliferative rather than differentiating. Transgenic mice engineered with this mutation formed monoclonal tumours only after a latency period of 5 months, indicating other oncogenic factors are required in addition to the *Myc* translocation.[16] Many cases of BL are described as 'MYC-simple', where there are no *BCL2* translocations or breakpoints in the *BCL6* gene occurring alongside the *IGH-MYC* translocation.[17] The 'MYC-simple' genetic status is associated with favourable outcome for patients.

Treatment of BL involves high-intensity chemotherapy. The lymphoma malignancy B treatment protocol involves systemic high-dose methotrexate and high-dose cytarabine and has shown high survival rates (>90%) in children. A modified version in adults resulted in a mean 2-year survival of 70%, with 65% rate of 2-year event-free survival.[10] Treatment is also successful using cyclophosphamide, doxorubicin, vincristine and prednisolone (CHOP) combined with methotrexate.[18]

Distinguishing between BL and DLBCL can be difficult, as DLBCL can also carry *c-MYC* translocation. Although only 5-10% of DLBCL cases have this translocation, the higher incidence of DLBCL means that this characteristic alone cannot identify a case of BL. Determining the correct diagnosis is important, as the course of treatment for BL and DLBCL is different, however only 53% of hematopathologists reach an agreement on the pathological diagnosis of BL, Burkitt's-like lymphoma (which has some morphological features of BL and some features resembling DLBCL), and DLBCL.[19] Gene expression analysis has been used to identify a molecular signature of BL, and many of these cases had been incorrectly diagnosed by pathologists as atypical BL or DLBCL based on morphological features. The signature includes many c-Myc target genes and genes associated with GC B cells.[17,20] Mutations in either *TCF3,* a transcription factor which is involved in regulation of genes associated with normal B cell development, and *ID3* a negative regulator of TCF3, have been found in many cases of BL.[21,22] Inactivating mutations of *ID3*, resulting in the upregulation of genes promoting transition from G1 to S phase of proliferation and higher expression of *MYC* target genes, were more common than mutations in *TCF3*, indicating a potential tumour suppressor function for this gene.

1.1.2 Follicular lymphoma

20% of cases of NHL are follicular lymphoma (FL), found predominantly in women with a median age of 60 years old. The disease typically presents as a slow progressing lymphadenopathy. There is some variability, with some patients undergoing transformation to a high-grade disease. 37% of patients with FL show disease transformation to DLBCL histologically within 15 years.[23] Although the median survival is 9 years, only 25% of patients remain disease free during this period, the rest experience several incidences of relapse and remission, whether the treatment approach is intensive or conservative.[24] Advanced FL appears relatively incurable, although the indolent nature means that many patients survive for long periods despite the incomplete treatment response. The median survival after first

round of treatment is 4.5 years, with the response rate and duration of remission decreasing with each subsequent round of treatment. There was a 48% response rate to the fourth round of treatment, showing the value of repeated, non-toxic therapy.[24]

The addition of the anti-CD20 antibody Rituximab to CHOP (R-CHOP), which is the standard treatment for difficult cases of FL, of showed an increase in the duration of remission.[25] The prognostic value of some biological markers may depend on the course of treatment, with the addition of rituximab overcoming the effects of some markers which had previously been poor prognostic indicators.[26]

FL phenotype is similar to a germinal centre B cell, with positive expression of BCL6, CD10, LMO2, and HGAL. Clonal and subclonal analysis showed that *BCL2* translocation to the *IGH* locus, t(14;18)(q32;21), was the primary event observed in 60% of FL cases.[27] However, the frequency of *BCL2* translocations decreases with increasing disease stage. Mutation of histone methyltransferases was also observed, with mutation of *CREBBP* observed in 32% of cases thought to be a disease-driving mutation and mutation of *MLL2* in 89% an accelerator mutation.

Mutations in genes which play a role in transcriptional regulation and somatic mutations have been found to be enriched in NHL. A study of germinal centre B cell lymphomas (FL, BL, and GCB-DLBCL) showed gain-of-function mutations in the histone methyltransferase gene *EZH2*, which leads to enhanced methylation of histone H3, in 22% of FL samples.[28] Another gene encoding a histone methyltransferase, *MLL2*, was found to be frequently mutated with loss-of-function modifications indicating that this gene acts as a tumour suppressor. Mutation were observed in 89% of FL samples, the same frequency as the t(14;18)(q32;q21) *BCL2* translocation, as well as 32% of DLBCL samples.[29]

1.1.3 Diffuse large B cell lymphoma

Diffuse large B cell lymphoma (DLBCL) is the most common NHL, accounting for 30-40% of NHL cases. Tumours are mainly found in lymph nodes; however, they can occur anywhere in the body and are also commonly observed in the GI tract and skin.

WHO classification has delineated DLBCL into a number of different subtypes, the two main subtypes defined by the 'cell-of-origin' immunophenotype. The germinal centre B cell type, GCB, retains the profile of GC B cells such as CD10, CD38, and BCL-6 and commonly has *BCL2* and *MYC* translocations, while the other type shows expression of genes associated with

activated B cells (ABC) and is observed more often with translocations of *BCL6* and expression of MUM1 and BCL-2.[30,31] These subtypes have different clinical responses, as the ABC type has been shown to have a poorer outcome than GCB type following R-CHOP therapy.[30–33] High levels of *MYC* translocation and expression levels in GCB DLBCL have also been associated with poor prognosis,[34] particularly with co-expression of BCL2.[35] The MYC/BCL-2 co-expressed cases had poorer progression-free survival (32%) and 5-year survival (36%) compared to those without co-expression (65% and 71%, respectively).[36]

Genes such as *EZH2*, *SGK1*, *BCL2*, *CD79B*, and *MYD88* are often observed to have mutations in DLBCL.[21,28]

1.2 Apoptosis

Apoptosis is an immune silent form of programmed cell death. Although the term 'programmed cell death' is often used interchangeably with apoptosis, there are other forms of programmed cell death such as autophagy, pyroptosis, and necroptosis.

1.2.1 Hallmarks of apoptosis

A number of morphological changes are evident in cells undergoing apoptosis, as described by Kerr *et al*.[37] Both the nucleus and the cell shrink in size, followed by fragmentation of the nucleus, membrane blebbing, finishing with the formation of apoptotic bodies. Many of these apoptotic bodies were seen in the cytoplasm of surrounding healthy cells, indicating that they are rapidly engulfed with no inflammation.[37]

Degradation of the nucleus was observed to yield double stranded fragments which were multiples of 180 bp, indicating that these fragments occur due to internucleosomal cleavage by an endonuclease.[38–40]

Apoptosis also causes the activation of ROCK I, a serine/threonine kinase which regulates Rho GTPases. This activation results in stabilisation of actin filaments and coupling of actin-myosin filaments to the plasma membrane, causing the characteristic morphology of membrane blebbing seen in apoptotic cells.[41]

An early event in apoptosis is the loss of plasma membrane lipid asymmetry, exposing phosphatidylserine (PS) on the outer membrane surface. This is caused by apoptosis-induced inactivation of flippase enzymes ATP11C and CDC50A, which internalise aminophospholipid molecules to the internal membrane leaflet,[42,43] and activation of scramblase enzyme Xkr8,

which can translocate both aminophospholipids and neutral moieties such as phosphatidylcholine (PC).[44] This provides a means of apoptotic cell detection. Annexin V (AxV) is a protein which shows preferential binding to PS over other membrane lipids, in a Ca^{2+}-dependent manner.[45] By labelling AxV with a fluorescent molecules such as FITC, a flow cytometric assay to detect apoptotic cells was developed.[46] Addition of propidium iodide, a membrane-impermeable dye which binds to DNA, can indicate whether the plasma membrane integrity has been lost.[46] Apoptosis in tissue sections can be studied by the detection of DNA fragmentation. The 3'-OH DNA strand breaks can be labelled with biotinylated deoxyuridine using terminal deoxynucleotidyl transferase (TdT). The signal is then detected and amplified using avidin-peroxidase. This technique is called TdT-mediated dUTP-biotin nick end labeling (TUNEL).[47]

1.2.2 Mechanisms of apoptosis

There are broadly two different means by which cells are activated to undergo apoptosis. Both of these pathways involve cysteine aspartyl proteases known as caspases. There are 12 members of the caspase protein family found in humans, each with different substrate specificity and functions, many of which are involved in apoptosis. Initiator caspases, such as caspase-8 and caspase-9, function to activate effector caspases, whereas effector caspases such as caspase-3 and caspase-7 cleave vital cell proteins in order to bring about the morphological changes observed in apoptosis. Caspases are proenzymes which are activated by cleavage of a prodomain from the N-terminus to form the active enzyme. Both pathways ultimately result in the activation of effector caspase-3 causing the morphological changes as described above.

1.2.2.1 Intrinsic pathway

The intrinsic apoptosis pathway is initiated by an internal stressor signal such as DNA damage, lack of growth factor, or infection. This pathway is regulated by the BCL-2 family of proteins. These proteins share BCL-2 homology (BH) domains BH1, BH2, or BH3 and can interact with each other via the BH3 domain. *BCL2* was first identified in B cell lymphoma, translocated to the immunoglobulin heavy chain locus. It was shown to have a protective effect against apoptosis in IL-3 dependent myeloid cells which had been deprived of the growth factor.[48] The suppression of apoptosis was shown to be due to blockage of release of cytochrome c from the mitochondria.[49–51]

BCL-2 and BCL-X_L pro-survival proteins are found primarily on the outer mitochondrial membrane, with some found on the perinuclear membrane.[52,53] Other members of the BCL-2 proteins, including BAX, BAK, and the BH3-only proteins such as BID, BIM, and BAD, are pro-apoptotic. The structures of these proteins are similar to pore-forming proteins found in bacteria,[54] indicating the interaction they may have with the mitochondria during apoptosis. An apoptotic stimulus causes activation of the pro-apoptotic BAX and BAK, causing BAX to oligomerise and form a pore in the mitochondrial membrane. This pore causes the release of cytochrome c from the mitochondria. These pro-apoptotic proteins may exist as dimers with the anti-apoptotic proteins in viable cells. BAD displays preferential binding to BCL-X_L and BCL-2, thereby displacing BAX from the BCL-X_L/BCL-2 dimer to form mitochondrial membrane pores and release cytochrome c.[55] The release of cytochrome c from the mitochondria during apoptosis occurs before depolarisation of mitochondria,[49,50,53] and mitochondrial depolarisation itself does not cause cytochrome c release.[53]

The cytochrome c released from the mitochondria binds to APAF-1 in the presence of dATP, which undergoes a conformational change allowing formation of a heptamer.[56] The APAF-1 heptamer can then recruit pro-caspase 9, which oligomerises and is activated, forming the apoptosome. Cytochrome c does not remain associated with the apoptosome, but caspase-3 is tethered to the apoptosome.[57] The apoptosome can then cause activation of the executioner caspases, such as caspase-3 and caspase-7. Caspase-3 cleaves proteins such as flippases ATP11A and ATP11C, which inactivates them,[43,45] and also activates a scramblase Xkr8,[44] causing loss of plasma membrane lipid asymmetry and the exposure of PS on the outer membrane leaflet. The endonuclease responsible for internucleosomal cleavage, caspase-activated deoxyribonuclease (CAD), is released from its inhibitor protein ICAD by caspase-3 activity,[58] and cleavage of ROCK I increases the activity of this protein causing membrane blebbing.[41]

1.2.2.2 Extrinsic pathway

The extrinsic apoptosis pathway is a receptor mediated pathway governed by the tumour necrosis factor (TNF) family of proteins. Transmembrane receptors such as FAS and TNFR1 contain death domains on the cytoplasmic region. The corresponding ligands for these receptors, death factors such as FASL, TNF-α, and TRAIL, are homotrimeric membrane proteins. The binding of FASL to FAS causes oligomerisation of the receptor which induces a conformational change in the Fas death domain, which can then bind FAS-associated death

domain (FADD) which recruits procaspase-8, forming a complex known as DISC (death-inducing signal complex), which then activates caspase-8 by auto-catalysis.[59,60] Activated caspase-8 acts in the same way as caspase-9, as an initiator caspase in order to activate caspase-3 which results in the biochemical and morphologic features of apoptosis.

Death factor proteins can be cleaved by metalloproteinase enzymes to release a soluble form of the ligand. While Fas is expressed in many cell types, FasL is mainly expressed in activated T cells and NK cells. The membrane-bound form of FasL is the active form and does not enter the cell to activate apoptosis, remaining bound to Fas at the membrane.[61] However, soluble FasL is actually protective against FasL-induced apoptosis,[61–63] possibly because soluble FasL binding to Fas causes internalisation and subsequent degradation of Fas receptor. Rapid degradation of Fas limits the amount of procaspase-8 which can be activated by DISC, while membrane-bound FasL binding to Fas retains Fas at the membrane and prolongs the DISC activity to release active caspase 8.

1.2.3 Apoptotic cell clearance

Apoptotic cells are rapidly cleared by phagocytes in a process known as efferocytosis. If cells are not cleared efficiently secondary necrosis occurs, where the integrity of the plasma membrane is lost, releasing danger associated molecular patterns and inducing an immune response. In order for phagocytes such as macrophages to efficiently clear apoptotic cells, they must be able to recognise which cells are apoptotic.

Apoptotic cells can release signals which recruit phagocytes to the site of apoptosis. These molecules include CXCL1,[64] lysophosphatidylcholine,[65] and sphingosine-1-phosphate,[66] and nucleotides.[67] The exposure of PS early in the process of apoptosis acts as an ‘eat-me’ signal to identify cells for efferocytosis.[68] Annexin I has also been shown to act as ‘eat-me’ signal after caspase-mediated recruitment from the cytosol to the outer leaflet of the plasma membrane.[69] Calreticulin has also been identified as an ‘eat-me’ signal.[70]

Different types of macrophages display surface receptors for different ‘eat-me’ signals, however PS is recognised by all types of macrophages.[71] Milk fat globule-EGF-factor 8 (MFG-E8) is a secreted glycoprotein which acts as a bridging molecule between the phagocyte receptor and the apoptotic cell. The factor 8-homologous domains recognise and bind PS, while the EGF domain contains an RGD motif to bind αvβ3 integrin on phagocytes.[72] Other bridging molecules include Protein S (PROS)[73] and GAS6,[74] which display Ca^{2+}-dependent

binding to PS and Tyro 3/Axl/MERTK receptor kinases on macrophages.[75,76] Recognition of apoptotic cells by these receptors is followed by the release of anti-inflammatory factors like TGF-β, IL-10, and PGE_2, and decrease in production of IL-6 and TNF-α pro-inflammatory cytokines.[77–79] Once the apoptotic cells have been recognised and bound to the phagocyte, the cells are engulfed by the phagocytes via the formation of phagosomes, which are transported to lysosomes to degrade the engulfed material.[80,81]

1.2.4 Oncoregenerative niche

The balance between cell proliferation and cell death is important. $10x10^9$ cells undergo apoptosis every day in the body,[82] in tight homeostatic balance with cell generation from stem cells. In cancer, this balance is tipped so that cell proliferation exceeds cell death, forming neoplasms. This occurs by mutations in the cancer cells resisting cell death, experiencing sustained proliferative signalling, evading growth suppressors, and cell immortality.[83] However, many types of aggressive tumours display high rates of spontaneous cell death within the tumour which is an indicator of poor prognosis.

It is known that, in order to maintain homeostatic balance, cells undergoing apoptosis can induce replication of surrounding cells, termed compensatory proliferation.[84,85] This process appears to be hijacked in some types of cancer, where apoptotic tumour cells induce proliferation of the surrounding cells. After exposure to radiotherapy, tumour cells *in vitro* have been observed to undergo a rapid repopulation, reaching pre-treatment levels after 2 days.[86] Co-injection of lethally irradiated cancer cells with untreated cells showed a higher rate of tumour growth in a xenograft model than injection of untreated cells alone, and this has been shown for glioblastoma,[87] breast cancer,[88] melanoma,[89] and stromal cells such as fibroblasts[88] and endothelial cells.[90] When caspase-3 is inhibited in these cells, the effect is abrogated.[88] The presence of active caspase-3 in tumours has been shown to be an indicator of poor clinical outcome for gastric cancer, ovarian cancer, and colorectal cancer.[91]

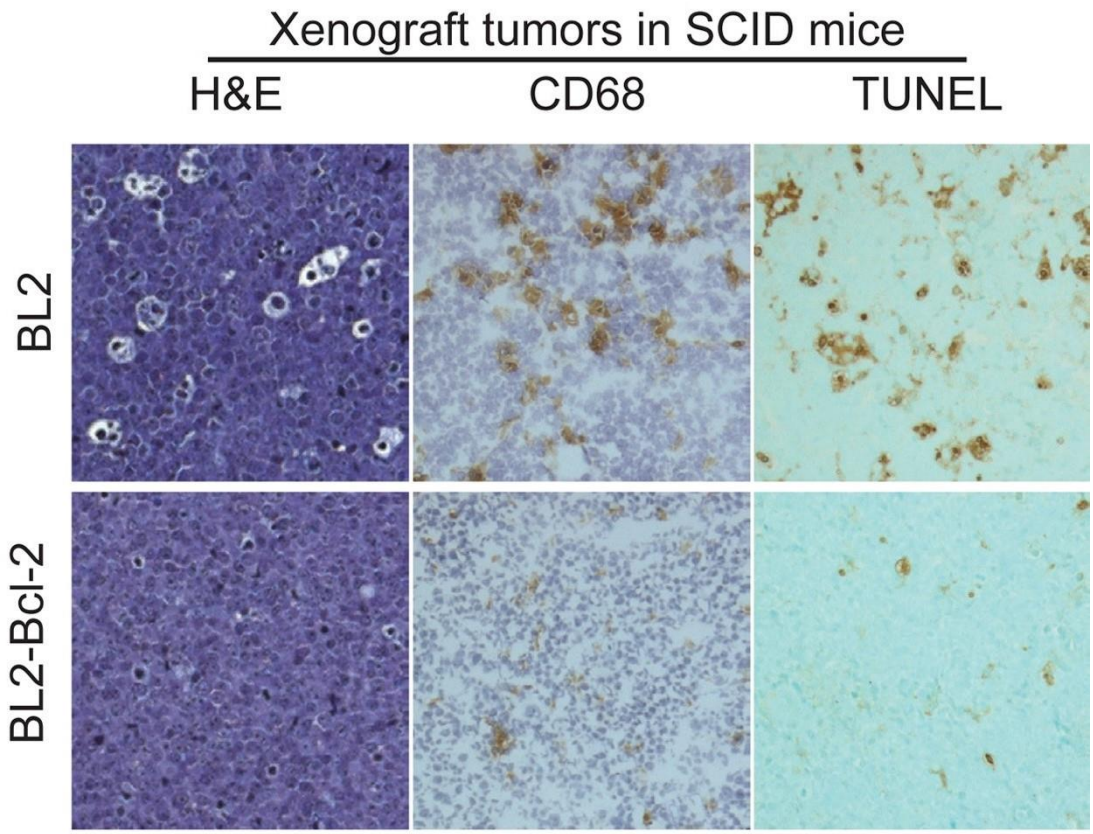

Figure 1.1: Apoptosis in BL, showing the typical starry sky morphology in the BL2 H&E section which is lost upon transfection with Bcl-2 in the BL2-Bcl-2 stained section. The apoptotic BL2 tumours also display positive staining for CD68 macrophage marker and TUNEL, indicating apoptosis, which is reduced in the BL2-Bcl-2 sections. Reproduced from *C. A. Ford et al., Curr. Biol., 2015, 25, 577–588.*

BL tumours have reasonably high rates of spontaneous apoptosis which causes the activation and accumulation of tumour-associated macrophages (TAMs). When BL cells transfected with *BCL2* were injected into mice, tumour growth was suppressed and the tumours which did result had reduced proliferation and TAM recruitment compared with tumours from BL cells not transfected with *BCL2* (Figure 1.1).[89] Gene expression analysis of TAMs isolated from BL tumour sections by laser capture microdissection showed an anti-inflammatory signature, with pro-angiogenic and tissue remodelling genes such as those encoding MMP2, MMP3, MMP12, CD13, galectin-3, and GPNMB, and growth factors IGF-1 and PDGF-CC. Thus, apoptosis in aggressive lymphoma drives the accumulation of pro-tumour TAMs, which in turn promote tumour cell proliferation.[89] The tissue repair mechanism has been termed the 'onco-regenerative niche'.[92] High levels of TAMs have also been correlated with poor prognosis in follicular lymphoma,[93] breast cancer,[94] prostate cancer,[95] and glioma.[96] As therapy-induced apoptosis has also been show to promote TAM accumulation, this effect

must be studied in order for effective therapies to be developed to counteract the onco-regenerative niche.

1.3 Extracellular vesicles

1.3.1 Definition and characteristics

In 1946, Chargaff and West discovered that there was a clotting factor present in blood which could be removed at high speed centrifugation (31,000 *g*) but not removed in low speed centrifugation (5000 *g*), and suggested that it may be associated with fragments of red blood cells.[97] Further study of these 'membrane fragments' by electron microscopy revealed a vesicular morphology with a triple membrane layer containing cytoplasm.[98] These vesicles were shown to transfer plasma membrane proteins off the cell surface, such as the transferrin receptor which is shed from reticulocytes during maturation.[99] Using gold nanoparticles (AuNPs) to track the loss of the receptor, it was observed that direct budding of the plasma membrane was not the mechanism of release. The membrane receptor was internalised, first to the limiting membrane of multivesicular bodies (MVB), followed by formation of small vesicles within the MVB of average size 30-50 nm by internal budding of the MVB membrane, with the receptor on the external surface.[100] These small vesicles were released from the cells by fusion of the MVB membrane with the plasma membrane, and were termed 'exosomes' (Figure 1.2).[101] Exosome formation and release was shown to be an active process which was dependent on protein and RNA synthesis, and glycolysis.[102] MHC class II-enriched compartments (MIICs) of antigen presenting cells, which have lysosomal characteristics such as LAMP1 and CD63, were shown to contain internal membrane structures, some of which release MHCII on exosomes which could act as antigen presenting molecules for T cells.[103] This study was the first to show exocytosis of extracellular vesicles (EVs) in cells other than reticulocytes, indicating a broader biological function of EVs.

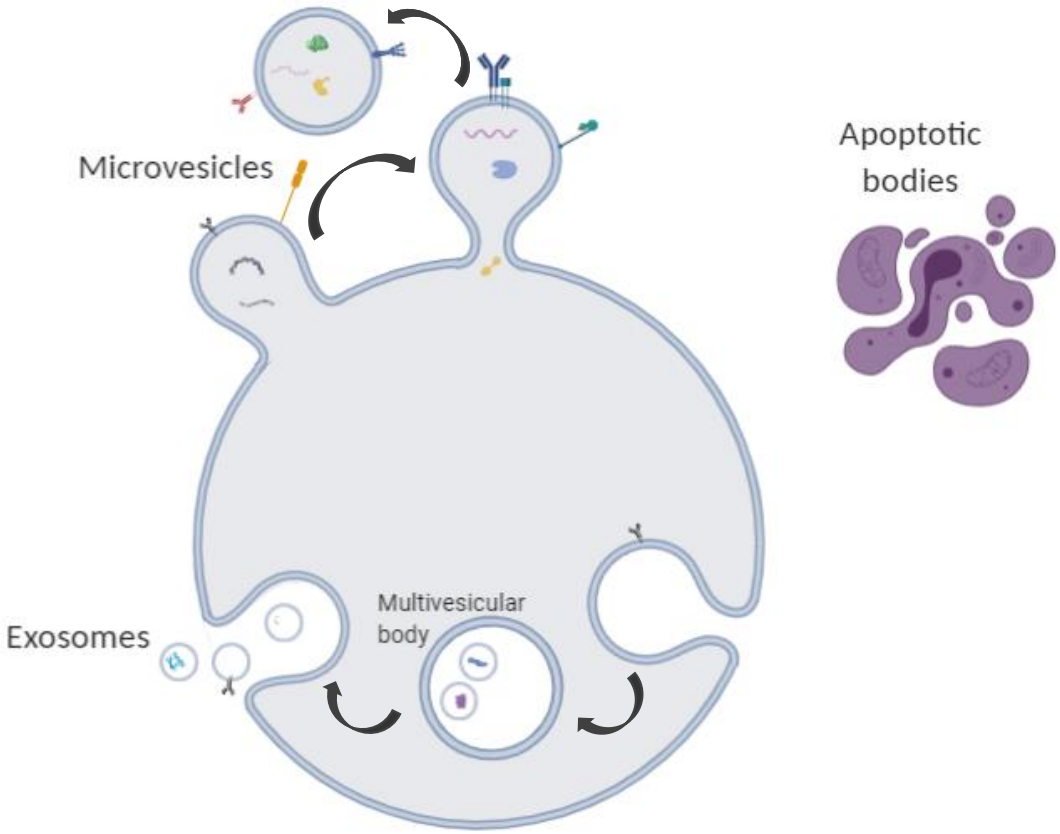

Figure 1.2: Biogenesis of EVs. Exosomes are formed via multivesicular bodies and released from the cell by exocytosis, microvesicles bud directly from the plasma membrane, and apoptotic bodies form as a result of apoptosis

Although the field of EV research is well established, and it is generally accepted that there are at least 3 different types of EVs (exosomes, microvesicles, and apoptotic bodies; Figure 1.2), there is still little consensus amongst researchers about important aspects such as nomenclature, categorisation, isolation techniques, and analysis. Exosomes, the smallest class of EVs, are defined by some researchers by the mode of biogenesis from endosomal compartments, others define exosomes as a secreted vesicle which "may serve a physiologic function", and others defining exosomes as the EV fraction that sediments at 100,000 *g*. Similarly, microvesicles (MVs, also called membrane vesicles, membrane particles, microparticles, ectosomes, etc.) can be defined as EVs which bud from the plasma membrane (Figure 1.2), EVs which sediment at 10,000 *g*, or some use this as a general term for EVs. A panel at the first annual meeting of the International Society for Extracellular Vesicles (ISEV) was unable to come to a consensus with the attendees, and instead has implemented some guidelines as to the nomenclature, as well as isolation and characterisation techniques for EVs, which should be kept in mind.[104] The generic term 'extracellular vesicle' is to be used to describe particles naturally released from the cell which are delimited by a lipid bilayer and

do not replicate. Assigning an EV to a particular subtype based on biogenesis should be avoided unless the EV is imaged while being released. Terms instead should be used which refer to the physical characteristics of the EVs (e.g. size with ranges, or density), biochemical composition (e.g. phenotype), or descriptions of the isolation conditions or parental cells.[105]

1.3.2 EV separation methods

Achieving a complete purification or isolation of EVs is unrealistic. The position of the ISEV, as set out in the minimal information for studies of extracellular vesicles 2018 (MISEV2018),[105] is that the appropriate terminology is separation of EVs from non-EV components, separation of EV subtypes, concentration of EVs by increasing the number of EVs per volume, or enrichment of EVs or EV markers relative to another metric. The most appropriate method of separation or concentration depends on the desired downstream study. Different techniques have different recovery/specificity e.g. high recovery, low specificity (precipitation); intermediate recovery, intermediate specificity (size exclusion chromatography (SEC), ultracentrifugation (UC) with intermediate speed/time), low recovery, high specificity (filtration combined with SEC, density flotation, immunoaffinity), or high recovery, high specificity (not currently achievable).

As there is no standard method for EV separation, the major focus of the ISEV guidelines is on transparency of reporting. For this, EV-TRACK was developed as a repository for detailed experimental protocols of published EV studies.[106] A checklist of 115 parameters, based on the MISEV recommendations, was established and used to develop EV-METRIC, a score of the methodology and reporting of 1226 EV publications. 30% of studies failed in all EV-METRIC components, 81% of these studies could have improved their metric by more detailed reporting without any additional experiments, this highlighting the importance of transparency and reproducibility in the field.[106]

A survey of EV researchers show that the most commonly used method for separation of EVs is differential centrifugation and UC, with more than half of respondents saying that they use a combination of different techniques for EV separation.[107] Other commonly used methods include density gradient centrifugation, filtration, and SEC.

The lack of specificity in the use of UC for the separation of EV subpopulations is highlighted in a study, where 2 distinct EV types are observed in the 100,000 *g* pellet from a mouse mammary carcinoma cell line.[108] Treatment of the cells with shRNA to inhibit Rab27a, a small

GTPase involved in the trafficking and release of exosomes, showed an expected decrease in the levels of four typical exosome markers in the pellet: Cd63, Tsg101, Alix, and Hsc70. However, the levels of Cd9 and Mfge8 were not reduced, indicating a population of Cd9+ EVs which are not formed in the endosomal pathway. There was a slight separation of the Rab27a-dependent Cd9+ EVs from the Rab27a-independent EVs by density gradient centrifugation, highlighting the importance of multiple separation and analysis techniques.[108] Centrifuges can have either swinging bucket rotors or fixed angle rotors, which have different sedimentation path lengths, and have been shown to pellet different populations of EVs using typical conditions of 100,000 *g* for 70 minutes. Thus, the rotor type used for separation and the k-factor should be reported for transparency and reproducibility.[109] The high sedimentation speeds may also damage the membrane structures of EVs.[110]

Density gradient centrifugation can be used in order to separate contaminants from an EV preparation which would co-sediment under ultracentrifugation but have different density. EVs separated using density gradient centrifugation have shown to be enriched in EV-associated proteins compared to EVs prepared by UC alone,[111,112] indicating a higher purity of the density gradient centrifugation sample. Sucrose-density gradient UC has been used to confirm the membranous nature of EVs.[103] However, the solution is hyperosmotic this can result in dehydration of the particles being isolated and slow sedimentation rates, as well as co-isolating particles with similar densities such as high density lipoproteins (HDL)[113] or virus particles.[114] Iodixanol has also been used as a reagent for establishing a velocity gradient, which has been shown to have better resolving power of EVs from viral particles.[114]

SEC has been used to separate 'membrane fragments' since the early days of EV research.[98,99] SEC to separate EVs typically uses Sepharose CL-2B which has a pore size of 75 nm, thus EVs smaller than 70 nm are expected to elute from the SEC with the protein fraction while larger EVs elute in the void volume.[115] This technique has been successful in the separation of EVs from lipoprotein contaminants in blood samples, with good recovery rates from 72% to 85% reported.[113,115] SEC has also been done using a methacrylate gel column, with analysis of eluent by dynamic light scattering (DLS) using a flow through cuvette coupled directly to the HPLC.[116] EVs have been separated by a commercially available SEC, qEV, to remove lipoproteins from a plasma sample.[115] SEC does cause dilution of the sample, typically 2-5 fold.

Immunoaffinity capture is a good method for the specific separation of subpopulation of EVs based on expected surface markers. This technique is useful when the volume is low. Although this method shows reduction in the concentration of EVs isolated, the purity of the preparation has been found to be higher than UC or density gradient separation of EVs.[112]

1.3.3 EV analysis techniques

MISEV2018 guidelines state that multiple complementary techniques should be employed for the analysis of EV preparations, including quantitative analysis based on particle number or concentration of protein or lipid in the EV sample, and qualitative analysis for the presence of EV-associated components as well as the absence or reduction of non-EV contaminant components.[105]

1.3.3.1 Electron microscopy

Electron microscopy (EM) has been used for the analysis of membrane structures for many years. Transmission electron microscopy (TEM) analysis can yield information on the size and the morphology of EVs simultaneously. TEM has shown that apoptotic bodies contain condensed chromatin structures.[117] TEM showed 12% reduction in EV size due to sample preparation compared with other methods, with a recovery of 21% of EVs from the separation procedure.[118]

As opposed to TEM, where drying of the sample causes collapse of the structure of EVs, cryo-EM samples remain hydrated and retain their structure. This gives a more realistic picture of the morphology of the sample. However, the contrast of cryo-EM is reduced because of the lack of staining. In one cryo-EM study of plasma, most of the particles observed were identified as lipoprotein contaminants, seen as small, electron dense particles which did not have a lipid bilayer.[119]

1.3.3.2 Atomic force microscopy

Atomic force microscopy (AFM) is a method of imaging that analyses nanoscale structural features of a sample. A cantilever tip is passed over the sample by raster scanning. The tip is oscillated during the scanning such that the tip is only in direct contact with the sample when it is at the lowest height of the oscillation. The frequency or amplitude of the oscillation and contact with the sample changes the height of the cantilever, and this height adjustment is measured to generate an image of the surface topology. This ‘tapping mode’ AFM is useful for biological samples as it minimises the mechanical perturbation of the sample. Non-

contact modes of AFM, such as amplitude modulated, where tip height is adjusted based on the amplitude of oscillation, or phase modulated, where the amplitude of oscillation is constant and the phase difference between oscillation and excitation is measured, have also been used for EV preparations.

Substrates for AFM must be very flat, with roughness less than 0.5 nm. Muscovite mica is often used as a substrate for AFM, as it is easily cleaved to generate an atomically flat surface with a negative charge to form an electrostatic interaction with EVs. EVs tend to form flattened structures,[120,121] or dome-like structures,[120] when adsorbed onto the mica surface.

To further stabilise the EV immobilisation, the substrate can be coated with antibodies specific for molecules expected to be on the EV surface. This also allows specific detection of EV subtypes, such as CD41-positive platelet-derived EVs.[122] This study also examined the freeze-thaw effect on EVs, and although there was no difference in the size distribution of the EVs, there were fewer CD41-positive EVs in the samples which had been previously frozen.

AFM can be carried out in air mode, where the sample has been dried onto the mica substrate, or in liquid mode. Air dried EVs can show an underestimation of particle size due to sample dehydration,[123,124] and can exhibit a cup-shaped morphology due to dehydration effects and force exerted on the EV surface by the AFM tip.[121,124] Measurements of EV diameter by AFM are comparable to those obtained by DLS.[120] As well as the size, AFM can also measure the surface topology of EVs, indicating the presence of biomolecular cargo within the EV or detecting the binding of antibody-coated AuNPs on the surface.[121] The mechanical stiffness can also be measured: cancer-derived EVs have been found to have reduced stiffness compared to EVs derived from healthy cells,[125] and hepatocyte-derived EVs were softer than EVs derived from hepatocyte progenitor cells.[126]

1.3.3.3 Dynamic light scattering

DLS is a well-established technique to analyse the size distribution of particle suspensions. Light scattered from the bulk solution is used to calculate the mean particle size. While this is useful for the analysis of monodisperse samples, results are not as accurate for heterogeneous sample populations such as EVs. The size profile is biased towards larger particles, as larger particles scatter light with greater intensity. Light is also scattered from large particles at lower angles, so instruments with options for the detection angle may be more suitable for analysis of the size distribution of EVs.[127]

Despite this drawback, DLS has been used in many studies to determine the size profile of EV samples. DLS is a high-throughput analysis technique requiring minimal sample preparation compared to techniques such as EM. Many comparative studies have shown that the results obtained from DLS analysis are not dissimilar to results obtained from techniques analysing particles individually.[116,120,128]

1.3.3.4 NTA

Nanoparticle tracking analysis (NTA) is a method which measures the size distribution of particles based on their velocity by Brownian motion. A sample is introduced into the 0.3 mL sample chamber and illuminated using a laser (Figure 1.3). The scattered light is detected by a camera which records a video of the particles moving under Brownian motion at a rate of 30 frames per second. The particles in each frame are then tracked individually to determine the mean square displacement of each particle, which is related to particle size via the Stokes-Einstein equation (1).[129] Particles larger than 1 µm cannot accurately be measured by NTA due to the slow diffusion rate of these particles.[130] NTA overcomes the limitations of DLS by monitoring particles on an individual basis rather than bulk solution and calculates an accurate size distribution of the particles for hydrodynamic radii between 30 nm and 1 µm. Sources of error with NTA are external vibration of the instrument, as well as inaccurate measures of sample viscosity and temperature, as these affect the Brownian motion of particles.[131] Larger particles scatter the laser light at greater intensity, so settings which are optimal for the detection of larger particles in the sample may not be sensitive enough to pick up on smaller particles and thus bias the size distribution towards larger particles.

$$< x, y >^2 = \frac{K_B T_{t_s}}{3\pi\eta d_h} \quad (1)$$

where $< x, y >^2$ is mean squared displacement, K_B is Boltzmann's constant, T is the temperature of the sample medium in Kelvin, t_s is the sampling time, η is the viscosity of the sample medium, and d_h is the hydrodynamic radius of the particle

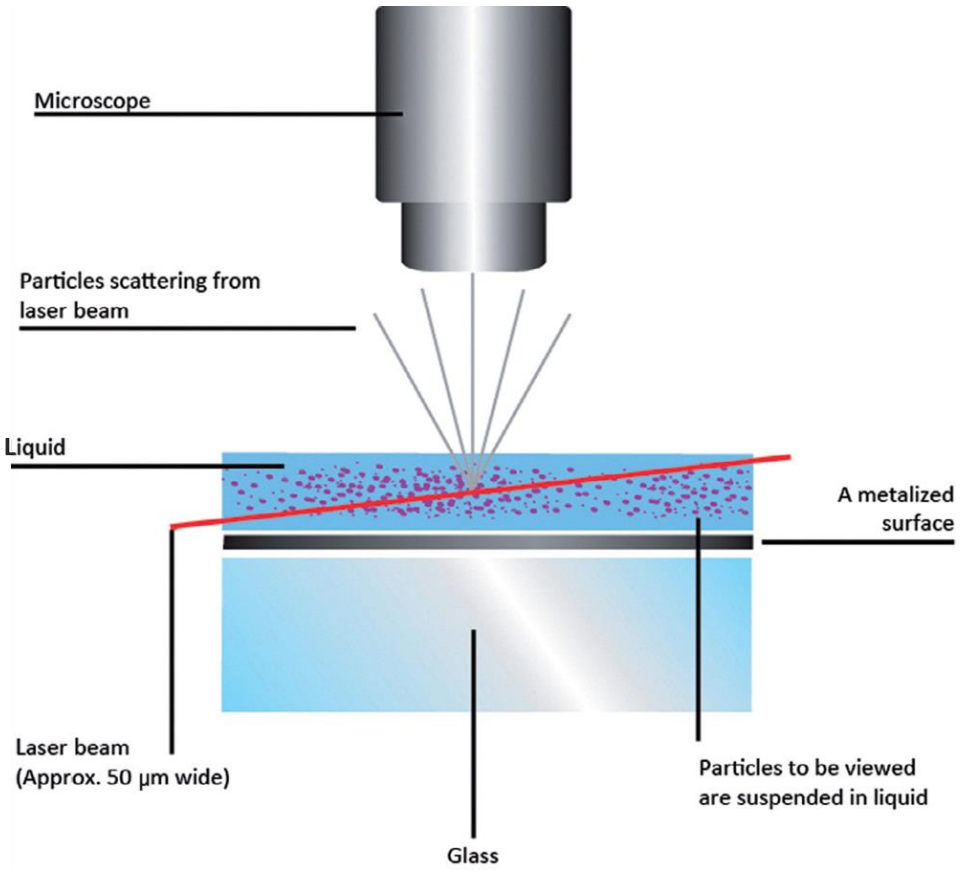

Figure 1.3: Schematic of NanoSight instrumentation for small particle analysis. Reprinted from *Materials Today, 14, Andrew Malloy, Count, size and visualize nanoparticles, 170-173., Copyright (2011)*, with permission from Elsevier

Analysis of EV populations with NTA has proven to be useful for both size distribution and concentration studies. Estimates of EV concentration by NTA give much higher results than counting by flow cytometry, by two orders of magnitude.[130,131] Concentrations obtained are accurate for samples within the range $1 \times 10^8 - 8 \times 10^8$ mL^{-1}, with size distribution comparable to electron microscopy.[130]

Different laser wavelengths are available for sample illumination, and bandpass filters can be added to the instrumentation to detect fluorescently-labelled particles. Comparing the profiles obtained by light scatter and fluorescent measurements can give an indication of population heterogeneity or could indicate the presence of non-EV contamination. For example, plasma samples labelled with quantum dot-labelled cell tracker peptide showed greatly reduced particle concentrations measured with the fluorescence filter than by light scatter, due to the presence of contaminating lipid particles.[130] The ability of NTA to measure proteins on EVs using fluorescence is a promising, high-throughput alternative to Western

blot analysis with reduced sample pre-processing, especially for samples obtained in small volumes, such as blood or urine from mice.[132]

NTA has also been useful to assess the separation efficiency and storage conditions of EV samples by measuring the changes in particle concentration and size distribution. No difference was found in the size or stability of EV samples after multiple centrifugation steps at 110,000 *g* for 2 hours.[133] The optimal conditions for storage of unprocessed urine was -80°C with protease inhibitors. This results in some particle loss compared to fresh samples, but the loss was reduced when compared to other storage temperatures (-20°C, 4°C, and room temperature) and when compared to samples without protease inhibitors. Isolated EV samples were found to be stable in storage at 4°C for up to 48 hours, and multiple freeze-thaw cycles had no effect on the size distribution.[133]

1.3.3.5 Tunable resistive pulse sensing

Tunable resistive pulse sensing (TRPS) calculates the size of particles based on the Coulter principle, which measures the resistive pulse generated by the particle moving through a pore. A membrane with a cylindrical or conical pore separates two chambers, one containing sample and the other with an electrolyte solution.[134] The resistance of the pore is determined by application of a voltage across the pore and measurement of the electric current. EVs move through the pore by a combination of convective and electrophoretic flow caused by the application of external pressure and voltage, respectively. Diffusion rates of EVs are negligible. When a particle moves through the pore, the resistance across the pore increases, measured as a drop in the current, termed 'blockade height'. The decrease in current is used to calculate the resistive pulse, which is proportional to the volume of the particle.[134,135] In TRPS, the lower detection limit is based on the pore size, stability of the current, and conductivity of the sample medium. Tunable resistive pulse sensing systems allow for the pore diameter to be changed by stretching of the membrane.[136]

The rate of particle flow across the membrane is determined by pressure and is not influenced by electro-osmosis or electrophoresis and diffusion rates of EVs are negligible, so difference in the zeta potential of samples and calibration beads is not a source of error, meaning concentration can be calibrated accurately.[118] Non-specific binding of sample constituents to the pore can cause blockages, leading to drops in current and unstable and reduced reproducibility of measurements. Application of a coating solution to the membrane can prevent this non-specific binding.[115]

The minimum detection size can be improved using high currents and low pore stretching, which causes increased blockade height. However, limiting pore stretching can cause clogging. Blockade height is reduced by an increase in pressure, however low sample concentrations require high pressures. Using a fixed blockade height strategy, the reproducibility of the minimum detectable size and concentration determination were improved.[137] Maximum detection size is also limited by the pore size. Clogging of the pore can occur for larger particles, and unclogging, which is fixed by reversing the pressure or applying a temporary high pressure using a plunger, may change the pore dimensions.

Sample volumes required for TRPS are small, approximately 40 µL. Measurement time for a sample is on the order of 30 minutes, consisting of 3 calibration measurements, sample measurement at 3 different pressures, with 3 replicate sample measurements.[115] Some instruments can give measurements of size distribution, concentration, and zeta potential of particles.

In a comparison to EV analysis by other methods, TRPS had the lowest observed error for determining concentration of an EV sample.[118] Dedicated small-particle flow cytometry showed the lowest error in the calculation of EV size, however it underestimates the particle concentration 15-fold. Thus, TRPS was determined to show the highest reproducibility for EV analysis. Measurements of EV size and concentration obtained by TRPS are comparable to TEM, NTA, DLS, and SAXS.[116]

1.3.3.6 Flow cytometry

The intensity of scattering of particles with diameters smaller than the wavelength of light, such as EVs, is inversely proportional to the sixth-power of particle size, meaning the scattering detection limits of many flow cytometers is 300-500 nm; reducing the detection limit from 200 nm to 100 nm would require 60-fold increase of signal to noise. However, virus particles down to 60 nm diameter have been detected by flow cytometry.[138] The refractive index of particles being measured is also important as sub-micron particles with higher refractive indices have greater forward scatter intensity in flow cytometry, which is used as an estimate of particle size. 0.4 µm polystyrene beads have the same light scattering intensity as 1 µm cellular particles, which is 36-times higher forward scattered light intensity than 0.4 µm synthetic lipid vesicles. Platelets have the same scatter profile as 0.9 µm polystyrene beads.[139] The resolving power of flow cytometers is instrument dependent, with older models unable to resolve 0.5 µm polystyrene beads and others resolving 0.2 µm beads.[139]

Analysis of EVs by flow cytometry can be misleading due to the presence of contaminants with similar biophysical properties such as size and scatter profiles. Immune complexes have been detected in the EV gate of flow cytometry.[128] Incubation of the sample with detergent, such as 0.05% Triton X-100, can cause EV-lysis, thereby estimating the EV contribution to the observed signal.[128] Platelet free plasma analysed by flow cytometry show continuous distribution of particles in the 1-2 µm gate down to the resolution limit of 0.4 µm, indicating that platelet-sized particles remain in the preparation.[139] The light scattering intensity of sub-cellular particles decreases non-linearly with size, and the angle of scatter also changes to larger angles for smaller particles. Cells typically scatter at angles <2°, so setting the minimum forward scatter detection angle to 14° increases the signal to noise ratio for smaller particles to be detected.[138,140] Using fluorescent threshold to trigger data acquisition rather than light scattering profiles allows the detection of particles which are too small to pass the light scatter threshold, and may help reduce spurious results due to coincident particles.[141] Equipping the instrument with a higher-powered laser, such as 200 mW rather than 25 mW, increases the sensitivity of the fluorescence triggering.[142] EVs can be analysed by dual staining with a lipid membrane dye for fluorescent triggering and general EV detection, alongside antibodies for analysis of surface markers.[140] BODIPY-maleimide, or bio-maleimide, can also be used to non-specifically stain EVs by binding of the maleimide to thiols of cysteine residues and thiols on membrane proteins,[143] and the lipid membrane intercalator PKH67 is also efficient at labelling EVs.[142] EVs should be quantified prior to staining for flow cytometric analysis to ensure optimal staining conditions are used.[144] Removal of unbound fluorescent labels from the EV sample is important, as dye aggregates may occur which could be mistaken for EVs. Separation of unbound dye by density gradient floatation is more effective than ultracentrifugation.[142]

The ImageStream imaging cytometer can be used to detect EVs. This instrument uses a CCD rather than photo multiplier tubes, and records 12 images in 10 fluorescent channels as the sample passes though the flow cell. EVs as small as 20 nm have been detected.[145]

1.3.3.7 EV clearance

EVs are released from many cell types in health and disease, and can be taken up by recipient cells. There has been a growing interest in the application of EVs in therapy, by using synthetic EVs to carry therapeutic agents directed against the target cells, or EVs from mesenchymal stem cells which may have regenerative properties. In order to make full use of this potential

application, the distribution and clearance of EVs has been studied. EVs can be taken up by Kupffer cells, which are specialised phagocytes in the liver, and phagocytes in the spleen, as well as undergoing endocytosis by dendritic cells and processed for antigen presentation.[146] EVs injected intravenously into mice were found to have a half-life of 2 minutes,[147] and localised mainly in the liver and spleen where they were taken up by Kupffer cells and macrophages,[147–152] similar to synthetic liposomes and other nanoparticles. EVs may also be trafficked to specific sites. For example, EVs derived from B16-BL6 melanoma cells, which has a tendency to form lung metastases, were observed to localise to the lung 4 hours after injection.[147,148] CD169 on macrophages in the subcapsular sinus and medulla of lymph nodes and marginal zone of the spleen has been shown to be important for the capture and clearance of EVs derived from B cells by binding with α2,3-sialic acid present on the EV surface.[153]

1.3.3.8 EVs in cancer

One of the major areas of study with regards to EV function is the role these particles play in cancer. The number of EVs present in the blood of cancer patients is often higher than that found in healthy controls,[154] however the concentrations observed depend on the pre-analytical variables and separation techniques used. The concentration of disease-specific EVs has been shown to decrease after treatment, such as surgical resection[155,156] or chemotherapy.[157,158] Most of the EVs found in the blood of healthy volunteers are derived from platelets.[154]

EVs retain markers of the tumour from which they are derived and can be used as a cancer biomarker. EVs from B cell lymphomas have been shown to express CD19[154] and CD20,[159] hepatocellular carcinoma EVs can be differentiated based on CD147,[155] CD138 is present on multiple myeloma EVs,[154,160] and a panel of protein markers has been used to identify EVs associated with prostate cancer.[161] EVs may carry copies of oncogenic mutations, such as *KRAS* mutants in pancreatic ductal adenocarcinoma,[162] the *c-MYC* oncogene,[163] or the oncogenic form of EGFRvIII in glioma,[164] as well as specific miRNA species[156,158] and functional mRNA which can activate translation to increase the metastatic potential of recipient cells.[165,166] The presence of these cargoes in EVs can be used as liquid biopsies to detect these specific disease subtypes in patients. EVs termed 'large oncosomes' have also been studied, which are cancer cell derived EVs larger than 1 μm. Organelles such as lysosomes and mitochondria have been observed in these large EVs.[167]

EVs in cancer have been shown to induce endothelial cell tube formation and angiogenesis.[168–170] EVs may also contribute to immunotherapy resistance by carrying on their surface the protein targets against which therapeutic antibodies are directed. For example, EVs derived from B cell malignancies can act as decoys of anti-CD19[167] or anti-CD20[159,171] immunotherapy, and HER2 expression on EVs can inhibit the anti-HER2 antibody Trastuzumab used in breast cancer therapy.[172] Breast cancer EVs have also been shown to display a larger form of VEGF which has reduced affinity for the anti-VEGF antibody Bevacizumab, thereby reducing the effects of this therapy.[168] EVs have also been shown to supress anti-tumour immune responses, by inactivating NK cells or CD4+ T cells,[173] activating regulatory T cells,[174] or induction of T cell apoptosis via FasL.[175,176]

Cancer derived EVs have been shown to alter the stromal cells within the tumour, such as chronic lymphocytic leukaemia EVs activating stromal cells to a cancer-associated fibroblast phenotype,[170,171] enhanced monocyte survival resulting from the transfer of CCR6 and CD44 after EV phagocytosis,[177] or inducing a metabolic switch from oxidative phosphorylation to aerobic glycolysis.[157] EVs released from pro-tumour stromal cells have also been shown to contribute to disease pathogenesis, such as cancer-associated fibroblast EVs conferring resistance to gemcitabine therapy in pancreatic ductal adenocarcinoma,[178] and TAM EVs conferring cisplatin resistance in gastric cancer.[179]

A number of studies have linked cancer-derived EVs with priming the pre-metastatic niche by travelling to sites such as lymph nodes, lungs, and liver, resulting in the recruitment of tumour cells to these distal sites.[180–183]

The concentration of EVs has been correlated with disease stage in a number of cancer types, including haematological malignancies,[154,160] ovarian cancer,[184] and prostate cancer.[166] Phenotypic associations have also been observed, such as the correlation between proteases carried within EVs and tumour malignancy and invasion,[184] the levels of transient receptor potential channel TRPC5 on EVs associated with chemoresistance in breast cancer,[185] IL-31 and IL-31R expression correlated with stage in FL patients,[186] and a panel of five proteins which can distinguish between high-grade and low-grade disease in prostate cancer patients.[161]

1.3.3.9 ApoEVs

EVs derived from apoptotic cells (apoEVs) appear to have different characteristics to EVs derived from their viable counterparts. Apoptotic cells release more EVs than non-apoptotic

counterparts.[187–190] Apoptotic cells also released larger EVs than untreated controls.[87,188] ApoEVs have been found to contain DNA which had undergone internucleosomal cleavage.[144,188,189,191] However, other studies have not detected histone proteins in apoEVs.[87,192] Apoptotic cells can release EVs which have autoantigens exposed on the surface, inducing dendritic cells to a pro-inflammatory phenotype thereby contributing to autoimmune disorders such as Sjögren's syndrome[193] and systemic lupus erythematosus.[194]

Apoptotic cells have been observed to shed the chemokine CX3CL1,[64] and the 'eat-me' signal ICAM3,[195] from the cell surface through apoEVs, and these apoEVs showed chemotactic recruitment of macrophages. IgM promotes the clearance of apoEVs and apoptotic bodies of < 2 μm by macrophages.[196] ApoEVs have been shown to exhibit desialylated glycoepitopes, an 'eat-me' signal caused by caspase activity during apoptosis, which can enhance macrophage clearance of apoEVs.[191]

Uptake of apoEVs by cancer cells increased cell motility and invasion properties both *in vitro* and *in vivo*.[87,197] Glioblastoma cells also showed increased resistance to apoptosis from different stimuli likely caused by spliceosomal proteins in the apoEVs affecting genes responsible for DNA damage repair and stress response.[87]

1.4 Raman spectroscopy

When light interacts with a molecule, the light can be absorbed or scattered. Absorption of light requires that the energy of the incident light is the same as the difference in energy between the ground electronic state (E_0) and an excited state (E_1), whereby the energy of the light is used to promote an electron to the higher energy orbital (Figure 1.4). Scattering of the incident radiation does not require a photon with a specific energy. The incident light interacts with the molecule by causing a distortion of the electron cloud due to polarisation, forming a short-lived 'virtual' energy state. This virtual state is not stable and so the light is released immediately as scattered radiation. If the electron polarisation occurs without any nuclear movement in the molecule, there is no change in the energy of the scattered light compared to the incident light and this is said to be an elastic process (Figure 1.4). This is known as Rayleigh scattering, and is the dominant mode of light scattering.

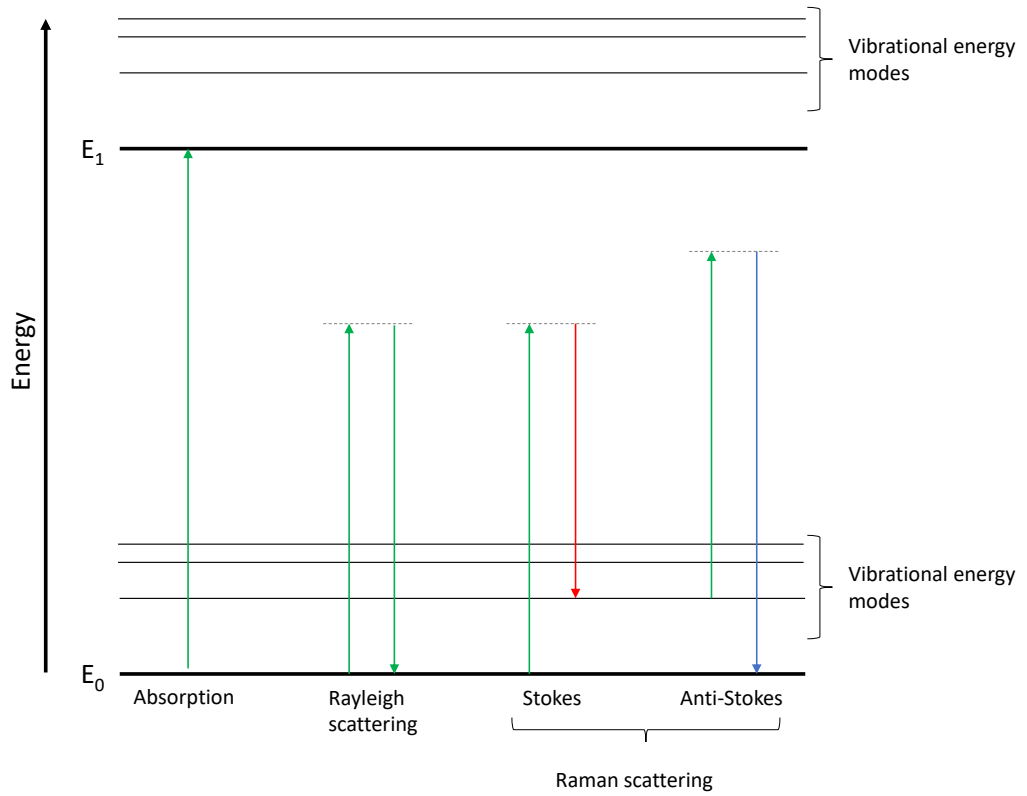

Figure 1.4: Jablonski diagram showing energy transfer in absorption and scattering. E_0 and E_1 represent the ground state and excited state orbitals, respectively. Upward arrows represent the incident radiation interacting with electrons of the molecule and downward arrows represent the scattered light.

However, if nuclear motion occurs when the molecule is in the virtual state, the photon will transfer energy to or from the molecule and the energy of the scattered light will no longer be the same as the incident radiation.[198] This is known as Raman scattering and occurs for every 10^6-10^8 incident photons. If the molecule originates in the ground state, then it will return to the first excited vibrational state and the scattered light will be of lower energy than the incident light, this is known as Stokes scattering. If the molecule interacts with the incident radiation when in a vibrationally excited state, then the scattered radiation is of higher energy and is known as anti-Stokes scattering (Figure 1.4). Stokes scattering is the dominant form of Raman scattering.

The amount of energy lost from the incident radiation during Raman scattering is equal to the frequency of the molecular vibrations. Bonds consisting of lighter atoms (e.g. C-H) vibrate with higher frequencies than bonds consisting of heavier atoms (e.g. C-S).[198] Bond strength also plays a factor in the vibration frequency, with stronger bonds having a higher frequency.[198] By measuring the frequencies present in the scattered radiation, information

about the molecular bonds present in the sample can be inferred. In this way, Raman spectroscopy is a label-free spectroscopic technique which gives detailed information about the functional groups present in a sample.

1.4.1 Application of Raman spectroscopy in biological analysis

The label-free nature of Raman spectroscopy makes it useful for the analysis and characterisation of biological systems. Traditional biochemical assays acquire measurements from bulk samples, such as ELISA and Western blots, and probe for only one analyte at a time, often requiring multiple complex sample preparation steps. Other single cell analytical techniques can be based on the use of fluorescent markers, such as flow cytometry or fluorescent microscopy, but the number of markers which can be analysed at one time is limited by the number of excitation wavelengths available and the number of fluorophores which can be resolved at those wavelengths. Raman spectra have narrow bands which allow the identification of multiple biomolecules in a single spectrum without any labelling required. Raman spectra also inherently contain a large amount of information about the sample, and multivariate analysis techniques can use this information to identify very small changes between samples of similar biochemical composition.

Raman spectroscopy has been used to distinguish between different modes of cell death,[199,200] differentiate cancerous cells from healthy cells[201,202] and tissue obtained from different anatomical sites,[203] determine the distribution of biomolecules within cells,[204–206] and the response of cells to toxins.[207] Raman spectroscopy can also be a useful tool when combined with biosensors.

1.4.1.1 Parameters for Raman data acquisition in biological systems

The development of Raman microscopes has allowed the simultaneous visualisation of sample and data acquisition. In this way, spectral data can be related back to the cellular localisation. Raman microspectroscopy has great potential for clinical applications but it is a low throughput technique. A Raman flow cytometer has been developed to try to overcome this issue.[208] Raman spectra were acquired from a sample moving through a flow cell, analogous to a conventional fluorescent flow cytometer. The collection of Raman spectra is triggered by a change in the forward scattered light. Signal intensity can be improved by reducing the flow rate of the sample to increase the integration time, using higher powered lasers, or using surface enhanced Raman spectroscopy nanoparticles for detection. This has the potential for sensitive multiplexed detection.

Thurn and Kiefer described the first use of optical trapping in combination with Raman spectroscopy in 1983.[209] The levitation of micron-sized particles resulted in the avoidance of background signal from a supporting substrate and the optimal focus of the particle within the laser beam. Optical levitation is caused by the exertion of forces of a continuous wave Gaussian-mode laser. Vertical forces act against gravity to support the weight of the particle, and deflection of laser light causes the transverse motion of the particle into the centre of the beam, creating an optical potential well. The particle will be suspended at a point above the beam waist, where the laser force acting upwards is equal to the gravitational force acting downwards, and any displacement from this position will cause restoring forces to bring the particle back to this position.[209] If the instrumentation is set up such that this optical potential well is at the sample focal position point of a spectrometer, simultaneous trapping and Raman measurements can be carried out. Using a 514.5 nm laser with 500 mW power, Thurn and Kiefer measured Raman spectra from 30 μm glass spheres and non-spherical quartz microcrystals. Optical levitation, or laser tweezers Raman spectroscopy (LTRS) was used for the first time on red blood cells in 2002.[210] The device was set up using a lower laser power to trap the cells and a higher power to acquire the Raman spectra, to reduce damage to the cells. Since then LTRS has been applied successfully for the study of individual cells many times.[210–215]

The excitation wavelength chosen for analysis is very important. The Raman scattering effect is inversely proportional to the fourth power of the wavelength, meaning that shorter wavelengths generate higher intensity scattering.[198] This is important to maximise the signal to noise ratio of the inherently weak Raman effect. However, shorter wavelengths are not compatible with biological systems; the damaging effects of UV and shorter visible wavelengths on cells are well documented.[216] Some studies have shown that photodamage and bleaching of samples can occur at wavelengths such as 457.9 nm, 488 nm, and 514.5 nm, but not 632.8 nm or 660 nm.[217] Fixed peripheral blood lymphocytes (PBLs) were observed to be resistant to photodamage using 647 nm laser excitation at 70 mW for up to 100 seconds exposure time,[205] but this wavelength can also cause photodamage of carotenoid protein after repeated spectral acquisition of the same cell.[218] Exposure of red blood cells to 785 nm excitation at 20 mW of power for 15 minutes also caused degradation of the Raman spectrum, which was not observed with 2 mW.[210] The overall energy dose of the irradiating light is the limiting factor rather than the laser power itself, and in general near IR wavelengths induce less damage than shorter wavelengths.[217]

1.4.1.2 Fixation of biological samples for Raman spectroscopy

Chemical fixation methods are often employed in biological analysis to preserve cells and tissues from damage which may occur in the time between sample preparation and analysis. However, these processing methods can alter the structure of the tissue and generate contaminating peaks derived from the fixative, impacting the Raman spectrum. Tissue sections are formalin-fixed paraffin preserved (FFPP) by embedding in a block of wax which allows easy cutting of tissue sections, however wax peaks can be present in the Raman spectra of these samples.[219] Often for immunohistochemical staining, a dewaxing procedure is carried out. Dewaxing using xylene is not always efficient and can leave some residual wax peaks in the spectrum.[219] Dewaxing can also remove lipids from the tissue, as these have a similar fatty acid chain structure to the wax.[203,220] This removal of lipids can have a profound impact on the Raman analysis of the tissue, as seen when tissue samples from the back of the hand and the thigh were analysed.[203] Analysis of unprocessed tissue samples showed discrimination between tissue obtained from the hand and the thigh, but this distinction between anatomical sites was removed after FFPP and dewaxing of the samples due to the loss of extracellular lipids. Structural alterations were also seen in the same study, where the thickness of the epidermal layers changed after processing. Freezing tissue is also used as a method to aid in cutting of tissue sections. However, freezing conditions are known to disrupt cytoskeletal proteins, and this can be observed as a decrease in some protein bands in cryosectioned tissue.[219] Tissue fixation with formalin caused a reduction in the amide I band at 1637 cm^{-1} due to the cross-linking of proteins in the sample. Treatment with xylene after formalin fixation can cause contaminating peaks due to the presence of xylene but can also reverse some of the cross-linking caused by formalin, restoring the amide I band.[219]

Studies have also been carried out on fixation methods used for single cells and the effects these can have on the resulting Raman spectra. It appears that different methods of fixation affect the spectra to varying degrees and may be dependent on the cell type used. HaCaT keratinocyte cells subjected to air-drying, desiccation, or formalin fixation showed that formalin fixation had the greatest impact on the cell spectra, showing greatly reduced peak intensities.[221] However, when principal component analysis (PCA) was carried out on the data, the formalin fixed cells had the tightest cluster of the three groups indicating high levels of sample consistency using this fixation method. The opposite was true for the macrophage line MM6, which had higher signal intensity observed in the formalin group, but PCA identified air-drying to generate the most reproduceable results for these cells. Another

study using formalin, Carnoy's fixative, and methanol-glacial acetic acid (Meth-Ac) to fix HaCaT keratinocytes, BEAS2B bronchial epithelial cells, and A549 adenocarcinoma cell lines gave mixed results.[222] Meth-Ac appeared to result in better preservation of lipid moieties in A549 cells, and Carnoy's fixative resulted in protein peaks having a greater similarity to unfixed cells in the BEAS2B line. However, PCA results showed that the formalin fixed cells were most similar to the unfixed cell of each type. A study in which B and T lymphoblastic cancer cell lines were fixed with either paraformaldehyde or -20°C methanol found that the duration of fixation was important, as the magnitude of the spectral changes were greater in the methanol fixed cells, but increasing the formalin incubation time increased the magnitude of the changes seen with this method.[212] Formalin fixed cancer cells could be distinguished from normal peripheral blood lymphocytes, while the methanol treatment impaired the delineation between these groups, indicating that formalin is the better fixative for these cells.[212] Thus the choice of fixative must be carefully considered before carrying out a Raman experiment.

1.4.1.3 Reproducibility of biological Raman data acquisition

Intracellular variation is one of the main challenges of obtaining representative Raman spectra of cells. Different organelles will have different spectral signals depending on their biomolecular composition, and features which are indicative of cell state, such as cell cycle, viability, or cell type, may be localised to a single organelle. This intracellular variability, combined with intercellular variability, requires a large number of cells to be sampled in order to develop an accurate model for the identification of different cell types and states. Intracellular variability may be overcome by acquiring Raman 'images' or 'maps' of the entire cell. A sample area is marked out for analysis and multiple Raman spectra are obtained at defined step sizes across this area to create a hyperspectral data cube. These data can then be used to generate a mean spectrum for the cell as a whole or measure the distribution of biomolecules across the cell by representing peak intensities for specific biomolecules as a false colour image. However, cell mapping can be time consuming and is not suited to high throughput applications. On the other hand, Raman spectra acquired from a small number of locations within a cell may not be representative of the cell as a whole. One study showed that, although individual spectra appeared to show that protein and lipid levels remained the same and nucleic acid content decreased after doxorubicin treatment of Jurkat T cells, analysis of whole cell data showed that the size of the treated cells had increased.[223] Thus, the nucleic acid concentration had not changed, and the amount of protein and lipid had

actually increased, but this was not represented by point spectra. Some studies have looked to find the minimum number of individual cell spectra which are needed to accurately represent the mean cell spectrum derived from a map. One study found that just 30 randomly selected spectra from a cell map could accurately replicate the total biomolecular content of cells which had been calculated using whole cell data.[224] When creating classification models, it was found that between 84 and 104 spectra from cell maps were needed to train the model in order to yield a sensitivity of greater than 90%, dependent on cell type. When a single point spectrum was used rather than mapping data, many more training spectra were required (164 in one cell type, >250 in the other two).[225]

1.4.1.4 Biochemical analysis using Raman spectroscopy

Raman microspectroscopy can be used to monitor the change in cells over time. Time-lapse imaging of PBLs was carried out to generate Raman maps of entire cells in under 2 minutes.[218] Successive maps could be acquired of the same cell until the cell either moved away from the acquisition area or the membrane started blebbing indicating cell death had occurred.

Raman maps of cells have been used to show the variation in intensity of a certain biomolecular peak over the cell area, to give an indication of the distribution of this group intracellularly. For example, the DNA signal in PBL nuclei was found to have much greater intensity than that found in the nuclei of lens epithelial cells.[204] The nuclei of the epithelial cells are larger in diameter than those of PBLs, and transcriptional activation in the epithelial cells causes decondensation of the chromatin, both of which lead to lower intensity Raman bands. Raman DNA peak intensities may also be able to distinguish between cells in different stages of the cell cycle.[226]

Different methods of data analysis of Raman spectra can give meaningful results. While univariate analysis, in which changes in individual peaks between samples are compared, may be useful in some situations, there are many methods of multivariate analysis of Raman spectral data that can take into account changes across the entire spectrum. PCA is a method of data reduction which can be used to infer the biochemical differences between different groups of cells. One study found that when a group of samples analysed by PCA had fewer contributing spectra than other groups in the analysis, the contribution of the spectra from the smaller group to the PC loading was decreased, resulting in the reduction of the relative scores of the smaller group for that PC.[227] Thus, the number of datapoints in each group for

PCA analysis should be equal when attempting to distinguish between different cell types or treatment effects.

Comparison of colorectal cancer cell lines derived from a primary and secondary tumour showed separation by PCA, suggesting that the secondary tumour had higher levels of β-sheet proteins and porphyrins while the primary tumour had higher levels of α-helix proteins and lipids.[228] PCA was able to distinguish melanoma cell lines from melanocytes, and separate melanoma cell lines with different mutations from the wild-type cells.[201]

Separation of different types of cells can be done by PCA in combination with linear discriminant analysis (LDA) to build a classification model. For LDA the number of input variables must be smaller than the number of samples, so the entire Raman spectrum cannot be analysed as the number of wavenumbers analysed is usually larger than the sample size.[229] In PCA-LDA, the PCs generated in PCA are used as the variables for LDA. PCA-LDA has been used many times to create classification models for cancer diagnosis. A classification accuracy of 98% was achieved in distinguishing the two colorectal cancer cell lines SW480, a primary colon adenocarcinoma, and SW620, a lymph node metastasis derived from the same patient.[230] A classification accuracy of 100% was obtained in distinguishing four different lung cancer cell lines and a normal lung epithelial cell line.[202] PCA-LDA has also been used to analyse serum samples from patients with colon cancer, rectal cancer, and healthy controls, with an identification accuracy of 88%.[231]

Support vector machine (SVM) models have also been using for classification. One group has carried out repeated studies to distinguish cancer cells from leukocytes and erythrocytes using SVM, with the goal of identifying circulating tumour cells in blood.[213,232,233] An acute myeloid leukaemia cell line (OCI-AML3) and two different breast cancer cell lines (BT-20 and MCF7) were used in these studies. The model was first tested using data from cell maps of dried samples, and the classification of a mixed sample of the cells was verified by staining the epithelial cells with an anti-EpCAM fluorescent antibody.[232] Using LTRS, the cells were analysed in suspension resulting in a prediction accuracy of 99.54% for leukocytes and erythrocytes and 99.74% accuracy in the cancer cell lines identification.[233]

K-means clustering is a technique where spectra can be clustered together based on their spectral similarity, identifying common biochemical signatures for groups of spectra. False-coloured maps can be produced identifying the clusters, along with the mean spectrum for each region. This has been successful for the analysis of tissue samples to detect different

layers of skin,[203] or different structural features of a tissue biopsy such as fibrosis or adipose cells.[220]

In classical least squares (CLS) analysis, a linear combination of reference spectra is used to estimate the percentage of pure components which make up the observed Raman spectrum of a sample, which allows quantitative analysis of spectral changes of cells under different conditions. This technique has been used to show that RNA levels decrease in embryonic stem cells undergoing differentiation.[229] Mouse embryonic stem cells showed a reduction of 38% in the amount of RNA present, while foetal osteoblasts displayed a 20% reduction in RNA after 7 days of differentiation and 45% reduction after 14 days, without changes to any other biomolecular components.

1.4.1.5 Analysis of cell death by Raman spectroscopy

There are many methods available to establish the viability of a cell population. As mentioned in Section 1.2.1, flow cytometry is often used to measure the exposure of PS and integrity of the membrane using fluorescently labelled AxV and propidium iodide. Caspase-3/7 substrates are also available which become fluorescent when cleaved by these enzymes and can be used in microscopy to detect apoptotic cells. However, these methods require exogenous labelling with fluorescent markers. Many studies have used Raman spectroscopy to distinguish between viable and apoptotic cells in a label-free manner, which can allow the same cells to be measured many times in a time lapse study[234] or even be used in further assays.

Cytochrome c, which is released form the mitochondria during apoptosis, shows absorbance at 413 nm, 520.8 nm, and 530.9 nm. Thus, cytochrome c is resonant at 532 nm laser excitation which is often used for Raman spectroscopy, resulting in enhancement of depolarised and amorphously polarised bonds due to π-π* Q transitions of the porphyrin ring.[235] Peaks due to resonant cytochrome c vibrations are observed at 714 cm^{-1} (symmetric pyrrole folding), 747 cm^{-1} (pyrrole breathing), 1127 cm^{-1}, 1314 cm^{-1}, and 1583 cm^{-1}.[202,235] Distribution of cytochrome c in apoptotic HeLa cells was analysed after treatment with Actinomycin D and the 750 cm^{-1} peak decreased, indicating release from the mitochondria causing loss of localised concentration and a drop in peak intensity (Figure 1.5).[206] Labelling the cells with the fluorescent mitochondrial stain Mitotracker confirmed that the cytochrome c signal was no longer in the mitochondria after treatment. Another study showed a decrease in the

cytochrome c peaks at 745 cm^{-1}, 1127 cm^{-1}, and 1314 cm^{-1} in Jurkat cells stored in PBS at 4°C for 3.5 hours using LTRS.[211]

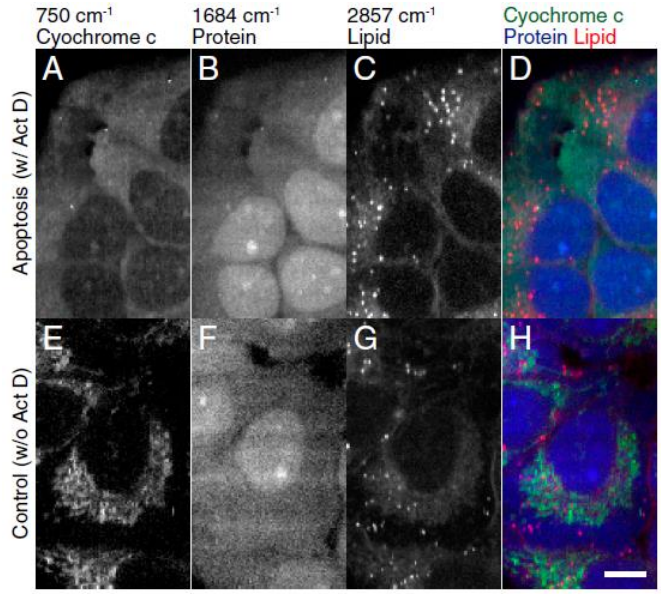

Figure 1.5: Distribution of cytochrome c (A,E), protein (B,F), and lipid (C,G) seen in apoptotic (A-D) and non-apoptotic control (E-H) HeLa cells shown as false coloured images generated from Raman spectral data. (D) was created through merging images A-C, and H was generated from merging images E-G. Reproduced from *M. Okada et al., Proc. Natl. Acad. Sci., 2012, 109, 28–32*.

Raman studies of apoptotic cells show changes in a number of peaks associated with nucleic acids. The 780-800 cm^{-1} band, which includes contributions from the phosphodiester DNA backbone, has been shown to decrease in apoptotic cells, [199,207,215,223,226,236–238] likely caused by internucleosomal cleavage.[236] Other nucleic acid peaks shown to be decreased in apoptotic cells include 1095 cm^{-1},[215,223,226,239,240] 1322 cm^{-1} and 1342 cm^{-1},[215,226,238] and the 1338 cm^{-1} adenine and 1578 cm^{-1} guanine bands.[215,223,240] CLS analysis has also showed a decrease in the contribution from DNA and RNA signals in apoptotic cells.[223,237,239] The 788 cm^{-1} phosphodiester band appears to be the most sensitive to change during apoptosis, and although the 1095 cm^{-1} phosphodioxy band is less sensitive, it has been shown to shift to 1090 cm^{-1}.[238]

Other studies have shown an increase in nucleic acid peaks in apoptotic cells, including an increase in the 788 cm^{-1} to 1005 cm^{-1} peak ratio in breast cancer cell lines treated with etoposide,[234] an increase in the 831 cm^{-1} phosphodiester peak in BL cells treated with paclitaxel,[240] and 4-fold increase in the DNA signals in apoptotic HeLa cells compared to viable counterparts.[205] It may be that these studies are detecting changes occurring at an earlier

stage of apoptosis, where the nucleus has condensed but not yet fragmented, thereby increasing the local nucleic acid concentration resulting in higher peak intensities.

Protein signals have also been observed to decrease in apoptotic cells, including bands at 623 cm^{-1} (phenylalanine, Phe),[236] 645 cm^{-1} (tyrosine, Tyr),[236] 938 cm^{-1} (α-helices),[236] 1005 cm^{-1} (Phe),[207,226,236,238,240] 1052 cm^{-1},[199,236] 1210 cm^{-1},[240] 1231 cm^{-1} (random coil),[226] and a decrease in width of 1660 cm^{-1} amide I band indicating a change in protein conformation.[226] However, CLS analysis of proteins in apoptotic cells has yielded mixed results, with some reports showing a slight increase in protein concentration,[223,224] one study showed no change in overall protein concentration,[237] and one report showed a decrease in the contribution of protein.[239]

Lipid peaks have been reported to increase in apoptotic cells, including those at 720 cm^{-1} corresponding to phosphatidylcholine,[237,238] 1158 cm^{-1},[237] 1303 cm^{-1},[207,214,236] 1649 cm^{-1} to 1005 cm^{-1} ratio,[234] and 1743 cm^{-1}.[214,236] An increase in lipid concentration was seen by CLS[223,224,237,239] and distribution of the lipid signals have shown the formation of lipid droplets.[205,234] Lipids can also be monitored in the high wavenumber region. After loss of membrane integrity in Jurkat cells, a decrease in the peaks at 2850 cm^{-1} and 2875 cm^{-1} were observed. These peaks have been associated with the packing and conformation of lipids, indicating that the membrane environment in these cells has been disrupted.[241]

Analysis of necrotic cells showed an increase in protein peaks and a shift in the 1658 cm^{-1} amide I band,[199] with a decrease in nucleic acid and lipid peaks.[239] The relative percentage of protein content in necrotic cells was seen to increase by CLS analysis, although the absolute protein concentration in these cells is lower than that of viable cells.[239]

Multivariate analysis has also been carried out on Raman data from cells at different stages of death to investigate the biochemical changes. PCA of Jurkat T cells exposed to different concentrations of doxorubicin for different amounts of time show differing biochemical groupings of cells based on the concentration and time, with the cells exposed to the higher concentrations showing spectral changes faster than the lower concentrations.[214] The treated cells were grouped into three clusters. Group 1, containing spectra from 24-hour 0.1 μM doxorubicin treatment, showed increases in lipid signals. Group 2, containing spectra from 48-hour 0.1 μM doxorubicin treatment and 24-hour 0.5 μM doxorubicin treatment, showed increases in DNA signals over control, possibly indicating nuclear condensation. Group 3, containing 48-hour and 72-hour spectra from the 0.5 μM doxorubicin treatment,

showed reduction in the nucleic acid bands compared to control, suggesting that nuclear fragmentation had occurred in this group. This suggests that the apoptotic process can be followed by Raman spectroscopy to identify different biochemical changes at the different stages. Other groups have also shown a separation of apoptotic cells from viable cells by PCA.[199,215,223,237,240] PCA of Raman spectra of melanoma cells which had been treated with either staurosporine to induce apoptosis, 3-bromopyruvate to induce necrosis, or resveratrol to induce autophagy, showed some slight separation of the three groups of treated cells and viable controls, although the autophagic cells were similar to viable.[201]

SVM models have also been used to distinguish between cell viability states. One study generated a model which had 100% accuracy for viable, 94% accuracy for early apoptotic, 92% accuracy for late apoptotic and 97% accuracy for necrotic cells.[199] Another study trained an SVM model using data from untreated, etoposide treated (apoptotic), and Triton X-100 (necrotic) A549 cells, which was then used to predict mode of death for cell exposed to mild heat (45°C). The etoposide, Triton X-100, and viable cells were all correctly classified, and the heat treatment was also correctly classified as apoptotic.[200]

PCA-LDA has also been used to classify apoptotic and necrotic cells. K562 leukaemia cells were classified as viable, apoptotic, or necrotic with 100% accuracy.[239] PCA-LDA was able to differentiate not only untreated from treated cells, but also distinguished between ricin and sulfur mustard treatment in A549 cells with a sensitivity of 71% and 88%, respectively, and could distinguish between the concentration of sulfur mustard used with an accuracy of 93%, as lower concentrations induce apoptosis and higher concentrations induces necrosis.[207] PCA-LDA of paclitaxel treated BL cells showed a classification specificity of 75%, 85%, 95%, and 100% for the 0.05 μg/mL, 0.5 μg/mL, 1 μg/mL, and 5 μg/mL treatment concentrations, respectively, when compared pair-wise with untreated control cells, with a sensitivity of 100% for each group.[240] Thus, Raman spectroscopy gives accurate representations of the biochemical changes occurring in cells undergoing cell death.

1.5 Surface-enhanced Raman spectroscopy

Surface-enhanced Raman spectroscopy (SERS) is a variant of Raman spectroscopy in which the Raman scattering intensity is increased due to plasmonic interactions. The phenomenon was first observed in 1974, when Fleischmann *et al*. recorded Raman spectra of pyridine at a silver electrode.[242] It had been proposed that the stronger signal intensity came from the increased surface area of the probe caused by the oxidation-reduction cycles, however

further study showed that the surface area was only increased by 10-20% whereas the signal intensity of the ring-stretching bands were 5-fold higher than for pyridine in solution.[243] As the spectra in solution were obtained as a result of light scattering from 4 x 10^5 times more molecules than were adsorbed on the sample area of the electrode, it was implied that the silver electrode increased the scattering cross-section of pyridine with an enhancement factor roughly of the magnitude 10^5. It was already known that electromagnetic fields applied to roughened metal surfaces could cause oscillations of the metallic conduction electrons, generating a plasmon resonance effect which localised the strength of the electromagnetic field about the particle (Figure 1.6), and it had even been proposed that monolayers of molecules on these metals could interact with the surface plasmon to cause Raman transitions.[244]

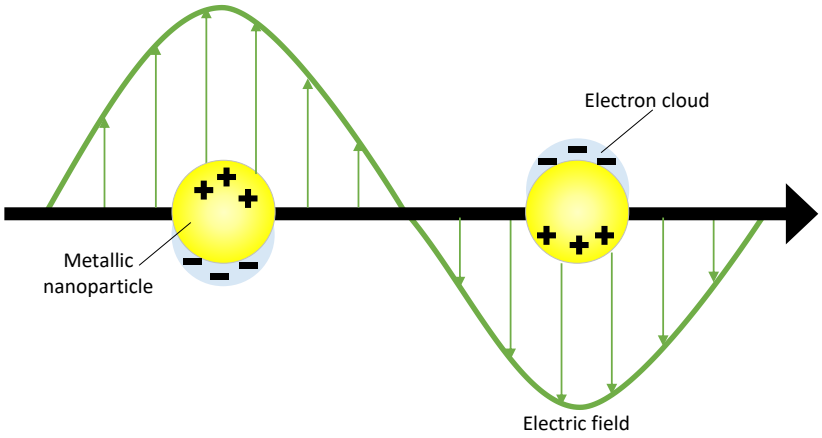

Figure 1.6: Schematic of the localised surface plasmon resonance of a noble metal nanoparticle in an electromagnetic field showing oscillation of the electron cloud of the metal to cause enhancement of Raman signals.

It is now generally accepted that the SERS effect is caused by two factors: the electromagnetic enhancement due to the surface plasmon resonance, and a chemical enhancement due to coupling of a molecule with the metallic surface. The electromagnetic enhancement is the dominating effect, which can cause enhancements of molecules not directly attached to the metal up to nanometre distances from the surface. The chemical enhancement effect can contribute enhancements factors of up to 10^4 due to charge transfer from the metallic surface to the molecule, or from the molecule to the metallic surface.[245]

The observed enhancement factor of a SERS system is dependent on a number of parameters, such as the wavelength of incident light, dielectric constant of metal used, the size and shape of nanoparticles (NPs).[246] The enhancement effect tends to increase as the NP

size increases. Larger NPs absorb less light and scatter more due to scaling differences between absorption and scattering. The surface plasmons of metal NPs in close proximity can couple with each other to form 'hot spots', generating enhancement factors of up to 10^{12}.[246] These coupled NPs show red-shifting of the plasmon resonant wavelength compared with isolated particles. The magnitude of the red-shift is dependent on the NP size and the distance between the NPs.[247] Large enhancement factors are also seen for non-spherical particles which have sharp protrusions.[246]

As SERS enhancement is strongly distance-dependent, dye molecules are often used to coat the surface of the SERS NPs for use as SERS reporter molecules. Reporters can be effective by adsorption onto the NP by electrostatic interaction, however choosing reporters which can chemisorb to the metallic surface can make use of the chemical enhancement effect to yield stronger signals. For example, malachite green (MG) is a dye molecule which has been used as a SERS reporter, and adsorbs onto the surface of gold nanoparticles (AuNPs) via a dimethylamino group (Figure 1.7A). However, modification with an isothiocyanate (ITC) group to MG (MGITC) adds a sulfur atom (Figure 1.7B), which has a strong affinity for gold and can thus chemically attach to the surface. Spectral analysis shows that MGITC has 200-fold higher enhancement factor than MG, due to the chemical coupling effect.[248] If the reporter has an absorption band at the wavelength used for SERS excitation, this gives a further enhancement factor, termed surface enhanced resonance Raman scattering (SERRS). Many different reporter molecules have been synthesised to optimise the chemical and resonant enhancement effects for sensitive SERS detection.[249–251] DNA also has a strong intrinsic Raman spectrum dominated by Stokes scattering of adenine giving a sharp peak at 736 cm^{-1} which could be useful as a SERS reporter.[252]

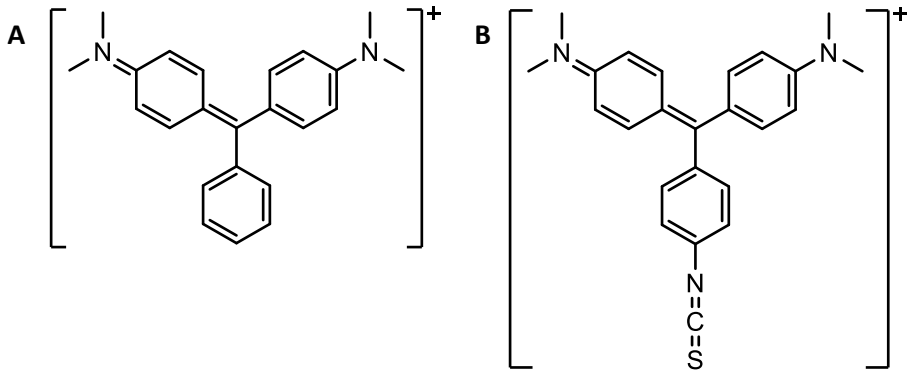

Figure 1.7: Structure of malachite green (A) and malachite green isothiocyanate (B)

Interest in the SERS effect became more widespread when the sensitivity of the technique was demonstrated by detection of single molecules. Typical scattering cross-sections of Raman-active molecules are 10^{-30} cm^2/molecule and require signal enhancement by a factor of 10^{14} to achieve single molecule detection. This was achieved by two groups in 1997, using silver nanoparticles (AgNPs) to detect the reporter molecules crystal violet[253] and rhodamine 6G (R6G).[254]

1.5.1 Applications of SERS

SERS has proven to be useful for a number of applications requiring the sensitive detection of different molecules, such as explosives,[255] drugs,[256] pH sensing,[257] and reactive oxygen species sensing.[258] As the spectral resolution of SERS is much greater than analogous techniques such as fluorescence, where the full width at half maximum (FWHM) of Raman spectral features can be as small as 2 nm, SERS has great potential for multiplexed analysis for the detection of multiple analytes in a single sample. This is very useful in biological systems, where complex biochemical information requires multiple measurement parameters to accurately reflect the conditions of the biological environment.

1.5.1.1 *In vitro* biochemical SERS sensing

The sensitive nature and rapid sample preparation and analysis times of SERS mean that it has great potential for use in the clinic. For example, rapid and accurate detection of different types and species of bacteria is important clinically in order to reduce the overuse of antibiotics to prevent the generation of antibiotic resistance. Multiplexed SERS analysis has been shown to be able to distinguish between different types of bacteria with a LOD of 10^2 CFU/mL,[259] and was even successful in distinguishing between different strains of *E. coli*.[260]

Gold is more biocompatible than silver for incorporation into cells, and the enhancement factors for AgNPs and AuNPs are similar when using NIR wavelengths.[261] Incubation of unlabelled AuNPs with HT29 epithelial cells showed enhancement of the biochemical Raman signals of the cells, showing peaks attributed to the DNA phosphate backbone at 1120 cm^{-1}, Phe at 1004 cm^{-1}, and other nucleic acid and protein signals.[261] The characteristic biochemical bands found in Raman spectra due to CH stretching at 1450 cm^{-1} and the amide I band at 1650 cm^{-1} are not seen in the SERS spectra.

Confocal mapping of the distribution of carbohydrates could be useful for the detection of cancer cells, as cancer cells show different glycan profiles to heathy counterparts.[262] Using

SERS nanotags conjugated with lectins to detect cell surface carbohydrates was found to have better discriminating power for distinguishing prostate cancer cells from prostate epithelial cells than using fluorescently-labelled lectins.

By combining Raman spectra with SERS detection of nanotags, 3D volume mapping of a cell can give detailed cellular localisation information of nanoparticle uptake. Multiplexed detection of a mixture of AgNPs with three different reporter molecules were observed within the cell volume, and showed that the AgNPs do not localise to the nucleus and are contained mainly in the cytoplasm.[263] Triplex detection has also been carried out on chronic lymphocytic leukaemia cells to detect CD20, CD19, and CD45 on the cell surface.[264] However, these mapping studies are not high throughput, with 3D volume maps taking between 3 and 5 hours to analyse a single cell.[263]

Flow cytometry is a standard high throughput biochemical analysis technique which uses fluorescently-labelled molecules for analysis of single cells. The broad spectral features of fluorophores limit the number of molecules which can be detected simultaneously. Many groups have adapted flow cytometers to be able to detect signals from SERS NPs, either by exchanging a fluorescent filter in the instrument with a narrow bandpass filter matching a peak in the SERS spectrum of the SERS reporter molecule,[264] or enabling the detection of a full spectrum of the reporter with just 10 μs acquisition time by transmitting Raman scattered light through an optical fibre for dispersion by spectrograph onto a CCD.[265] This 'flow spectroscopy' technique can detect single SERS NPs in order to determine interparticle signal variability within batches which are not detectable in bulk spectroscopic analysis or by analysis of a narrow spectral band.[266,267] A microfluidic chip has also been used for the detection of SERS NPs on cells.[268] In this study, cells were incubated with NPs against a cancer-specific protein target or a general cell targeting molecule in order to distinguish between cancer and normal cell populations. Cells were individually flowed through the device with an integration time of 5-8 ms, allowing the analysis of approximately 1700 events in an overall run time of 8 minutes.

SERS techniques have also been used to examine the biochemical changes in cells caused by apoptosis. SERS NPs with different reporter molecules were conjugated with antibodies against either BAX or BAD, two pro-apoptotic members of the BCL-2 family of proteins, and used to stain mouse lung tissue.[269] By mapping the distribution of the characteristic peaks for each reporter, colocalization of BAX and BAD were seen using a single tissue sample. Cellular

uptake of AuNPs labelled with nuclear localisation signal were used to monitor nuclear changes in response to apoptosis. SERS signals increased over the course of progression of apoptosis, with the distribution of signal becoming more widespread throughout the cell as the nucleus fragmented.[270] Silicon wafers decorated with AgNPs have also been used to monitor the nuclear changes in cells grown on the wafer after exposure to an apoptotic stimulus. The SERS signal intensity of the 788 cm^{-1} DNA peak increased up to 24-hours post-incubation with low concentrations of Triton X-100, indicting nuclear condensation. Fragmentation and internucleosomal cleavage was then seen by the decrease in SERS signal at 48 and 72-hour time points.[271] AgNPs have also been formed *in situ* on apoptotic cells using negatively-charged PS as the nucleation centre for Ag^{+} reduction. Cells treated with staurosporine showed formation of AgNPs on the membrane surface and generation of SERS signals from membrane components such as proteins and lipids.[272] A combination SERS-fluorescence resonance energy transfer (SERS-FRET) assay making use of the quenching effect of AuNPs has been used to quantitatively detect cytochrome c release in apoptotic cells, with accuracy similar to ELISA.[273]

1.5.1.2 *In vivo* biochemical sensing

SERS can also be used for *in vivo* biochemical sensing. The biodistribution of NPs is dependent on the NP size, charge, and hydrophobicity. Smaller NPs show increased permeability and diffusion coefficients through tissue than larger particles.[274] 15 nm AuNPs have been found to traverse the blood brain barrier after intravenous injection,[275] and were also found in the lungs and circulation. Increasing the particle size reduces the accumulation of NPs in lungs, brain, and blood and increases the distribution in sites such as liver and spleen.[275] Studies of biodistribution of NPs after intravenous injection has found that that particles are rapidly taken up by cells of the reticuloendothelial system (RES) and can be found in Kupffer cells and macrophages in the spleen.[276] Alteration of the nanoparticle surface by coating with hydrophilic polymers such as polyvinylpyrrolidone (PVP)[276] or polyethylene glycol (PEG)[277] results in reduced uptake by the RES and longer half-life in circulation.

Multiplexed detection of SERS NPs has been shown in *in vivo* systems. The accumulation of a mixture of four different non-targeted nanotags in the liver of mice was detected, with a correlation observed between the concentration of each reporter and the signal obtained.[278] Targeting of SERS NPs has also been achieved, where AuNPs conjugated with anti-EGFR antibody localised to an oral squamous cell carcinoma in a mouse xenograft model after

intravenous injection; AuNPs without the targeting antibody were only detected in the liver.[279] The signal was stably detected in the tumour up to 8 days post-injection, whereas the signal in the liver was cleared after 48 hours. Targeted detection of three nanotags in a breast cancer xenograft in mice has also been successful.[280] Multi-modal NPs have also been used *in vivo*. Lanthanide-based upconversion fluorescent nanoparticles conjugated with SERS AgNPs subcutaneously injected into mice could be detected using both fluorescence and SERS.[281]

These multiplexed detection experiments require high-resolution maps of the target area, which can take many hours and is not suitable for clinical applications. One group has developed a widefield imaging system using bandpass filters at varying angles, which changes the centre wavelength of transmission to correspond to a particular peak in a reporter molecule.[282] This system has a spatial resolution of 50 µm and 1 cm^2 illumination spot, for an acquisition time of less than 5 seconds per bandpass image using 785 nm laser excitation at a power within the American National Standards Institute (ANSI) exposure limit for skin and tissue penetration depth of 5 mm. Using this system, a mixture of four SERS nanotags injected subcutaneously into mice was deconvoluted, with a linear response achieved between each tags concentration in the mixture and the signal intensity of a characteristic peak of the nanotag (Figure 1.8).[282] A fibre-optic device has been designed for the acquisition of SERS spectra during endoscopy. The fibre bundle can fit through the instrument channel of a clinical endoscope and detect Raman signals with working distances of 1-10 mm.[283] Multiplexed detection of four nanotags was achieved with this system after topical application to ex vivo human colon tissue with 300 ms integration time. The device has been further adapted to allow signal detection by circumferential scanning, scanning the entire area of 2 feet of colon in just 10 minutes which can be carried out in parallel with the white light endoscopy procedure.[284]

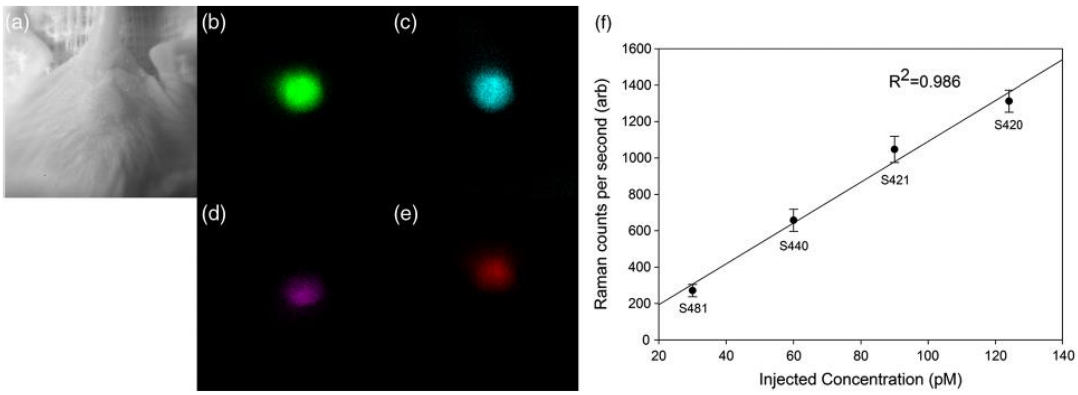

Figure 1.8: Multiplexed in vivo delineation of SERS nanotags using a widefield imaging technique. A single injection site into a mouse (A) was used, containing four different reporters (B-E) was used, and the detection algorithm could distinguish between each reporter and a linear response was observed between concentration and signal intensity of a characteristic peak of the reporter molecule (F). Image reproduced from *P. Z. Mcveigh, R. J. Mallia, I. Veilleux and B. C. Wilson, J. Biomed. Opt., 2013, 18, 046011*.

Although SERS AuNPs and AgNPs show little cytotoxicity, and the biocompatible coatings used prevent leaching of the reporter molecules from the NP surface, FDA approval is required before SERS NPs can be injected and studied in human trials.

1.6 Aims

It is well established that certain cancer types, such as Burkitt's lymphoma (BL), have high rates of 'constitutive' apoptosis occurring within the growing tumour before any cytotoxic treatment is administered. In these tumours, apoptosis is correlated with poor prognosis, as the tumours also display rapid proliferation and pro-tumour survival pathways. It is also known that, while EVs are released from all cells to varying extents depending on disease status or conditions of environmental stress, apoptotic cells can release more EVs and larger EVs than their viable counterparts which may contribute to the conditioning of the tumour microenvironment to promote tumour growth and survival mechanisms.

The central hypothesis of this work is that comparison of Raman spectral data obtained from EVs derived from apoptotic and control BL cells could be used as a label-free technique to determine whether there are biochemical differences between cargo of apoEVs and EVs which are not derived from apoptotic cells which could underlie distinct functional behaviours for these particles.

Sensitive analyte detection can be achieved using SERS, which can also identify subpopulations within a sample by using targeting molecules attached to the surface of the

SERS nanoparticles. In order to identify targets for the preferential detection of lymphoma-derived EVs over those derived from healthy B cells, gene expression profile data will be used. This is an unbiased, bioinformatic method to identify genes which are upregulated in lymphoma samples when compared to normal B cell counterparts, with the hypothesis that genes which are overexpressed in lymphoma would be suitable targets for the preferential detection of lymphoma-derived EVs in the peripheral blood of patients. Proteomic analysis of BL apoEVs and viable EVs will also be used to identify potential targets which can discriminate between these subgroups for SERS detection.

2 Materials and Methods

A full list of consumables and equipment used can be found at the end of the chapter (Section 2.11).

2.1 Cell line maintenance

All cell lines were kept at 37°C in 5% CO_2 humidified atmosphere.

2.1.1 BL2 and BL2-bcl2

BL2 and the apoptosis-resistant stable transfection of BL2 cells with *BCL2*[285] (BL2-bcl2) cell lines were grown in serum-free conditions, using a 1:1 mixture of RPMI 1640 and X-VIVO 20.[286] Cells were kept at a density below 1 x 10^6 mL^{-1} by passaging with fresh medium every 2-3 days.

2.1.2 HeLa

HeLa cells were grown in 75 cm^2 tissue culture flasks in Minimum Essential Medium Eagle (MEM) supplemented with 10% foetal calf serum (FCS), 2 mM L-glutamine, 100 U/mL penicillin, 100 µg/mL streptomycin, and 1% non-essential amino acids (100 X). When cells reached 80% confluency, the culture medium was removed, and the monolayer was washed with 20 mL Hank's balanced salt solution (HBSS) without calcium or magnesium. 5 mL of 0.05% trypsin/EDTA was added and incubated at room temperature for 1 minute, then the excess trypsin/EDTA was removed and the flask incubated at 37°C for 5 minutes or until the cells had detached from the culture flask. 6 mL of culture medium was then added to neutralise the trypsin. 1 mL of this cell suspension was added to a fresh 75 cm^2 tissue culture flask and 20 mL of culture medium added.

2.2 Bioinformatic analysis of gene expression profiles

2.2.1 Selection of datasets

Gene expression microarray datasets were downloaded from the online database Gene Expression Omnibus (GEO; http://www.ncbi.nlm.nih.gov/geo/). The database was accessed in February 2015. The datasets chosen were all from human samples and had all been carried out on the Affymetrix Human Genome U133 Plus 2.0 Array chip (Platform GPL570).

B cell samples were found by searching GEO Datasets for the term "healthy B cells". Data series were examined to find experiments which had used untreated B cell samples from healthy donors, and these CEL files were downloaded. The combined files contained samples

from peripheral blood mononuclear cells in which the B cells had not been isolated, as well as B cells which had been isolated based on specific cell surface antigens (e.g. CD19+ CD27+; CD20+ CD10- CD27+) and samples derived from tonsillar tissue and bone marrow.

Lymphoma samples were found by searching for "Burkitt lymphoma" or "non-Hodgkin lymphoma" and choosing samples from untreated cell lines or from fresh biopsy tissue.

2.2.2 Data pre-processing

The downloaded CEL files were combined into one folder for data pre-processing in the R environment (version 3.1.2) using packages from BioConductor version 3.0 (http://www.bioconductor.org).

The arrayQualityMetrics package[287] (version 3.22.1) was used to quality control the raw data. Samples were assessed for outliers using six different outlier detection metrics: distances between arrays, boxplots, relative log expression, normalised unscaled standard error, MA plots, and spatial distribution of M. If any sample was identified as an outlier by more than one metric, this sample was not used in further analysis. The data were normalised using the fRMA package[288] (version 1.18.0). The samples were annotated with Probe ID, Entrez ID, and HGNC symbol using hgu133plus2.db Affymetrix Human Genome U133 Plus 2.0 Array annotation data (version 3.0.0). The data were arranged into a table such that each row corresponded to a single probe sequence from the array, and the columns represented the expression levels of each probe sequence in a particular sample. The annotation data were used to generate a unique identifier for each row by concatenating the Probe ID, Entrez ID, and HGNC symbol.

2.2.3 Network generation and analysis

The expression table was imported into BioLayout *Express*^{3D} Version 3.3.[289,290] The Pearson correlation was set to 0.85 and Markov Cluster (MCL) analysis carried out with an inflation value of 2.2. This generated a 3D network graph consisting of over 1200 clusters. The mean expression pattern for each cluster was viewed, with the sample information available as coloured blocks annotating each sample. The expression levels of the genes for healthy B cell data, which were grouped together, was visually compared to the expression level in the lymphoma samples. When the expression level was considered to be higher in the lymphoma samples, the genes in that cluster were investigated for cellular localisation. Gene products that showed localisation to the plasma membrane were investigated further, cross-

referencing against gene expression profile data for the BL2 cell line which had been generated previously in the group (unpublished data), and a brief literature review of the protein function was carried out to determine whether the protein localised to the cortical membrane or had an external portion which could be used as an imaging target.

2.3 EV generation and separation

Extracellular vesicles (EVs) were generated from BL2 cells, BL2-bcl2 cells, and HeLa cells. BL2 cells and BL2-bcl2 cells were both UV-irradiated to generate apoptotic cell derived EVs (apoEVs) and EVs, respectively. For HeLa cells, apoEVs were generated from UV-irradiated cells and EVs were separated from HeLa cells under the same conditions but with no exposure to UV-B radiation.

2.3.1 Induction of apoptosis in cells

2.3.1.1 UV treatment of BL2 and BL2-bcl2 cells

BL2 and BL2-bcl2 cells were taken from culture and centrifuged at 300 *g* for 5 minutes at room temperature. The cells were resuspended in a small amount of 0.1 µm filtered RPMI/X-VIVO culture medium. 10 µL of this cell suspension was diluted with 990 µL of 0.1 µm filtered RPMI/X-VIVO and counted by flow cytometry. The acquisition volume was set to 150 µL with a flow rate of 100 µL per minute. 50 µL of the suspension was allowed to run through the cytometer before data was recorded. 10,000 events were recorded in the cell gate, and the concentration of cells (events/µL) in the viable cell gate was used to calculate the number of viable cells in the sample. The cell suspensions were then diluted accordingly to give a final density of cells of 20 x 10^6 mL^{-1}. The cell suspension was then placed in either a 25 cm^2 tissue culture flask (12.5 mL) or in the well of a 12-well tissue culture plate (1.5 mL per well). The cells were then exposed to 300 mJ/cm^2 UVB radiation in the form of six 50 mJ/cm^2 doses, with swirling of the flask between each exposure. The flasks were then incubated at 37°C in a humidified atmosphere with 5% CO_2 and progression of apoptosis was monitored every hour by dual staining samples with Annexin V (AxV) and Sytox Blue (SB) (2.5.1).

2.3.1.2 UV treatment of HeLa cells

1.5 x 10^6 mL^{-1} HeLa cells were seeded in a 25 cm^2 tissue culture flask in 5 mL of HeLa culture medium and incubated for 24 hours. Each flask was washed with 5 mL of 0.1 µm filtered HBSS before adding 5 mL of 0.1 µm filtered HeLa culture medium, made up without any FCS. Flasks were exposed to a single dose of 600 mJ/cm^2 UVB radiation. Control cells were seeded in the same manner but not exposed to UVB. The flasks were then incubated at 37°C in a humidified

atmosphere with 5% CO_2. The progress of apoptosis was not monitored, as the dose of UVB and appropriate incubation time to achieve apoptosis was optimised as described in Section 2.3.1.2.1

2.3.1.2.1 IncuCyte analysis of apoptosis progression in HeLa cells after UVB irradiation

HeLa cells were seeded in 100 µL of complete HeLa medium at 6000 cells per well in a 96-well tissue culture plate overnight. The culture medium was then removed and replaced with 100 µL of fresh medium. Each 96-well plate was exposed to a different dose of UVB radiation (0 mJ/cm^2, 450 mJ/cm^2, 600 mJ/cm^2, and 900 mJ/cm^2). After irradiation, 50 µL of the culture medium was removed and replaced with a 2x concentration of fluorescent reagents for measuring apoptosis (15 µM CellEvent, 6 µM DRAQ7). The plates were then placed into the tray of an IncuCyte ZOOM imaging plate reader. Plates were imaged using a 10x objective, with 4 images per well taken every hour for 17 hours using phase contrast, red fluorescent channel (DRAQ7) and green fluorescent channel (CellEvent). Three wells were imaged for each UVB dose, one well containing both CellEvent and DRAQ7, one well containing DRAQ7 only (as a control for the DMSO solvent for the CellEvent stock solution), and one well containing no fluorescent reagents. The number of fluorescent events was calculated using the IncuCyte ZOOM 2016B software. The number of green events per well was used to indicate CellEvent positive apoptotic cells, red events indicates DRAQ7 positive cells which are necrotic, and the number of cells showing overlap of green and red giving the dual positive cells which are secondarily necrotic.

To calculate the percentage apoptotic cells, the phase contrast images were used to count the total number of cells imaged using the Cell Counter plugin for ImageJ (version 1.51k). The number of red/green events per image was multiplied by 4 to find the total number of fluorescent events identified in the four acquired images. The percentage of CellEvent or DRAQ7 positive events was calculated as the total number of events divided by number of cells. The percentage viable (unstained) cells was calculated as 100-[(% CellEvent positive) + (% DRAQ7 positive) – (% Overlap)].

In order to find the optimum UV dose and incubation time, the ratio of CellEvent-positive events to DRAQ7-positive events was used to find the sample which had the highest number of apoptotic cells with the least amount of secondary necrosis.

2.3.2 Separation procedure for EVs

EVs were separated from cells which had been UVB-irradiated (Sections 2.3.1.1 and 2.3.1.2).

2.3.2.1 BL2 and BL2-bcl2

When the UVB-irradiated BL2 cells had reached approximately 70% AxV+ SB- as measured by flow cytometry dual staining (typically 5-6 hours post-UVB), the process of EV separation was initiated.

2 mL of the cell suspension was made up to 5 mL with 0.1 µm filtered PBS and centrifuged at 25 *g* for 60 minutes at 4°C in a 15 mL tube to remove the cells from the suspension. The top 4 mL of supernatant was removed and passed through a 5 µm mesh filter under gravity. This filtrate was then passed through a 1.2 µm syringe filter, where the plunger of the syringe had been removed to allow the suspension to filter under gravitational pressure. This 1.2 µm filtrate was used as the final EV suspension.

Where necessary, EVs in this 1.2 µm filtrate were pelleted by centrifugation at 20,000 *g* at 4°C for 60 minutes and resuspended in 0.1 µm filtered PBS.

2.3.2.2 HeLa

For the study of the kinetics of EV release from HeLa cells, cells were seeded and irradiated as described in Section 2.3.1.2. Six 25 cm^2 tissue culture flasks were irradiated, and six flasks were used as non-irradiated controls. At two-hour time points, beginning immediately after irradiation, both an irradiated and non-irradiated culture flask were removed from the incubator, the contents of the flask were swirled and the entire culture supernatant (5 mL) was removed. This supernatant was centrifuged at 250 *g* for 5 minutes to remove any cells which had detached from the culture flask. The supernatant was then filtered through a 5 µm mesh filter under gravity, and then a 1.2 µm syringe filter under gravity, as described in Section 2.3.2.1.

For comparison of UVHeLa EV and HeLa EV, the 1.2 µm filtrate of the 8-hour post-UV HeLa and UVHeLa samples was used. Where necessary, EVs in this 1.2 µm filtrate were pelleted by centrifugation at 20,000 *g* at 4°C for 60 minutes and resuspended in 0.1 µm filtered PBS.

2.3.3 Characterisation of EVs

The number of EVs present in each sample and the size profile of the EVs was determine by nanoparticle tracking analysis (NTA) using a NanoSight.

2.3.3.1 NanoSight analysis

EVs, as 1.2 µm filtrate or as resuspended 20,000 *g* pellet, were diluted 1 in 5 with 0.1 µm filtered PBS. The sample was loaded into the chamber of the NanoSight using a 1 mL syringe.

The camera level was set to 14, the low particle threshold was set at zero and the high particle threshold was set to 1495, and the instrument was calibrated to 187 nm/pixel. For each sample, 3-5 60 second videos were recorded at a rate of 30 frames per second, with the sample in the chamber being advanced by depression of the syringe plunger between each recording. For analysis of the videos, the detection threshold was set to 12 and the minimum expected particle size set to the minimum of 30 nm.

If the total particle concentration of the sample was outside of the 10^8-10^9 range advised by the manufacturer, the dilution of the sample was adjusted accordingly, and the sample was analysed again.

2.4 Western blot

2.4.1.1 Cell lysis

$3x10^6$ cells were pelleted and stored at -80°C. Samples were thawed on ice and lysed using 50 µL of cell lysis buffer (10 mM HEPES, 1 mM EDTA, and 1% Triton X-100) with 3.3 µL of protease inhibitor cocktail for 30 minutes.[291] The lysate was cleared by centrifugation at 14,000 *g* for 10 minutes at 4°C and the supernatant retained.

2.4.1.2 EV lysis

50×10^8 EVs, as quantified by NTA (Section 2.3.3.1), were pelleted by centrifugation at 20,000 *g* at 4°C for 60 minutes, and stored at -80°C. Samples were thawed on ice and lysed using 60 µL of cell lysis buffer with 6 µL of protease inhibitor cocktail for 20 minutes before syringing ten times with a 23G needle and syringe. Samples were left for a further 30 minutes on ice. Lysates were not cleared.

2.4.1.3 Bradford assay

The concentration of protein in the cell lysates was determined using a Bradford's protein assay.[292] The cell lysates were diluted 1 in 30 with water. Human IgG was used as a standard. A stock solution of 1 mg/mL was used, and six serial dilutions were performed. 10 µL of each sample, including a control sample containing only water, was added to a well of a 96-well plate and 190 µL of Bradford reagent diluted 1 in 5 with water was then added. Each sample was set up in triplicate. The absorbance at 595 nm was acquired using a Varioskan Flash plate reader. The mean absorbance of each sample was calculated, the absorbance of the control sample was subtracted, and the human IgG sample absorbances were used to draw a

standard curve of protein concentration against absorbance. The equation of this line was used to calculate the protein concentration in the cell lysate.

2.4.1.4 SDS-PAGE

For cell lysate samples, 10 µg of protein was made up to 6.5 µL with water. To this, 1 µL of 10x reducing agent and 2.5 µL of 4x sample buffer were added.

For EV lysate samples, to each 60 µL of EV lysate, 9 µL of 10x reducing agent and 22 µL of 4x sample buffer were added.

Samples were heated at 70°C for 10 minutes. 10 µL of cell lysate sample (10 µg protein) and 40 µL of EV lysate (equivalent to 25 x 10^8 EVs) were loaded into the wells of a pre-cast 4-12% Bis-Tris, 1.5 mm, 10-well protein gel. Gels were run in MOPS running buffer with the addition of 0.5 mL of NuPage Antioxidant at a constant voltage of 170 V for 70 minutes.

2.4.1.5 Protein transfer and membrane staining

The SDS-PAGE gel was equilibrated in transfer buffer for 5-30 minutes, then transferred onto a polyvinylidene difluoride (PVDF) membrane which had been pre-wet with methanol and equilibrated for 10 minutes in transfer buffer with 10% methanol at a constant voltage of 30 V for 90 minutes.[291] The membrane was washed in water for 10 minutes, then PBS + 0.1% Tween 20 (PBST) for 10 minutes. The membrane was blocked with 5% goat serum in PBST for 1 hour at room temperature, then incubated with 1-in-1000 dilution of primary antibody (anti-CD20 or anti-CD53) in 5 mL of 5% goat serum in PBS for 1 hour at room temperature, or at 4°C overnight. The membrane was washed with 5 mL of PBST three times for 10 minutes each, then incubated with a 1-in-5000 dilution of goat anti-mouse HRP secondary antibody in 5 mL of 5% goat serum in PBS for 1 hour at room temperature. The membrane was washed with 25 mL of PBST eight times for 10 minutes each, the developed with Amersham ECL Prime Western blotting detection reagent for 5 minutes. The membrane was then exposed to x-ray film in the dark and developed using Photon Imaging Systems Ecomax Automatic X-ray film processor.

For detection of β-actin, the membrane was incubated with a 1-in-5000 dilution of mouse anti-β-actin primary antibody, washed, and incubated with secondary antibody as above. The membrane was developed with Pierce ECL Western blotting substrate, exposed to x-ray film for 30 seconds and developed as above.

2.5 Flow cytometry

2.5.1 Cells – evaluation of apoptosis

For cell suspensions at a density of 20 x 10^6 mL^{-1}, 10 µL of cell suspension was diluted with 90 µL of cold Annexin V binding buffer (AxVBB; 10 mM HEPES, 2.5 mM $CaCl_2$, 140 mM NaCl, pH 7.4).[293] For other suspensions, 0.2-0.3x10^6 cells were pelleted in a FACS tube, the supernatant was removed, and the cells resuspended in 100 µL AxVBB.

1 µL of AxV488 was added to the tube and incubated for 15 minutes at 4°C in the dark. 400 µL of AxVBB was then added, followed by 0.5 µL of Sytox Blue (SB), which was allowed to incubate with the cells for 1 minute before analysis.

2.5.2 Cell phenotyping

BL2 cells were taken from cell culture and counted using a haemocytometer. Enough quadrants were counted in order to ensure the total number of cells counted exceeded 100, and the count was carried out in duplicate. Cells were pelleted at 300 *g* for 5 minutes and resuspended in cold PBS with 5% goat serum at a density of 1 x 10^6 mL^{-1}. 100 µL of this cell suspension was incubated in a FACS tube with the appropriate volume of antibody, or isotype control. Samples were incubated for 40 minutes at 4°C. The cells were washed three times with 3 mL of 5% goat serum in PBS, the cells were then resuspended in 500 µL of 5% goat serum in PBS and run on the flow cytometer with a stop point of 10,000 events recorded in the cell gate.

2.5.3 EV phenotyping

2.5.3.1 EV staining

80 µL of 1.2 µm EV filtrate, generated as described in Section 2.3.2.1, was diluted with 20 µL of 0.1 µm filtered 5% goat serum in PBS, to give a final concentration of 1% goat serum. The appropriate volume of antibody or isotype control was added, and 0.1 µm filtered PBS to give a total sample volume of 120 µL. The samples were incubated for 30 minutes at 4°C. 1.2 µL of 10 µM ATTO390-maleimide membrane dye was added and the samples incubated for a further 15 minutes at 4°C. 880 µL of 0.1 µm filtered PBS was then added. A no EV diluent control was made by adding 400 µL of RPMI/X-VIVO to 1.6 mL of PBS and 400 µL of 5% goat serum in PBS (all 0.1 µm filtered). The appropriate volume of ATTO390-maleimide dye or antibodies were added to 100 µL of this diluent and made up to 1 mL with 0.1 µm filtered PBS and analysed on the flow cytometer to optimise the settings as no EV controls.

2.5.3.2 Instrument set-up and EV analysis

For the flow cytometric analysis of EVs, the side scatter (SSC) filter of the instrument, an OD2-488/10 single-pass bandpass filter off of the 488 nm laser, was replaced with a custom filter which had a lower OD to allow more SSC light to pass through, making the instrument more sensitive in order to detect the small EVs. Fluorescence thresholding using the ATTO390-maleimide membrane dye (VL1 channel) was employed to further increase the sensitivity of detection for small particles. The acquisition volume was set to 500 µL, and flow rate was set to 12.5 µL/minute. Plots of SSC-H vs VL1-H and SSC-H vs FSC-H with axes set to log scale were used to detect EVs. 0.1 µm-filtered PBS was run in order to optimise the voltage settings. The VL1 threshold was adjusted so that background events were just visible in the SSC-H vs VL1-H plot with an event rate of 1-10 per second. The SSC voltage was adjusted to 50-500, and the FSC voltage set to 10,000. Unstained EVs were used to adjust the fluorescent voltages, so that the unstained particles had fluorescent values of 10^2-10^3. When samples were analysed, at least 25 µL of the sample was run through the cytometer before recording to allow the particles to focus. If the event rate was >500 events per second, the sample was diluted to achieve <500 events per second to avoid swarming artefacts. Samples were recorded with a time stop option of two minutes, to allow >10,000 events to be recorded.

2.6 Raman spectroscopy of EVs and cells

All Raman spectra were acquired using a Renishaw inVia spectrometer, with 532 nm laser excitation wavelength using a point illumination beam configuration, 2400 l/mm grating, slit opening of 65 µm, Renishaw CCD camera with dimension 1040x256 pixels, and 60x water immersion objective (NA 1.00). Samples were prepared and analysed on a CaF_2 window under PBS. At least 200 µL of each sample was used in order to have enough liquid on the 1 cm diameter CaF_2 window for the focal length of the objective to be achieved. Non-adherent samples were attached to the surface of the CaF_2 window using CellTak. 0.85 µL of 1 mg/mL Cell-Tak was diluted with 75 µL of 0.1 M $NaCO_3$ buffer pH 8 and placed on the CaF_2 window for at least 30 minutes. The CaF_2 window was then washed with 2 x 100 µL sterile water and allowed to dry.

2.6.1 Acquisition of Raman spectra from cells

2.6.1.1 BL2 and BL2-bcl2 cells

UV-treated BL2 and BL2-bcl2 cells were obtained from EV preparations as described in Sections 2.3.1.1 and 2.3.2.1. The remaining supernatant above the 25 *g* cell pellet was

removed and the cells were resuspended in PBS and fixed in 4% neutral buffered formalin (NBF) at a density of 1 x 10^6 mL^{-1} for 20 minutes at room temperature. The fixed cells were washed with PBS and resuspended in PBS at a density of 1 x 10^6 mL^{-1}.

Viable BL2 and BL2-bcl2 cells were taken directly from cell culture without any treatment. The viability was assessed by dual staining with AxV and SB as described in Section 2.5.1. The cells were fixed in the same manner as the UV-treated cells.

100 µL of these fixed BL2 and BL2-bcl2 cell suspensions (1 x 10^5 cells) were incubated on a Cell-Tak coated CaF_2 window for at least 1 hour in order to settle under gravity onto the Cell-Tak coating and allow the cells to adhere to the surface. An additional 200-300 µL of PBS was then applied to the window.

Viable and UV-treated BL2 and BL2-bcl2 cells were mapped in a single plane with a step size of 0.7 µm in both the x- and y-axis. Each spectrum of the map was acquired with an exposure time of 1 second and a laser power of approximately 35 mW with the spectrum centred at 1250 cm^{-1}. 10 cells were mapped for each experiment, and three independent experiments were carried out for a total of 30 cell maps for each condition.

Each map was pre-processed using the *Noise filter* function on the WiRE 4.2 Renishaw software to remove the noise components from the acquired map spectra.

2.6.1.2 HeLa and UVHeLa cells

1 x 10^5 HeLa cells were seeded onto a CaF_2 window which was placed in a 6-well tissue culture plate with 3 mL of complete HeLa culture medium for 48 hours.

For viable HeLa cells, the cells were washed with 3 mL of PBS and fixed with 4% NBF for 20 minutes. The cells were then washed with 2 x 3 mL of PBS.

For UV-treated HeLa cells (UVHeLa), cells on the CaF_2 window were washed with 3 mL of PBS before 3 mL of fresh culture medium was added. The cells were irradiated with one dose of 600 mJ/cm^2 of UVB radiation and incubated for 8 hours at 37°C in a 5% CO_2 humidified atmosphere. The cells were then washed gently with 3 mL PBS and fixed with 4% NBF for 20 minutes. The cells were then washed with 2 x 3 mL of PBS.

HeLa and UVHeLa cells were Raman mapped in a single plane with a step size of 1 µm in both the x- and y-axis. Each spectrum of the map was acquired with an exposure time of 1 second and a laser power of approximately 35 mW with the spectrum centred at 1250 cm^{-1}. 10 cells

were mapped for each experiment, and three independent experiments were carried out for a total of 30 cell maps for each condition.

Each map was pre-processed using the *Noise filter* function on the WiRE 4.2 Renishaw software to remove the noise components from the acquired map spectra.

2.6.2 Acquisition of Raman spectra from EVs

EVs from UV-treated BL2 and BL2-bcl2 cells, and HeLa and UVHeLa cells were prepared as described in Section 2.3. EVs from each cell condition were analysed by the same method.

200 µL of 1.2 µm filtrate EV suspension was incubated overnight at room temperature on the surface of a Cell-Tak coated CaF_2 window. The bulk of the remaining liquid was removed from the CaF_2 window with a pipette, and the window was washed gently with 2 x 100 µL of 0.1 µm filtered PBS before adding 200-300 µL of PBS. EVs were visualised using the white light source of the spectrometer. Two spectra were acquired for each EV at different spectral regions, one centred at 1250 cm^{-1} and one centred at 2850 cm^{-1}, with an exposure time of 10 seconds at a laser power of approximately 35 mW. The spectra of 50 EVs were acquired for each sample, with three independent replicate experiments, for a total of 150 EV spectra per sample.

2.6.3 Data-processing of Raman spectra

All spectra were converted to *.spc* files using the Renishaw inVia software WiRE 4.1 for import into MATLAB for data processing and analysis.

2.6.3.1 Data processing of Raman cell maps

Non-cellular background spectra of the Raman maps were removed by thresholding on the Phe peak at 1004 cm^{-1} to create a mask of the area of the cell and removing the spectra outside of the cell mask. The mean and standard deviation (SD) of the remaining spectra were calculated and any spectra lying outside the range of ±1 SD from the mean were removed as a quality control step. The mean spectrum for each of these cell maps was then found. The mean cell spectra were baseline corrected using the *baseline_correction* function from the cluster-toolbox-v2.0 on https://github.com/Biospec which employs an asymmetric least squares algorithm. The data were then scaled so the peak with the highest intensity was given an arbitrary intensity value of 1, so the different spectra could be easily compared. The spectra were converted to the first derivative and principal component analysis (PCA) was carried out on the data.

2.6.3.2 Data processing of EV spectra

The EV spectra were imported into MATLAB as *spc* files. These spectra were baseline corrected using the *baseline_correction* function from the cluster-toolbox-v2.0 on https://github.com/Biospec, which employs an asymmetric least squares algorithm. The data were then scaled so the peak with the highest intensity had an arbitrary intensity value of 1, so the different spectra could be easily compared. The spectra were converted to the first-order derivative and principal component analysis (PCA) was carried out on the data.

2.7 Synthesis of nanoparticles for surface enhanced Raman spectroscopy

2.7.1 Gold nanoparticle synthesis

Gold nanoparticles (AuNPs) were prepared using a modified version of the Turkevich, Stevenson, and Hillier citrate reduction method for preparation of gold colloid.[294]

All glassware was thoroughly cleaned and soaked overnight in aqua regia (3:1 v/v $HCl:HNO_3$). The clean glassware was rinsed with water until the washings were of neutral pH. 60.5 mg of sodium tetrachloroaurate was dissolved in 500 mL of deionised water and brought to boiling point with continuous stirring. A solution of 57.5 mg sodium citrate dissolved in 7.5 mL of deionised water was added rapidly and the solution was boiled for 15 minutes. The solution was cooled with stirring, and the AuNPs were analysed for LSPR by UV-vis spectrometry and for size and zeta potential using a Malvern Zetasizer.

2.7.2 Functionalisation of AuNPs with Raman reporter

A 100 mM stock solution of malachite green isothiocyanate (MGITC) was prepared in deionised water. 1 mL of AuNPs (0.2 nM) was placed in a 1.5 mL Eppendorf tube with the appropriate volume of MGITC stock to yield final MGITC concentrations ranging from 0.1-1 mM. The tube was placed on a shaker for 30 minutes, then the AuNPs were pelleted by centrifugation at 2320 *g* for 20 minutes. The supernatant was carefully removed and the AuNP pellet was resuspended in 1 mL of water.

2.7.3 Conjugation of antibodies to nanoparticles

A 1 mg/mL stock solution of *N*-Hydroxysuccinimide (NHS), and a 1 mg/mL stock solution of 1-ethyl-3-(3-dimethylaminopropyl) carbodiimide HCL (EDC) were made with deionised water. 74 µL of the EDC solution was added to 40 µL of 12.5 µM polyethylene glycol ($CT(PEG)_{110}$, MW 5000) solution, or to 40 µL of 1mM $CT(PEG)_{12}$ (MW 635). To 217 µL of NHS solution, 10 µL of anti-CD20 or anti-CD53 monoclonal antibody (mAb) (both at a

concentration of 1 mg/mL) was added. These NHS/mAb and EDC/PEG solutions were then combined in a 1.5 mL Eppendorf tube to which 709 µL of 10 mM HEPES buffer pH 7 was added and the solution was stirred overnight to generate PEG-functionalised mAb.

The PEG-functionalised mAb was added to the MGITC-functionalised AuNP (Section 2.7.2) split across two 1.5 mL Eppendorf tubes and placed on a shaker for 2.5 hours. The AuNPs were pelleted by centrifugation at 2320 *g* for 20 minutes. The supernatant was carefully removed and the mAb- and MGITC-functionalised AuNP pellet was resuspended in either 1 mL of water, for UV-Vis and Zetasizer analysis, or in 100 µL of 0.1% bovine serum albumin (BSA) in 10 mM phosphate buffer (PB; 7.54 mM sodium phosphate dibasic, 2.46 mM sodium phosphate monobasic) pH 7 for surface enhanced Raman spectroscopy (SERS).

2.8 SERS of MGITC- and antibody-functionalised AuNPs

2.8.1 SERS of functionalised AuNPs in solution

The MGITC-AuNPs, as prepared by the method in Section 2.7.2, were placed in a clear glass vial. The SERS spectrum of each concentration of MGITC-AuNP was acquired using a Snowy Range Sierra spectrometer using a 785 nm laser excitation with 45 mW laser power and integration time of 1 second.

2.8.2 SERS of MGITC-AuNPs on nitrocellulose

10 µL of MGITC-AuNPs as prepared by the method in Section 2.7.2 were dropped onto raw nitrocellulose and allowed to dry. SERS measurements were acquired using a Renishaw inVia Raman microscope, with 785 nm diode laser excitation wavelength using the StreamLine line illumination beam configuration, 1200 l/mm grating, slit opening of 50 µm, Renishaw CCD camera with dimension 1040 x 256 pixels, and 20x objective (NA 0.4). Three replicate maps were acquired at different areas of the AuNP spot for each MGITC concentration, of size 200 x 200 steps in x and y directions with 3.5 µm step size using 9 mW laser power with an integration time of 2 seconds. Maps were pre-processed using the cosmic ray removal wizard in WiRE version 4.4 and converted to *spc* files using WiRE version 4.1. The *spc* files were imported into MATLAB and the mean spectrum for each of the three maps was calculated individually, and the mean of these three mean spectra was then calculated as the representative SERS spectrum for that concentration of MGITC-functionalised AuNPs.

2.9 SERS MGITC-AuNP detection of biological samples

All SERS spectra of biological samples on nitrocellulose were acquired as StreamLine maps on the Renishaw inVia configured as described in Section 2.8.2. For the biological samples, the map size was 500 x 500 steps in the x and y direction with a step size of 3.5 µm. Spectra were acquired with 785 nm laser excitation using 9 mW laser power with an integration time of 2 seconds.

2.9.1 SERS measurements of cells

8.5 mL of BL2 cell suspension was taken directly from culture, pelleted at 300 *g* for 5 minutes, resuspended in 8.5 mL of PBS and counted using a haemocytometer. 4 quadrants were counted in order to ensure the total number of cells counted exceeded 100, and the count was carried out in duplicate. The BL2 cells were pelleted again and resuspended in PBS at a cell concentration of 10 x 10^6 mL^{-1}. The sample was further diluted so that six solutions with BL2 cell concentrations of 10 x 10^6 mL^{-1}, 9 x 10^6 mL^{-1}, 8 x 10^6 mL^{-1}, 7 x 10^6 mL^{-1}, 6 x 10^6 mL^{-1}, and 5 x 10^6 mL^{-1} were obtained. 1 µL of these cell solutions were spotted onto 1 cm x 1cm squares of raw nitrocellulose, with care being taken not to touch the tip of the pipette to the nitrocellulose, and the edges of the spot were marked with a pencil. When the nitrocellulose squares were dry, each was placed into the well of a 24-well tissue culture plate and blocked with 5% BSA in phosphate buffer (PB) for 1 hour at room temperature. 20 µL of anti-CD20 conjugated MGITC AuNP (0.84 nM), prepared as described in Section 2.7.3, was added to the nitrocellulose with 150 µL of 0.1% BSA/0.05% Tween 20 in 10 mM PB (BSA/PBT) and the samples were placed on a shaker for 1 hour at room temperature. The nitrocellulose squares were then washed with three 500 µL aliquots of BSA/PBT for 5 minutes each. SERS maps of the samples were then acquired as described in Section 2.9, with the area at the centre of the pencil marks chosen for analysis if there was not a visible AuNP spot. Maps were pre-processed using the cosmic ray removal wizard in WiRE version 4.4 and converted to *.spc* files using WiRE version 4.1. The *.spc* files were imported into MATLAB. The peak intensity at 1171 cm^{-1} was used to identify the presence of MGITC AuNPs, and to remove any false positive results due to high background, a signal-to-baseline peak intensity was generated by subtracting the intensity at 1140 cm^{-1} from the peak intensity at 1171 cm^{-1}. A false-coloured map was generated of this signal and the *thresh_tool* function was then used to generate a mask of the false-coloured map keeping only the pixels with an intensity value of greater

than 100. The number of pixels in this mask was used as a measure of the number of MGITC AuNPs bound on the sample.

2.9.2 SERS measurements of EVs

BL2 and BL2-bcl2 EVs were prepared as described in Section 2.3.2.1. Two 500 µL aliquots of 1.2 µm EV filtrate were pelleted at 20,000 *g* for 1 hour at 4°C. One pellet was resuspended in 1 mL of 0.1 µm filtered PBS and the concentration of EVs were quantified on the NanoSight as described in Section 2.3.3.1. The other EV pellet was resuspended in 100 µL of 0.1 µm filtered PBS and the concentration of EVs in this suspension was assumed to be 10x that found in the 1 mL suspension. If the EV concentration was >$40x10^8$ mL^{-1} then the sample was diluted to this concentration. If the EV concentration in the sample was <$40x10^8$ mL^{-1} then the sample was diluted to either $20x10^8$ mL^{-1} or $10x10^8$ mL^{-1}, as appropriate. Four EV suspension concentrations were investigated: $40x10^8$ mL^{-1}, $20x10^8$ mL^{-1}, $10x10^8$ mL^{-1}, and $5x10^8$ mL^{-1}. 1 µL of EV suspension (multiple 1 µL drops where necessary to reach desired EV concentration) was placed onto 1 cm x 1cm squares of raw nitrocellulose, with care being taken not to touch the tip of the pipette to the nitrocellulose, and the edges of the spot were marked with pencil. When the nitrocellulose squares were dry, each was placed into the well of a 24-well tissue culture plate and blocked with 5% BSA in PB for 1 hour at room temperature. 20 µL of either anti-CD20 (0.84 nM) or anti-CD53 (0.81 nM) conjugated MGITC AuNP, prepared as described in Section 2.7.3, were added to the nitrocellulose with 150 µL of BSA/PBT and the samples were placed on a shaker for 1 hour at room temperature. The nitrocellulose squares were then washed with three 500 µL aliquots of BSA/PBT for 5 minutes each. SERS maps of the samples were then acquired as described in Section 2.9, with the area at the centre of the pencil marks chosen for analysis if there was not a visible AuNP spot. Maps were pre-processed using the cosmic ray removal wizard in WiRE version 4.4 and converted to *spc* files using WiRE version 4.1. The *spc* files were imported into MATLAB. The peak intensity at 1171 cm^{-1} was used to identify the presence of MGITC AuNPs, and to remove any false positive results due to high background, a signal-to-baseline peak intensity was generated by subtracting the intensity at 1140 cm^{-1} from the peak intensity at 1171 cm^{-1}. A false-coloured map was generated of this signal and the *thresh_tool* function was then used to generate a mask of the false-coloured map keeping only the pixels with an intensity value of greater than 100. The number of pixels in this mask was used as a measure of the number of MGITC AuNPs bound on the sample. This experiment was carried out in triplicate, with

three independent EV preparations and the mean and standard deviation pixel number for each EV concentration was calculated. A control where no EVs were spotted on the nitrocellulose was also carried out, to identify background binding level of AuNP to nitrocellulose.

2.10 Chemicals and reagents

Reagent	Supplier	Catalogue number
1-Ethyl-3-(3-dimethylaminopropyl) carbodiimide HCL (Pierce)	ThermoFisher Scientific	22980
Amersham ECL Prime Western blotting reagent	GE Healthcare, Little Chalfont, Buckinghamshire, UK	RPNM2232
Amersham Hybond blotting paper	GE Healthcare	RPN6101M
Amersham Hybond P 0.45 PVDF Blotting Membrane	GE Healthcare	10600023
Amersham Hyperfilm ECL	GE Healthcare	28906837
Annexin V, Alexa Fluor 488 conjugate	Life Technologies (ThermoFisher)	A13201
ATTO390-maleimide	ATTO-TEC GmbH, Siegen, Germany	AD 390-41
Bovine Serum Albumin (BSA) Low Endotoxin Powder	ThermoFisher Scientific Leicestershire, UK	BP9705-100
Bradford reagent	BioRad, Hercules, CA,USA	500-0006
Calcium chloride	Sigma Aldrich, Poole, UK	C4901-100G
CellEvent Caspase 3/7 2 mM in DMSO	Life Technologies (ThermoFisher)	C10423
Corning Cell-Tak	ThermoFisher Scientific	CB-40240
CT(PEG)$_{12}$ Carboxy-PEG-Thiol	ThermoFisher Scientific	26133
DRAQ7 0.3 mM	abcam, Cambridge, UK	ab109202
Dulbecco's Phosphate buffered saline	Gibco, Paisley, UK	14190-094
EDTA Disodium Salt, Molecular Biology Grade	Promega, Southampton, UK	
FCS-SA	Biotech	Lot 30401
Goat serum	Biosera, Ringmer, UK	GO-605/500 (Lot 10075)
Hank's Balanced Salt Solution	Gibco	14175-053
HEPES	Sigma Aldrich	H4034-100G
L-Glutamine 200 mM (100 X)	Gibco	25030-024
Malachite green isothiocyanate	ThermoFisher Scientific	
MEM NEAA (100 X)	Gibco	11140050
Methanol analytical grade	ThermoFisher Scientific	M/4000/17

Millex-VV Syringe Filter Unit 0.1 µm	Merck Millipore, Hertfordshire, UK	SLVV033RS
Minimum Essential Medium Eagle	Sigma Aldrich	M2279-500ML
N-Hydroxysuccinimide	Sigma Aldrich	130672-5G
Novex NuPAGE 4-12% Bis-Tris protein gels, 1.5 mm, 10-well	Invitrogen, Paisley, UK	NP0335BOX
Novex NuPAGE MOPS SDS Running Buffer (20 X)	Life Technologies (ThermoFisher Scientific)	NP0001
Novex NuPAGE Transfer buffer (20X)	Life Technologies (ThermoFisher Scientific)	NP0006-1
NuPAGE Antioxidant	Invitrogen	NP0005
NuPAGE LDS Sample Buffer (4 X)	Invitrogen	NP0007
NuPAGE Sample Reducing Agent (10 X)	Invitrogen	NP0009
Pen/Strep	Gibco	15140-122
Pierce ECL Western blotting substrate	ThermoFisher Scientific	32106
pluriStrainer 5 µM	pluriSelect	43-50005-01
Poly(ethylene glycol) 2-mercaptoethyl ether acetic acid (average M_n 5000, n~110)	Sigma Aldrich	757845-500MG
Protease inhibitor cocktail	Sigma Aldrich	P8340
Richard-Allan Scientific 10% Neutral buffered formalin	ThermoFisher Scientific	9400-5
RPMI 1640	Gibco	31870-025
SeeBlue Plus2 Prestained Standard	Invitrogen	1829199
Sodium bicarbonate	Honeywell	S6014-500G
Sodium chloride	ThermoFisher Scientific	S/3120/63
Sodium citrate	Sigma Aldrich	
Sodium phosphate dibasic	ThermoFisher Scientific	BP332-1
Sodium phosphate monobasic	ThermoFisher Scientific	BP329-1
Sodium tetrachloroaurate	Sigma Aldrich	
Sterile Water for Irrigation	Baxter, Zurich, Switzerland	UKF7114
SYTOX Blue dead cell stain	Invitrogen	S34857
Triton X-100	Sigma	9002-93-1
Trypsin-EDTA (0.05%), phenol red	Gibco	25300054
Tween 20	Sigma Aldrich	P1379-250ML
Whatman Protran BA 85 Nitrocellulose	GE Healthcare	10 401 197
Whatman Puradisc FP 30 Cellulose Acetate Syringe Filter 1.2 µm	GE Healthcare	10462260
X-VIVO	Lonza, Slough, UK	BE04-448Q

2.11 Equipment and instrumentation

2.11.1 UV-Vis

Agilent Cary 60 UV-Vis Spectrophotometer, with Cary WinUV software.

Spectral range recorded 400-800 nm

2.11.2 DLS

Malvern Zetasizer Nano ZS with Zetasizer μV and software APS 6.20, standard Malvern Dip Cell.

2.11.3 Snowy 785

Snowy Range Instruments, Sierra series reader, 785 nm excitation wavelength with 45 mW laser power

2.11.4 InVia

Renishaw InVia Raman microscope, WiRE software versions 4.1 and 4.4.

2.11.4.1 Lasers

785 nm diode laser, power at sample 175 mW

532 nm diode laser, power at sample 74 mW

2.11.4.2 InVia objectives

60x water immersion objective – Olympus LUMPlanFL 60x/1.00

20x – Leica N plan EP 20x/0.4

Laser spot diameter = 1.22 λ / NA

Diameter = (1.22)(532 nm) / 1 [60x] = 649 nm

Diameter = (1.22)(785 nm) / 0.4 [20x] = 2394 nm

2.11.5 MATLAB

Version 2017a, The MathWorks, Natrick, MA, USA

2.11.6 Flow cytometry

Life Technologies Attune NxT acoustic focusing cytometer

2.11.6.1 Custom SSC filter

OD1-488/10 bandpass filter, Catalogue number LAS-026086, Laser 2000 Huntingdon, Cambridgeshire, UK

2.11.7 Plate reader

Thermoscientific Varioskan flash

2.11.8 NanoSight

Malvern NanoSight NS14c/b

2.11.9 UV light source

UVP CL-1000 Ultraviolet Crosslinker

2.11.10 IncuCyte

Essen Bioscience IncuCyte ZOOM, IncuCyte ZOOM 2018A software, 10x Nikon objective, Dual Color Model 4459 filter

2.11.11 ImageJ

ImageJ 1.51k

2.11.12 X-ray developer

Photon Imaging Systems Ecomax Automatic X-ray film processor

2.11.13 Centrifuge

2.11.13.1 25 g spin

Hettich Zentrifugen Rotina 420R

2.11.13.2 20000g spin

Hettich Zentrifugen Mikro 200R

2.12 Tissue culture

BD Plastipak syringes	Various
Corning 25 cm^2 Cell Culture Flask	Catalogue Number 430639
Corning 75 cm^2 Cell Culture Flask	Catalogue Number 431464U
Corning Costar 96 Well Cell Culture Cluster Flat Bottom with Low Evaporation Lid	Catalogue Number 3595
FACS tubes: Falcon 5 mL Polystyrene Round-Bottom Tube	Catalogue number 352008
Falcon 15 mL High-Clarity Polypropylene Conical Tube	Catalogue Number 352096
Falcon 50 mL Polypropylene Conical Tube	Catalogue Number 352070
Thermo Scientific Nunclon Delta Surface 12 Well	Catalogue Number 150628

2.13 Antibodies

Antibody (conjugate)	Species	Isotype	Clone	Supplier	Catalogue number	Concentration (dilution)
anti-human CD146 (BV510)	Mouse	IgG1	P1H12	BD Horizon	563255	25 µg/mL

anti-human CD20	Mouse	IgG2a	L26	Thermo Scientific Pierce	MA5-13141	1 mg/mL
anti-human CD46 (PE)	Mouse	IgG2a	E4.3	BD Pharmingen	564252	50 µg/mL
anti-human CD53	Mouse	IgG1	MEM-53	Invitrogen	MA1-19010	1 mg/mL
anti-human CD59 (BV421)	Mouse	IgG2a	p282	BD Horizon	564329	100 µg/mL
anti-human β-actin	Mouse	IgG1	AC-15	Sigma	A1978	2 mg/mL (1 in 5000)
anti-mouse IgG (peroxidase)	Goat		Polyclonal	Sigma	A3673-1ML	(1 in 5000)
Isotype control (BV421)	Mouse	IgG2a	G155-78	BD Horizon	562439	200 µg/mL
Isotype control (BV510)	Mouse	IgG1	X40	BD Horizon	562946	200 µg/mL
Isotype control (PE)	Mouse	IgG2a	G155-78	BD Pharmingen	556653	50 µg/mL

3 Raman spectroscopy of cells and tumour cell-derived extracellular vesicles

3.1 Introduction

Many methods are currently used to analyse extracellular vesicles (EVs). Flow cytometry is often used, but the limit of spatial detection of these instruments is often 300 nm, overlapping with the size profile of EVs. Confocal imaging can be used, but the broad emission bands of fluorophores mean that a limited number of molecules can be investigated at any one time.

3.1.1 Raman spectroscopy of EVs

Raman spectroscopy, as it is inherently a label-free technique, has the potential to be a useful tool in the analysis of EVs. As the diameter of the laser is on the same order of magnitude as EVs, the entire particle can be analysed with a single point spectrum in order to analyse multiple biomolecules with a single measurement. However, to date only a limited number of studies have used Raman spectroscopy to explore the biochemistry of EVs. Initial studies examined synthetic lipid vesicles, and showed that Raman spectroscopy can be used to examine particles of this scale, and also that phase transitions of the vesicle membrane can be monitored.[295] The eukaryotic cell model organism *Dictyostelium discoideum* constitutively release 'nanovesicles' during growth phase and under starvation conditions, and these have been analysed by Raman spectroscopy.[296,297] Spectra of *Dictyostelium discoideum* EVs dried onto a CaF_2 window were shown to contain many bands typically found in cells, such as the 782 cm^{-1} nucleic acid peak, 1450 cm^{-1} CH_2 vibration, amide I band at 1656 cm^{-1}, and amide III band at 1257 cm^{-1}.[297] Some studies used laser trapping to capture EVs for Raman analysis. Differences in the spectra of EVs released during the growth phase and starvation conditions were observed.[296]

EVs from cancer cell lines have also been differentiated from non-cancer derived EVs based on Raman spectral data.[298] Amide I and amide III bands corresponding to α-helices were shifted and reduced in prostate cancer EV samples compared to benign prostate hyperplasia EVs, whereas the amide III 1240 cm^{-1} vibration corresponding to β-sheet conformation was increased in prostate cancer EVs. One drawback of Raman spectroscopy for the analysis of EVs is the long integration times needed to generate good signal-to-noise from the small particles. One study using laser tweezers Raman spectroscopy (LTRS) analysed each particle for a total of 5 minutes to generate spectral data.[299] However, principal component analysis

(PCA) of the data was able to distinguish between microvesicles and exosomes separated from the same cancer cell line, further showing the potential for using Raman spectroscopy to distinguish between EV subpopulations. EVs derived from mesenchymal stromal cells (MSCs) have also been studied by Raman. MSC EVs from bone marrow and adipose tissue were distinguished based on their Raman spectra, and PCA combined with classical least squares (CLS) fitting showed that the difference between these populations was due to the different lipid moieties present.[300] Raman spectroscopy could also be used as a rapid assay to determine purity of an EV sample, as EVs separated by methods with different efficiencies could be distinguished based on the higher signal to noise profiles of the higher purity samples.[301] The more efficient separation methods also yielded Raman spectra with lower protein to lipid and nucleic acid to lipid ratios. Raman spectroscopy can also be used in conjunction with fluorescent microscopy, which showed that the CD9-positive population of EVs had lower Raman signals than the CD9-negative counterparts.[302] This difference in signal intensity indicates that the CD9-positive population are smaller and less dense than the CD9-negative EVs, and can be detected more easily in conjunction with a fluorescent assay.

Thus, Raman spectroscopy has great potential to distinguish between subpopulations of EVs in a label-free manner.

3.2 Aims of the chapter

The aim of this chapter is to use Raman spectroscopy to investigate the changes in both tumour cells and EVs derived from the tumour cells after exposure to UVB radiation.

The Burkitt's lymphoma (BL) cell line BL2 was used since this cell line becomes apoptotic in response to UVB irradiation. The BL2-bcl2 transfectant cell line does not initiate cell death after an apoptotic stimulus such as UVB irradiation due to the expression of the anti-apoptotic *BCL2* gene.[285] BCL-2 is a protein located in the membrane of mitochondria, and blocks cell death by preventing the formation of a mitochondrial pore and thus the release of cytochrome c. The BCL-2 protein was first discovered in B cell lymphoma, from which it derives its name, and is upregulated in a number of different lymphomas, however it is characteristically absent in BL. The BL2-bcl2 transfectant cell line was therefore generated as a non-apoptotic control for the BL2 line since, even when no stimulus is applied, BL2 cells have a level of constitutive apoptosis of approximately 10%. The BL2-bcl2 line has a higher level of viability, and when used as an experimental control, the same stimulus and

conditions can be applied to the BL2-bcl2 cells and these cells will remain viable and have a higher level of viability than untreated BL2 cells.

HeLa cells were also used in the investigation as a cell line with a different lineage to that of the BL cells. A non-apoptotic genetic transfectant control for HeLa cells was not available as this line has a low level of constitutive apoptosis. For this cell line, the experimental control used was cells under the same conditions as the irradiated cells, but without exposure to UVB.

When obtaining Raman spectral data for whole cells, the whole cell was mapped at high resolution, with 1 μm step sizes in both x and y directions. The cells were fixed with formalin and spectra were acquired with the cells in phosphate buffered saline (PBS). The non-cellular PBS background was removed, and the remaining spectra averaged to generate a single Raman spectrum representative of each cell in order to remove the intracellular variability.

EVs were also separated from each of the different cell lines. The EVs from the UV-irradiated BL2 cells (apoEV) are a heterogeneous population, with EVs coming from both apoptotic cells and viable cells throughout the course of the incubation after the cells have been irradiated. However, the EVs from the BL2-bcl2 cells should be relatively homogenous as these cells do not undergo apoptosis and therefore will only release a single population of EVs. Raman spectroscopy was carried out on these EVs to ascertain if differences between EVs released from viable and apoptotic tumour cells could be observed spectroscopically using a label-free technique, combined with multivariate analysis.

The Raman spectra of these EVs were acquired by attaching the EVs to the surface of a CaF_2 window. Because of the small size of EVs (<1.2 μm, mostly <500 nm), the entire EV could fit within the laser spot of the Raman microscope system, therefore only a single spectrum needed to be acquired for each EV. Therefore, the EVs characterised by Raman spectroscopy were limited to those which were large enough to be seen clearly under the white-light lamp of the microscope on the Raman spectrometer, meaning many of the smaller 'exosome'-type EVs could not be included in this analysis.

3.3 Raman maps of whole cells

3.3.1 Viable and apoptotic BL2 and BL2-bcl2 cells

3.3.1.1 Induction of apoptosis and assessment of cellular viability

BL2 cells and BL2-bcl2 cells at a density of $20x10^6$ mL^{-1} were irradiated with 300 mJ/cm^2 of UVB light and incubated at 37 °C for a period of 5-7 hours. A sample of cells was taken every hour to monitor the progression of apoptosis using flow cytometry by dual staining with Annexin V (AxV) and Sytox Blue (SB). AxV binds to phosphatidylserine (PS), which is a phospholipid normally localised to the cytosolic surface of the cell membrane. During apoptosis, PS is translocated to the outer surface of the membrane, where it is then free to bind AxV and is thus used as a marker of early apoptosis. SB is a membrane impermeable dye which is only fluorescent when bound to nucleic acids. During necrosis, the cell membrane loses its integrity, which allows SB to enter the cell and bind to DNA, becoming fluorescent. This dual staining technique identifies viable cells which are unstained (AxV- SB-), early apoptotic cells (AxV+ SB-), secondarily necrotic cells (AxV+ SB+), and necrotic cells (AxV- SB+). The progression of apoptosis of the UV-irradiated BL2 cells was used to determine the end point of the experiment (>70% AxV+ SB- with a minimal overall SB+ population). As shown in Figure 3.1A and Figure 3.1B, the population of AxV+ SB- BL2 cells (UVBL2) increases steadily over the course of the incubation. Immediately prior to UVB exposure the cells are 94% viable, not staining with either AxV or SB. The AxV+ population steadily increases at each timepoint post-irradiation, reaching 67% AxV+ SB- at the 6-hour post UV timepoint. The necrotic population does not increase, remaining at approximately 4% throughout the course of the experiment. The BL2-bcl2 cells remain >90% AxV- SB- over this time period (UVBL2bcl2). There is a slight increase in the population of apoptotic BL2-bcl2 cells after irradiation. This is most likely due to an incomplete transfection of the *BCL2* gene, or varying levels of expression in the population causing some cells to be susceptible to apoptosis.

The cells were isolated from the irradiated suspension after 5 hours, or when the cells reached at least 70% AxV+, by centrifugation at 25 *g*. The cell pellets were resuspended in a 4% solution of neutral buffered formalin for 10-15 minutes at a concentration of $1x10^6$ mL^{-1} to fix the cells before Raman spectroscopy was carried out. Viable BL2 cells and BL2-bcl2 cells from culture, which were 90% and 93% AxV- SB-, respectively (Figure 3.2) were also fixed in the same manner for analysis by Raman spectroscopy.

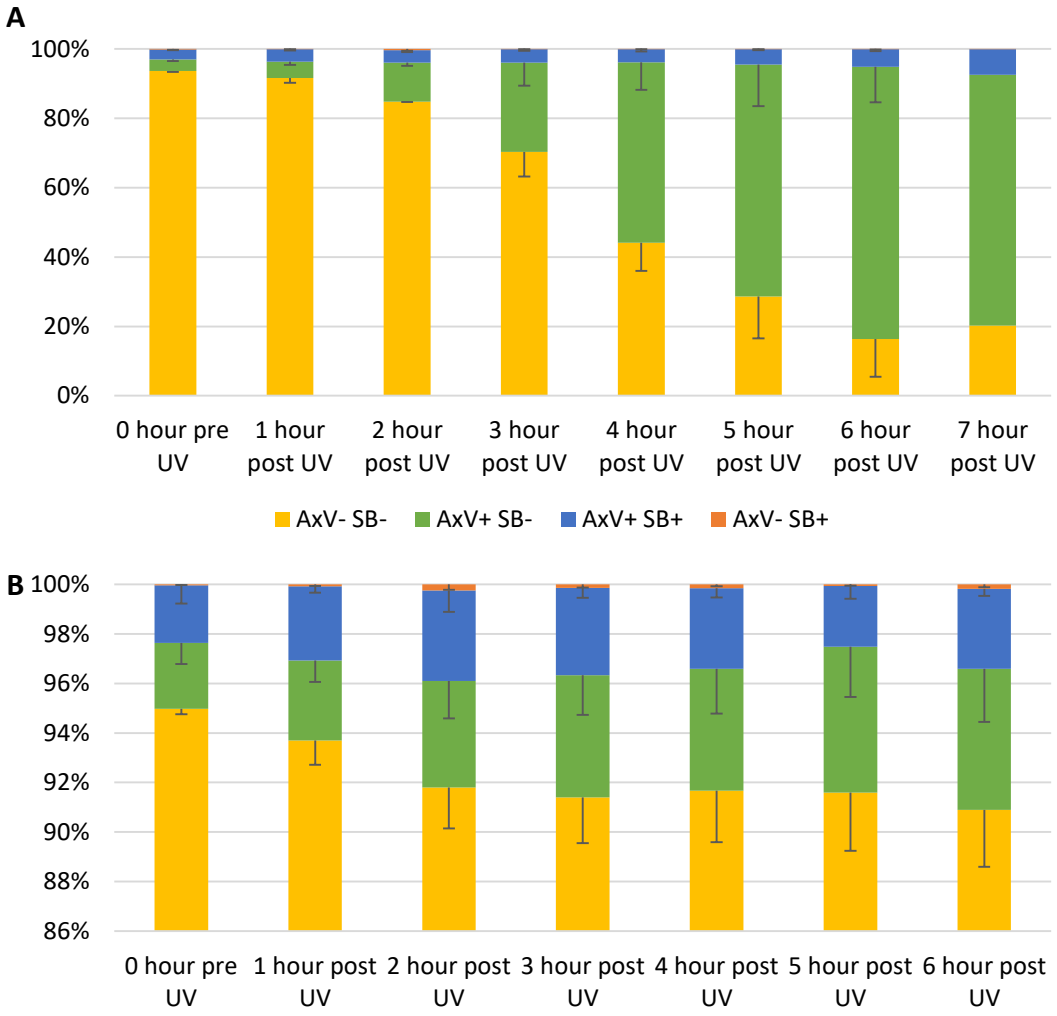

Figure 3.1: Assessment of viability of BL2 cells (A) and BL2-bcl2 cells (B) after exposure to 300 mJ/cm^2 UVB radiation for Raman spectroscopy. Cells were irradiated at a concentration of 20x10^6 mL^{-1} and incubated at 37 °C after UV exposure. Viability was assessed by dual staining with Annexin V (AxV) and Sytox Blue (SB), quantified by flow cytometry. Graph shows mean of 3 experiments, with the exception of BL2 6 hour post UV (2 experiments) and 7 hour (1 experiment). Error bars show one standard deviation.

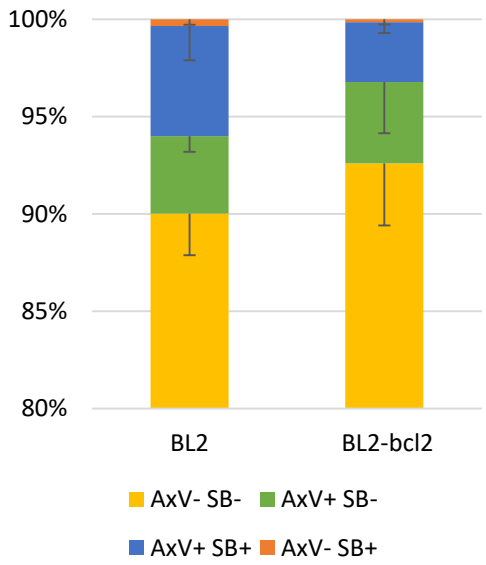

Figure 3.2: Assessment of viability of BL2 and BL2-bcl2 cells from culture for Raman spectroscopy. Viability was assessed by dual staining with Annexin V (AxV) and Sytox Blue (SB), quantified by flow cytometry. Graph shows mean of 3 experiments. Error bars show one standard deviation.

3.3.1.2 Raman spectroscopy of viable and apoptotic BL cells

The fixed apoptotic and viable BL cells were then analysed by Raman spectroscopy to identify changes in the cells based on viability status. A CaF_2 window was coated with Cell-Tak, a protein solution derived from marine mussels which allows cells and tissue sections to attach to surfaces. The cells to be analysed were applied in PBS to the window and allowed to settle under gravity in order to adhere to the window. Raman images of step size 0.7 µm of single cells were acquired using 532 nm excitation wavelength at 35 mW for 1 second acquisition time using a 60x water immersion objective. Three replicate experiments were carried out for each cell condition, with 10 cells mapped for each experiment, for a total of 30 cell maps per condition. The PBS background spectra were extracted from the cell spectra using MATLAB, and a mean spectrum for each cell generated. The spectra were baseline corrected and scaled so the highest intensity peak was scaled to unity. The mean spectra of the 30 cells for each condition is shown in Figure 3.3A and 3.3B, plotted with ± standard deviation (SD) shaded. The UVBL2 cells show higher intensities for a number of points in the spectrum, including 783 cm^{-1}, 1004 cm^{-1}, 1095 cm^{-1}, 1255 cm^{-1}, 1300-1320 cm^{-1}, 1340 cm^{-1}, and 1449 cm^{-1}. However, the SD of these peaks all overlap with those of the viable cells. The shoulders at 1606 cm^{-1} and 1620 cm^{-1}, which have lower intensity in the UVBL2 cell spectrum, have a SD which does not overlap the SD of the other spectra, indicating that these peak changes are not likely to simply be due to biological variation. The SD of the spectra are shown in

Figure 3.3C, where the UVBL2 cells can be seen to have a larger SD than the other cell conditions at a number of points, including those at 1004 cm^{-1}, 1095cm^{-1}, 1255cm^{-1}, and 1449cm^{-1}. The SD at the other peaks in the spectrum are comparable for each condition. The larger variation in the UVBL2 is to be expected, as this cell population is more heterogeneous due to the application of UVB radiation and subsequent induction of apoptosis. The cells are undergoing programmed cell death in a relatively synchronous manner – as can be seen in the flow cytometry data (Figure 3.1) – and are mostly in early apoptosis (AxV+ SB-). However, the cells are not completely synchronised, and some may be further along in the apoptotic programme than others. As the BL2 cells are non-adherent, it is quite difficult to distinguish the viability of the cell by morphology alone. Thus, some of the cells analysed may be viable, and some may be secondarily necrotic. Similarly, for the non-apoptotic cell populations, the cells were not cell-cycle synchronised before analysis, so variation in the Raman spectra could be caused by differing cell-cycle stages, viability (as there is a low level of constitutive cell death in every cell population), and stress (as the UV-irradiated BL2-bcl2 cells were at quite a high cell density for irradiation which may have induced metabolic stress).

The mean individual cell spectra were used to compare the conditions using the unsupervised multivariate analysis technique principal component analysis (PCA). PCA is a statistical method of data reduction which creates components which are orthogonal and have the maximum variability between them without any bias to the data groups. This makes it a useful method for reducing the dimensions of a Raman spectrum in a way that is easy to interpret back to the original spectrum in order to determine differences between groups of data.

The baseline corrected spectra were converted to the first derivative for PCA, and the principal component (PC) scores plotted against each other. Figure 3.4A shows the score plot for PC1 vs PC2, where each data point represents the mean spectrum of a single cell. The apoptotic UVBL2 cells show some separation from the viable cell groups along PC1 axis, which corresponds to 24.7% of the total variance. The spectral loading of PC1 is shown in Figure 3.4B. The main contributions to this PC are the phosphodiester peak at 785 cm^{-1}, the phenylalanine (Phe) peak at 1004 cm^{-1}, and the DNA phosphodioxy band at 1095 cm^{-1} (Table 3.1).

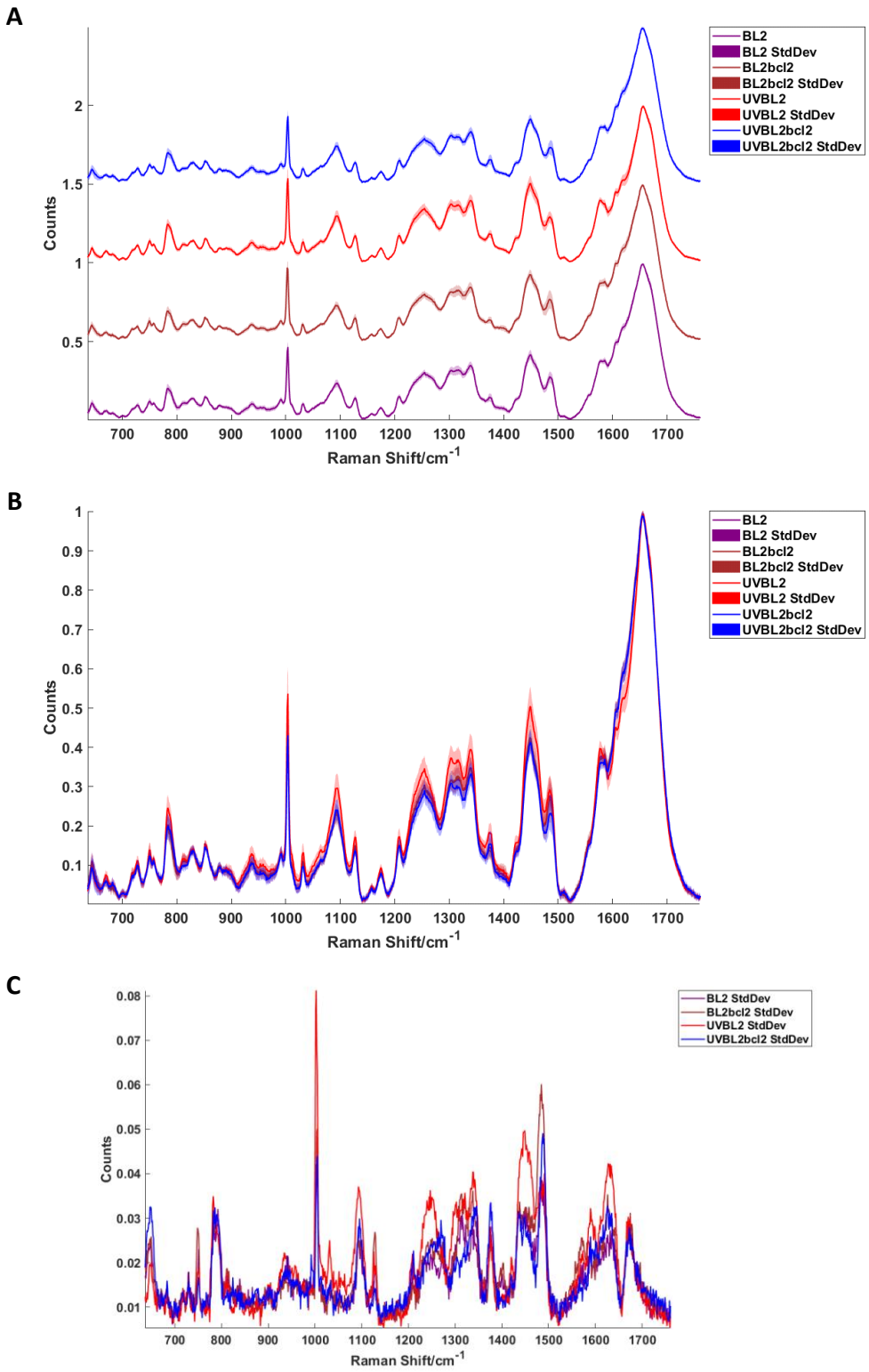

Figure 3.3: (A) The mean spectra of 30 cells for each condition, plotted offset with ± 1 SD (shaded) – viable BL2 cells (BL2), viable BL2-bcl2 cells (BL2bcl2), UV-irradiated BL2 cells (UVBL2) and UV-irradiated BL2-bcl2 cells (UVBL2bcl2). The spectra with SD are overlaid in (B), showing that the UVBL2 cells have higher intensity peaks at a number of points in the spectrum. The SD of the 30 spectra for each condition is plotted in (C). Data acquired with 532 nm excitation wavelength at 35 mW for 1 second acquisition time.

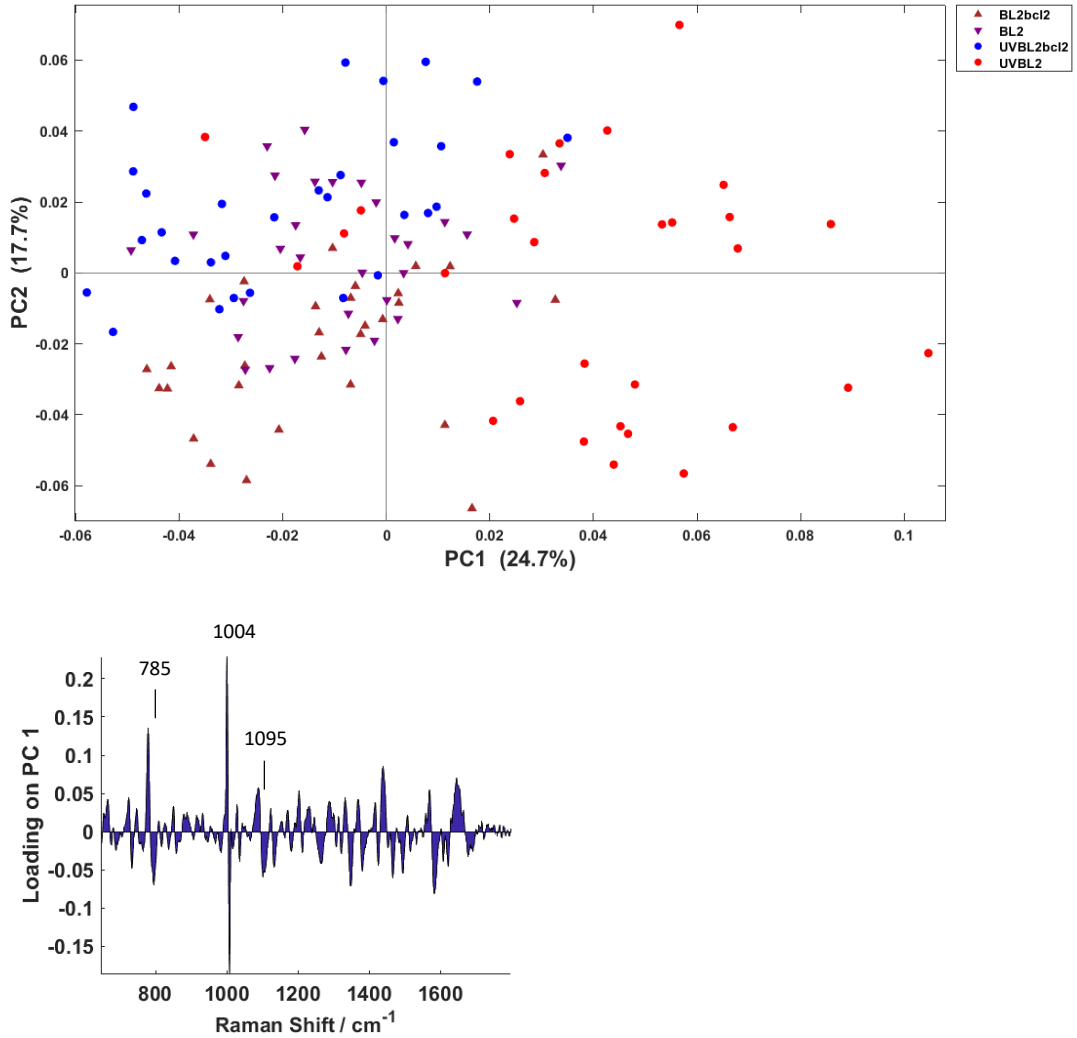

Figure 3.4: Principal component analysis (PCA) results of the first derivative Raman spectrum for the comparison of viable and apoptotic BL2 and BL2-bcl2 cells. (A) Plot of principal component (PC) scores PC1 vs PC2, showing a separation of the apoptotic UVBL2 cells from the rest of the viable cell populations along PC1. (B) Loading of PC1, showing the main peaks contributing to this PC are those at 785 cm^{-1}, 1004 cm^{-1}, and 1095 cm^{-1}.

Table 3.1: Peak assignments for PC1 loading

Raman shift (cm^{-1})	Assignment
784	Phosphodiester; nucleic acid ring breathing
1004	Phenylalanine
1095	DNA, phosphodioxy

The PC loading agrees with published literature, where the main changes in the spectra of apoptotic cells are seen in nucleic acid bands, such as the 784 cm^{-1} phosphodiester band and the 1095 cm^{-1} DNA band, due to the alterations of the nucleus during cell death. Some reports state that the nucleic acid peaks increase in intensity due to the nuclear condensation which causes a localised increase in nucleic acid concentration,[205,234,240] while other reports state that the nucleic acid bands have reduced intensity due to nuclear fragmentation causing a decrease in DNA concentration.[215,236] Based on the PC1 loading shown in Figure 3.4B, and the mean cell spectra shown in Figure 3.1, it appears that in this study the nucleic acid bands have increased in intensity in the Raman spectra of the UVBL2 cells compared to the viable counterparts. This suggests that the cells are in early apoptosis, as the nucleus of the cells has condensed but not fragmented. This is in agreement with the flow cytometry assessment of viability indicating that the majority of UVBL2 cells are AxV+ SB-, while the UVBL2bcl2, BL2, and BL2bcl2 are mostly viable (AxV- SB-).

3.3.2 Viable and apoptotic HeLa cells

HeLa cells were chosen for comparison to the BL2 cell lines in this experiment as these two cell lines have different physiological lineages. BL2 cells are of haematopoietic origin, whereas HeLa cells are of epithelial origin. Therefore, it would be expected to observe differences seen between these two cell types by Raman spectroscopy.

3.3.2.1 Induction of apoptosis and assessment of viability

In order to induce the HeLa cells into apoptosis in a manner analogous to the BL2 cells, optimisation of the UVB dose and incubation period of the HeLa cells was carried out. The progression of apoptosis in the cells was monitored using the IncuCyte Zoom (Essen Bioscience), which is a fluorescent imaging plate reader housed inside an incubator, allowing images to be taken automatically at specified timepoints without removing the plate. HeLa cells were seeded into 96-well plates (6000 cells per well for 24 hours), exposed to various doses of UVB radiation (450 mJ/cm^2, 600 mJ/cm^2, 750 mJ/cm^2, and 900 mJ/cm^2), and incubated in the IncuCyte with images taken every hour to determine the progression of apoptosis (Figure 3.5). The viability was determined using CellEvent, a caspase-3/7 substrate which is fluorescent upon cleavage by active caspase-3 or caspase-7, indicating that the cell is apoptotic. The membrane impermeable dye DRAQ7 is used to identify necrotic populations in the same way as SB in flow cytometry assays described in Section 3.3.1.1. The number of cells in each well which had stained positively for CellEvent and DRAQ7 at each UV dose is

shown in Figure 3.5A. Cells that were not irradiated were included as a negative control. The ratio of CellEvent positive events to DRAQ7 positive events is shown in Figure 3.5***Figure 3.6***B, showing that the highest proportion of cells in early apoptosis with minimal secondarily necrosis is 8 hours after irradiation with 600 mJ/cm^2 UVB. However, although this appears to be the optimal conditions with regards to the proportion of early apoptotic cells, by counting the total number of cells in the phase contrast images and comparing this to the number of fluorescent cells, only 31% of the cells were apoptotic (Figure 3.6). 68% remained unstained at this time point, indicating that the majority of the cells were still viable. Therefore, the levels of apoptosis reached with the HeLa cell assay are not analogous to those observed in the BL2 assay, and the UV-irradiated HeLa cell population is thus more heterogeneous.

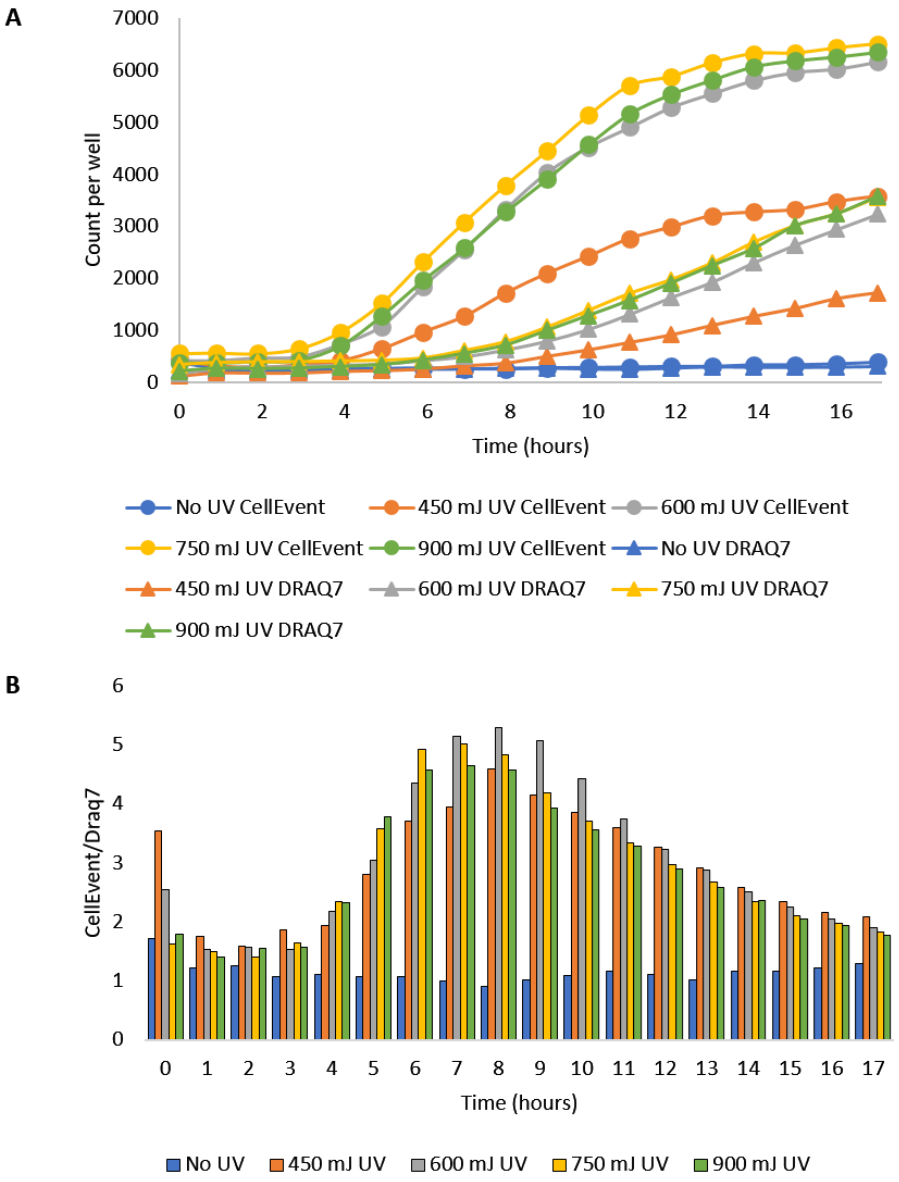

Figure 3.5: Monitoring the response of HeLa cells to different doses of UVB radiation. (A) Plot of CellEvent positive cells and DRAQ7 positive cells as a function of time post UV exposure. Cells that had not been irradiated were used as a control. The ratio of CellEvent positive events to DRAQ7 positive events is shown in (B). The highest ratio is 8 hours post-irradiation with 600 mJ/cm^2.

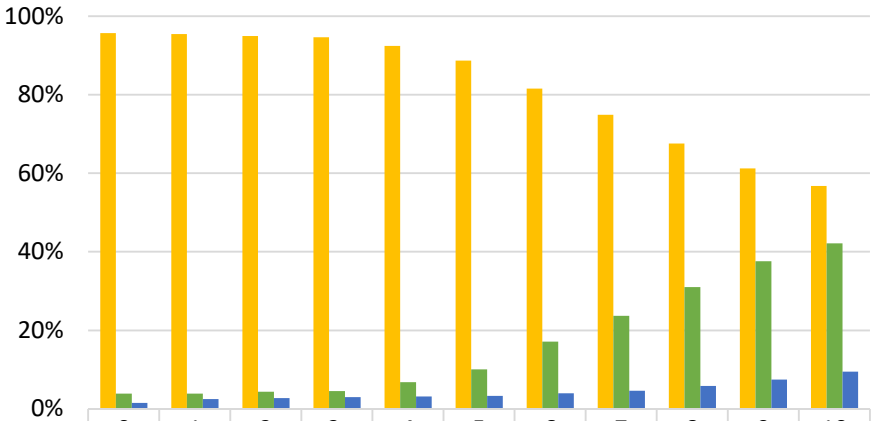

	0 hour	1 hour	2 hour	3 hour	4 hour	5 hour	6 hour	7 hour	8 hour	9 hour	10 hour
CellEvent- DRAQ7-	96%	95%	95%	95%	92%	89%	82%	75%	68%	61%	57%
CellEvent+	4%	4%	4%	5%	7%	10%	17%	24%	31%	38%	42%
DRAQ7+	2%	3%	3%	3%	3%	3%	4%	5%	6%	7%	10%

Figure 3.6: Viability of HeLa cells after exposure to 600 mJ/cm^2 UV. At 8 hours, only 31% of the cells stain positive for CellEvent. 6% are necrotic, staining with DRAQ7. Accounting for the cells which stain positively for both CellEvent and DRAQ7, this leaves 68% of the cells unstained with either CellEvent or DRAQ7, indicating that those cells are viable.

3.3.2.2 Raman spectroscopy of viable and apoptotic HeLa cells

HeLa cells were seeded onto CaF_2 windows and allowed to attach and grow for 24 hours. The cells on the window were irradiated with 600 mJ/cm^2 UVB and incubated at 37 °C for 8 hours before fixing with 4% NBF (UVHeLa). Cells which had been seeded onto the window without being irradiated were used as the viable control (HeLa). Raman images of step size 1 µm of single cells were acquired using 532 nm excitation wavelength at 35 mW for 1 second acquisition time using a 60x water immersion objective. Three replicate experiments were carried out, and 10 cells were Raman mapped under PBS for each experiment, with a total of 30 cell maps obtained per condition. The cell spectra were extracted from the background spectra of PBS using MATLAB, and a mean spectrum for each cell was generated. The spectra were baseline corrected and scaled. The mean spectra of the 30 cells for each condition is plotted offset in Figure 3.7A and overlaid in Figure 3.7B, with ±1 SD shaded. The peaks and SD of the spectra overlap for many bands, but a difference is seen in the intensities of the peaks at 852 cm^{-1}, 1004 cm^{-1}, 1031 cm^{-1}, and 1207 cm^{-1}. The SD for the HeLa and UVHeLa cells are quite similar at most peak positions (Figure 3.7C). The main points of difference are the larger SD for the UVHeLa cells in the nucleic acid band region 783-792 cm^{-1}, and the higher deviation of the Phe peak at 1001 cm^{-1} and the 1338 cm^{-1} peak in the HeLa cells.

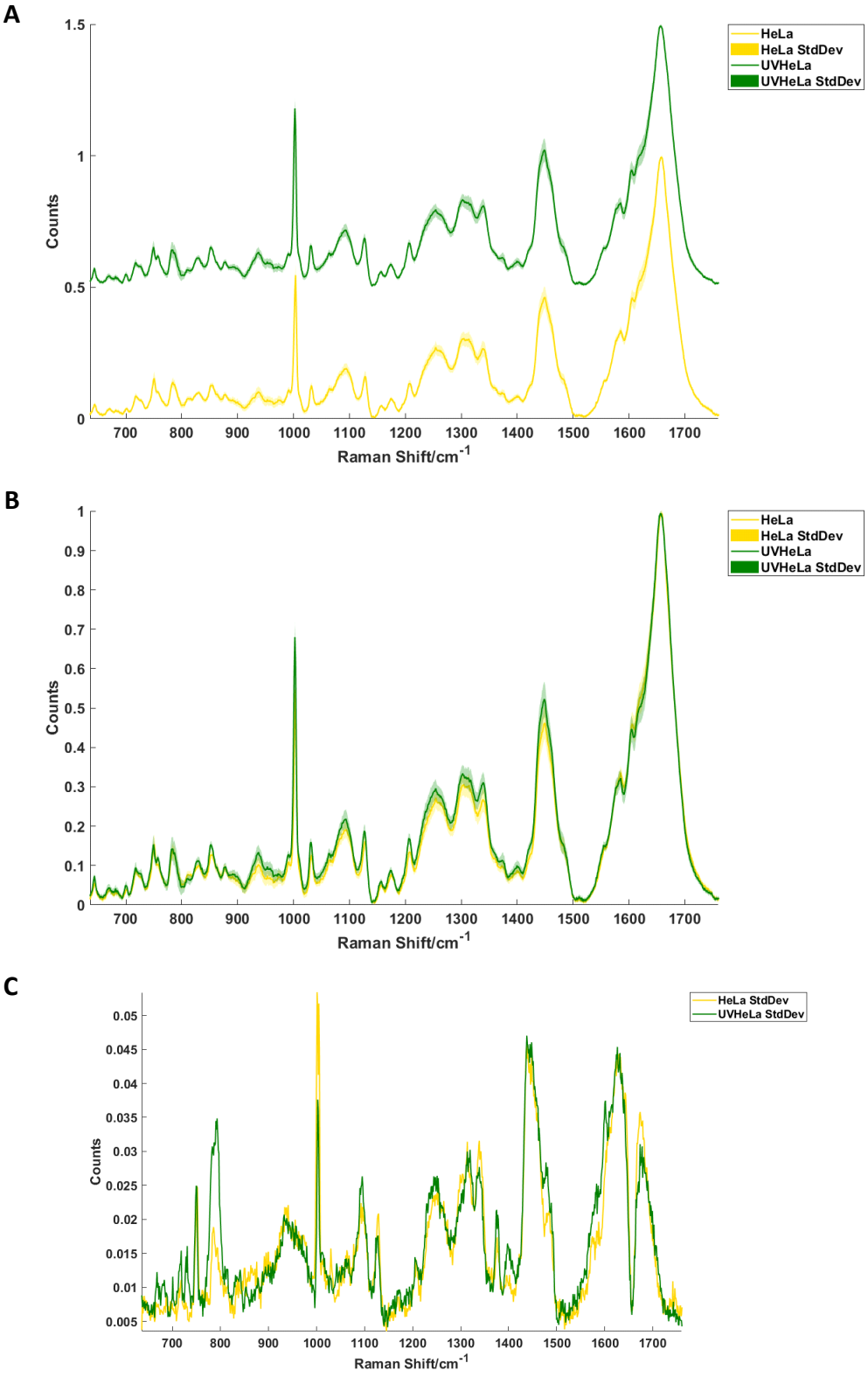

Figure 3.7: (A) The mean of 30 cells for each condition, plotted offset with ±1 SD (shaded) – viable HeLa cells (HeLa), and UV-irradiated HeLa cells (UVHeLa). The spectra with SD are overlaid in (B), showing that the spectra overlap at most points. The SD for each condition is plotted in (C). Data acquired with 532 nm excitation wavelength at 35 mW for 1 second acquisition time.

One issue with the acquisition of the UVHeLa cell spectra is the low percentage of early apoptotic cells in the population (Figure 3.6). Thus, in order to be certain that the cells analysed were apoptotic, the morphology of the cells was taken into account when choosing which cells to analyse. Adherent cells which are apoptotic become detached from the surface of the CaF_2 window and have a rounded appearance with some membrane blebbing. The cells with these morphological features may even have advanced from being early apoptotic to being secondarily necrotic, which would cause a large amount of variation in the spectra. However, the SD of the UVHeLa and HeLa cells are reasonably similar to one another, implying that this did not affect the data.

PCA was then carried out on the first derivatives of the HeLa and UVHeLa cell data, the results of which are shown in Figure 3.8. As seen in Figure 3.8A, there is clear separation of the UVHeLa cells from the HeLa cells along PC1, which accounts for 56.9% of the variance in the spectra. The HeLa cells have a positive score for PC1, while the UVHeLa cells have a negative PC1 score. The loading on PC1 is shown in Figure 3.8B, indicating that the main variation contributing to this variation is the Phe peak at 1001 cm^{-1}. As can be seen in Figure 3.7B, the main cause of variation at this peak between HeLa and UVHeLa is the shift of the peak from 1004 cm^{-1} in the HeLa cells to 1001 cm^{-1} in the UVHeLa cells. This shift could be caused by a number of factors, such as a change in the secondary structure of the proteins in the cell, changes in hydrogen bonding or changes in pH.[198] It may also be an artefact of batch processing cells, as the temperature of the CCD can affect the Raman shift positions of the peaks.[211]

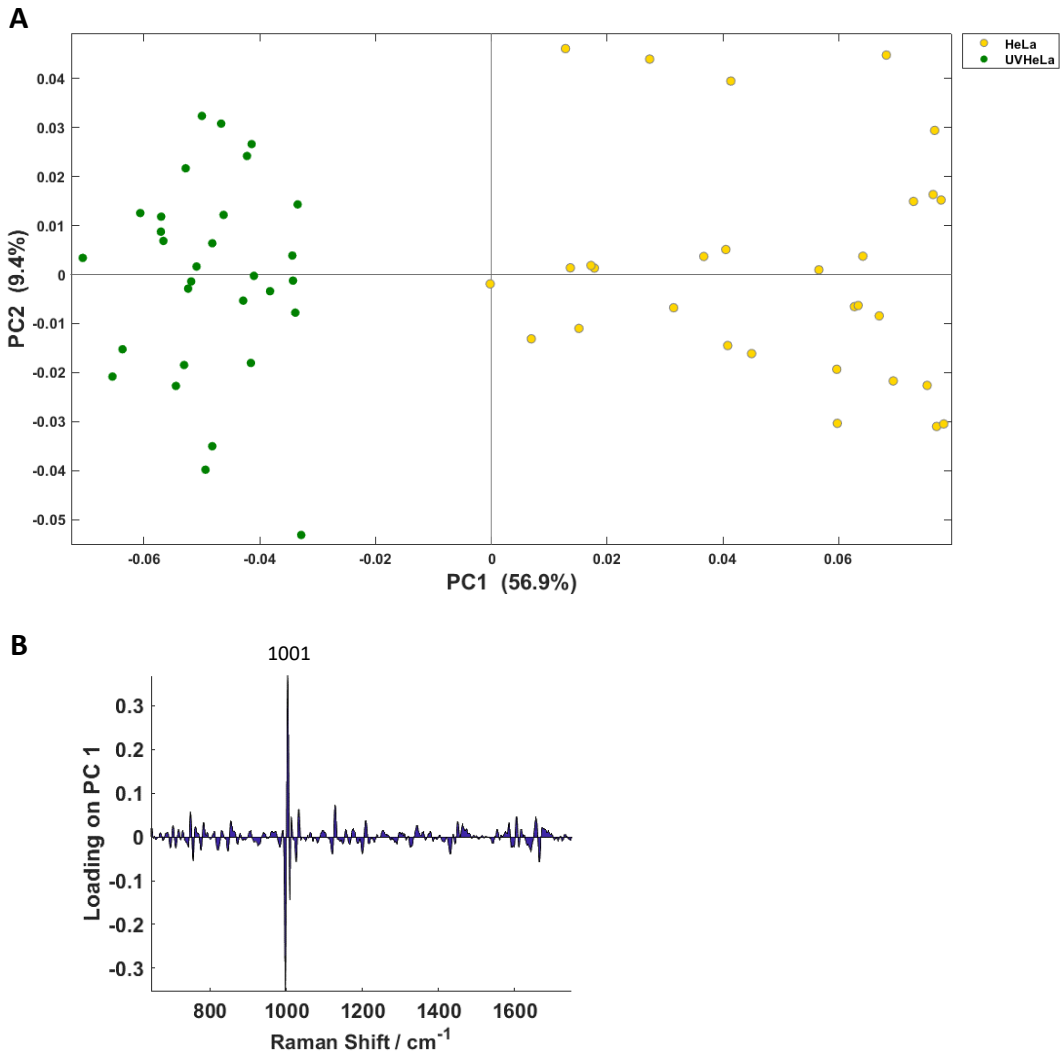

Figure 3.8: PCA results of the first derivatives of the Raman spectra for the comparison of viable and apoptotic HeLa cells. (A) Plot of PC1 vs PC2 scores, showing a separation of the apoptotic UVHeLa cells from the viable HeLa cells along PC1. (B) Loading of PC1, showing the main peak contributing to this PC is that at 1001 cm^{-1}.

3.3.3 BL2 cells, BL2-bcl2 cells, and HeLa cells

As outlined in Section 1.4.1.5, apoptotic cells and viable cells can be differentiated by Raman spectroscopy and different cell types can also be distinguished from one another. Published work by other groups has shown that different forms of cell death can be distinguished,[239] and cell death induced by different stimuli can also be distinguished.[207] However, it is not yet known whether viable and apoptotic cells of more than one cell type can be distinguished based on their viability or cell type, since apoptotic and viable cells of more than one cell type have not been directly compared.

The Raman data obtained from the viable and apoptotic BL2 and BL2-bcl2 cells were therefore compared against the viable and apoptotic HeLa cells, in order to distinguish whether these cells could be separated based on cell type as well as viability. The result from the PCA of the first derivatives of the Raman spectra of this group of cells is shown in Figure 3.9.

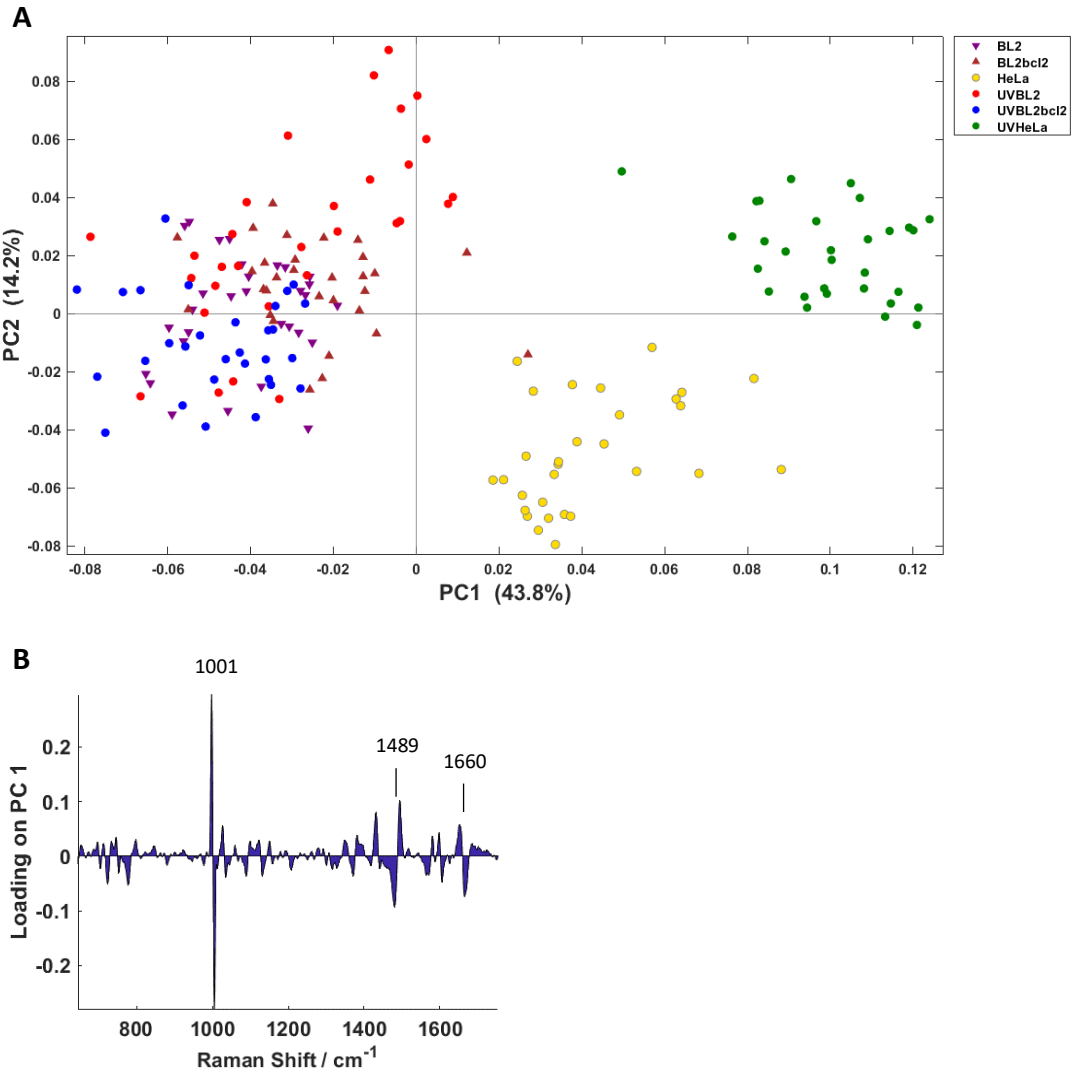

Figure 3.9: (A) PCA plot of the first derivative Raman spectrum of all cells (BL2, BL2bcl2, UVBL2, UVBL2bcl2, HeLa, UVHeLa). The HeLa cells and UVHeLa cells separate from the BL cells along PC1, with some separation of HeLa and UVHeLa along PC2. (B) Loading of PC1 shows contributions from peaks at 1001 cm^{-1}, 1489 cm^{-1}, and 1660 cm^{-1}.

The scores plot of PC1 (43.8% of variance) vs PC2 (14.2% of variance), is shown in Figure 3.9A. This shows that the cells separate based on type rather than viability, with the HeLa and UVHeLa having positive scores for PC1, and the BL cells mainly having negative scores for PC1, with some outliers. There is also slight separation of the viable and apoptotic cells,

where the UVHeLa and UVBL2 cells mostly have positive scores for PC2 and HeLa cells have negative scores, however there is no separation of the viable BL2 and BL2-bcl2 cells along this axis. The loadings of PC1 are shown in Figure 3.9B, with the main contributory peaks to this component found at 1001 cm^{-1}, 1489 cm^{-1}, and 1660 cm^{-1}. The peak at 1489 cm^{-1} is most likely due to DNA or nucleic acid ring breathing modes, and this peak is absent in the spectra of the HeLa and UVHeLa cells when compared to the BL cells (Figure 3.10A and Figure ***3.10***B). This may be due to the relative size of these cells. BL2 cells, and B cells in general, are smaller than epithelial cells, with a relatively small volume of cytoplasm as the majority of the cell is taken up by the nucleus. The nuclear material is also more concentrated in lymphocytes because of their smaller size. Thus, the concentration of nucleic acids in the mean spectrum of the BL2 and BL2-bcl2 cells will be higher than that in the HeLa cells, as the nucleus makes up a smaller proportion of the HeLa cells. This difference in the nucleic acid concentrations of the two cell types can also be seen in the band at 782 cm^{-1}, which also corresponds to DNA ring breathing modes. Although this peak has lower intensity in the HeLa and UVHeLa cells (Figure 3.10C), when plotted with ±1 standard deviation in Figure 3.10D, the standard deviations overlap, indicating that the variation in the intensity of this peak is not significant. However, the 1489 cm^{-1} peak, in Figure 3.10B, does show clear differences in the standard deviations in this peak, reflecting the different nucleic acid concentration in the two cell types.

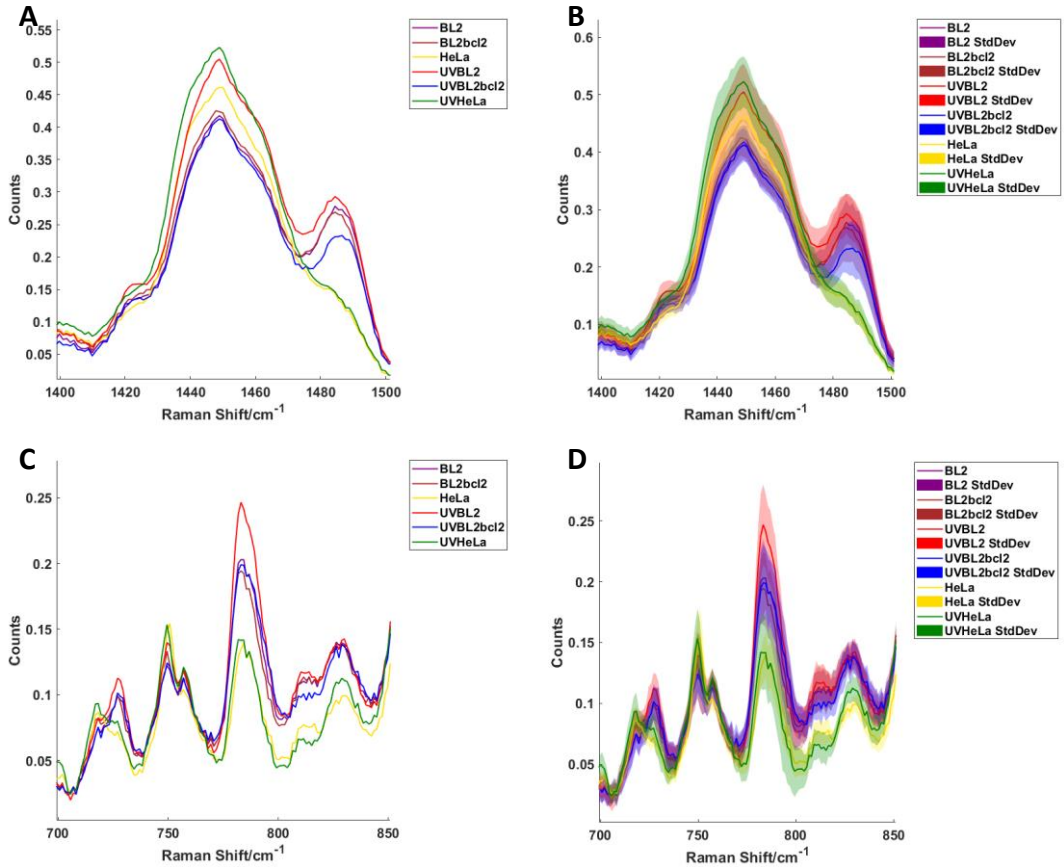

Figure 3.10: Plot of all cell spectra (BL2, BL2bcl2, UVBL2, UVBL2bcl2, HeLa, UVHeLa) showing nucleic acid bands. (A) Zoom in on the region 1400-1500 cm^{-1} region, showing the reduction of the 1489 cm^{-1} peak in the HeLa cells, and the same region plotted with ± 1 standard deviation in (B). The region from 700-850 cm^{-1} is shown in (C) showing the reduction in peak intensity at 782 cm^{-1}, and the same region is plotted in (D) with ± 1 standard deviation, showing overlap of the standard deviations of the 782 cm^{-1} peak for all cell types.

The contribution from the peak at 1660 cm^{-1}, corresponding to the amide I vibration, could be due to differing secondary structure of the proteins within the cell types. However, as the spectra have been scaled so that the peak with the highest intensity in the spectrum is 1, the changes in this peak may be due to slight shifts in the peak maximum for this band in the different cells analysed.

Therefore, it appears that in the analysis of spectral data from a mixed group of viable and apoptotic cells from different lineages, the lineages differences between the cells dominate over the viability status of the cells. However, the data from the HeLa cells were acquired at a much later time than BL2 group data. This may play a role in the differentiation of these groups, due to variation in the spectrometer over this time period. Another factor influencing this analysis is the growth medium of the cells. The BL2 and BL2-bcl2 cells were grown in a chemically defined medium, a mixture of RPMI 1640 and X-VIVO 20. The HeLa cells were

grown in MEM supplemented with 10% FCS. These differences in growth conditions may also influence the Raman data obtained from these cells, skewing the PCA of the data based on these factors rather than true biological differences.

3.4 Separation of EVs from apoptotic and non-apoptotic cells

EV-related research is a growing field; as the functions of these particles are revealed, the interest in these particles grows. EVs released during early apoptosis are of particular interest due to the observation that some tumours with high rates of apoptosis, and corresponding infiltration of tumour-associated macrophages (TAMs), have aggressive growth phenotypes. The hypothesis is that the EVs released from the apoptotic tumour cells (apoEV) play a role in the conditioning of the tumour microenvironment or the activation of macrophages to form the 'onco-regenerative niche'. The reasons for avoiding secondary necrosis in the *in vitro* system is two-fold: these cells are not present in great numbers *in vivo* as they are phagocytosed by the TAMs in the tumour, and the presence of these cells with their disrupted cell membranes in the culture system could create artefacts due to the release of the intracellular contents into the extracellular milieu, and membranous EV artefacts.

ApoEVs and EVs were separated from UV-irradiated BL2 and BL2-bcl2 cells respectively, in order to study them by Raman spectroscopy. A similar procedure was used for HeLa cells, either irradiated or not irradiated, in order to be able to compare the EVs from the two cell lines. Some changes to the protocol were necessary as the HeLa cells are adherent rather than suspension cells.

3.4.1 Separation of EVs from BL2 and BL2-bcl2 cells

BL2 and BL2-bcl2 cells were irradiated with UVB light as described in Section 3.3.1.1 and Figure 3.1. The cells were removed from suspension by low speed centrifugation at 25 *g* for 60 minutes at 4°C. The low speed is to ensure that the delicate membranes of the early apoptotic cells are not disrupted by the shear force generated by centrifugation, which could create artefacts in the preparation. The supernatant was then passed through a 5 µm mesh filter, to remove any remaining cells from the suspension, followed by a 1.2 µm syringe filter, in order to remove any larger EVs and apoptotic bodies from the preparation. The filters used were chosen to limit the shear force exerted on the EV suspension – the mesh filter is normally used for pluripotent cells, which have plastic morphology, and the 1.2 µm syringe filter was used without the plunger applied to the syringe, instead allowing the suspension to pass through the filter aided only by gravitational force.

The size and concentration of the EVs were determined using a NanoSight (Malvern), which measures the EVs using nanoparticle tracking analysis. By recording the Brownian motion of particles and tracking this motion frame-by-frame, the hydrodynamic radius of the EVs can be determined, and the number of particles tracked in the analysis is used to determine the concentration of particles in the sample.

Figure 3.11 shows the concentration and size distribution of the EVs released from UV-irradiated BL2 and BL2-bcl2 cells. The BL2 cells release more EVs than BL2-bcl2 cells under the same conditions of cell concentration and stimulus (Figure 3.11A). The size distributions of these EV populations also differs, as the BL2 cells release a much more heterogeneous distribution of particle sizes than the BL2-bcl2 cells. Figure 3.11B shows that the BL2 EVs have a population of EVs between approximately 300 nm and 700 nm which are much lower in the BL2-bcl2 EVs. The BL2 cells also release more of the 'exosome'-sized EVs with a diameter of <100 nm than released by the BL2-bcl2 cells. This size difference could indicate that the BL2 EVs, or apoEVs, can carry more functional cargo in order to affect the tumour microenvironment.

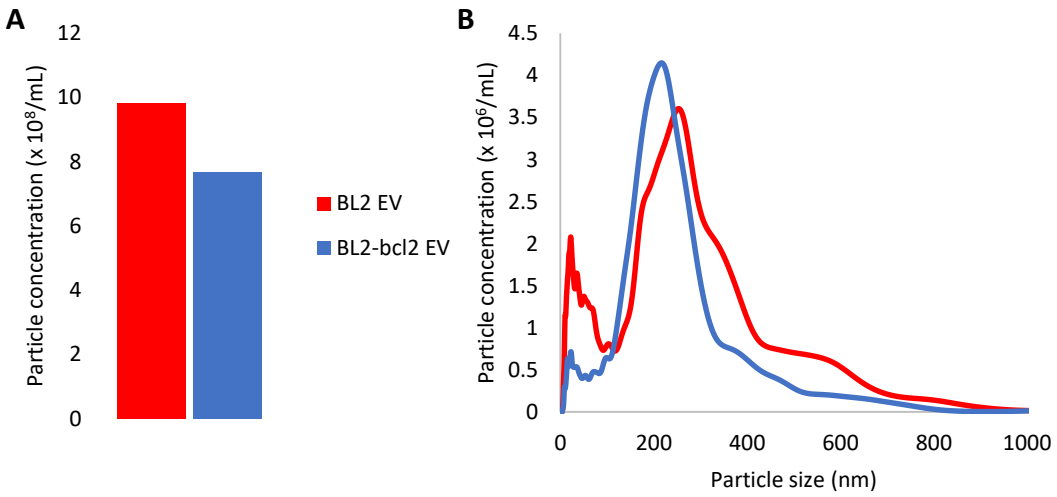

Figure 3.11: NanoSight analysis of EVs released from UV-irradiated BL2 and BL2-bcl2 cells. (A) Total particle concentration of BL2 EVs and BL2-bcl2 EVs in the 1.2 µm filtrate from the EV preparation. (B) Size distribution of the EVs as determined by nanoparticle tracking analysis. BL2 cells release more EVs and larger EVs than BL2-bcl2 cells.

3.4.2 Separation of EVs from HeLa cells

A number of changes needed to be made to the EV separation protocol in order to adapt it for the HeLa cell line. The BL2 cells were irradiated with 300 mJ/cm^2 UV at 20 x 10^6 mL^{-1}. The HeLa cells, as discussed in 3.3.2.1 and Figure 3.5, respond best to 600 mJ/cm^2 UV, and since

they are adherent, they cannot reach the same cell concentrations as the non-adherent BL2 cells. In order to yield an acceptable concentration of EVs for further analysis and quantification, a number of different cell densities of HeLa were examined in different culture vessels. 1.5 x 10^6 cells seeded for 24 hours in a 25 cm^2 culture flask, with 5 mL of culture medium, was sufficient to yield an adequate concentration of EVs.

The BL2 cells were grown in a chemically-defined medium without serum (RPMI/X-VIVO mixture). However, the HeLa cells are grown in a medium which does contain serum, and foetal bovine serum (FBS) is known to contain EVs just as serum from humans contains EVs. The HeLa cells, both UV-irradiated and the non-irradiated control cells, were washed with Hank's balanced salt solution (HBSS) and transferred into 0.1 µm filtered serum-free medium immediately prior to UV-irradiation and incubation.

A timecourse of the EV release from the UV-irradiated HeLa cells (UVHeLa) and the control cells (HeLa) was carried out to determine if the HeLa cells have the same pattern of EV release as the apoEVs from BL2 cells and BL2-bcl2 EVs. A different flask was used for each timepoint and the entire culture supernatant of 5 mL was used for EV separation. This was because the HeLa cells are adherent and taking a sample of the supernatant to analyse at different timepoints would artificially inflate the concentration of EVs in the later timepoints. The EVs were separated in the same manner as the BL2 EVs, a centrifugation step was used to remove any cells which may have detached from the culture flask due to apoptosis, followed by dual filtration through a 5 µm mesh filter and 1.2 µm syringe filter under gravity.

The total number of EVs released from the UVHeLa and control HeLa cells can be seen in Figure 3.12A. The UVHeLa cells produced a higher concentration of EVs than the non-irradiated control HeLa cells at each timepoint, including the sample which was taken immediately after UV-irradiation. This could indicate that the process of EV release occurs rapidly enough after a stimulus to be observable in the few minutes needed to retrieve the cell culture supernatant after irradiation. However, the optimum concentration of particles for the NanoSight to give an accurate quantification is between 10^8-10^9, so the difference seen between UVHeLa and HeLa cells at this timepoint may due to the lack of sensitivity of the instrument at these low particle concentrations.

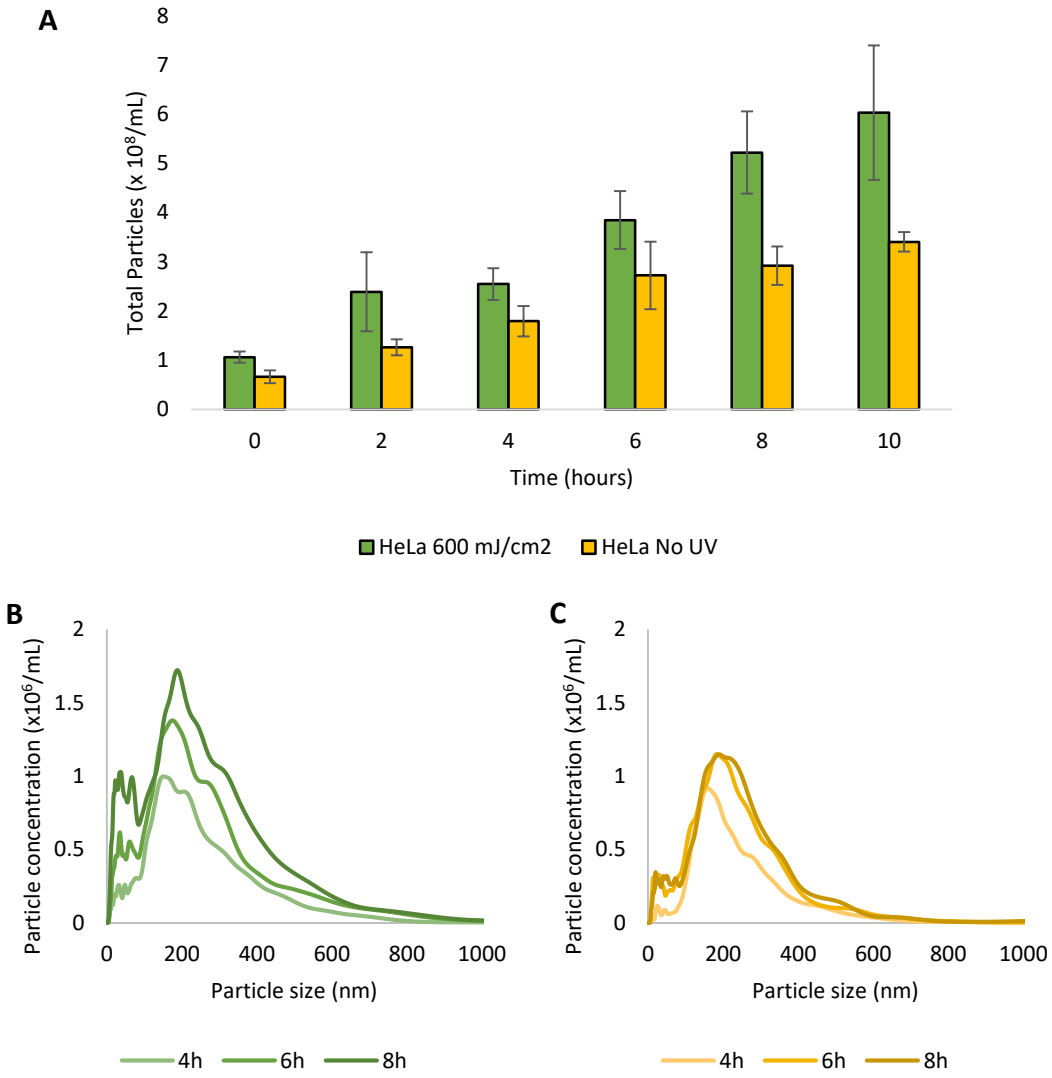

Figure 3.12: NanoSight analysis showing timecourse of EV release from UV-irradiated and control HeLa cells. (A) Total concentration of EVs released from HeLa cells at 2-hour intervals. Three independent experiments were carried out, the error bar shows standard deviation. Size distribution of UVHeLa (B) and HeLa (C) EV, showing only the 4-hour, 6-hour and 8-hour timepoints for clarity.

The differences in the size profiles of the UVHeLa and HeLa EVs are not as striking as those of the BL2 and BL2-bcl2 EVs (Figure 3.12B and Figure 3.12C). The UVHeLa cells do seem to release a higher proportion of smaller <100 nm EVs, but the difference in concentration of the larger (>400 nm) population seems to be increased in the UVHeLa EVs only due to the increase in overall EV number, while the HeLa EV concentration remains rather static between the 6 and 8-hour timepoints.

The increase in the number of EVs released from the UVHeLa cells is more striking when considering that the proportion of cells in this population that are apoptotic (24%, Figure 3.6)

is much lower than the proportion of BL2 cells which are apoptotic after UV irradiation (78.5% Figure 3.1).

3.5 Raman spectroscopy of EVs

As demonstrated in Figure 3.11B and Figure 3.12B and 3.13C, the EVs are < 1 µm in diameter, having been passed through a 1.2 µm filter. The majority of these EVs are < 400 nm. This small diameter means that the entire EV can be investigated by Raman spectroscopy using single point spectra, rather than mapping, of the EV adhered onto a CaF_2 window in a label-free manner. All EV Raman spectra were acquired in PBS with a 60x water immersion objective using a 532 nm laser excitation with a power of 35 mW for 10 seconds.

3.5.1 Raman spectroscopy of BL2 and BL2-bcl2 EVs

The EVs separated as described in Section 3.4.1 were incubated overnight on a CaF_2 window which had been pre-coated with Cell-Tak. Cell-Tak is a protein solution derived from mussels used to adhere cells and tissues to surfaces. This allowed the EVs to adhere to the CaF_2 window in order to be visualised using the white light source on the instrument and to remain stationary while in the path of the laser for data acquisition.

Spectra of 50 EVs were acquired for each experiment, and three independent experiments were carried out, giving a total of 150 EV spectra. The mean spectra for BL2 EVs and BL2-bcl2 EVs are shown in Figure 3.13. As can be seen from the raw mean spectrum, the BL2 EVs have a much higher background than the BL2-bcl2 EVs. This could be due to the presence of fluorescent material such as cytochrome c, which is resonant at the visible wavelength used to obtain the Raman spectra.[235] Cytochrome c is ordinarily found in the mitochondria, but is released into the cytoplasm during apoptosis. This cytoplasmic cytochrome c could then be packaged into the BL2 apoEVs as cargo, causing a fluorescent background effect. This is not observed in the apoptotic cells, as the dispersion of cytochrome c throughout the cytoplasm would decrease the local concentration, thereby reducing the contribution this molecule has to the signal.[206]

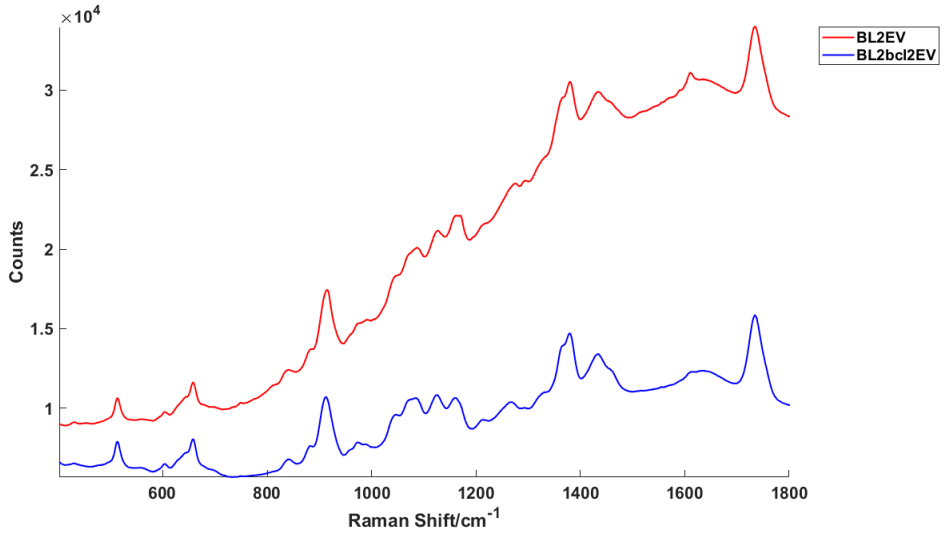

Figure 3.13: Mean Raman spectra of 150 BL2 EVs (red) and 150 BL2-bcl2 EVs (blue) from three independent experiments. The BL2EV spectra have a much higher fluorescent Raman background than the spectra of BL2bcl2EV. Raman spectra were acquired in PBS with a 60x water immersion objective using a 532 nm laser excitation with a power of 35 mW for 10 seconds.

The peaks seen in the Raman spectra of the EVs are assigned in Table 3.2. These peaks include lipid peaks, such as the membrane phospholipid phosphatidylinositol at 514 cm^{-1} and lipid ester peak at 1736 cm^{-1}; nucleic acid peaks, including ribose peaks at 916 cm^{-1} and 974 cm^{-1}, DNA phosphate backbone at 1070-1090 cm^{-1}, and guanine and cytosine peaks at 1369 cm^{-1} and 1611 cm^{-1}, respectively; and protein peaks, such as tyrosine at 643 cm^{-1} and 1161 cm^{-1}, and the amide III peak at 1260 cm^{-1}. On the basis of the peaks observed in the spectra, it can be inferred that the particles investigated are membrane enclosed structures containing both protein and nucleic acids and are thus likely to be EVs.

These EV Raman spectra are very different to the parental cells from which they derive (Figure 3.7). One of the most prominent differences is the absence of the Phe peak at 1004 cm^{-1} from the EVs spectra. This is also seen in a number of literature studies of Raman spectroscopic analysis of EVs.[299–301] It may be that peaks associated with the molecular vibrations of proteins are diminished in the EV spectra. When considering the size and composition of EVs, the majority of the biomolecular components will be the phospholipids making up the plasma membrane. The small volume of the particle would not be able to contain a high concentration of soluble proteins or nucleic acids to balance the strong signal from the lipids in the membrane, thereby giving the Raman spectra of the EVs a drastically different relative composition to the Raman spectra of the cells.

Due to the high background of the BL2 EVs Raman spectra, the two types of EV could not be directly compared without performing baseline correction on the data, as the PCA separated them based on the different background of the BL2-bcl2 EVs. The spectra were scaled to unity. In the EV spectra, the peak with the greatest intensity is the 1736 cm^{-1} lipid peak, which would have a significant contribution from the lipid membrane which delimits the EVs. As EVs are spherical particles with a radius in the nanometre scale, the surface area of the particle will be relatively high with very little cytoplasm inside. Thus, by scaling to a lipid peak the spectra are essentially normalised to the size of each EV.

Table 3.2: Assignment of Raman peaks seen in spectra of BL2 EVs and BL2-bcl2 EVs.

Raman shift (cm^{-1})	**Assignment**
514	Phosphatidylinositol
643	Tyrosine
658	Cystine
839	Polysaccharide
916	Ribose (RNA)
974	Ribose (RNA)
1046	Glycogen
1070-1090	PO_2^- of DNA
1125	Acyl lipid backbone
1161	Tyrosine
1260	Amide III
1365	Guanine, Tryptophan
1380	Lipid CH_3
1434	CH_2
1611	Cytosine
1736	C=O ester (lipids)

The baseline corrected spectra, plotted with ±1 SD shaded, are shown in Figure 3.14A and Figure 3.14B. The mean spectra show differences between the BL2 and BL2-bcl2 EVs at a number of peak positions, including the presence of a small shoulder peak in the BL2 EV spectrum at 810 cm^{-1}, the higher intensity of the DNA band at 1070-1090 cm^{-1} in the BL2-bcl2 EVs, the higher peak intensity due to cytosine at 1161 cm^{-1} in the BL2 EVs, the higher intensity of the shoulder peak at 1365 cm^{-1} in the BL2 EVs, and the peak at 1611 cm^{-1} which

is present in the BL2 EVs but absent in the BL2-bcl2 EVs. However, as can be seen in Figure 3.14B, the SD of the spectra overlap at all points, indicating that these differences may be due to biological variability. This is particularly evident when plotting the SD itself, shown in Figure 3.14C. The SD of the BL2 EV mean spectrum has much higher peak intensities than the SD of the BL2-bcl2 EV spectrum. The main peak in the BL2-bcl2 EV SD is the band in the 1500-1700 cm^{-1} region, with smaller contributions at 536 cm^{-1}, 917 cm^{-1}, 991 cm^{-1}, 1173 cm^{-1}, 1279 cm^{-1}, and 1354 cm^{-1}. In contrast, the SD of the BL2 EV spectrum has significant peaks at many points, indicating that the BL2 EV population is more heterogeneous than the BL2-bcl2 EV population. This is expected, since the BL2 EV population will contain some EVs released as a result of apoptosis, but there will also be some EVs released constitutively, or as a result of the nutritional stress that the cells are under by being at a high cell density of 20 x 10^6 mL^{-1}. The BL2-bcl2 cells are all viable over the course of the EV preparation, so no EVs are released as a result of apoptosis and only constitutive EVs are released, thereby yielding a more homogeneous EV population than the mixed population of BL2 EVs.

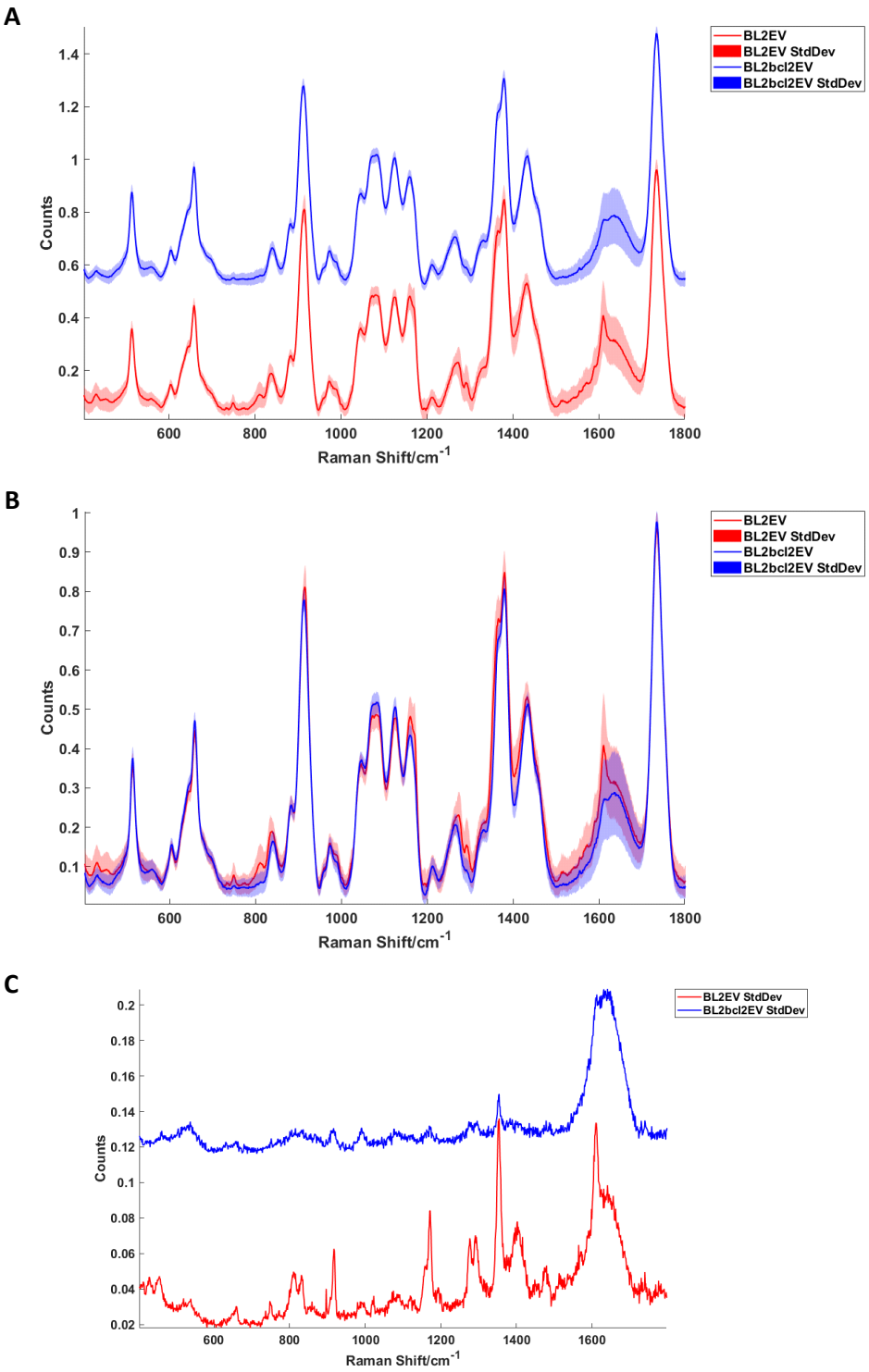

Figure 3.14: Mean, baseline corrected spectrum of BL2 EV and BL2-bcl2 EV plotted with ±1 SD shaded. (A) shows the mean spectrum for each EV type offset for clarity. The spectra are overlaid in (B), showing that, despite differences in the two spectra, the SD overlaps at all points for the mean spectra of the two EV types. (C) shows the SD for each condition plotted. The SD of the BL2 EVs spectra is much higher than that of the BL2-bcl2 EVs spectra, showing that the BL2 EVs are a more heterogeneous population than the BL2-bcl2 EVs. Raman spectra were acquired in PBS with a 60x water immersion objective using a 532 nm laser excitation with a power of 35 mW for 10 seconds.

The PCA results of the BL2 and BL2-bcl2 derived EVs are shown in Figure 3.15, where each point represents a single EV spectrum. The plot of scores for PC1 (41.4%) vs PC2 (3.2%) in Figure 3.15A shows that the BL2 EVs display some moderate separation from the BL2-bcl2 EVs along the PC1 axis. The BL2-bcl2 EVs have a negative PC1 score, with some outliers having a positive score. The BL2 EVs have a wider distribution of scores, where more than half have a positive PC1 score but there are many BL2 EVs with a negative PC1 score. There is not a clear separation of these two groups, most likely due to the heterogeneity of the BL2 EVs population.

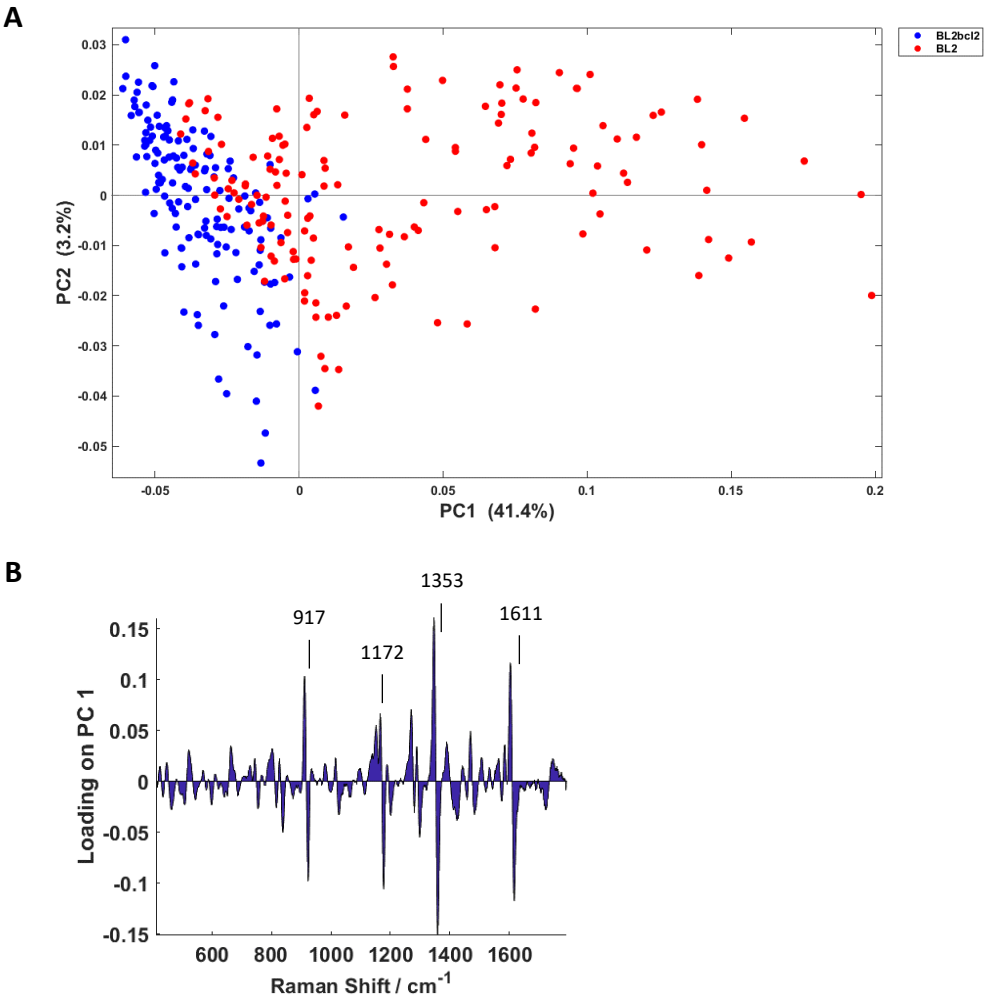

Figure 3.15: PCA of the first derivative Raman spectrum of BL2 EV and BL2-bcl2 EV Raman spectra. (A) Plot of scores of PC1 vs PC2, showing separation of the BL2 EV along the axis of PC1. (B) The loading of PC1, showing contribution from peaks at 917 cm^{-1}, 1172 cm^{-1}, 1353 cm^{-1}, and 1611 cm^{-1}.

Table 3.3: Assignment of peaks in PC1 loading for BL2 and BL2-bcl2 EVs

Raman shift (cm^{-1})	Assignment
917	Ribose (RNA)
1172	Tyrosine
1353	Guanine
1611	Cytosine

The loading of PC1 is shown in Figure 3.15B, and the peaks contributing to this loading are assigned in Table 3.3. The contributions of PC1 are made up mostly of nucleic acids, with peaks corresponding to ribose at 917 cm^{-1}, guanine at 1353 cm^{-1}, and cytosine at 1611 cm^{-1} observed. This suggests that the BL2 EVs have a higher nucleic acid content than the EVs derived from the BL2-bcl2 cells. This agrees with the hypothesis that when the cells undergo apoptosis, the nucleus condenses and fragments, thus allowing the transport of nuclear material in the EVs.

3.5.2 Raman spectroscopy of HeLa and UVHeLa EVs

The EVs separated from HeLa cells were incubated on a CaF_2 window overnight, in the same way as the BL2 and BL2-bcl2 EVs. Three independent experiments were carried out, and 50 EV spectra were acquired in each experiment, giving a total of 150 spectra for both HeLa EVs and UVHeLa EVs.

The mean spectra are shown in Figure 3.16. On first inspection, the spectra are very similar to those of the BL2 and BL2-bcl2 EVs (Figure 3.14), showing the same pattern of peaks.

The background in the mean Raman spectra of the HeLa EV and UVHeLa EV are similar, with the UVHeLa EV spectrum having a slightly higher background. Both types of EV show a higher background than observed in the BL2-bcl2 EVs spectra, but lower than the BL2 EVs (Figure 3.13). Although the background for both types of HeLa-derived EVs was comparable, the spectra were baseline corrected and scaled in the same manner as the EVs from the BL2 and BL2-bcl2 cells.

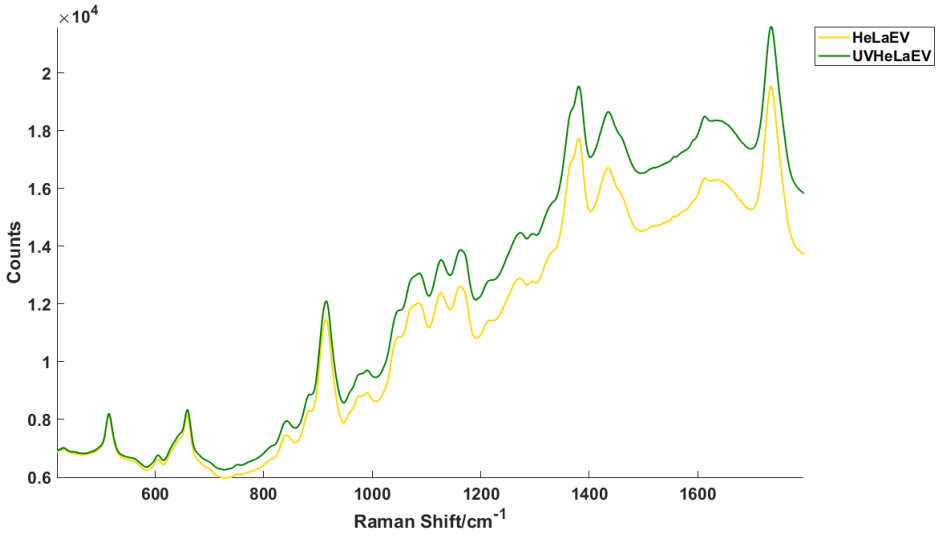

Figure 3.16: Mean Raman spectra of 150 HeLa EVs (yellow) and 150 UVHeLa EVs (green) from three independent experiments. Raman spectra were acquired in PBS with a 60x water immersion objective using a 532 nm laser excitation with a power of 35 mW for 10 seconds.

The baseline corrected and scaled spectra are plotted with ±1 SD in Figure 3.17A and Figure 3.17B. The mean spectra for the HeLa EVs and UVHeLa EVs do not show any visible differences at any location in the spectrum, even before the SD is plotted. This is not entirely unexpected, as the EVs released from the irradiated and non-irradiated HeLa cells did not display the same divergence of size profile seen in the EVs from the irradiated BL2 and BL2-bcl2 cells. This may be due to the exchange of the cells into serum-free medium before the EV separation procedure, which could have resulted in the activation of starvation-induced stress responses in both the irradiated and non-irradiated cells. This is evident in the plot of the SD, shown in Figure 3.17C, where the SDs of the spectra are very similar. For most peaks the deviation is actually higher in the control HeLa EVs than the irradiated UVHeLa EVs, which should not be the case if the HeLa EVs are all released as the result of a constitutive process as anticipated. The fact that the control HeLa EVs show a similar, if not greater amount, of heterogeneity than the UVHeLa EVs is indicative of the alteration of the cell state after being placed in the serum free medium, despite this being a common method for the separation of EVs from cells which are grown in a serum-containing medium.

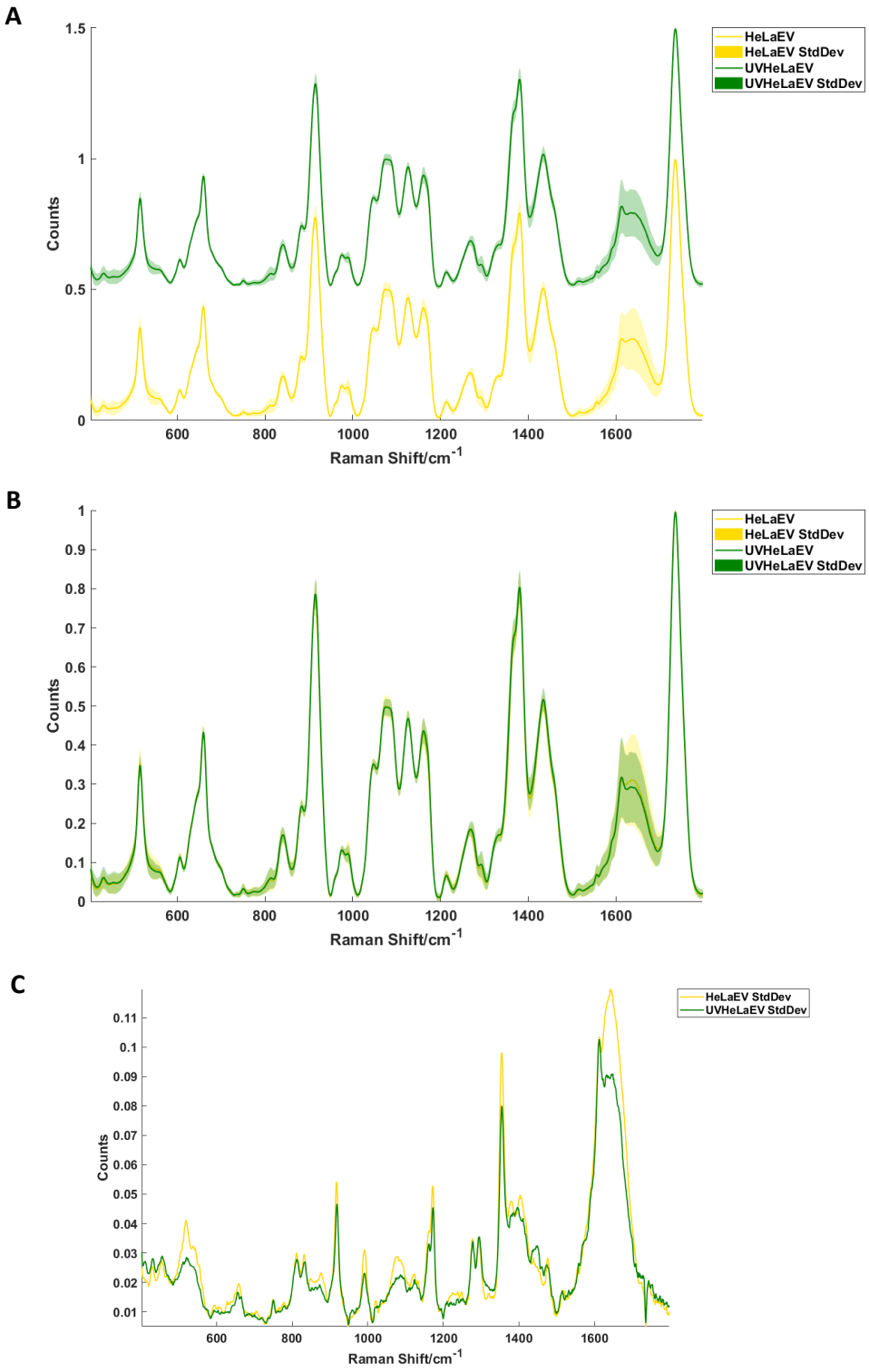

Figure 3.17: Baseline-corrected mean spectrum of HeLa EVs and UVHeLa EVs plotted with ±1 SD shaded. (A) shows the mean spectrum for each EV type offset for clarity. The spectra are overlaid in (B), showing that there is no difference in the Raman spectra of the two EV types and the SD overlaps at all points. (C) shows the plotted SD for each condition. The SD of both EV spectra are reasonably high, with the SD of the HeLa EVs having a higher intensity at almost all points. Raman spectra were acquired in PBS with a 60x water immersion objective using a 532 nm laser excitation with a power of 35 mW for 10 seconds.

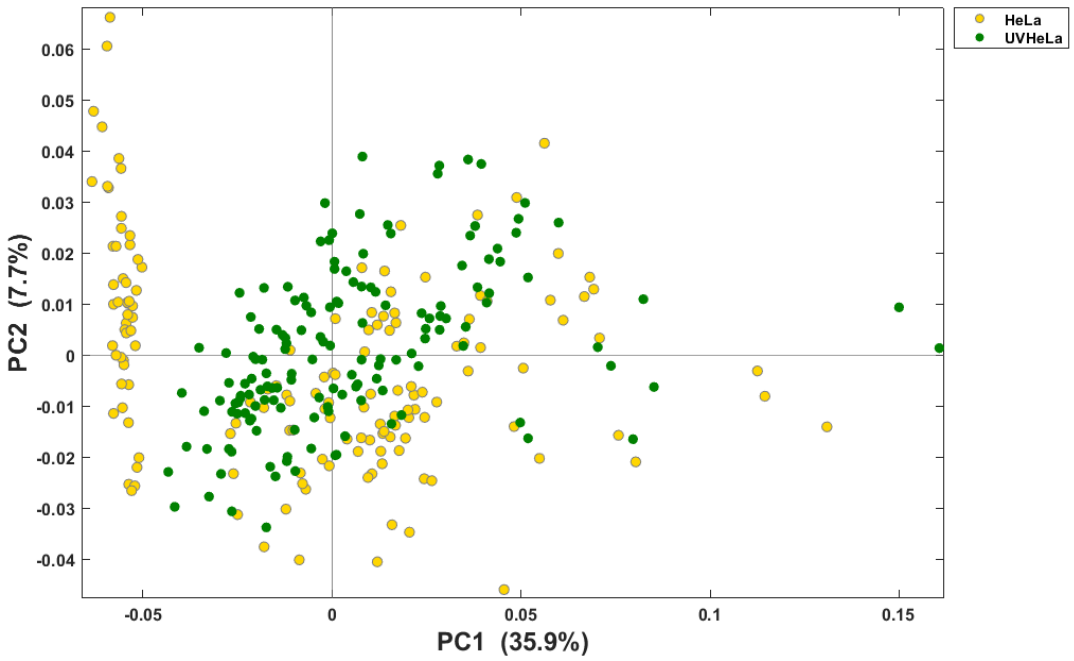

Figure 3.18: PCA plot of PC1 scores vs PC2 scores for HeLa EVs and UVHeLa EVs. PCA did not reveal any further differences between the two groups of EVs which were not discernible from the spectra alone.

PCA of the HeLa EVs and UVHeLa EVs spectra also shows that there is no observable difference between the two groups of EVs. The plot of PC1 vs PC2 scores is shown in Figure 3.18, where each point on the plot represents a single EV spectrum. Both groups have an even distribution of positive and negative scores for PC1 and PC2, clustering about the origin. This is observed for plots of the first 4 PC scores against each other (PC1 accounts for 35.9% of the variation, PC2 7.7%, PC3 6.2%, and PC4 1.8%). Therefore, the low levels of cellular apoptosis in the HeLa cells were likely not high enough to produce a population of apoEVs from these cells in sufficient numbers for this population to be observed in this small sample size of Raman spectra.

3.5.3 Comparison of Raman spectra for BL2 EVs, BL2-bcl2 EVs, HeLa EVs, and UVHeLa EVs

The Raman spectra of the BL2 EVs and BL2-bcl2 EVs, and the spectra of the HeLa EVs and UVHeLa EVs, were each compared pairwise using PCA, which showed that the BL2 EVs have a different composition to the BL2-bcl2 EVs (Figure 3.15), and there is no observable difference between the HeLa EVs and the UVHeLa EVs (Figure 3.18). Since different cell types can be discriminated by Raman spectroscopy,[224,230,232,233] the spectra of the EVs from the UV-irradiated BL2 and BL2-bcl2 cells were analysed together with the EVs separated from the

HeLa and UVHeLa cells in order to determine whether EVs deriving from different cell types can also be distinguished from each other. The mean spectra are plotted together in Figure 3.19A, which shows a striking similarity between the spectra of EVs separated from the two different cell types. The SD is plotted in Figure 3.19B, showing that the BL2-bcl2 EVs have the lowest SD of the four groups of EVs. The SD for the BL2 EVs is quite similar to that of the HeLa EVs and the UVHeLa EVs.

PCA was carried out on the four groups of EVs, shown in Figure 3.20A. Although there is not a distinct separation between the EVs from the two cell types, there is a very slight separation of the EVs derived from the HeLa cells along the axis of PC3, which accounts for 7% of the variance between the spectra. The majority of the HeLa EVs and UVHeLa EVs have a positive score for PC3, while the BL2-bcl2 EVs all have a negative PC3 score. Many of the BL2 EVs have a negative PC3 score, but there are some with a positive score, so this alone cannot be used to distinguish the EVs from the two cell groups.

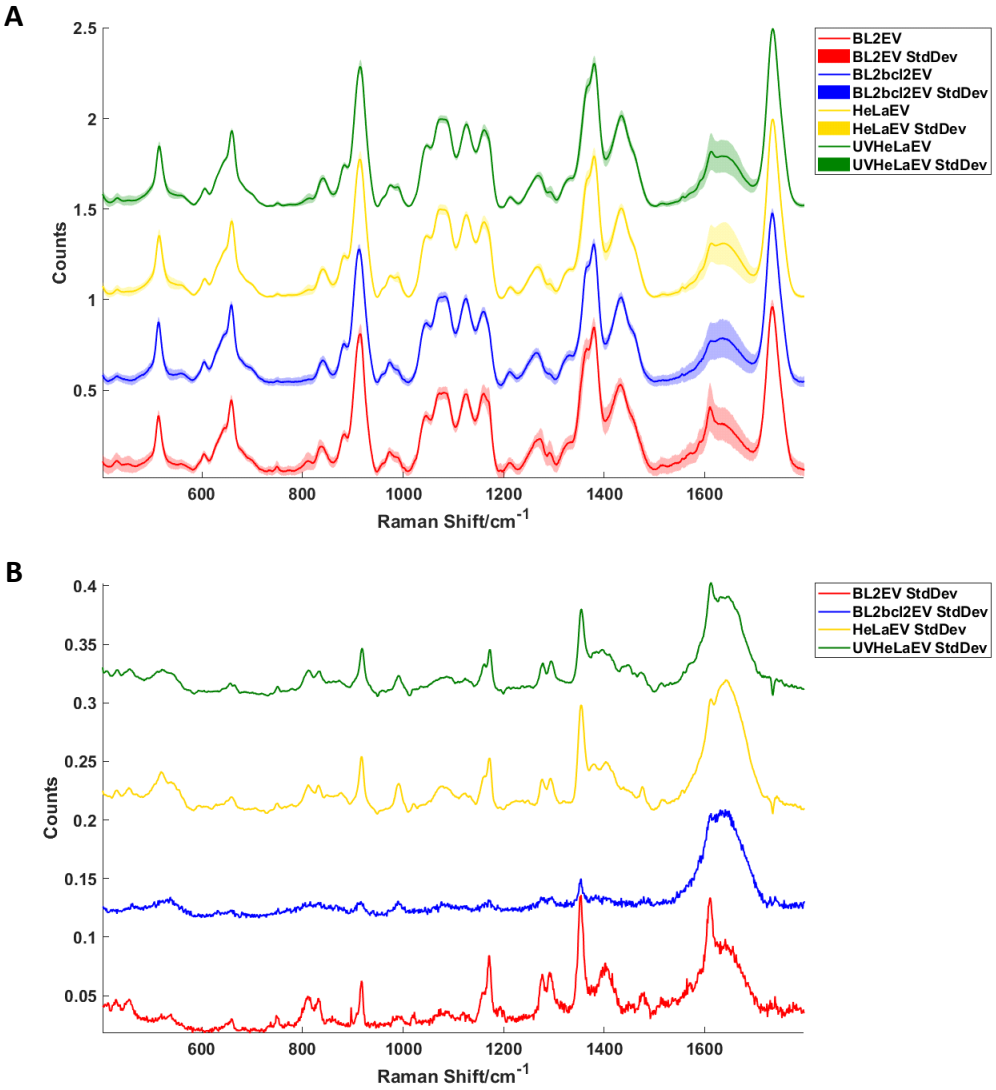

Figure 3.19: (A) Mean, baseline corrected spectra of BL2 EV, BL2-bcl2 EV, HeLa EV, and UVHeLa EV plotted with ±1 SD shaded. The spectra are offset for clarity, but the SD of the spectra overlap for the two groups at almost all points. (B) The SD for each mean spectrum is plotted, offset for clarity. Raman spectra were acquired in PBS with a 60x water immersion objective using a 532 nm laser excitation with a power of 35 mW for 10 seconds.

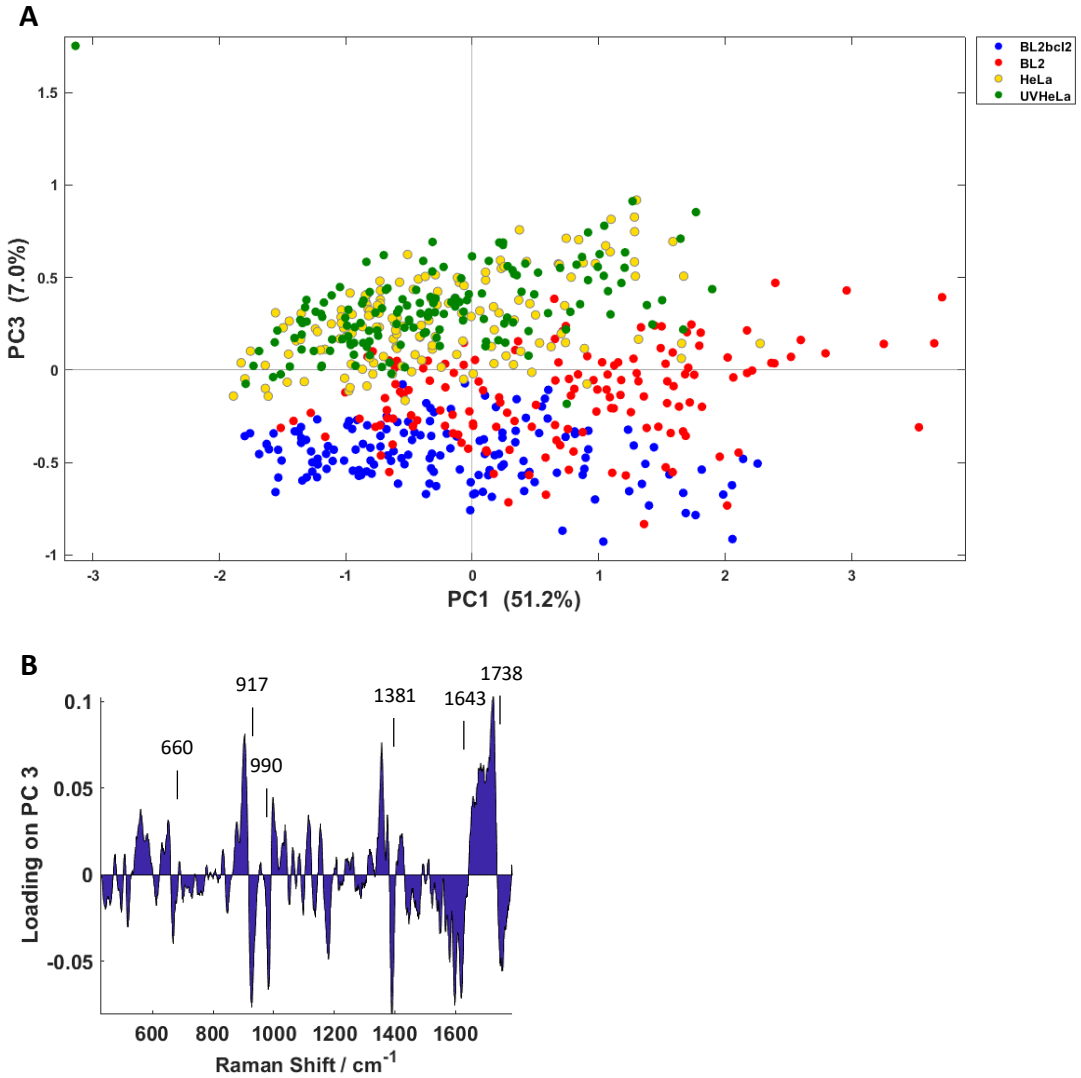

Figure 3.20: PCA of the first derivative Raman spectrum of BL2 EVs, BL2-bcl2 EVs, HeLa EVs, and UVHeLa EVs. (A) Plot of PC1 scores against PC3 scores, showing that the HeLa EVs and UVHeLa EVs show some separation from the BL2 EVs and BL2-bcl2 EVs along the PC3 axis. (B) Plot of the loading on PC3, showing contributions from peaks at 660 cm^{-1}, 917 cm^{-1}, 990 cm^{-1}, 1381 cm^{-1}, and 1738 cm^{-1}.

The PC3 loading is shown in Figure 3.20B, with peaks assigned in Table 3.4. These peaks correspond to functional groups found in nucleic acids, such as cytosine at 660 cm^{-1} and ribose at 917 cm^{-1} and 990 cm^{-1}; proteins, with the amide I band at 1643 cm^{-1}; and lipids are represented by the peak at 1738 cm^{-1}. This shows that, while the spectra look very similar, there are slight differences in the composition of EVs from the two different cell types corresponding to a variety of biomolecules. These are minor differences however, as the loading of PC3 explains just 7% of the variance of the spectra, while PC1 and PC2 explain 51.2% and 18.2%, respectively. This distinction between EVs of different cell types by PCA of Raman spectra has been shown in the literature for different stem cells,[300] and between

cancer cell-derived and non-cancer cell derived EVs,[296,298,299] so it is not surprising that EVs from cancer cells of two different cell lineages may also be distinguished using this technique.

Table 3.4: Assignment of peaks in PC3 loading comparing BL2 EVs and BL2-bcl2 EVs with HeLa EVs and UVHeLa EVs

Raman shift (cm^{-1})	**Assignment**
660	Cytosine
917	Ribose (RNA)
990	Ribose
1381	CH3
1643	Amide I
1738	Lipids

3.6 Discussion

Raman spectroscopy combined with multivariate analysis is a powerful tool for the analysis of biological systems. As shown in this work, Raman maps of cells can be used to distinguish between viable and apoptotic BL2 cells, without any observable difference between the viable BL2 cells and both untreated and UV-irradiated BL2-bcl2 cells. Comparing this BL cell line with viable and apoptotic HeLa cells under the same apoptotic stimulus again shows both that the UV-irradiated HeLa cells can be distinguished from the untreated cells, and that the HeLa cells of epithelial origin can be distinguished from the lymphocytes. Within this large dataset, the apoptotic cells do not clearly separate from their viable counterparts, showing that the variation between cells of different lineages overrides the distinguishing features of early cell death.

Similarly, EVs released from different cell types and states can also be distinguished by Raman spectroscopy. The spectra of the EVs are quite different to those of their parental cells, showing that the EVs have different relative biomolecular constituents to the cells from which they derive. The BL2 EVs are relatively heterogeneous whereas the BL2-bcl2 EVs are quite homogeneous, as seen from the SD of their spectra. This population variability is to be expected due to the different status of these cells, where the apoptotic BL2 cells will be releasing both apoEVs and constitutive EVs but the BL2-bcl2 cells will be releasing only

constitutive EVs. These two groups of EVs can be distinguished from one another using PCA, showing that the apoEVs released from dying cells are fundamentally different from the EVs released constitutively from cells which are viable. This is mainly due to an increase in the nucleic acid bands in the BL2 apoEVs, showing that the fragmentation of the nucleus during apoptosis results in nuclear fragments which can be transported in EVs released from the cells. Although no discernible difference could be detected in the EVs released from HeLa cells which had been exposed to UVB irradiation and those which were untreated, the EVs released from HeLa cells could be distinguished from the EVs released from BL2 cells. This potentially has a great significance in the characterisation of EVs from clinical samples. If EVs from different cell types and different viability states can be distinguished from each other using Raman spectroscopy, it is possible that EVs from healthy and cancer cells are also distinguishable using this technique. This could be used to monitor cancer EVs in the peripheral blood of patients. A drawback of this is that Raman spectroscopy is currently not high-throughput enough to analyse the number of EVs required for this to be clinically relevant.

4 Bioinformatics and proteomics to identify plasma membrane proteins present on extracellular vesicles

4.1 Introduction

Gene expression profiling is a technique used to determine which genes are active in a particular sample by measuring the amount of mRNA present for each gene sequence. This analysis is both qualitative and quantitative, giving not only information on which particular mRNAs are present, but also how many copies of these nucleic acid sequences are detected. In this way, a global picture of the gene expression in a sample can be investigated, rather than techniques such as quantitative reverse-transcriptase polymerase chain reaction, where only a single gene can be investigated at one time. This picture can then be used to compare the genes being expressed in different environmental conditions, or between healthy and diseased tissue, in order to establish a genetic hypothesis for the changes occurring between samples.

4.1.1 Affymetrix gene expression microarrays and BioLayout *Express*^{3D}

4.1.1.1 Affymetrix GeneChip

Affymetrix GeneChip microarrays are gene expression platforms composed of perfect match probes for nucleic acid analysis. Each probe is 25 bp long, designed to match a particular gene sequence. Each gene is represented on the microarray by many different probes, typically 11 probes per gene, making up a probe set for that gene. Each chip contains tens of thousands of these probe sets in order to investigate gene expression in a sample. The nucleic acid sample is labelled with biotinylated nucleotides during an amplification process, which is incubated with the array, washed, and then stained in order to detect the nucleic acids which have hybridised with the probe arrays. The array is then scanned, and each scan location corresponds to a particular known probe sequence, so that the staining intensity can be then used as a readout for the expression level of that nucleic acid sequence in the sample.[303]

4.1.1.2 Microarray data pre-processing

The gene expression data must be quality controlled and normalised before input into a network graph for visualisation. This pre-processing is carried out using a frozen robust multiarray analysis (fRMA) algorithm. Each array undergoes background correction, then normalisation. A quantile normalisation algorithm is used, where each quantile across all of the arrays are normalised, which gives a more equalised distribution of probe intensities.[288]

The normalised data are then summarised as gene expression, often represented by a mean of probe set intensities. fRMA has been developed to allow for analysis of multiple batches of array data together, which was not possible using the original RMA algorithm due to the inter-batch variability observed with microarrays.[288]

4.1.1.3 BioLayout *Express*^{3D}

The software BioLayout *Express*^{3D} was used to interrogate the gene expression microarray data obtained from the online repository Gene Expression Omnibus. This software is an open-source application designed to display a large amount of data as a 3D network, which has been extremely useful for the display of the large data outputs of microarray gene expression analysis.

The 3D graph generated by BioLayout follows classical graph theory in that it is made up of nodes which are connected by edges (Figure 4.1A). In biological systems, the nodes represent genes, transcripts, or proteins, and the edges represent similarities or functional linkages between nodes.[290] The network is constructed using a modified Fuchterman and Rheingold graph layout algorithm, in which the nodes of the graph experience a repulsive force, and the edges exert an attractive force on the nodes which they connect.[304] The graph undergoes successive iterations of node and edge repulsion and attraction, initially with a high temperature function allowing the nodes to move more freely. Successive rounds are carried out with slowly lowering temperatures to limit the movement of the nodes, until the final rounds of iteration at a set low temperature refine the final positions of the nodes, generating a stable and 'aesthetically pleasing' graph.[304]

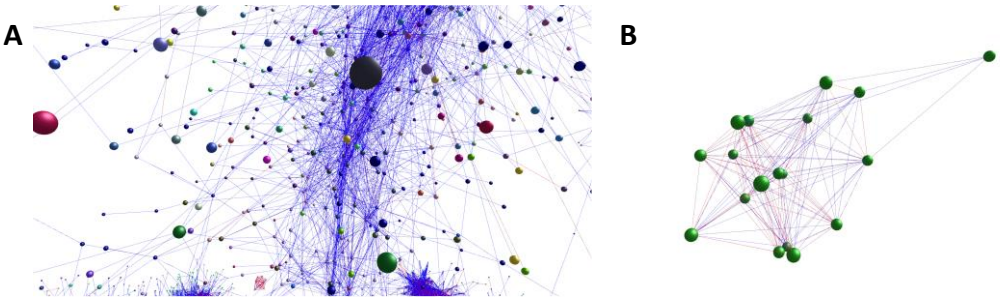

Figure 4.1: Representative example of BioLayout Express^{3D} graphical output. A) Close-up of the network graph, showing the nodes, which represent genes, connected by edges, representing a functional linkage between genes. B) An example of a cluster, where each of the nodes is given the same colour to distinguish from other clusters.

For analysis of gene expression profiles, the similarity between the gene expression in different samples is determined by a statistical test (Pearson correlation coefficient). The

minimum correlation value is a Pearson coefficient of 0.7, as a lower coefficient would generate a graph with a very high number of edges and would be difficult to interpret. Nodes with no connections above the selected threshold are removed from the graph. Increasing the Pearson threshold even further removes more edges, and large networks fragment into smaller graphs.[290] Smaller graphical components commonly form; due to redundancy in gene representation in the microarray chips, multiple probes for a single gene may be present, and these may only correlate with each other. A clustering algorithm (Markov cluster, MCL) is used to partition the structured graph into clusters of nodes expected to be biologically significant, used to identify genes which may be coexpressed and likely to share regulatory mechanisms and functional relationships (Figure 4.1B). MCL discovers clusters by the identification of nodes which share higher-order connectivity rather than pairwise linkages, avoiding false positive clustering in the presence of spurious edges. Typically, an MCL inflation value of 2.2 is used in analysis.

Each cluster has an associated graph showing the mRNA expression level in each sample across the cluster for the genes represented in the cluster. In order to identify the proteins which were upregulated in the B cell cancer samples, these graphs were inspected for each cluster, and the clusters which showed a higher expression level of the genes in the cancer samples were taken for further analysis. The genes in these clusters were researched in order to determine which of these gene products were known to localise to the plasma membrane.

4.1.2 Aims of the chapter

The aim of this chapter is to use bioinformatic techniques to identify proteins which could be transferred onto the EVs which can be used as targets for EV detection. As EVs are released from all types of cells, both lymphoma cells and the healthy B cell counterparts will be releasing EVs, and both of these EV populations could be found in the blood. Thus, in order to preferentially detect EVs from lymphoma cells in the blood of a patient, identifying proteins which are upregulated in lymphoma cells compared to healthy B cells would suggest that these upregulated proteins are found in greater abundance in the lymphoma EVs. The hypothesis is that the larger size of EVs being studied are the MV type, and thus derive from the plasma membrane, so these EVs should have plasma membrane markers on their surface. Upregulated plasma membrane proteins will be present in greater numbers on the lymphoma EVs, thus preferentially detecting these EVs in a blood sample from a patient. The first method investigated was to use public gene microarray databases in order to identify

plasma membrane proteins which are upregulated in B-cell cancers compared to healthy B cell samples.

The BioLayout Express^{3D} software was used to compare the gene expression profiles of healthy B cells at various stages of maturity to gene expression profiles of lymphoma biopsy samples and lymphoma cell lines. In this way, plasma membrane proteins which are overexpressed in the lymphoma samples compared to healthy B cells can be identified and investigated as potential B cell lymphoma EV detection targets.

Proteomic analysis of the apoEVs from BL2 cells and the EVs from UV-irradiated BL2-bcl2 cells was also carried out. The results of this analysis were searched for proteins localised to the plasma membrane. This analysis is beneficial because proteins which are found only on the apoEVs can be identified and used to selectively detect apoEVs in the presence of constitutively released EVs.

4.2 Datasets chosen

The gene expression datasets chosen for analysis were obtained from the GEO database. A number of healthy B cell datasets were available, isolated from blood or tonsillar B cells. Some samples consisted of peripheral blood mononuclear cells analysed without further purification, some were B cells isolated based on specific surface markers such as CD19, CD20, CD10, or immunoglobulins. 135 healthy B cells samples were chosen for analysis. Brief descriptions of the sample types and accession numbers for the healthy B cell samples used are given in Table 4.1.

Lymphoma samples were also available, isolated from patient biopsy tissue or from established non-Hodgkin's lymphoma (NHL) cell lines. The cell line being used is the Burkitt's lymphoma (BL) cell line BL2. A number of BL datasets were available on GEO, from both cell lines and from biopsies of sporadic, endemic, and HIV-associated tissue. However, BL is not common and only 43 gene expression datasets were available. In order to balance the number of healthy and oncological datasets, samples from other types of NHL were included. Diffuse large B cell lymphoma (DLBCL) is the most common form of NHL, and can present with a morphology that is similar to BL with some cases intermediary between BL and DLBCL. 9 samples were available on GEO of biopsy tissue that was classified as BL-like DLBCL, along with 49 DLBCL biopsy samples. Combined with 24 NHL cell line datasets, this brought the number of lymphoma samples in the dataset to 126 to be compared to the 135 healthy B cell samples. The GEO accession numbers and brief descriptions of the lymphoma gene

expression array data are given in Table 4.2. A full description of all of the samples used including GSE accession number and GSM sample names is included as an appendix (Appendix 1).

Table 4.1: GEO accession number and brief sample description for healthy B cell gene expression array data used for BioLayout *Express*^{3D} analysis

Accession number	Cell type (source)
GSE46062	PBMC
GSE58208	PBMC
GSE64028	B cell (PBMC)
GSE10831	GC B cell (tonsil)
GSE12366	GC B cell (tonsil) Naïve GC B cell (tonsil) Naïve B cell (PBMC) Memory B cell (PBMC)
GSE17186	Naïve B cell (PBMC) Memory B cell (PBMC) Transitional B cell (PBMC) Transitional B cell (Cord blood)
GSE17269	Naïve B cell (PBMC)
GSE19599	Immature B cell (Bone marrow) Pre-B cell (Bone marrow) Pro-B cell (Bone marrow)
GSE26725	B cell (PBMC)
GSE28491	B cell (PBMC)
GSE36907	Mature B cell (PBMC) Class switched B cell (PBMC) B cell (PBMC) Splenic B cell (PBMC) Naïve B cell (PBMC)
GSE38697	GC B cell (Tonsil light zone) GC B cell (Tonsil dark zone)
GSE39411	B cell (PBMC)

Table 4.2: GEO accession number and brief sample description for the lymphoma gene expression array data used for analysis using BioLayout *Express*^{3D}

Accession number	Sample type
GSE20011	Namalwa (BL cell line) SU-DHL-4 (NHL B cell line)
GSE26673	BL biopsies
GSE36133	BL cell lines (various) DLBCL cell lines (various) B cell lymphoma (unspecified)
GSE38885	BL biopsies DLBCL (BL-like) biopsies DLBCL biopsies
GSE64085	BL biopsies

4.3 Evaluation of gene expression in datasets

The combined B cell and lymphoma gene expression array table was annotated with the probe ID, Entrez gene ID, the HGNC gene symbol, and the gene name using the annotation library from Bioconductor. A gene signature was also applied, using data indicating any known function that is associated with a particular gene, which was obtained from collaborators on the project. The annotated expression table was imported into BioLayout *Express*^{3D} Version 3.3. The Pearson correlation was set to 0.85, increased from the minimum value of 0.7 in order to reduce the size of the graph while maintaining some of the smaller clusters which contained only redundant probes on the array measuring the same gene, which could still identify upregulated genes. MCL clustering analysis was used with the default inflation value of 2.2.

This generated a 3D network graph consisting of over 1200 clusters, shown in Figure 4.2. The mean expression pattern for each cluster was viewed, with the sample information available as coloured blocks underneath each sample. The expression levels of the genes in the healthy B cell data, which were grouped together on one side of the cluster samples, was visually compared to the expression level in the lymphoma samples. When the mean expression levels of the genes were considered to be higher in the lymphoma samples than in the healthy B cell samples, the genes involved in that cluster were investigated to determine the cellular localisation of the gene products. Proteins which showed localisation to the plasma

membrane were investigated further, cross-referencing against gene expression profile data for the BL2 cell line which had been generated previously in the group (unpublished data), and a brief literature review of the protein function was carried out to determine whether the protein localised to the cortical membrane or had an external portion which could be used as an imaging target. The results of this analysis are given in Table 4.3, giving the gene name, level of expression of the gene found in gene expression profile array data carried out on the BL cell line BL2, and function of the gene product. The expression profiles of each of these genes from the BioLayout cluster analysis are given in Figure 4.3.

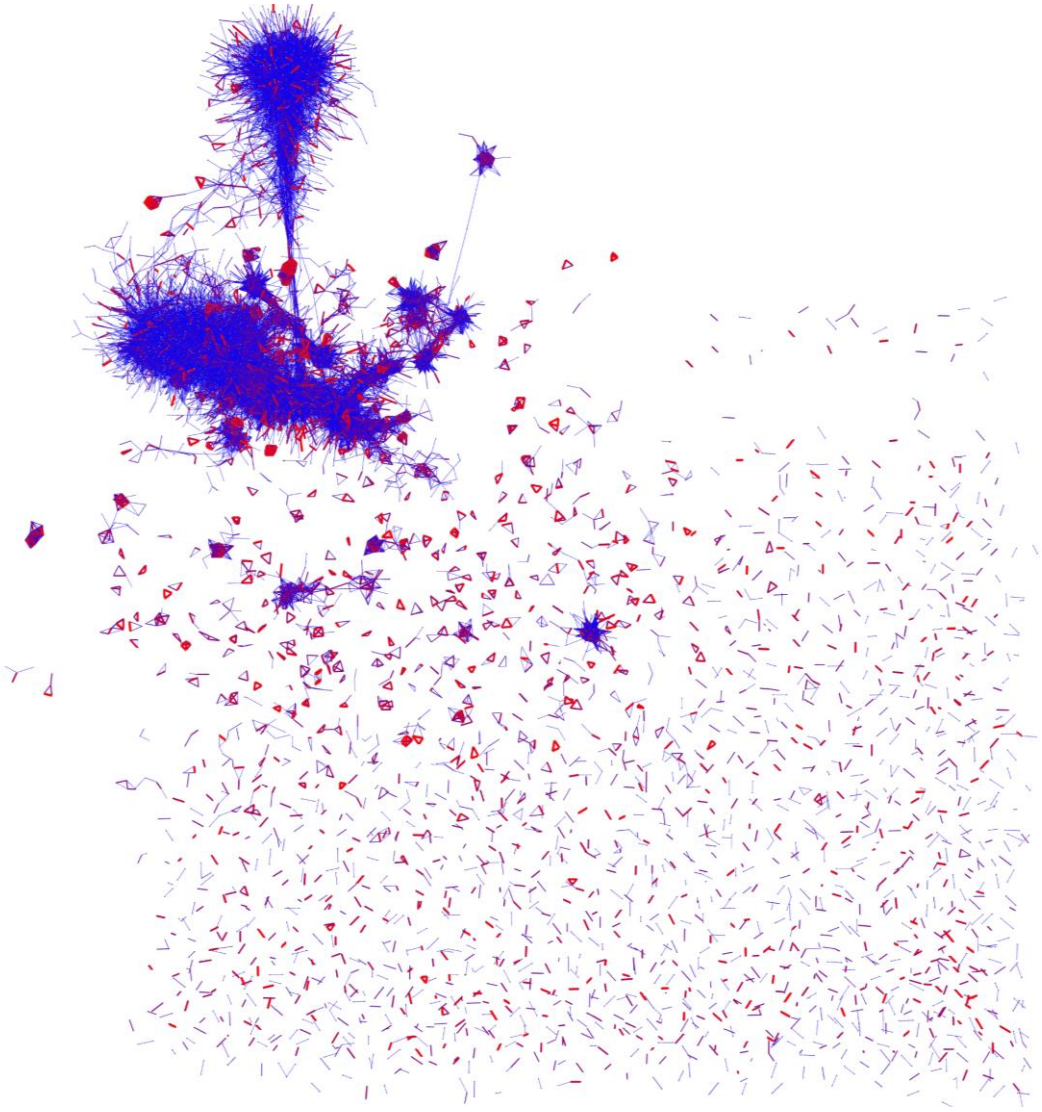

Figure 4.2: Full network graph generated by BioLayout. Due to the Pearson correlation value chosen, many small graphical components form which consist of clusters of redundant probe sequences for the same gene.

Table 4.3: Final results of BioLayout analysis to identify plasma membrane proteins which have higher expression levels in lymphoma samples than in healthy B cell samples. Genes which showed increased expression were evaluated for cellular localisation of the gene product, and then cross referenced with gene expression profile data of the BL2 cell line, which is shown in the table along with a brief description of the protein function.

Gene name	BL2 expression	Function
CD59	132.07-289	Regulator of complement-mediated cell lysis
MCAM	595.94	Cellular adhesion
LDLR	131.36/394.45	Endocytosis of LDL
BEST3	309.7	Cl^- channel
CD46	366.97-1219.52	Regulator of complement-mediated cell lysis
TMEM165	130.81-626.77	Unknown
SLC16A1	100.85-553.27	Monocarboxylate transporter

Seven genes were identified as plasma membrane locating proteins which showed greater expression in the lymphoma samples than in the healthy B cell samples. *CD59* and *CD46* were among the genes identified as upregulated. Both are membrane-bound complement regulatory proteins (mCRPs), ubiquitously expressed on human cells to prevent damage of cells by the complement system. CD46 acts as a cofactor in the inactivation of C3b and C4b complement components.[305] CD59 inhibits pore formation by the membrane attack complex, blocking the insertion of C9 into the plasma membrane by inhibiting the C5b-8 complex.[306] The expression of mCRPs in lymphoma is associated with treatment response to the anti-CD20 antibody rituximab combined with CHOP.[307] Exosomes derived from antigen presenting cells have been shown to have CD59 on the surface, which acts to protect the EVs from lysis by complement.[308] CD46 and CD59 have also been observed on exosomes derived from B cells analysed by proteomics.[309]

MCAM was also identified in these results, showing one of the highest level of gene expression in the BL2 data amongst the identified plasma membrane proteins. *MCAM*, melanoma cellular adhesion molecule, so called because it was first identified as a poor prognostic indicator in melanoma,[310] is also known as CD146. Although this protein has mainly been associated with epithelial cells, particularly having a role in the metastatic progression of tumours of the prostate[311] and ovary,[312] it has also been shown to have expression in certain lymphocyte subsets[313,314] and also in some leukaemias.[315] CD146 has also been observed on EVs.[316,317]

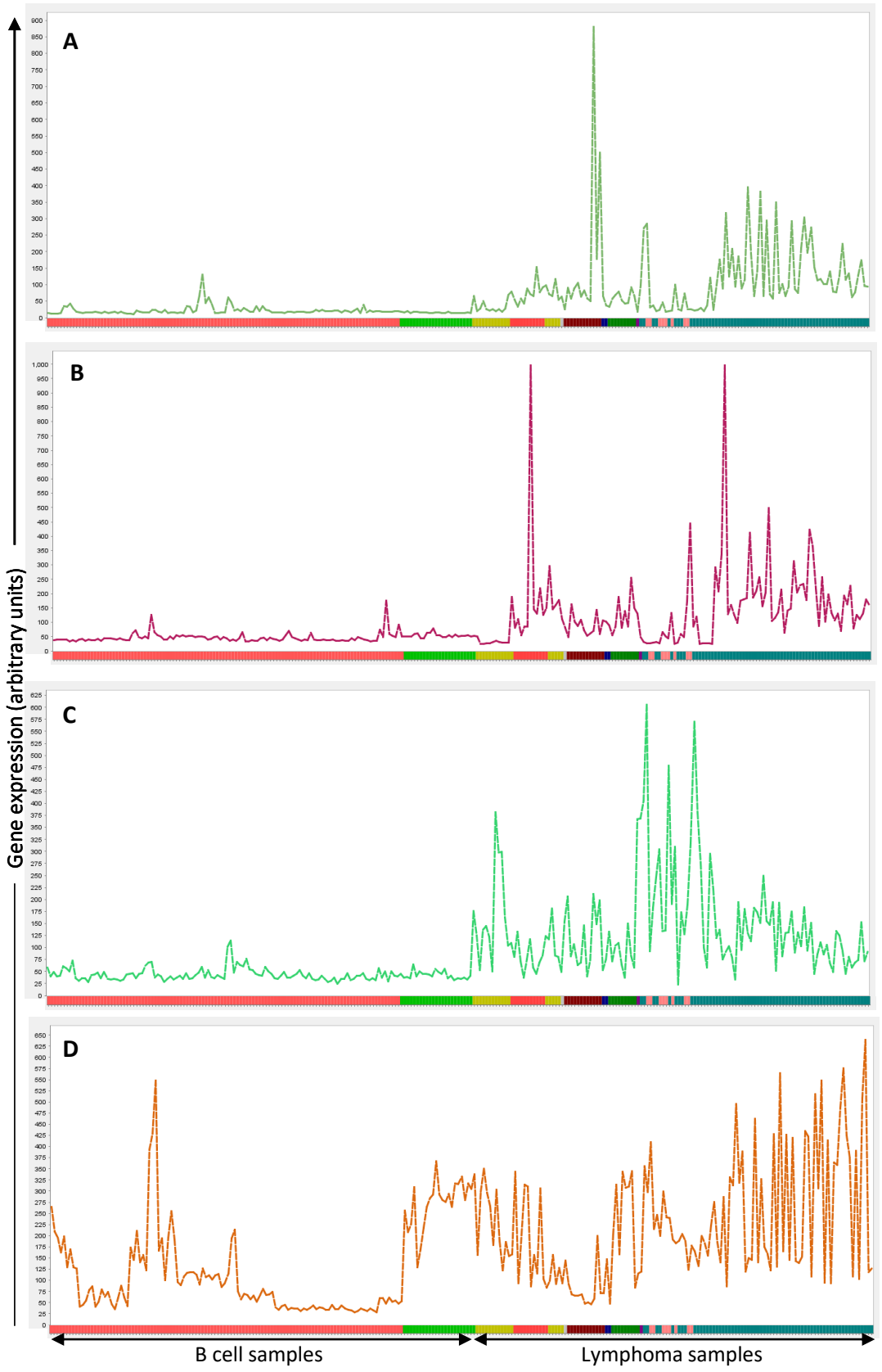
A
B
C
D
Gene expression (arbitrary units)
B cell samples
Lymphoma samples

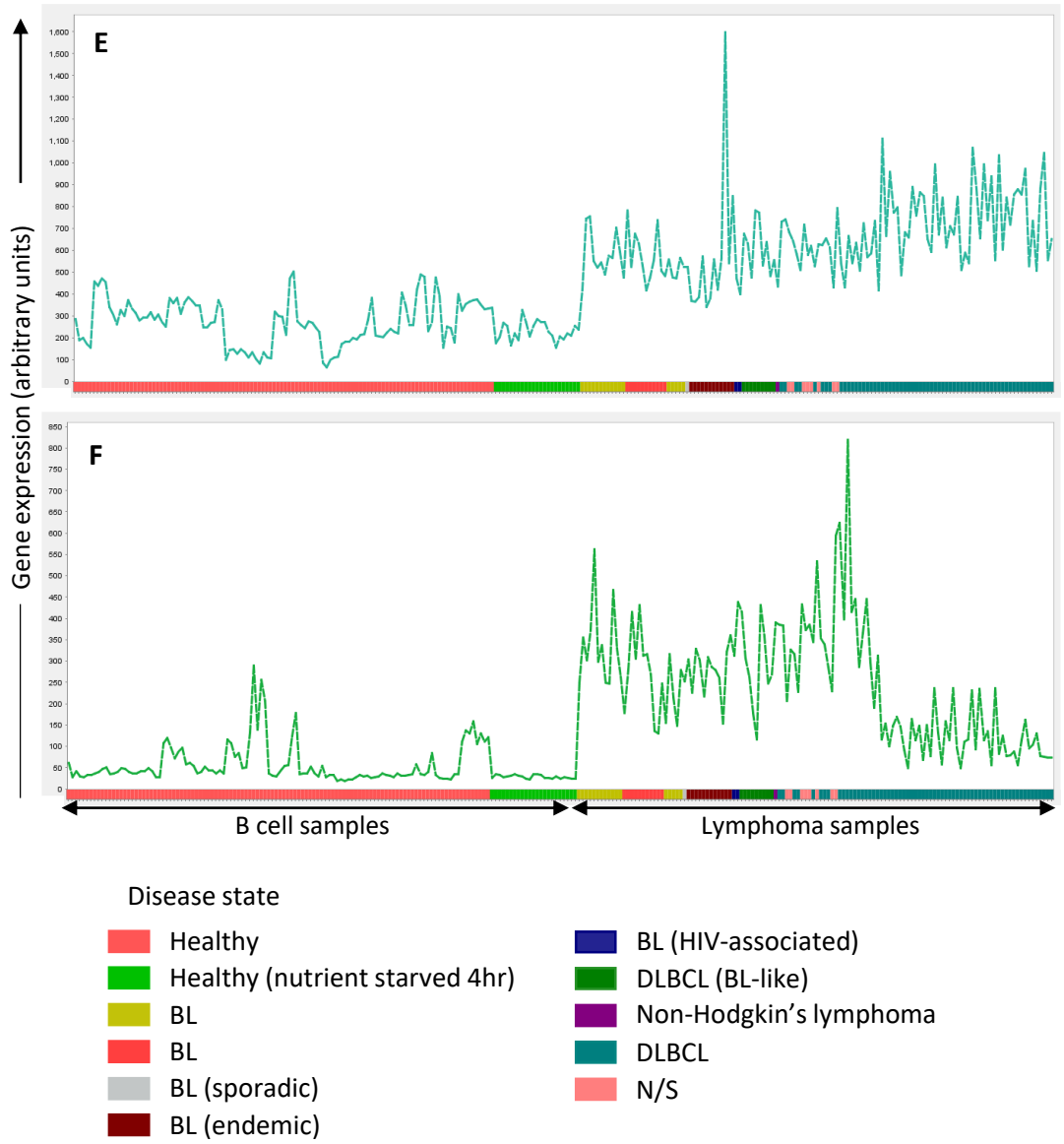

Figure 4.3: Gene expression profiles of BioLayout clusters identified as having increased expression in lymphoma datasets compared to healthy B cell datasets. The row along the bottom of each profile displays colour-coded disease state characteristics of each sample with the legend given at the bottom of the figure, where BL is Burkitt's lymphoma, DLBCL is diffuse large B cell lymphoma, and N/S is not specified NHL. A) Cluster 374, expression profile of CD59 B) Cluster 461, expression profile of MCAM C) Cluster 680, expression profile of LDLR D) Cluster 852, expression profile of CD46 E) Cluster 882, expression profile of TMEM165 F) Cluster 1236, expression profile of SLC16A1

Therefore, based on the literature search results CD59, CD46, and CD146 were initially chosen to be investigated for potential use as proteins to identify preferentially identify BL EVs.

4.4 Validation of protein targets

In order to use the results of the gene expression analysis, the proteins first had to be experimentally validated for expression on the BL line BL2. If the proteins were confirmed to be present on the surface of the BL2 cells, then the EVs derived from the cells can be analysed to determine whether the proteins are transferred to the surface of the EVs.

4.4.1 Detection of proteins on cells

BL2 cells were analysed by flow cytometry in cold PBS with 5% goat serum at a density of 1 x 10^6 mL^{-1}. 100 µL of this cell suspension was incubated with the appropriate monoclonal antibody, or isotype control for 40 minutes at 4°C. The washed cells were then resuspended in 500 µL of 5% goat serum in PBS and run on the flow cytometer with a stop point of 10,000 events recorded in the cell gate. The results of this analysis are shown in Figure 4.4. BL2 cells are almost all positive for CD46, showing 99.9% of cell events in the positive gate (Figure 4.4A), and are overwhelmingly positive for the presence of CD59, with 99.6% of cell events in the positive gate (Figure 4.4B). However, despite showing a reasonably high level of expression in the BL2 gene expression profile analysis (Table 4.3), BL2 cells did not stain positively for CD146, as only 0.8% of cell events were over the threshold set by the isotype control to enter the positive event gate (Figure 4.4C).

Thus, although identified by bioinformatic analysis, CD146 was not analysed further and dropped from the potential panel of markers for the detection of EVs derived from BL cells. CD46 and CD59 showed strong expression levels on the BL2 cells, which is expected as these proteins are ubiquitously expressed on all tissue types, so these were brought forward to investigate for their presence on EVs.

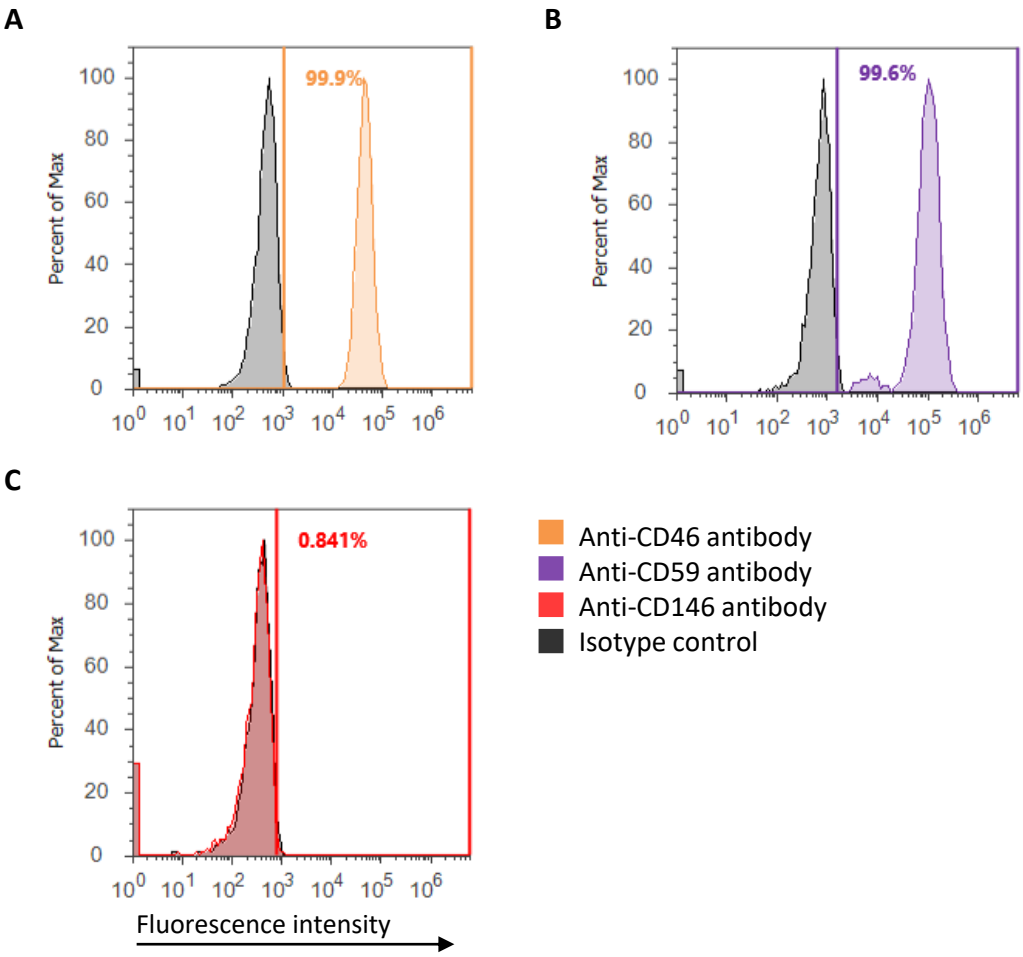

Figure 4.4: Flow cytometry of BL2 cells. A) BL2 stained with anti-CD46 antibody and the corresponding isotype control, showing 99.9% CD46-positive cells B) BL2 stained with anti-CD59 antibody and the corresponding isotype control, showing 99.6% CD59-positive cells C) BL2 stained with anti-CD146 antibody and the corresponding isotype control, showing 0.84% CD146-positive cells

4.4.2 Detection of proteins on EVs

As BL2 cells showed strong staining with antibodies against CD46 and CD59, the presence of these proteins on the surface of EVs was investigated. EVs were separated from BL2 and BL2-bcl2 cells as described in Section 2.3. The 1.2 µm filtrate from the EV separation procedure was used in flow cytometry analysis, diluted 4 in 5 with 0.1 µm filtered 5% goat serum in PBS, giving a final concentration of 1% goat serum. After 30 minutes incubation with the appropriate monoclonal antibody or isotype control, a 1 in 100 dilution of 10 µM ATTO390-maleimide membrane dye was added and incubated with the sample for 15 minutes in order to non-specifically fluorescently label the EVs membrane proteins. The stained samples were run through the instrument such that the event rate was <500 events per second in order to

avoid swarm detection, and events were recorded for 2 minutes. A fluorescent threshold was set based on the ATTO390-maleimide membrane dye, and thus only events positive for ATTO390-maleimide were detected. This removes any events due to electronic noise, or lipid particles, from the analysis, as only particles with a lipid membrane are fluorescent using this dye. A typical plot for this detection is shown in Figure 4.5E. The ATTO390-maleimide is measured on the VL1-H (440/50 nm) channel, and any events registered by the instrument which are not positive in this channel are removed. The SSC-H axis gives a rough indicator of particle size. Two gates were used in this detection strategy; the R2 gate shown in Figure 4.5E contained the majority of the EVs of interest to this study (63.9% of total ATTO390-maleimide positive events reside in this gate), the R1 gate is thought to contain a minority of larger particles which may be some debris which passed through the 1.2 μm filter during separation, so the events in this gate are not included in the analysis.

Detection of proteins on the surface of the EVs was done using both monoclonal antibodies and the appropriate isotype control which was conjugated with the same fluorophore that was conjugated to the monoclonal. A gate is drawn on the histogram for the isotype control sample so that approximately 2% of events from the R2 ATTO390-maleimide gate are 'positive' for the isotype control. This gate is then applied to the monoclonal antibody sample to gauge the number of events which stain positively for the protein under investigation.

Separated BL2 EVs were analysed for the presence of both CD46 and CD59, shown in Figure 4.5. Figure 4.5B and Figure 4.5D show the isotype control samples for the anti-CD46 antibody and the anti-CD59 antibody, respectively, giving less than 2% positive events from the R2 scatter gate. Approximately 5% of the BL2 EVs stained positively with anti-CD46 monoclonal antibody (Figure 4.5A), which is not detectable over isotype control. Similarly, only 12% of BL2 EVs are stained positively with anti-CD59 monoclonal antibody (Figure 4.5C), which does not represent much of an increase from isotype control.

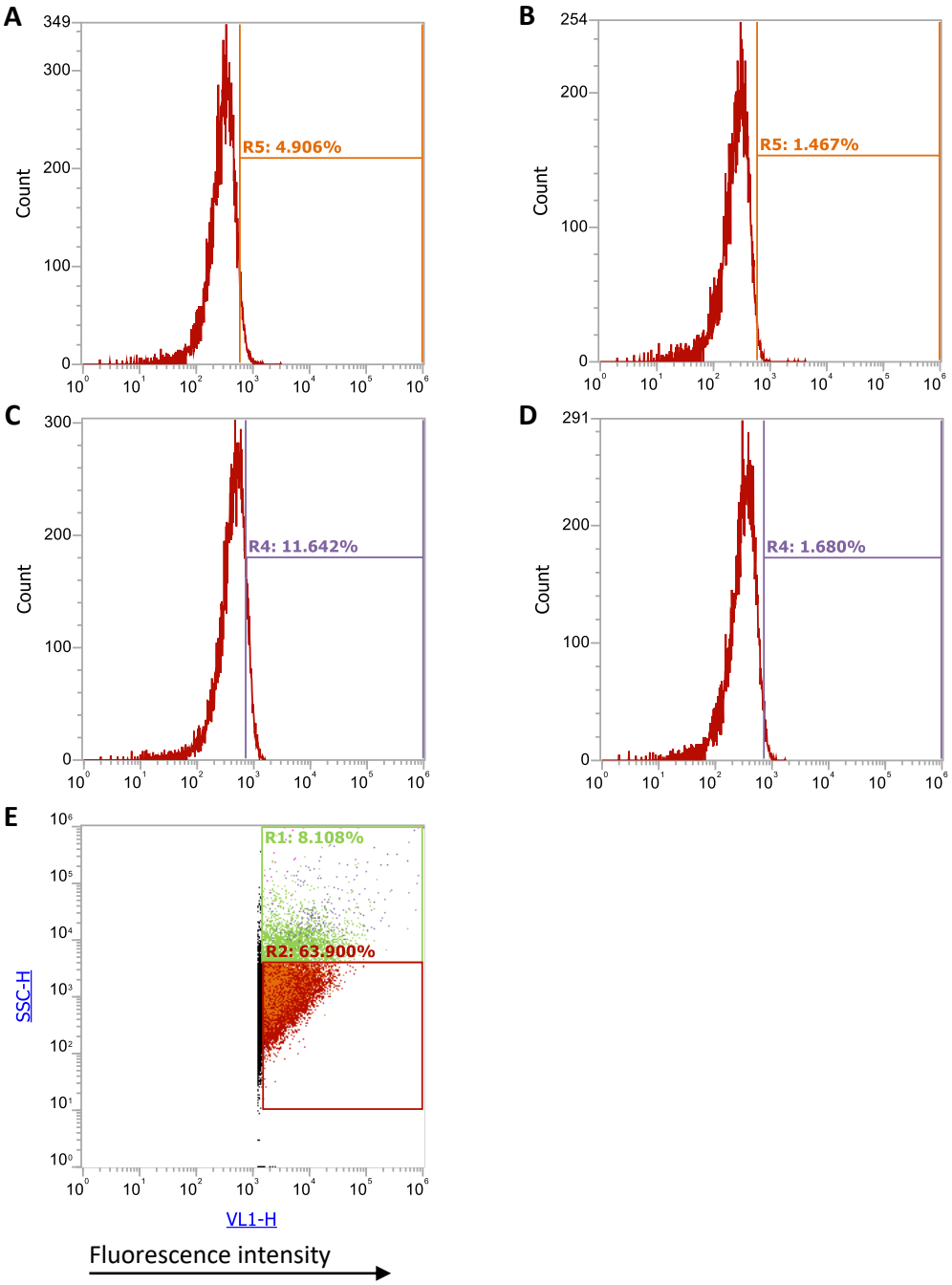

Figure 4.5: Investigation of the presence of CD46 or CD59 on the surface of EVs derived from BL2 cells A) Histogram of BL2 EVs stained with anti-CD46 mAb showing 4.9% positive events B) Histogram of BL2 EVs stained with IgG2a isotype control for anti-CD46 mAb showing 1.5% positive events C) Histogram of BL2 EVs stained with anti-CD59 mAb showing 11.6% positive events D) Histogram of BL2 EVs stained with IgG2a isotype control for anti-CD59 mAb showing 1.7% positive events E) Scatter plot showing the events positive for ATTO-390 maleimide on VL1 (440/50 nm) channel against the SSC-H

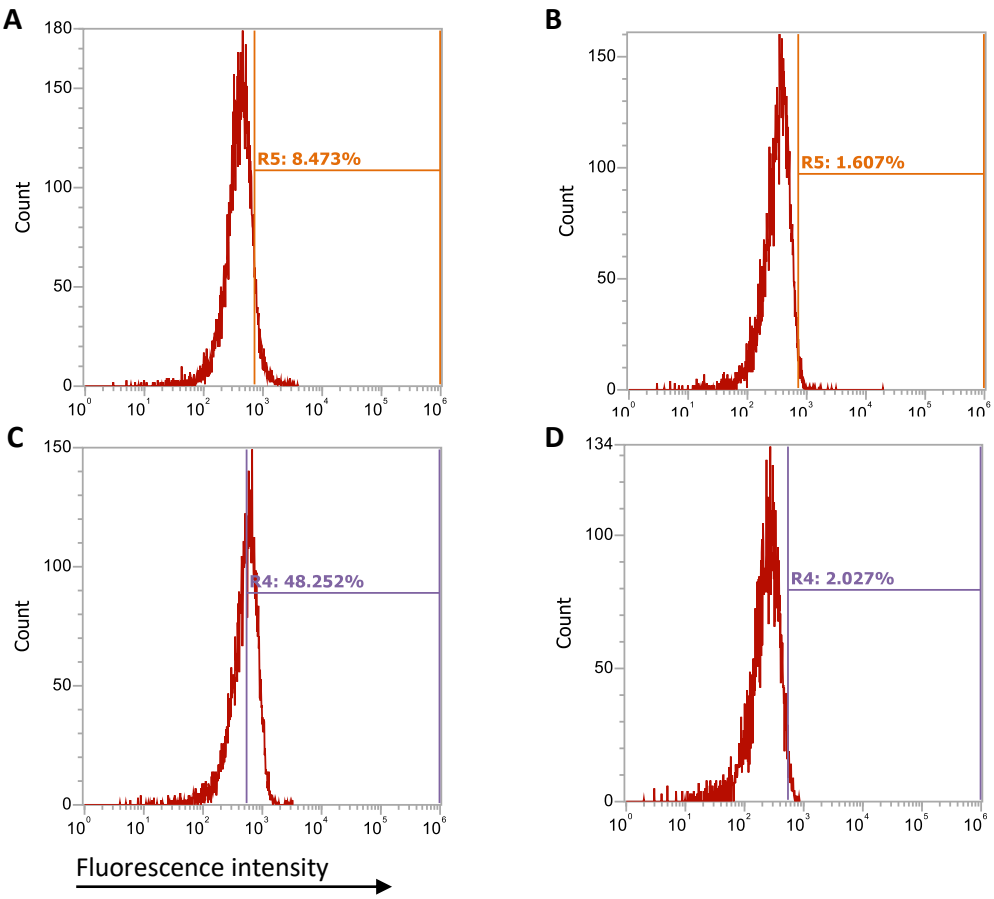

Figure 4.6: Investigation of the presence of CD46 or CD59 on the surface of EVs derived from BL2-bcl2 cells A) Histogram of BL2-bcl2 EVs stained with anti-CD46 mAb showing 8.4% positive events B) Histogram of BL2-bcl2 EVs stained with IgG2a isotype control for anti-CD46 mAb showing 1.6% positive events C) Histogram of BL2-bcl2 EVs stained with anti-CD59 mAb showing 48.2% positive events D) Histogram of BL2-bcl2 EVs stained with IgG2a isotype control for anti-CD59 mAb showing 2.0% positive events

The same procedure was carried out using EVs separated from BL2-bcl2 cells, shown in Figure 4.6. Figure 4.6B and Figure 4.6C shows the isotype control samples for the anti-CD46 antibody and the anti-CD59 antibody, where the number of positive events are approximately 2% in each case. 8.5% of BL2-bcl2 EVs stain positively with anti-CD46 monoclonal antibody (Figure 4.6A), which again is not much of a shift from the isotype control level. However, the number of BL2-bcl2 EVs which are positive for staining with anti-CD59 monoclonal antibody is 48%, which is a reasonable increase above the isotype control.

These data suggest that the CD46 membrane protein is not transferred onto the surface of either BL2 EVs or BL2-bcl2 EVs during their formation under these conditions. CD59 also does not appear to transfer to the surface of BL2 EVs. However, a larger proportion of BL2-bcl2 EVs stain positively for the CD59 protein by flow cytometry. The shift in this population is not

well separated from the isotype control, meaning that it is likely that a large population of EVs contain a low copy number of these proteins. This may make detection using this protein difficult in other assays such as a SERS assay, thus neither CD46 nor CD59 were taken forward as proteins to use for the EV detection assay.

4.5 Proteomics analysis of BL2 and BL2-bcl2 EVs

Samples of BL2 EVs and BL2-bcl2 EVs were prepared for proteomics analysis by Margaret Paterson, and carried out in collaboration with the research group of Prof Tony Whetton at the University of Manchester.

As proteomics data were available within the group, these were used to try to identify plasma membrane proteins present on the EVs surface.

The data received were split into three categories: BL2 EVs only, BL2-bcl2 EVs only, and proteins which were found in both BL2 EVs and BL2-bcl2 EVs. This categorisation was useful, as proteins which were found on both BL2 EVs and BL2-bcl2 EVs could prove useful in the detection of BL EVs generally, whereas proteins which were found on the surface of only the BL2 derived EVs could be useful in the detection of apoEVs specifically. In total, 995 unique proteins were identified across both the BL2 EVs and BL2-bcl2 EVs; 864 proteins were detected in the BL2 EVs sample and 531 proteins detected in the BL2-bcl2 EVs sample. 400 (40%) of these proteins were common to both the BL2 and BL2-bcl2 EVs, 464 proteins (47%) were found in the BL2 EVs only, and 131 proteins were unique to the BL2-bcl2 EVs (13%).

In order to identify which of these proteins were located in the plasma membrane, the list of proteins was annotated with the gene ontology (GO) data using the biomaRt package for R.[318] There are three GO domains; 'molecular function' and 'biological process' describe the function of the gene, while 'cellular component' gives information on the cellular localisation of the gene product. Many cellular component labels describe locations which are associated with membranes, for example 'plasma membrane', 'cell surface', or 'receptor complex'. Other terms of interest included those associated with EVs, such as 'extracellular vesicle', or 'extracellular exosome'. Other labels specifically describe locations which are associated with the cytosolic side of a membrane, such as 'cell cortex'. These labels were used to rule out proteins which only associate with the internal structures of the plasma membrane, as these would not be useful as imaging targets. The full list of GO components used to identify potential plasma membrane proteins from the proteomics results is given as an appendix (Appendix 2).

Using the GO annotated proteomics data, a number of plasma membrane associated proteins were identified. The proteins common to both BL2 and BL2-bcl2 EVs are given in Table 4.4, alongside the expression in BL2 identified by gene expression profile array. Many of these common proteins are associated with B cell function, such as the pan-B cell marker CD20, CD79B, and CD45. CD10 is also present, which is a B cell marker known to be associated with BL.

Table 4.4: Plasma membrane proteins which are common to both BL2 EVs and BL2-bcl2 EVs identified from proteomics data using GO components

HGNC symbol	Protein name	BL2 expression (arbitrary units)	Origin
RPSA	ribosomal protein SA (67 kD laminin receptor)	10476	Common
HSPA8	heat shock protein family A (Hsp70) member 8	7784.323	Common
MS4A1	membrane spanning 4-domains A1 (CD20)	2230.575	Common
CD37	CD37	2168.75	Common
CD48	CD48	2126.93	Common
CD79B	CD79B	1893.41	Common
ATP1B3	ATPase Na+/K+ transporting subunit beta 3	1528.83	Common
SLC7A5	solute carrier family 7 member 5	1031.58	Common
ATP1A1	ATPase Na+/K+ transporting subunit alpha 1	676.29	Common
PTPRCAP	protein tyrosine phosphatase, receptor type C associated protein	502.72	Common
BSG	Basigin (CD147)	502.42	Common
PTPRC	protein tyrosine phosphatase, receptor type C (CD45)	498.6	Common
SLC3A2	solute carrier family 3 member 2 (CD98)	479.87	Common
CD38	CD38	422.295	Common
BST2	bone marrow stromal cell antigen 2	333.72	Common
F11R	F11 receptor (Junctional adhesion molecule-A)	310.0867	Common
SLC1A5	solute carrier family 1 member 5	298.76	Common
MME	membrane metalloendopeptidase (CD10)	289.695	Common
SLC16A1	solute carrier family 16 member 1	252.445	Common
SLC29A1	solute carrier family 29 member 1	184.825	Common

As CD20 is a pan-B cell marker which has been observed on EVs,[319] this was chosen for initial studies to detect BL EVs using a SERS assay.

The plasma membrane proteins detected in only the BL2 EVs is given in Table 4.5. Fewer of these proteins were identified as plasma membrane localising compared to the common proteins; only 10 BL2 EV proteins were found to be plasma membrane bound compared to 20 for the group common to BL2 and BL2-bcl2 EVs, indicating that most of the changes observed in the apoEVs only are due to cytosolic proteins rather than those on the surface. Nucleolin is included in Table 4.5, despite this protein being ordinarily found in the nucleolus. However, nucleolin has been shown to localise to the plasma membrane, where it can interact with Fas to inhibit apoptosis.[320] Nucleolin has a very high expression level in the gene expression profile data, however this is likely due to the nucleolar fraction, so nucleolin was not considered for detection of apoEVs. CD46 is also shown in Table 4.5, however as shown earlier this protein was not detectable above isotype control in a flow cytometry assay (Figure 4.5).

Table 4.5: Plasma membrane proteins which are unique to BL2 EVs identified from proteomics data using GO components

HGNC symbol	Protein name	BL2 expression (arbitrary units)	Origin
NCL	nucleolin	3749.45	BL2
CD53	CD53	760.37	BL2
CD46	CD46	675.4	BL2
ST14	suppression of tumorigenicity 14 (matriptase)	602.445	BL2
ITGB1	integrin subunit beta 1	338.5633333	BL2
MPZL1	myelin protein zero like 1	298.395	BL2
SLAMF6	signaling lymphocytic activation molecule family member 6	296.32	BL2
IGSF8	immunoglobulin superfamily member 8	152.08	BL2
ROR1	receptor tyrosine kinase like orphan receptor 1	120.91	BL2
EMB	embigin	58.19	BL2

The protein CD53 is also shown in Table 4.5. CD53 is a tetraspanin protein associated with signal transduction in monocytes and B cells. Tetraspanins are well-known to be associated with EVs and CD53 has also been documented on EVs derived from B cells.[321] CD53 has also

been shown to play a role in apoptosis, as CD53 is upregulated in a murine B cell lymphoma with increased resistance to radiation therapy,[322] and cleavage of CD53 on a rat B cell lymphoma line protected the cells from apoptosis due to serum starvation.[323] Therefore, CD53 appears to be a good candidate for use in detecting apoEVs.

4.6 Discussion

Open access gene expression profile data were used in order to identify plasma membrane proteins which could be useful in detecting BL EVs in a SERS assay. The gene expression data were analysed in the programme BioLayout *Express*^{3D}. This software was designed to analyse functional linkages between genes in array data, not to identify upregulated genes. In order to identify genes which appeared to have higher expression in samples from lymphoma cases compare to healthy B cell samples, the expression profile of every cluster in the network graph had to be analysed and a judgement call was made on whether the expression pattern seemed higher for the lymphoma samples. This method may have introduced some user bias, as a large number of clusters had to be analysed, and the decision as to what constituted higher expression was arbitrary.

Three candidate proteins were selected from this analysis: CD46, CD59, and CD146. Although there were data to suggest that CD146 was expressed in BL2 cells, flow cytometric analysis showed that CD146 was not detectable on the surface of the cells. Flow cytometry showed that CD46 and CD59 were abundant on the BL2 cell surface, so the presence of these proteins on the EVs surface was then investigated. A specific EV flow cytometric detection method was used, whereby the EV membrane was stained with a fluorescent membrane dye, ATTO390-maleimide, and the fluorescence of this compound was used as a detection threshold to record events. This strategy is common in the analysis of EVs in order to reduce instrument noise and non-EV sample contaminants. However, using this strategy neither CD46 nor CD59 appeared to be present on the EVs surface with enough abundance for use in a detection assay. It may be that the flow cytometry assay was not sensitive enough to detect all of the EVs present in the samples, and many positive events could have been missed. For this reason, flow cytometry is not always the best technique for the analysis of proteins on EVs, unless the instrument is specifically adapted and dedicated for the detection of small particles.

Proteomics data for the BL2 EVs and BL2-bcl2 EVs became available for analysis, generated by another researcher in the group as part of a collaboration. Analysing these data for the

presence of plasma membrane-localising proteins gave a number of promising candidates for use in a BL EV detection assay. Thus, CD20 was brought forward as a target for the detection of both BL2 EVs and BL2-bcl2 EVs, and CD53 was identified as a potential target for the preferential detection of BL2 apoEVs.

5 Detection of extracellular vesicles by surface enhanced Raman spectroscopy

5.1 Introduction

Traditional methods of EV analysis include ELISA, flow cytometry, and Western blotting. Many of these are bulk analysis techniques which require large amounts of purified sample and cannot distinguish subpopulations of EVs. One method which overcomes some of the limitations of EV analysis is surface enhanced Raman spectroscopy (SERS). A small sample volume can be used, the signal enhancement results in sensitive assays, and using multiplexed analysis allows EV subpopulations to be investigated.

5.1.1 EV characterisation using SERS

Fabrication of nanostructures to enhance the Raman signal of a sample has been previously successful in characterising EVs. In one study, Si micropillars coated with nanograins of Ag formed super-hydrophobic surfaces to detect EVs by SERS. This device was used to compare spectra obtained from colon cancer and colon epithelial exosomes, and differences in protein and lipid composition were observed.[324] However, a commercial reagent called ExoQuick was used to separate the EVs, which is a polymer solution that causes precipitation of exosomes from solution allowing separation using a much lower speed of centrifugation. Although the manufacturers state that the polymers do not bind or interact with the exosomes, Lee *et al.* showed in their study of EVs by SERS that a similar reagent, total exosome isolation reagent, (TEIR) did contaminate the EV sample.[325] In this work, hexagonal wells of 800 nm diameter and 300 nm depth were fabricated on dimethylpolysiloxane and sputter coated with Ag to create plasmonic nanobowls big enough to fit only a single exosome. With an enhancement distance of only 5 nm, this generated signal only from the exosome surface. Comparing the signal obtained from the EV sample in solution with the spectrum of TEIR, all of the observed peaks in the EV sample can be attributed to the polymer. However, the authors then left the device to dry completely, causing lysis of the exosomes and disappearance of the TEIR signals from the spectra. Exosomes derived from ovarian cancer cells were used to compare the TEIR isolation with ultracentrifugation, the most commonly used separation technique. The exosomes separated by ultracentrifugation were not contaminated by the separation procedure and therefore had a more consistent SERS signal between the samples in solution and dried. However, they were found to have a more heterogeneous size distribution, and

larger standard deviation (SD) of SERS spectra than the corresponding TEIR-isolated exosomes.[325]

Another device fabricated to characterise EVs using SERS contained gold nanopyramids (200 x 200 nm^2) covered with a layer of graphene. The graphene was chosen to act as an internal standard which allowed the normalisation of signal in order to overcome the variability of signal enhancement due to non-uniform hotspots. This device required only 2 µL of sample and could distinguish between exosomes separated from foetal bovine serum (FBS) and human serum using PCA, as well as exosomes from two different lung cancer cell lines, with an overall sensitivity of 84%.[326]

By non-specifically binding EVs with roughened metal surfaces, their Raman spectral signature can be greatly enhanced for sensitive characterisation of the EVs. Stremersch *et al.* took advantage of the negative surface charge of EVs by incubating with positively charged 4-dimethylaminopyridine capped 10 nm AuNPs. These small AuNPs coated the outside of the EVs, allowing for the sensitive characterisation of individual EVs by SERS while remaining in solution. This analysis technique showed differentiation of EVs derived from B16F10 melanoma cells and red blood cells with a discrimination specificity of 95% and 98%, respectively.[327] Another group used 10 nm gold nanoparticles (AuNPs) with positively-charged branched polyethyleneimine as a capping agent to electrostatically adsorb the EVs.[328] The sample was then dried onto a gold slide to further enhance the Raman signals. Using a principal component analysis-discriminant function analysis (PCA-DFA) algorithm, exosomes from pancreatic epithelial cells and two pancreatic cancer cell lines were distinguished with an overall classification accuracy of 90%.

One study used targeted capture of exosomes onto silver nanoparticles (AgNPs) for characterisation using SERS. A thiolated peptide against α3β1 integrin (LXY30-SH) was incubated with exosomes from α3β1-expressing SCOV-3 cells or exosomes from Jurkat cells, which do not express α3β1 integrin. AgNPs were then added, which bound to the exposed thiol of LXY30 and were separated by centrifugation. The SERS spectrum of AgNP-LXY30-SCOV-3 exosomes had peaks which were not present in the AgNPs, AgNP-LXY30, or AgNP-LXY30-Jurkat spectra, showing that targeted binding of exosome subsets can be used for characterisation by SERS.[329]

Other groups have brought the EVs into contact with signal enhancing material by drying. By drying a solution of AuNPs onto a glass coverslip, and drying EVs on top, exosomes from lung

epithelial cells were distinguished from two non-small cell lung cancer cells lines using PCA.[330] The same group then went on to alter this method, by drying AuNPs onto a coverslip and then coating the particles with cysteamine to give a positive charge. The negatively charged exosomes could then associate with the AuNPs and spectra of the EVs in solution were obtained.[331] The aim of this study was to identify surface proteins present on pancreatic cancer exosomes by first comparing the spectra of cancer exosomes to those derived from non-cancerous epithelial cells by PCA. The loadings which separated the cancer exosomes were then compared to SERS spectra of possible surface markers (CD9, CD81, epithelial cell adhesion molecule (EpCAM), and epidermal growth factor receptor (EGFR)), obtained by labelling the AuNPs with a capture antibody for each protein. EGFR was found to contribute most to the cancer exosome identification and was validated by western blot.[331] Exosomes derived from ovarian cancer cells grown either in normoxia (21% O_2) or hypoxia (1% O_2) were characterised using SERS by incubating the exosome solutions with citrate-capped AuNPs in PBS and drying onto CaF_2.[332] However, only 20 spectra from each exosome type were acquired and half of these had evidence of thermal damage, so although spectral differences were observed between hypoxic and normoxic EVs the results are not reliable.

5.1.2 EV detection using SERS

In order to create sensitive biosensors to detect the presence of EVs, surfaces can be labelled with antibodies and the captured EVs detected using SERS active nanoparticles coated with specific antibodies and Raman reporter molecules. In this way, non-target EVs can be removed from the system, allowing the analysis of a specific subpopulation. Using large or paramagnetic beads as a capture method, the EV sample can be concentrated for population analysis, or using a functionalised chip can yield information from individual EVs.

5.1.2.1 Capture with magnetic beads

One facile method for the detection of EVs by SERS is using magnetic beads to separate the desired subpopulation from a sample. Antibody-functionalisation of magnetic beads causes specific EVs to be pulled from solution, which then can be incubated with SERS-active nanoprobes to form a sandwich-type immunocomplex for detection.

One group used a depletion assay in order to detect subpopulations of EVs. Using anti-CD63 functionalised magnetic beads to capture all exosomes, SERS probes against cell-specific proteins were incubated with the sample. The decrease in signal for a specific probe indicated the presence of exosomes from that cell type, and the assay was successful with pure and

mixed samples of both different SERS probes and exosome types.[333] Using only 2 µL of exosome solutions from both cell culture and patient blood samples, exosomes from breast cancer cells could be detected using anti-HER2 probes, prostate cancer exosomes using anti-prostate-specific membrane antigen probes, and colorectal cancer exosomes using anti-carcinoembryonic antigen SERS NPs, with limits of detection (LOD) of 32 exosomes/µL, 203 exosomes/µL, and 73 exosomes/µL, respectively.[333] Another study also used anti-CD63 functionalised magnetic beads to capture exosomes and anti-HER2 labelled SERS nanoparticles for specific detection of breast cancer derived exosomes, but with positive detection rather than depletion. Only 1 µL of purified exosome solution was needed, or 100 µL of unpurified cell culture supernatant, and the LOD was calculated to be 1200 exosomes.[334] Although this LOD is much higher than that achieved in the depletion study, in this work the EVs concentration was determined by labelling with a fluorescent cytoplasmic dye and counting on a total internal reflection fluorescence microscope, which is by no means a standard technique to determine EV concentration. Anti-CD9 functionalised magnetic beads have also been used to capture exosomes, with detection using gold nanostars with cholesterol-labelled DNA strands on their surface. The cholesterol is incorporated into the EV membrane, allowing detection of all captured exosomes. 200 µL of exosome sample was used, and the LOD of this system was found to be 27 exosomes/µL.[335] This system was also tested using serum samples, from three healthy controls and three patients with liver cancer. The SERS quantification of exosome number correlated well with the concentration found by TRPS, although the SERS assay required a long incubation (10 hours) of the EVs with the magnetic beads.

5.1.2.2 Capture on functionalised surface

Rather than using magnetic beads for capture, one study used the self-assembly of polydopamine (PDA) on glass slides to encapsulate antibodies against proteins known to have increased expression in pancreatic cancer for detection of pancreatic cancer exosomes.[336] The SERS probes were composed of an AuNP core with a silver shell and also used PDA encapsulation to functionalise the probes with antibodies. Only 2 µL of exosome solution and 3 µL of SERS probes were required, making this a very sensitive and effective assay. Two exosome markers, CD9 and CD63, were used for detection of exosomes from pancreatic cancer and epithelial cell lines, as well as two pancreatic cancer markers, glypican 1 (GPC-1) and migration inhibitory factor (MIF). Using the same antibodies for both capture and detection, pancreatic exosomes and pancreatic epithelial exosomes were found to have

similar levels of CD9 and CD63, but GPC-1 and MIF were preferentially detected on cancer exosomes with a LOD equivalent to 1 exosome in the 2 µL test sample. The assay was also used on serum from patients with pancreatic cancer and healthy controls. Not only could the anti-MIF immunosensor differentiate between exosomes from patient and healthy samples, when the pancreatic patients were divided into subgroups, the results were also significant in detecting early vs late stage disease and metastatic vs non-metastatic disease.[336]

Another study reports the fabrication of an antibody-coated gold chip microarray for the capture of exosomes from different breast cancer cell lines.[337] Using a 3D-printed plastic array template, wells of 2 mm diameter and 15 µL capacity were created on a gold chip and functionalised with HS-PEG-antibody. Antibodies were chosen based on breast cancer surface markers (EpCAM, CD44, EGFR, IGFR) and exosome markers (CD81, CD63, CD9). Binding of exosomes to the antibodies was validated by staining with a fluorescent membrane dye visualised by microscopy. The presence of exosomes in the wells was detected using gold nanorods (AuNRs) with QSY21 Raman reporter molecule. The capping agent (CTAB) is positively charged and could electrostatically adsorb to the exosomes for detection. The protein markers detected on the exosome surface by SERS were found to reflect the expression of those proteins on the parental cell, indicating that plasma membrane proteins can be transferred to the exosome surface. The SERS results were validated by ELISA, with a 0.97 correlation coefficient between the SERS and ELISA signals. The SERS assay was also carried out on plasma samples from HER2-positive breast cancer patients, which were found to have significantly higher levels of EpCAM and HER2 compared to healthy controls.[337]

5.1.3 SERS on nitrocellulose

Nitrocellulose is a commonly used material to non-specifically bind proteins. Proteins are adsorbed onto the surface by hydrophobic interactions and can be bound either by transferral using an electric current, as in Western blotting, or by simply placing a drop of protein solution on the membrane. Nitrocellulose is extremely useful for immunodetection of specific proteins and has been combined with SERS to yield sensitive detection assays.

5.1.3.1 Protein detection on nitrocellulose

SERS immunoblots have been used as an alternative to fluorescence or enzyme detection such as ELISA due to a higher sensitivity and ability to multiplex. SERS immunoblots have been used for the detection of purified samples of IL-6 and duplexed detection of IL-6 and

IL-8.[338] IgG was detected using a SERS assay on nitrocellulose, but the LOD was calculated to be greater than the highest concentration of protein tested (20 ng in 2 µL) due to non-uniform distribution of the protein on the membrane.[339] The same study also detected bovine β-lactoglobulin, and CACNA1F retinal membrane protein in cell lysate. IgG has also been detected using small (2-5 nm) AuNPs using a silver enhancement step after nanoparticle binding to increase the scattering cross-section for sensitive detection by SERS.[340]

5.1.3.2 Cells binding on nitrocellulose

Circulating tumour cells (CTCs) are rare events which can be found in the blood of cancer patients. Much like EVs, they are being investigated as a liquid biopsy method of cancer diagnosis or prognosis. One study has used nitrocellulose to capture lung cancer cells by adsorbing anti-EpCAM antibody to the nitrocellulose and detecting the captured cells using anti-EpCAM functionalised SERS nanoparticles.[341] The membrane had been made transparent prior to the adsorption of antibody, so the detection of cells was verified by brightfield microscopy. Capture efficiency increased with an increase in the number of cells applied to the membrane. Cells were also detected which had been spiked into blood as a proof-of-concept for the detection of CTCs, but the detection efficiency was only 34%.

In a microfluidic device for the detection of glucose in blood, a nitrocellulose channel was included in the design to bind the protein and cells in the whole blood samples to allow on-chip separation of blood components before detection with SERS nanoparticles.[342] This study shows that whole cells can be adsorbed onto the nitrocellulose surface as well as proteins and smaller molecules.

5.2 Aims of chapter

The aim of this work was to develop a SERS-based assay for the detection of EVs. The proteomics results discussed previously in Section 4.5 were used to identify proteins that could be used as targets for a SERS probe. Due to the high centrifugation speeds required to pellet EVs, separation of the unbound reporter-labelled nanoparticles could not be easily achieved by a centrifugation method. In order to get efficient washing of unbound AuNPs from EVs, a capture method was used. Published literature of SERS detection of EVs have all studied exosomes, which have known protein markers enriched on the surface to non-specifically capture all exosomes in the sample. Due to the differences in biogenesis of the EVs studied here and exosome-type vesicles in the literature, and a lack of knowledge of surface markers present on EVs in this study, another approach was required.

A nitrocellulose membrane was used in order to non-specifically bind the EV membrane proteins. This was chosen as a capture method as it would non-specifically capture all EVs present in the sample. The SERS nanoparticles functionalised with antibodies against the chosen plasma membrane proteins were then applied, and the unbound nanoparticles could be washed off the membrane.

5.3 Synthesis of SERS nanoparticles

5.3.1 Synthesis of gold nanoparticle colloid

A colloid of gold nanoparticles was synthesised using the citrate reduction method.[294] Gold tetrachloroaurate was dissolved in boiling deionised water, and sodium citrate was added in order to form gold nanoparticles. The nanoparticles were characterised using UV-vis to measure the local surface plasmon resonance (LSPR) and to determine the concentration of nanoparticles in the colloidal suspension. The surface charge and hydrodynamic radius were analysed by dynamic light scattering (DLS) using Zetasizer Nano ZS (Malvern).

UV-vis analysis of the citrate-capped AuNPs show that the LSPR reaches a maximum at 530 nm (Figure 5.1), which is expected for gold nanoparticles of this size. The concentration of AuNPs, calculated using the Beer-Lambert law with an extinction coefficient[343] of 7.66×10^9 M^{-1} cm^{-1} and a path length of 1 cm, was found to be 0.2 nM.

The DLS results, given in Table 5.1, show that the particles are approximately 22 nm in diameter, with a zeta potential of -40 mV indicating that they are stable against aggregation. However, the polydispersity index (PdI) of the nanoparticles was reasonably high at 0.66, indicating that the nanoparticles are not monodisperse in size and there is a high variation in diameter.

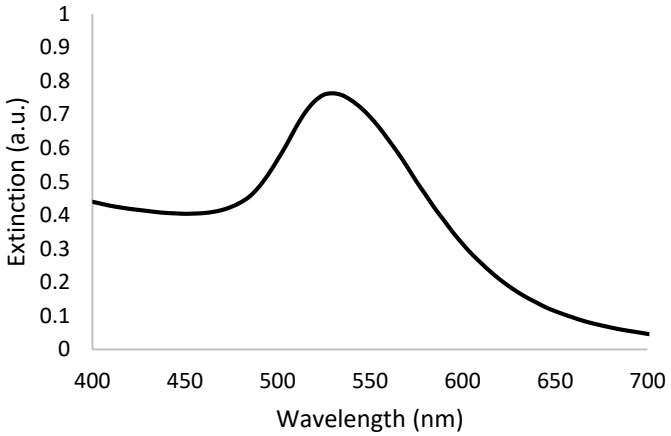

Figure 5.1: Extinction spectrum of citrate-capped gold nanoparticles

Table 5.1: Z_{avg} and zeta potential of citrate-capped gold nanoparticles with standard deviation (SD) of three replicates measured by DLS

Size	**Z_{Avg} (nm) ± SD**	**PdI**
	21.69 ± 0.15	0.66
Zeta potential	**mV ± SD**	
	-40.1 ± 1.1	

5.3.2 Functionalisation of gold nanoparticles

5.3.2.1 Raman reporter concentration

A Raman reporter molecule was used in order to increase the sensitivity of analyte detection. Malachite green isothiocyanate (MGITC) was chosen as the reporter, as it has low background fluorescence and a Raman enhancement factor on AuNPs of approximately 3 x 10^6.[344] MGITC also exhibits strong absorbance at 621 nm, and would therefore be in resonance with 633 nm laser excitation to give surface enhanced resonance Raman (SERRS). MGITC binds to gold surfaces *via* the sulfur of the isothiocyanate, which can be seen by the presence of an Au-S band in the SERS spectrum at 218 cm^{-1}, and the presence of -$N(CH_3)_2$ bending and rocking bands at 1433 cm^{-1} and 1475 cm^{-1} indicates that the positively charged dimethylamino group is also in contact with the metal surface.[344]

In order to determine the optimal concentration of MGITC on the AuNP surface to yield good SERS signal, both in solution and on nitrocellulose, a dilution series of different concentrations of MGITC were added to the AuNPs. A stock solution of 100 µM MGITC was made up and the appropriate volume added to 1 mL of AuNPs to yield final concentrations of 0.1-1 µM. Excess unbound MGITC was removed from the AuNP suspension by

centrifugation and the MGITC AuNPs were resuspended in 1 mL water for characterisation. The LSPR, size, and SERS spectra of each MGITC concentration was then measured.

The sizes of the MGITC coated AuNPs, acquired by DLS, are given in Table 5.2. There is a slight increase in the size of the MGITC AuNPs compared to unfunctionalised nanoparticles, which is to be expected as DLS measures the hydrodynamic radius, which will be changed by the addition of a charged molecule such as MGITC to the surface of the nanoparticles. The 0.5 µM MGITC AuNP suspension had obvious aggregation, which can be seen as this sample had the highest measured diameter of 108 nm. For 0.1-0.3 µM MGITC, the size increased to approximately 25 nm, compared to 22 nm measured for the unfunctionalised particles. 0.4 µM and 0.6 µM MGITC were 28 nm diameter, and 0.8-1 µM were approximately 29 nm. The increase in average diameter seen with increasing MGITC concentration could be due to the formation of small aggregates. It has been reported that the addition of a small volume of highly concentrated MGITC stock solution to an AuNP colloid can form stable multimeric aggregates, due to the high local concentration of MGITC displacing citrate molecules from the surface of a small number of particles, and the higher positive charge on these nanoparticles attract the more negatively charged citrate-capped AuNPs to irreversibly form aggregates.[344] However, the largest diameter was not observed for the AuNPs with the highest concentration of MGITC as would be expected, as the 0.7 µM MGITC AuNPs were measured to have a diameter of 33 ± 1.07 nm. This sample also had the lowest PdI value of 0.56

Table 5.2: Z_{avg} of different concentrations of MGITC added to AuNPs with SD of three replicates and PdI to indicate monodispersity. Data acquired by DLS.

	Z_{avg} (nm) ± SD	**PdI**
AuNP citrate	21.69 ± 0.15	0.66
AuNP MGITC 0.1 µM	25.55 ± 0.28	0.60
AuNP MGITC 0.2 µM	24.95 ± 0.13	0.59
AuNP MGITC 0.3 µM	25.9 ± 0.14	0.61
AuNP MGITC 0.4 µM	28.1 ± 0.99	0.58
AuNP MGITC 0.5 µM	108 ± 3.13	0.22
AuNP MGITC 0.6 µM	28.05 ± 1.37	0.61
AuNP MGITC 0.7 µM	33.66 ± 1.07	0.56
AuNP MGITC 0.8 µM	29.19 ± 0.94	0.59
AuNP MGITC 0.9 µM	29.04 ± 0.29	0.56
AuNP MGITC 1 µM	29.92 ± 0.21	0.57

When the AuNPs are functionalised with MGITC, the LSPR red-shifts to 535 nm (Figure 5.2). This is in line with the increase in size seen by DLS, as the LSPR increases with an increase in particle size.

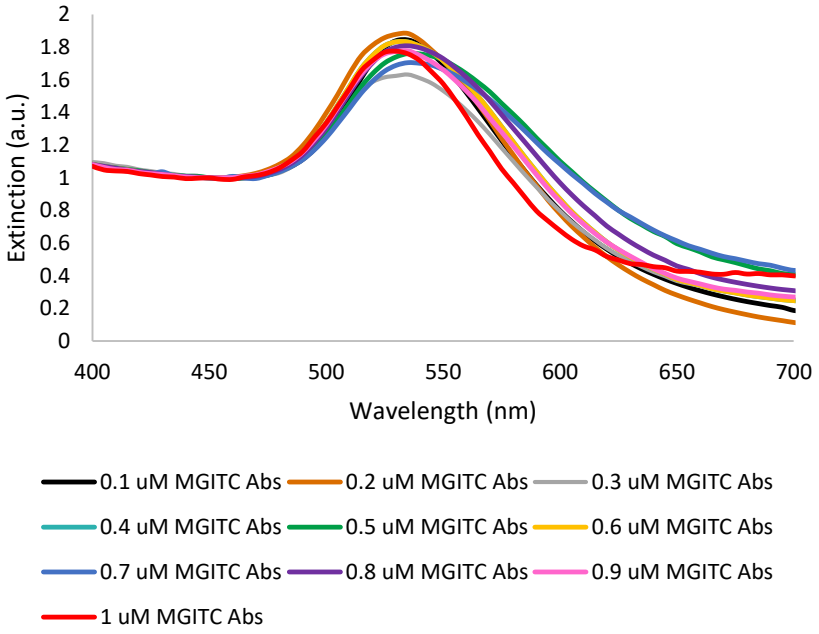

Figure 5.2: Extinction spectra (normalised to extinction at 450 nm) of MGITC-functionalised AuNPs over a range of MGITC concentrations.

The SERS spectra of the MGITC AuNPs in water were acquired using a Snowy Range spectrometer using 785 nm excitation wavelength with 45 mW power and an integration time of 1 second (Figure 5.3A). The aggregation of the 0.5 µM MGITC AuNPs can be seen in the SERS spectrum of these particles, as some of the peaks have shifted. The intensities of the spectra for the lowest concentrations of MGITC (0.1 and 0.2 µM MGITC AuNPs) are noticeably reduced when compared to the spectrum of 1 µM MGITC AuNP, by 4-fold and 2.5-fold, respectively. The concentration that gives the highest intensity spectrum is 0.6 µM MGITC AuNPs, but the intensities in this spectrum are not greatly increased over either the 1 µM MGITC AuNP or 0.8 µM. The results of this dilution study show that MGITC is easily adsorbed onto the surface of the AuNPs and gives a good SERS signal over a range of concentrations.

As the aim of this experiment was to preform SERS of EVs captured onto nitrocellulose, it was necessary to obtain SERS spectra of the MGITC AuNPs dried onto this substrate to ensure that a robust signal was also seen when the particles were not in solution and analysed under the same spectral conditions that will be used for EV detection. 10 µL of MGITC AuNPs were

dried onto raw nitrocellulose. Raman maps of three areas of the AuNP spot were acquired using the streamline beam configuration of a Renishaw InVia spectrometer, using 785 nm laser excitation at 9 mW power with a 2 second integration time. The mean signal of the three maps of each spot were calculated, to reduce the variation in intensity due to the coffee-ring drying effect or heterogeneity in density of the MGITC AuNPs on the nitrocellulose. The mean spectra are shown in Figure 5.3B. The overall signal intensity is greatly reduced when comparing the spectra acquired on the nitrocellulose to the MGTIC AuNPs in solution. A reduced laser power must be used for the samples on nitrocellulose, as if the laser power and integration time are too high then the substrate will heat up and burn. There will also be less MGITC AuNPs present within the laser irradiation spot on the nitrocellulose than are present within the laser volume when examined in solution. However, although the SERS signal of the MGITC AuNPs is reduced on nitrocellulose, the MGITC peaks can still be clearly seen. The concentration of MGITC which gave the highest SERS signal is 0.7 µM MGITC AuNPs, so this concentration was used for all future experiments.

There are some peaks present in the spectra of the MGITC AuNPs on nitrocellulose which are background signal from the substrate, such as the shoulder at 850 cm^{-1} and the 1374 cm^{-1} peak which causes the lack of resolution between the 1363 cm^{-1} and 1430 cm^{-1} peaks of MGTIC (Figure 5.4). A comparison of the peaks observed in the SERS spectrum of MGITC AuNPs in solution and the intrinsic Raman spectrum of the nitrocellulose substrate are listed in Table 5.3. Some MGITC distinguishing peaks, such as those at 1169 cm^{-1} and 1581 cm^{-1}, do not contain significant overlap with peaks produced by the nitrocellulose. Since the 1169 cm^{-1} peak has the highest intensity of the MGITC peaks, and no contributing noise from the capture substrate, the intensity of this peak can be used as the marker of MGITC AuNP presence in the EV detection assay. On nitrocellulose, this peak is shifted to 1171 cm^{-1}, which could be due to the influence of the nitrocellulose on the MGITC signal or could possibly be due to the differences between the spectrometers on which these data were acquired.

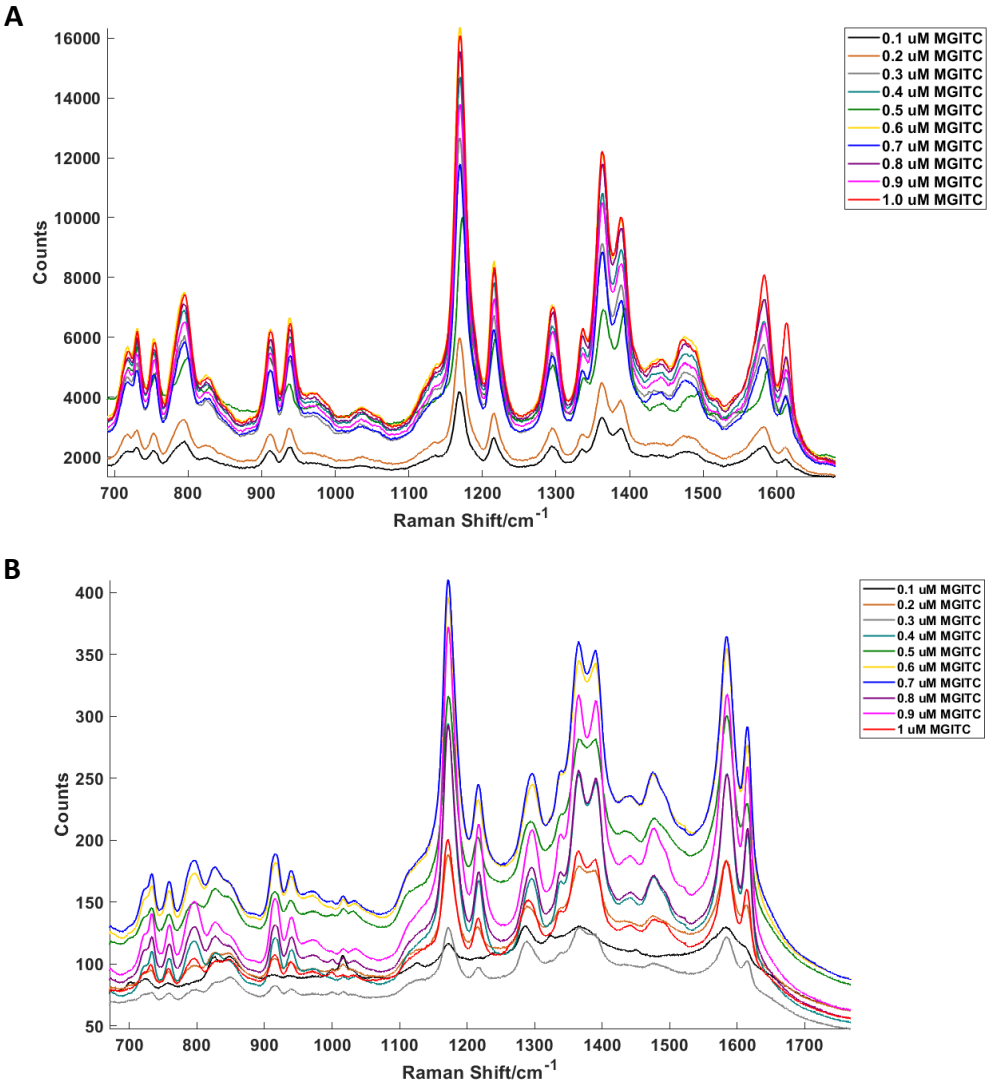

Figure 5.3: SERS spectra of various concentrations of MGITC adsorbed onto the surface of AuNPs. A) MGITC AuNPs in solution. Spectra were acquired on a Snowy spectrometer using 785 nm excitation with integration time of 1 second at 45 mW. B) MGITC AuNPs spotted and dried onto raw nitrocellulose. Spectra represent the mean of three areas of the AuNP spot mapped using the streamline configuration of a Renishaw InVia with 785 nm laser excitation, 2 second integration time, and 9 mW power.

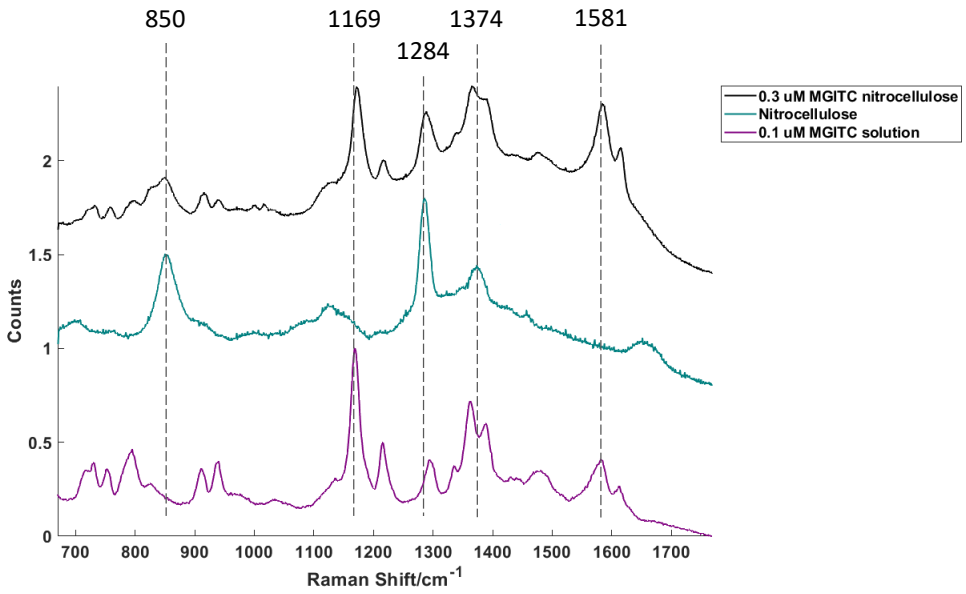

Figure 5.4: Comparison of SERS spectra of MGITC AuNPs in solution and adsorbed onto nitrocellulose, with the intrinsic Raman spectrum of nitrocellulose acquired under the same conditions as the MGITC AuNP maps. All spectra were acquired using 785 nm laser excitation. Spectra were scaled to unity in order for the spectral intensities to be comparable. The main nitrocellulose peaks observed at 850 cm^{-1} , 1284 cm^{-1}, and 1374 cm^{-1} can be observed in the 0.3 µM MGITC AuNP nitrocellulose spectrum, and the two most prominent MGITC peaks which do not overlap with nitrocellulose peaks are those at 1169 cm^{-1} and 1581 cm^{-1}. Nitrocellulose samples were acquired with a Renishaw inVia spectrometer with 9 mW laser power and 2 second acquisition time and the sample in solution was acquired using a Snowy Range Sierra spectrometer using 45 mW laser power and 1 second acquisition time.

Table 5.3: SERS peaks observed in the spectrum for MGITC AuNPs in solution and the intrinsic Raman peaks of nitrocellulose

MGITC Raman shift (cm^{-1})	**Nitrocellulose Raman shift (cm^{-1})**
718	703
730	
753	
795	
826	850
911	
940	
1035	1088
1136	1124
1169	
1216	
1294	1284
1335	
1363	1374
1430	1458
1482	
1581	
1612	1655

5.3.2.2 Antibody conjugation to AuNPs

Based on the results of the proteomics analysis of the BL2 and BL2-bcl2 EVs, CD20 and CD53 were chosen as biomarker targets for binding to SERS AuNPs. CD20 is a pan-B cell marker and was found to be present on both BL2 apoEVs and BL2-bcl2 EVs. CD53 is a tetraspanin protein found predominantly on leucocytes. Proteomics results indicated that CD53 is present only on the apoEVs and was not detected in the BL2-bcl2 EVs. These two proteins were chosen as targets for detection by SERS as the anti-CD20 SERS AuNPs should bind to both types of EVs but the anti-CD53 should be specific for apoEVs.

Monoclonal antibodies against both of these proteins were conjugated to MGITC-functionalised AuNPs using polyethylene glycol (PEG), giving two different SERS probes consisting of AuNPs functionalised with MGITC Raman reporter and the appropriate antibody. For initial studies, the same reporter was used for both SERS probes, however once the assay is optimised a different reporter molecule could be used for each SERS probe so that both proteins could be detected in the same assay. Two different carboxy-PEG-thiol molecules, carboxy-PEG_{12}-thiol with a molecular weight of 635 g/mole (PEG635) and PEG with a molecular weight of 5000 g/mole (PEG5000), were used in order to determine whether the length of the polymer had an effect on the stability of the AuNPs and the SERS signal. The thiol group of the PEG moiety has an affinity for the gold surface of the nanoparticle, and the carboxy group on the other end of the linker allows coupling of NH_2 groups of the antibody via EDC/NHS coupling. The spectra of anti-CD20 monoclonal antibody conjugated to MGITC-functionalised AuNPs using both PEG635 and PEG5000 is shown in Figure 5.5A. The PEG635-conjugated AuNPs give a much weaker SERS signal than the AuNPs which had been conjugated using PEG5000. PEG5000 was therefore used to conjugate both antibodies to the AuNPs surface. The SERS spectra of anti-CD20 monoclonal antibody conjugated to MGITC-functionalised AuNPs using PEG5000 and anti-CD53 monoclonal antibody conjugated to MGITC-functionalised AuNPs using PEG5000 are shown in Figure 5.5B. The spectrum of MGITC-functionalised AuNPs is also shown for reference, to show that the conjugation of antibodies to the nanoparticle surface does not change the spectrum of MGITC.

The antibody-conjugated SERS nanoparticles were also characterised by extinction spectroscopy and DLS. The extinction spectrum of anti-CD20 and anti-CD53 functionalised AuNP are shown in Figure 5.6. The LSPR of citrate-capped AuNP is 530 nm, whereas the functionalised AuNPs have a slightly red-shifted LSPR at 535 nm. The concentration of AuNPs in the antibody conjugated samples was calculated to be 8.2×10^{-11} M for anti-CD53 SERS AuNP and 8.4×10^{-11} M for anti-CD20 SERS AuNP when resuspended in 1 mL of water. The sizes of the different conjugates are given in Table 5.4. The anti-CD53 conjugates are larger than the anti-CD20 AuNPs, with the PEG635 AuNPs measuring 47.44 ± 0.39 nm and 37.98 ± 0.33 nm, respectively. The PEG5000 anti-CD20 conjugated AuNPs are larger than the PEG635 counterpart, at 40.44 ± 0.14 nm in diameter. The anti-CD53 antibody conjugated with PEG5000 are slightly smaller than the PEG635 equivalent AuNPs however, at 45.57 ± 0.15 nm. These are increased from the unfunctionalized citrate-capped AuNP, which were 21.69 ± 0.15 nm, indicating that the conjugation was successful.

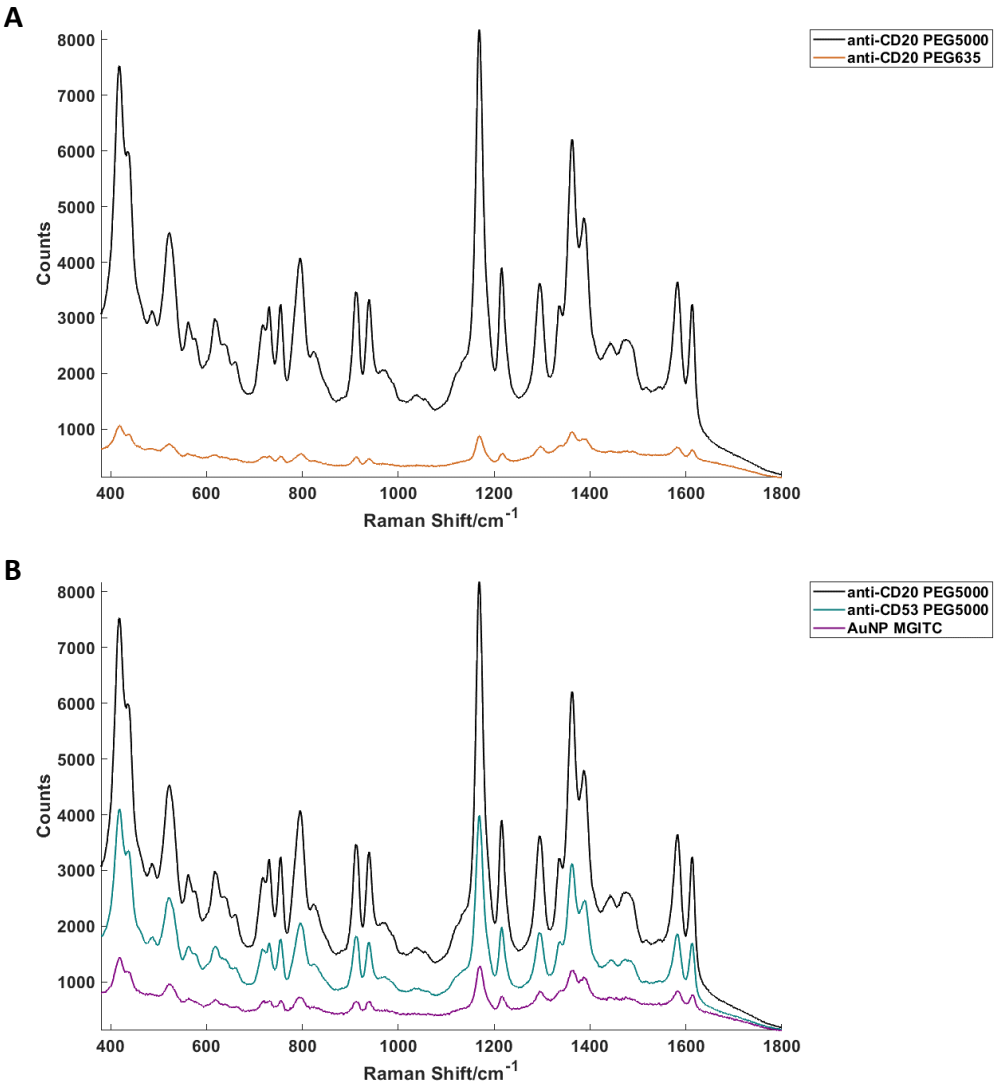

Figure 5.5: Conjugation of monoclonal antibodies to AuNPs using PEG. A) anti-CD20 monoclonal antibody was conjugated to MGITC-functionalised AuNPs with both PEG635 and PEG5000. The PEG5000 conjugated SERS nanoparticles give a stronger SERS signal than the nanoparticles conjugated using PEG635. B) The SERS spectra of anti-CD20 conjugated with PEG5000 to MGITC-functionalised AuNPs and anti-CD53 conjugated with PEG5000 to MGITC-functionalised AuNPs. The spectra of MGITC-functionalised AuNPs is also shown as a comparison to show that the antibody conjugation does not affect the MGITC spectrum. All spectra were acquired with 785 nm laser excitation on a Snowy Sierra spectrometer using 45 mW laser power and 1 second acquisition time.

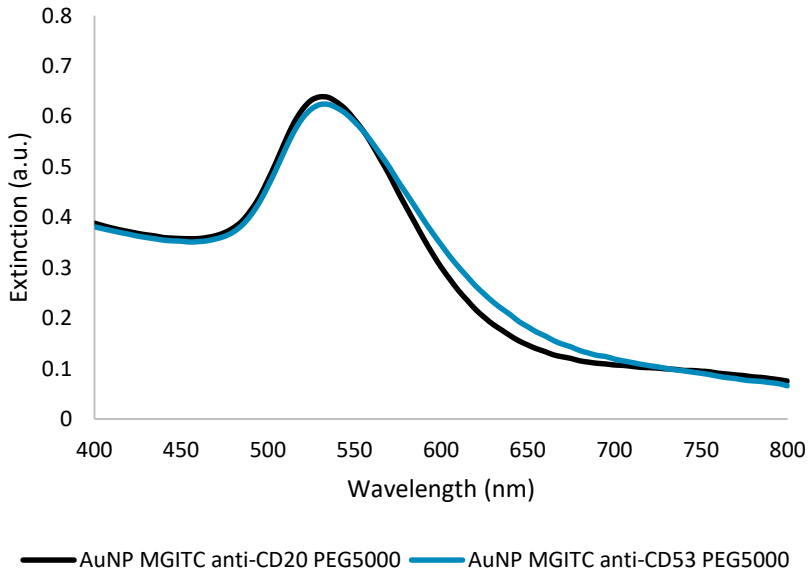

Figure 5.6: Extinction spectroscopy of functionalised gold nanoparticles. The LSPR of the antibody-conjugated AuNPs is 535 nm.

Table 5.4: Size of antibody-conjugated AuNPs measured by DLS

	Size mean ± SD
AuNP MGITC anti-CD53 PEG635	47.44 ± 0.39
AuNP MGITC anti-CD53 PEG5000	45.58 ± 0.15
AuNP MGITC anti-CD20 PEG635	37.98 ± 0.33
AuNP MGITC anti-CD20 PEG5000	40.44 ± 0.14

5.4 Detection of BL2 cells using SERS nanoparticles

In order to test the SERS detection method on nitrocellulose and optimise the data acquisition and processing, the anti-CD20 SERS AuNPs were first used on BL2 cells adsorbed to nitrocellulose.

Unfixed viable BL2 cells from culture were diluted in PBS to give cell solutions with concentrations varying from 10 x 10^6 mL^{-1} to 5 x 10^6 mL^{-1}. 1 µL of each of these cell suspensions was dropped onto a 1 cm x 1 cm square of nitrocellulose, the edges of the spot were marked, and the nitrocellulose was allowed to dry. Care was taken not to allow the tip of the pipette to touch the nitrocellulose when applying the cells, as this would create a groove in the nitrocellulose in which AuNPs could accumulate. When the nitrocellulose was dry, each square was placed in a separate well of a 24-well plate and blocked with 5% BSA

for 1 hour at room temperature. 20 µL of anti-CD20 conjugated MGITC AuNPs (0.84 nM) was then added with 150 µL of 0.1% BSA/0.05% Tween 20 in 10 mM phosphate buffer (BSA/PBT) and placed on a shaker at room temperature for one hour. The nitrocellulose squares were then washed with 0.05% Tween 20 in 10 mM phosphate buffer (PBT) to remove any SERS AuNPs which had bound non-specifically. For the samples with higher cell concentrations, a visible red spot of AuNPs was observed.

Raman maps of control untreated nitrocellulose, nitrocellulose blocked with BSA, and nitrocellulose blocked and incubated with BSA/PBT were taken, in order to ensure that these molecules do not interfere with the signal obtained. The spectra are shown in Figure 5.7. The untreated nitrocellulose has a relatively high Raman background, which is greatly reduced when the samples are blocked and exposed to BSA/PBT. No additional Raman peaks were observed due to these agents, therefor no additional background peaks should be observed and the MGITC signal will not be masked further.

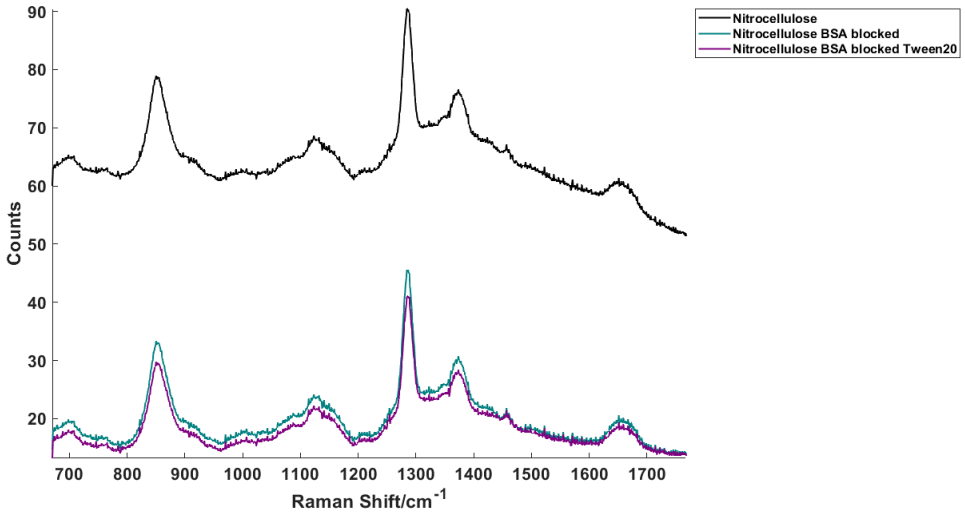

Figure 5.7: Raman spectra of control nitrocellulose samples. The untreated nitrocellulose has a high background, which is reduced when blocked with BSA and incubated with Tween 20 in phosphate buffer. No additional peaks were observed in these samples. All spectra were acquired with 785 nm laser excitation in streamline beam configuration on a Renishaw inVia spectrometer with 9 mW laser power and a 2 second acquisition time.

Raman maps were then taken of the cell samples on nitrocellulose which had been incubated with the anti-CD20 SERS AuNPs. An area of 500 x 500 steps in both the x and y was mapped, with a step size of 3.5 µm, which covered the area of the visible AuNP spot. For samples without a visible nanoparticle spot, the centre of the marked droplet was mapped. The cosmic ray removal tool on the WiRE 4.4 software was used to remove any spurious peaks

which may interfere with the data processing. The intensity of the MGITC peak at 1171 cm^{-1} was measured and a false colour map of intensity was plotted. However, some areas of the maps were giving an intensity value which seemed anomalously high. Upon investigating the original data, it was found that the samples had some regions of very high background, despite the observed effect of the nitrocellulose blocking. Therefore, in order to remove the areas of high background from the results the intensity at the base of the nitrocellulose peak 1140 cm^{-1}, was subtracted from the intensity at 1171 cm^{-1}, and this value was then used in the data processing. A minimum threshold of 100 was set, and a mask was created to remove any areas of the map which had a relative intensity of below 100 (Figure 5.8). The BL2 cell concentrations where the AuNP spots were visible, 8 x 10^6 mL^{-1} (Figure 5.8D), 9 x 10^6 mL^{-1} (Figure 5.8E), and 10 x 10^6 mL^{-1} (Figure 5.8F), have clear round spots in the mask where the AuNPs have bound to the BL2 cells. The lower concentrations which did not have visible spots, 5 x 10^6 mL^{-1} (Figure 5.8A), 6 x 10^6 mL^{-1} (Figure 5.8B), and 7 x 10^6 mL^{-1} (Figure 5.8C), still have areas of SERS signal in the mask, demonstrating that NPs had bound but the concentration was so low that it was not visible to the eye. The PBS no cell control has no visible signal from the MGITC anti-CD20 SERS AuNPs (Figure 5.8G). It appears that most of the signal comes from the edge of the spot, indicating that there may be a slight coffee-ring effect occurring when the cell solutions dry on the nitrocellulose, leading to the majority of cells drying in the outside of the spot which yields an uneven SERS signal distribution. In Figure 5.8E, an area on the bottom-right edge of the AuNP spot was found to have burned after the Raman map had completed, which may have been due to a high concentration of AuNPs becoming hot when in the path of the laser and causing the underlying nitrocellulose to burn. This coffee-ring effect can be concentration dependent and can be reduced by reducing the volume of the droplet.[345] However, only 1 µL of each cell suspension was applied to the nitrocellulose and if this were to be reduced further the droplet would not easily detach from the pipette tip without the tip touching the surface of the nitrocellulose. The coffee-ring effect can also be supressed by the addition of molecules such as PEG or sugar to increase the viscosity of the droplet.[346,347]

The number of pixels in the mask showing relative intensity of >100 was used as a measure of the number of MGITC-functionalised AuNPs detected. This is shown in Figure 5.9. The PBS no cell control has negligible detected signal. The number of pixels in the mask of the BL2 cell samples generally increased with an increasing number of cells applied to the nitrocellulose. The highest concentration of cells, 10 x 10^6 mL^{-1}, was measured to have 9814 AuNP pixels, 9

x 10^6 BL2 cells mL^{-1} had 9334 pixels, and the 7 x 10^6 mL^{-1} sample had 5470 pixels above the threshold. The highest number of pixels was detected in the 8 x 10^6 mL^{-1} sample, with 16490. The two lowest concentrations, 5 x 10^6 mL^{-1} and 6 x 10^6 mL^{-1}, had a very low level of detected signal, at 738 and 1242 pixels, respectively. The 5 x 10^6 mL^{-1} sample has less than 10% of the detected signal of the 10 x 10^6 mL^{-1} sample, indicating that the number of pixels is not directly proportional to the number of cells. It may be that the addition of more cells causes the AuNPs to form larger hot spots on the nitrocellulose, increasing the signal intensity and therefore the number of pixels detected above the threshold value of 100. Therefore, although the AuNPs are binding to the cells, the SERS signal intensity relationship with the cell concentration is not linear.

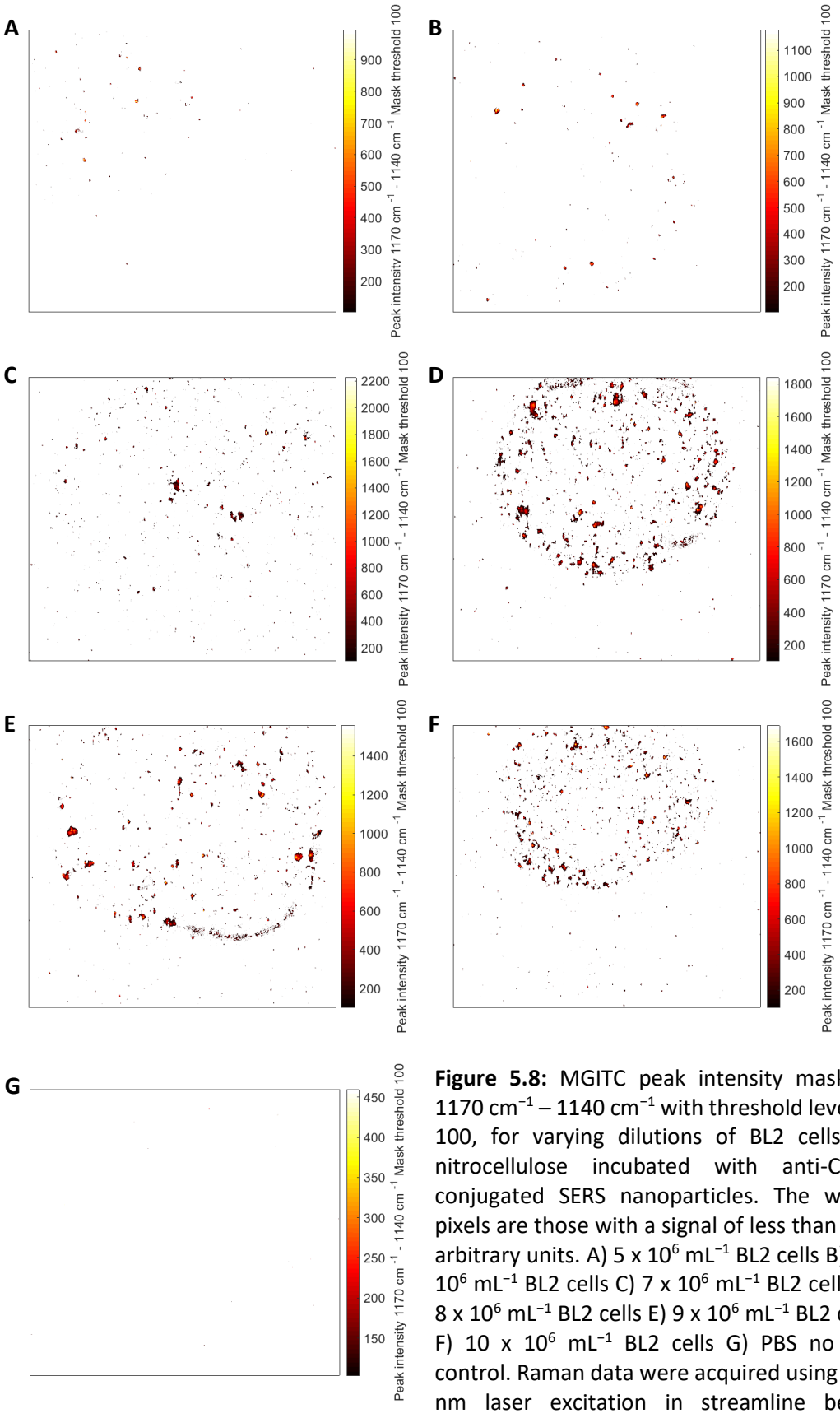

Figure 5.8: MGITC peak intensity mask of 1170 cm^{-1} – 1140 cm^{-1} with threshold level of 100, for varying dilutions of BL2 cells on nitrocellulose incubated with anti-CD20 conjugated SERS nanoparticles. The white pixels are those with a signal of less than 100 arbitrary units. A) 5 x 10^6 mL^{-1} BL2 cells B) 6 x 10^6 mL^{-1} BL2 cells C) 7 x 10^6 mL^{-1} BL2 cells D) 8 x 10^6 mL^{-1} BL2 cells E) 9 x 10^6 mL^{-1} BL2 cells F) 10 x 10^6 mL^{-1} BL2 cells G) PBS no cell control. Raman data were acquired using 785 nm laser excitation in streamline beam configuration on a Renishaw inVia spectrometer with 9 mW laser power and 2 second acquisition time.

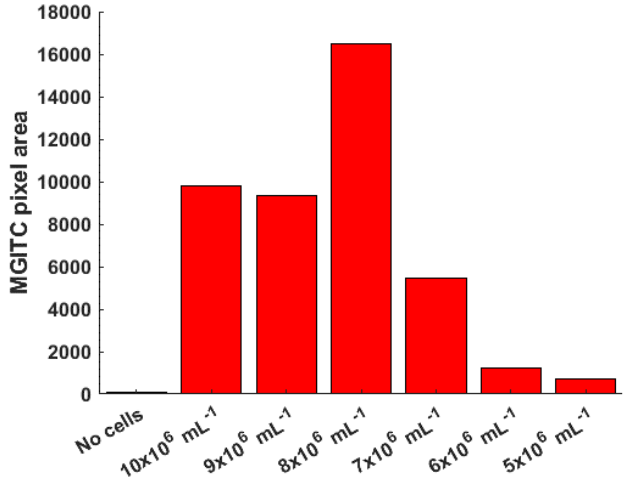

Figure 5.9: The quantification of the number of pixels in the MGITC peak intensity mask of 1170 cm^{-1} – 1140 cm^{-1} with a threshold level of 100 for varying concentration of BL2 cells. The number of pixels in the mask is roughly dependent on the concentration of cells applied to the nitrocellulose.

5.5 Detection of BL2 and BL2-bcl2 EVs with SERS nanoparticles

As the preliminary SERS assay using the BL2 cells appeared successful, the assay was then attempted for the detection of EVs captured on the nitrocellulose. The EVs were prepared from UV-irradiated BL2 and BL2-bcl2 cells and separated by dual filtration through a 5 µm mesh filter and 1.2 µm syringe filter as described in Section 2.3. In order to increase the concentration of EVs in the suspension, and to remove the proteins present in the media which would bind to the surface of the nitrocellulose, the EV suspensions were centrifuged at 20,000 *g* for 1 hour at 4°C. Two separate 500 µL aliquots of each EV suspension were pelleted. One pellet was resuspended in 1 mL of 0.1 µm filtered PBS and used to quantify the number of EVs in the pellet using a NanoSight. The other pellet was resuspended in 100 µL of 0.1 µm filtered PBS and assumed to have a concentration of 10x that of the 1 mL EV suspension. Based on reports of EV concentrations in the blood of cancer patients and healthy controls of approximately $50x10^8$ mL^{-1},[158] and the concentrations of EVs found in the *in vitro* preparations, a serial dilution with concentrations ranging from 40 x 10^8 mL^{-1} to 5 x 10^8 mL^{-1} was used.

The samples were spotted onto the nitrocellulose and incubated with anti-CD20 SERS nanoparticles or anti-CD53 SERS nanoparticles, as described in Section 5.4. Three independent EV preparations were carried out. For two of these three, the 20,000 *g* pellet had a concentration of less than 40 x 10^8 mL^{-1}. In one of these instances, the sample was diluted with 0.1 µm filtered PBS to yield a concentration of 20 x 10^8 mL^{-1}, and so for the 40 x

10^8 mL^{-1} sample two 1 µL spots were applied to the nitrocellulose, allowing the drop to dry in between applications. In the other instance, the 20,000 *g* pellet had a concentration of only 10 x 10^8 mL^{-1}, so two and four 1 µL drops were applied for the 20 x 10^8 mL^{-1} and 40 x 10^8 mL^{-1} samples, respectively.

The data were acquired and analysed as described in Section 5.4, where the peak height of the 1171 cm^{-1} peak was found by subtracting the peak intensity at 1140 cm^{-1} from the 1171 cm^{-1} intensity and using this to generate a mask of MGITC signal with a threshold level of 100. The mean number of pixels in the masks of the three replicate experiments was calculated along with the SD and is shown in Figure 5.10. The No EV control was found for each type of SERS nanoparticle. The PBS control used in the cell detection described in Section 5.4 was used, together with a second PBS control carried out alongside the EV samples and a region outside of the sample droplet area was mapped as a third control. The number of pixels in the anti-CD20 SERS nanoparticle no EV control samples was 69 ± 72, which is low when compared to the signals achieved for the cell samples in Figure 5.9, although the SD is high. However, the signals achieved for the BL2 EV samples with anti-CD20 SERS nanoparticles are comparable to this control (Figure 5.10A). The 40 x 10^8 mL^{-1} droplet had a pixel area of 170 ± 111, the 20 x 10^8 mL^{-1} sample gave a pixel area of 103 ± 68, 10 x 10^8 mL^{-1} yielded an area of 83 ± 51 pixels and the sample with the lowest concentration of 5 x 10^8 BL2 EVs mL^{-1} actually generated the highest MGITC pixel area, of 239 ± 425 pixels.

The results for the BL2-bcl2 EVs incubated with anti-CD20 SERS nanoparticles are similarly unreliable (Figure 5.10B). Only the 40 x 10^8 mL^{-1} sample had a pixel number greater than that of the no EV control, at 74 ± 50 pixels. For the 20 x 10^8 mL^{-1}, 10 x 10^8 mL^{-1}, and 5 x 10^8 mL^{-1} samples the areas were 22 ± 19 pixels, 21 ± 13 pixels, and 51 ± 50 pixels, respectively. Again, the lowest concentration of BL2-bcl2 EVs sees an increase in the MGITC signal detected when compared to some of the higher EV concentrations analysed.

For the anti-CD53 SERS nanoparticles, the no EV control samples had a mean area of 130 ± 170 pixels. This large SD indicates the high variability in SERS AuNP detection by this method. Based on the proteomic results, CD53 should only be found on BL2 EV and should not be present on BL2-bcl2 EVs. The BL2 EV samples incubated with anti-CD53 SERS nanoparticles each had similar values for the MGITC pixel area (Figure 5.10C). 40 x 10^8 EV mL^{-1} had 80 ± 31 pixels above the threshold, and 20 x 10^8 mL^{-1} yielded 84 ± 54 pixels. The pixel area found for 10 x 10^8 mL^{-1} was 65 ± 69, and the 5 x 10^8 mL^{-1} sample was found to have 67 ± 100 pixels. All

of the BL2 EV samples incubated with the anti-CD53 SERS nanoparticles had a fewer pixels above the threshold than the control. The same was found of the BL2-bcl2 EV samples incubated with anti-CD53 SERS nanoparticles (Figure 5.10D). The number of pixels was found to be 45 ± 30, 31 ± 14, 30 ± 36, and 138 ± 261 for the 40 x 10^8 mL^{-1}, 20 x 10^8 mL^{-1}, 10 x 10^8 mL^{-1}, and 5 x 10^8 mL^{-1} samples, respectively.

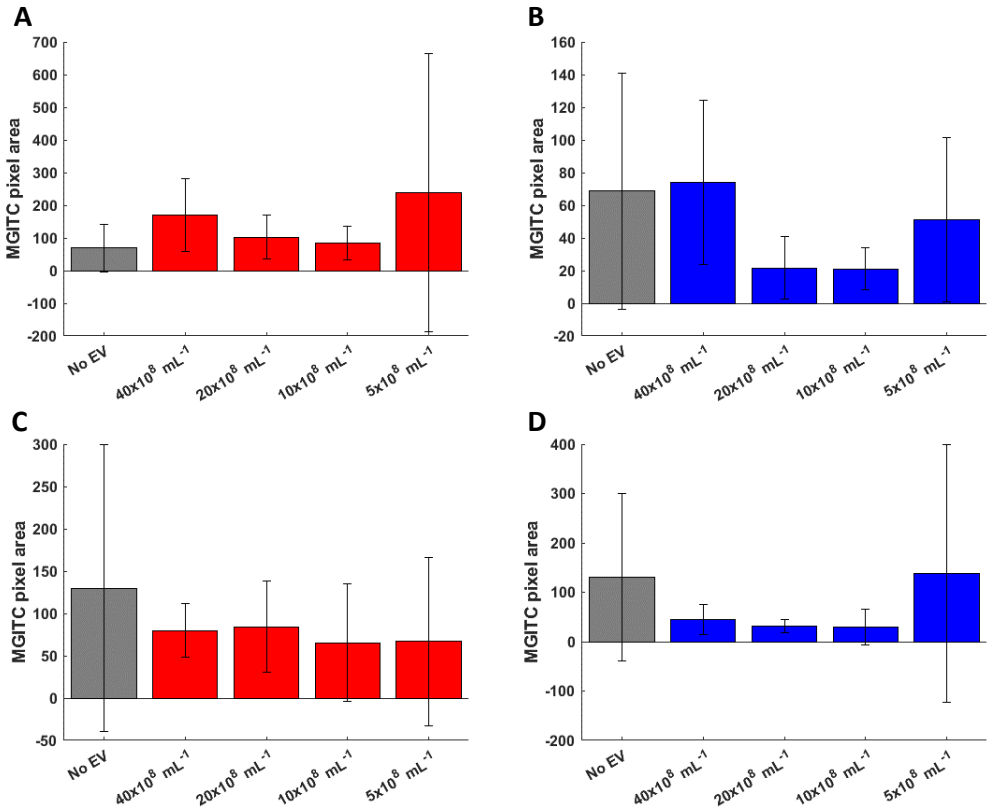

Figure 5.10: Quantification of MGITC signal from SERS EV detection assay. Each pixel area represents the mean of three independent experiments with ±1 SD A) BL2 EVs at various concentrations on nitrocellulose incubated with anti-CD20 conjugated MGITC AuNPs. B) BL2-bcl2 EVs at various concentrations on nitrocellulose incubated with anti-CD20 conjugated MGITC AuNPs. C) BL2 EVs at various concentrations on nitrocellulose incubated with anti-CD53 conjugated MGITC AuNPs. D) BL2-bcl2 EVs at various concentrations on nitrocellulose incubated with anti-CD53 conjugated MGITC AuNPs.

These results indicate that the detection of EVs using SERS nanoparticles is not effective at the concentrations examined. It could be that, unlike the cells from which they came, the EVs are too small to be detected in this manner. The majority of the EVs population are less than 300 nm in diameter, and the SERS AuNPs were found to be approximately 45 nm by DLS, thus a limited number of AuNPs can bind to each EV. The number of CD20 and CD53 protein molecules on their surface may be very low, and as half of the EV surface is bound to the nitrocellulose, this further reduces the available area for SERS AuNPs to bind. While on the

cell surface there may be several protein molecules in close proximity, allowing the formation of AuNP hotspots, the EVs are too small with too low protein copy number for this to occur.

5.6 Western blot analysis of EVs

In order to determine whether the lack of detectable signal in the SERS assay was due to the sensitivity of the assay or due to the amount of protein found in the EVs, a Western blot was carried on both BL2 and BL2-bcl2 EVs for CD20 and CD53. Western blotting has been successfully carried out on EV preparations,[107,113,132] so this was chosen as a validated technique for the detection of specific proteins in EVs.

EVs were quantified by NTA, and 50 x 10^8 EVs were pelleted by centrifugation at 20,000 *g* for 1 hour. The pellets were frozen at -80°C until ready to use. Three pellets of BL2 EVs and BL2-bcl2 EVs were used in each blot. The Western blot results are shown in Figure 5.11A and Figure 5.11B probing for CD20 and CD53, respectively. The expected molecular weight of CD20 protein is 33-37 kDa, and CD53 protein is expected at 32-40 kDa. As can be seen from the blots, neither CD20 nor CD53 was detected in the BL2 or BL2-bcl2 EV lysates. However, the same band was present at a much higher molecular weight present in both blots. To test whether this band was due to non-specific binding of the secondary antibody to a protein present in the lysates, a blot was performed where the secondary antibody was added directly to the blocked membrane without the addition of the primary antibody. This analysis showed no non-specific binding of the secondary antibody (Figure 5.11C).

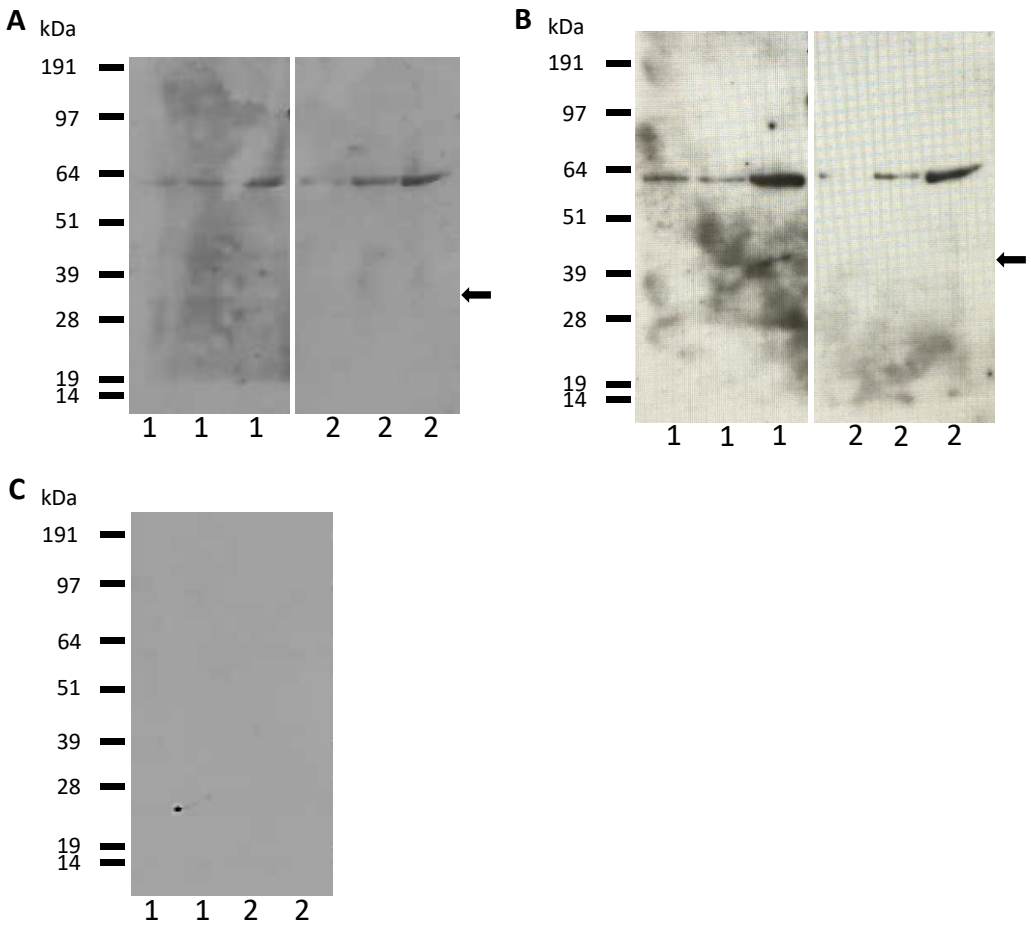

Figure 5.11: Western blots of BL2 (1) and BL2-bcl2 (2) EV lysates. A) Blot probed with anti-CD20, 1 minute exposure to x-ray film. The arrow indicates where CD20 should appear. B) Blot probed with anti-CD53, 5 minutes exposure to x-ray film. The arrow indicates where CD53 should appear. C) Secondary only control.

The unexpected bands observed in the Western blot are present in both the blot probed with anti-CD20 antibody and anti-CD53 antibody, indicating that they are not likely to be caused by dimerization of the target proteins. It may be that the antibodies are both recognising an epitope in a third protein, as both antibodies were raised against B cells (anti-CD20 against human tonsil B cells, and CD53 against leucocytes from a leukaemia patient). The fact that there are no bands visible at the expected molecular weights for CD20 and CD53 indicates that neither protein is present in sufficient quantities to be detectable by Western blot, and therefore SERS, despite being identified by proteomics.

5.7 Discussion

In order to detect the BL2 and BL2-bcl2 EVs by SERS, the EVs were captured on nitrocellulose and then incubated with antibody-conjugated SERS reporter AuNPs. Two different antibodies were used, one against CD20 which was shown by proteomics to be present on both EV types,

and the other against CD53 which was shown by proteomics to be present only on the BL2 apoEVs.

The assay was first tested using BL2 cells captured on nitrocellulose and detected using anti-CD20 SERS AuNPs. The system showed a good response, with the signal decreasing with a decrease in the number of cells applied to the nitrocellulose. The signal obtained from the 6 x 10^6 mL^{-1} and 5 x 10^6 mL^{-1} samples were much lower than the higher cell concentrations, potentially indicating that the assay was reaching its limit of detection at these concentrations. However, signal was still observed above the PBS control, so the assay and data processing technique were deemed suitable for use with the EV samples.

When the SERS signals of EV dilutions on nitrocellulose was compared to those of no EV controls, no difference in the number of pixels above the intensity threshold was observed. In fact, for most EV samples the signal was actually lower than the corresponding control. This result was unexpected. It could be due to an inherent issue with the AuNP signal enhancement. Although it was sufficient for cells, the cell surface would have many copies of CD20 on the surface, and proteins in close proximity to each other with bound SERS AuNPs could form hotspots in order to further enhance the signal. EVs are much smaller than cells, and may therefore only have a few, or one, copy of each protein on their surface. The EVs binding to the nitrocellulose will also block up to half of the EVs surface area, and therefore further limit the number of target proteins available for binding. If there are insufficient numbers of proteins in close proximity to form hotspots, the signal generated by a single SERS AuNP may not be enough to detect above the chosen threshold. SERS particles with stronger enhancement, such as core-reporter-shell nanoparticles, or signal amplification using silver enhancement after AuNP binding, may enhance the signal sufficiently for single particle detection.

In order to determine why the assay was unsuccessful, Western blot analysis was carried out on the EV lysates to ensure that CD20 and CD53 protein were present in sufficient quantities. No CD20 or CD53 was detected on either the BL2 EVs or BL2-bcl2 EVs, despite these proteins being detected in proteomics analysis. As there was no detectable protein by Western blot, it is likely that this is the reason that the EVs were not detected by SERS.

Therefore, although the SERS assay carried out here was unsuccessful, the assay may work if the proteins chosen are expressed at a high enough level to be detected by Western blot.

6 Conclusion and perspectives

6.1 Conclusions

Current methods used in the biochemical characterisation of EVs typically involve bulk analysis techniques, such as Western blot,[113,328] ELISA,[348] or proteomics.[87,112] Flow cytometry, well established for the investigation of individual cells, is not reliable in the study of EVs due to the inability of the instrumentation to detect small particles.[138] High-resolution fluorescence microscopy techniques may be used to study EVs, however the number of different analytes which can be detected simultaneously is limited by the broad emission spectra of the fluorophores used. Raman spectroscopy, however, is a label-free method which can be used to semi-quantitatively identify biochemical functional groups present in a sample due to the narrow peaks produced, and when used in conjunction with multivariate analysis can distinguish between biological samples treated under different conditions.[211,225,230]

The aim of this work was to use Raman spectroscopy and surface enhanced Raman spectroscopy (SERS), in conjunction with some bioinformatics techniques, in order to characterise and detect extracellular vesicles (EVs) derived from aggressive tumour cells, in an attempt to distinguish EVs released from apoptotic cells (apoEVs) and EVs released from non-apoptotic cells. The cells predominantly used in this work were the Burkitt's lymphoma (BL) cell line BL2, and a line of BL2 which had been transfected with the anti-apoptosis gene *BCL-2*.

Raman spectroscopic analysis of BL2 EVs and BL2-bcl2 EVs revealed features that indicate apoEVs are a distinct population from their non-apoptotic counterparts. The BL2 apoEVs signals indicated the presence of higher levels of nucleic acids as cargo within these particles compared to the BL2-bcl2 EVs, potentially derived from the nuclear fragmentation occurring as a result of the apoptotic process. As well as distinguishing between the apoEVs and non-apoEVs, some differences were also observed when the BL EVs Raman data were compared with HeLa EVs spectral data. The distinction between EVs derived from cells of different lineages and between different EV populations released from cells of the same type show that Raman spectroscopy has great potential for the label-free classification of EVs.

Despite the benefits of Raman spectroscopy for the analysis of EVs in a label-free manner, there are also limitations to this method. The Raman microscope instrumentation used in

this study require the EVs to be observed on the surface of the CaF_2 window. The majority of the particles measured are less than 300 nm in diameter, and thus may not be distinguished easily due to the diffraction limit of light. A way of overcoming this would be to use an optical trapping system, where the particles in suspension are trapped by the electromagnetic field of a laser in order to interrogate the spectrum of the EV. This strategy has been used to study exosome-type EVs, which are typically defined as having a diameter below 100 nm.[296,299,302] The analysis of EVs by Raman spectroscopy is also not very high throughput. Raman cytometry, whereby flow cytometer instrumentation is used to acquire Raman spectra, has been proposed to increase the throughput of Raman spectroscopic analysis.[208] However, the same limitations of flow cytometry would likely apply to the analysis of EVs by this technique.

As well as these drawbacks, Raman signals are inherently weak. SERS analysis is better suited for the analysis of biological specimens such as EVs. The metal nanoparticles can enhance the Raman signals by many orders of magnitude, acquisition times are reduced, and by using different Raman reporter dye molecules to identify particular biomarkers, sensitive, multiplexed detection of complex samples can be achieved.

Publicly available gene expression microarray datasets were used in order to identify plasma membrane proteins which showed higher levels of expression in aggressive non-Hodgkin lymphoma samples when compared with healthy B cell data, in order to identify biomarkers that would preferentially be found on cancer-derived EVs over the constitutively released B-cell derived EVs. Three candidate proteins were identified, CD46, CD59, and CD146. Validation of these markers showed that CD146 was not present on the surface of the parental BL2 cells, and CD46 and CD59 were not detected on the surface of the EVs by flow cytometry. However, flow cytometric analysis of EVs is sometimes disputed. Many flow cytometers are not set up to analyse such small particles, and the limit of detection in terms of particles size can often be larger than the size range of EVs to be analysed. Dedicated flow cytometers, which have altered settings and specialised filters, may be more relevant for the analysis of EVs, but these are not widely available. Therefore, a negative result of EVs analysed by flow cytometry may indicate that the protein of interest is not expressed in the sample, but it may also indicate that the EVs which do carry that particular biomarker are below the limits of detection of that particular instrument. Further methods of validation, such as Western blot or ELISA, could be carried out in conjunction with flow cytometry to give more confident results.

Proteomics data for samples of BL2 EVs and BL2-bcl2 EVs was available, generated by Maggie Paterson in collaboration with a Prof Tony Whetton at the University of Manchester. These data generated more candidate biomarkers which could be used for the detection of BL2 EVs. CD20 and CD53, which had been identified by proteomics in BL2 EVs and BL2-bcl2 EVs, and BL2 EVs only, respectively, were used in the development of a SERS-based assay for the detection of these EV subsets.

Gold nanoparticles (AuNPs), functionalised with the Raman reporter molecule malachite green isothiocyanate (MGITC) and either anti-CD20 or anti-CD53 antibodies, were generated. Due to the presence of a reporter molecule on the AuNPs, a washing step was necessary in order to only detect those AuNPs which had bound to their respective target. Nitrocellulose was chosen as a substrate to capture the EVs due to the property of non-specifically binding proteins on the nitrocellulose surface via hydrophobic interactions. This substrate could then be exposed to the SERS AuNPs and subsequently washed to remove any unbound AuNPs without losing any of the EVs in the sample. Preliminary testing of the assay using BL2 cells showed binding of the anti-CD20 MGITC AuNPs with encouraging signal intensities. However, when the BL2 EVs and BL2-bcl2 EVs were used in the assay the SERS signals obtained from both anti-CD20 MGITC AuNPs and anti-CD53 MGITC AuNPs samples was no different to no EV controls. Western blot analysis of the BL2 EVs and BL2-bcl2 EVs showed that neither protein was detectable, despite being identified in the proteomics analysis.

In future, better care must be taken to correctly validate the presence of biomarkers identified through bioinformatics analyses such as gene expression microarrays and proteomics. A number of promising candidates remain on the list of potential biomarkers, including proteins known to be associated with B cells or lymphoma such as CD10, or CD79b. Interestingly, CD46, which was identified as potentially upregulated in lymphoma samples by gene expression analysis, also appears on the list of proteins found on the BL2 apoEVs by proteomics. Thorough investigation using multiple complementary assays should be used to ascertain whether these markers are actually present in the sample in order to be used as targets for detection with SERS nanoparticles.

The nitrocellulose-based capture assay may not be the most suitable method for the characterisation of EVs by SERS. The results show that many of the EV samples analysed in this assay had a lower SERS signal intensity than the control samples containing no biological sample of any kind. The pore size of the nitrocellulose was 450 nm, so it may be that case

that the EVs were becoming trapped within the pore of the nitrocellulose membrane, thereby reducing the area available for the binding and detection of the SERS AuNPs to the EV targets. Published works have used magnetic beads to capture EVs for phenotype analysis and detection by SERS in a sandwich type assay, where an antibody against a general EV marker is placed on the magnetic bead to capture the majority of the EVs in the sample, and then SERS NPs targeted against markers of interest are added.[333–335] By applying a magnetic field, the unbound SERS NPs can be removed from the sample of captured EVs. These studies have all been looking at the exosome-type EVs, which are the most well-studied of the different subtypes of EVs, and have a number of proteins which are considered to be 'exosome markers' commonly displayed on their surface, such as tetraspanins CD9, CD63, and CD81. Thus, there are known proteins which could be used to capture all exosomes, which were then investigated for the presence of other markers. However, there are no well-characterised proteins known to be present on the surface of MV-type EVs or apoEVs. These EVs do tend to have markers of the cells from which they derive, but preliminary work by to capture BL EVs on magnetic beads using B-cell markers CD19 and CD20 for detection with fluorescence by flow cytometry were not proving successful, so the more general method of non-specific capture by using nitrocellulose was chosen. EVs tend to have a negative charge, so the assay may be improved by using magnetic beads coated with a positively-charged polymer, such as 4-dimethylaminopyridine (DMAP)[327] or cysteamine,[331] in order to non-specifically capture EVs via electrostatic interactions. Cholesterol could also be used as a targeting molecule for EV-binding, as it can incorporate into the lipid bilayer of the EVs.[335]

6.2 Perspectives

Since the first studies into the shedding of 'membrane fragments' in the 1970s, the field of EV research has rapidly grown and matured. In fact, the wide range of topics to which EV research has been applied has led to a persistent lack of consensus around EV definitions and nomenclature, as each field of interest appears to have developed separate terminology to describe the particles. For example, those studying EVs derived from cancer cells coined the term 'oncosome', prostate epithelia were designated as producing 'prostosomes', and EVs shed from platelets are generally termed 'microparticles'. In 2013, when the International Society for Extracellular Vesicles (ISEV) held a meeting attempting to create standardised definitions and nomenclature, no consensus could be reached.[104] Concomitant with the lack of consensus on nomenclature is wide variation in EV separation and analysis techniques. The creation by ISEV of guidelines for the definition, separation, and analysis of EVs,[105] as well

as the development of tools for transparent reporting of EV studies,[106] should go a long way to advance the field of EV research by creating concordance between the different research areas.

Due to the small size of EVs, advances in technology have been necessary in order to characterise these particles. Nanoparticle tracking analysis and tunable resistive pulse sensing have been developed as high-throughput methods of characterising the size distribution of EVs, however biochemical analysis still relies heavily on lengthy bulk analysis techniques such as Western blot and ELISA. Many groups are developing methods and instrumentation to make flow cytometry more sensitive for small particles, suitable for the analysis of EVs; this would be an enormously beneficial tool in the EV research arsenal.

As the myriad functions of EVs are revealed, there is clear potential for their use as treatment agents. It has been shown that, for example, EVs released by tumour cells can prime the pre-metastatic niche[182,183] or block the action of targeted anti-tumour antibodies,[171,172] thus preventing the release or function of these EVs could provide a novel therapeutic avenue. EVs derived from mesenchymal stem cells show clinical benefits, having been purported to increase the speed of tissue recovery after injury.[151] EVs are present in all biological fluids, and could potentially be used as non-invasive disease biomarkers. One study has shown that the detection of EVs in urine can be more successful in screening for prostate cancer than the current prostate specific antigen test.[349] This hypothesis could be applied to any number of diseases in which EVs have been shown to have pathological activity.

The field of EV research still has many obstacles to overcome. However, due to the diverse array of functions and applications of these particles, the interest in the field continues to grow. With this increased attention will come technological advances over the coming years to allow EVs to be investigated and utilised to their full clinical potential.

References

1 K. R. Shankland, J. O. Armitage and B. W. Hancock, *Lancet*, 2012, **380**, 848–857.
2 S. H. Swerdlow, World Health Organization and International Agency for Research on Cancer, *WHO classification of tumours of haematopoietic and lymphoid tissues*, .
3 D. Burkitt, *Br. J. Surg.*, 1958, **46**, 218–223.
4 D. Burkitt and G. T. O'Conor, *Cancer*, 1961, **14**, 258–269.
5 G. T. O'Conor, *Cancer*, 1961, **14**, 270–283.
6 M. a Epstein, B. G. Achong and Y. M. Barr, *Lancet*, 1964, **1**, 702–703.
7 W. Henle, V. Diehl, G. Kohn, H. zur Hausen and G. Henle, *Science (80-.).*, 1967, **157**, 1064–1065.
8 P. H. Levine, G. T. O'Conor and C. W. Berard, *Cancer*, 1972, **30**, 610–615.
9 D. H. Wright, *Blood*, 1999, **93**, 758–759.
10 M. Divine, P. Casassus, S. Koscielny, J. Bosq, C. Sebban, C. Le Maignan, A. Stamattoulas, B. Dupriez, M. Raphael, J.-L. Pico and V. Ribrag, *Ann. Oncol.*, 2005, **16**, 1928–1935.
11 P. C. Bishop, V. K. Rao and W. H. Wilson, *Cancer Invest.*, 2000, **18**, 574–583.
12 C. D. Gregory, T. Turs, C. F. Edwards, C. Tetaud, M. Talbot, B. Caillu, A. B. Rickinson and M. Lipinskit, *J. Immunol.*, 1987, **139**, 313–318.
13 R. Dalla-Favera, M. Bregni, J. Eriksont, D. Patterson, R. C. Gallo and C. M. Croce, *Proc. Natl. Acad. Sci.*, 1982, **79**, 7824–7827.
14 R. Dalla-Favera, S. Martinotti, R. Gallo, J. Erikson and C. Croce, *Science (80-.).*, 1983, **219**, 963–967.
15 J. J. Yunis, M. M. Oken, M. E. Kaplan, K. M. Ensrud, R. R. Howe and A. Theologides, *N. Engl. J. Med.*, 1982, **307**, 1231–1236.
16 J. M. Adams, A. W. Harris, C. A. Pinkert, L. M. Corcoran, W. S. Alexander, S. Cory, R. D. Palmiter and R. L. Brinstert, *Nature*, 1985, **318**, 533–538.
17 M. Hummel *et al.*, *N. Engl. J. Med.*, 2006, **354**, 2419–2430.
18 S. Smeland, A. K. Blystad, S. O. Kvaløy, I. M. Ikonomou, J. Delabie, G. Kvalheim, J. Hammerstrøm, G. F. Lauritzsen and H. Holte, *Ann. Oncol.*, 2004, **15**, 1072–1078.
19 The Non-Hodgkin's Lymphoma Classification Project, *Blood*, 1997, **89**, 3909–3918.
20 S. S. Dave *et al.*, *N. Engl. J. Med.*, 2006, **354**, 2431–2442.
21 R. Schmitz *et al.*, *Nature*, 2012, **490**, 116–120.
22 C. Love *et al.*, *Nat. Genet.*, 2012, **44**, 1321–1325.
23 K. Koch, E. Hoster, M. Unterhalt, G. Ott, A. Rosenwald, M. L. Hansmann, M. Engelhard, W. Hiddemann and W. Klapper, *Hum. Pathol.*, 2012, **43**, 2274–2281.
24 P. W. M. Johnson, A. Z. S. Rohatiner, J. S. Whelan, C. G. A. Price, S. Love, J. Lim, J. Matthews, A. J. Norton, J. A. L. Amess and T. A. Lister, *J. Clin. Oncol.*, 1995, **13**, 140–147.
25 W. Hiddemann *et al.*, *Blood*, 2005, **106**, 3725–3732.
26 J. W. Sweetenham, B. Goldman, M. L. Leblanc, J. R. Cook, R. R. Tubbs, O. W. Press, D. G. Maloney, R. I. Fisher, L. M. Rimsza, R. M. Braziel and E. D. Hsi, *Ann. Oncol.*, 2010, **21**, 1196–1202.
27 Y. Tsujimoto, J. Cossman, E. Jaffe and C. Croce, *Science (80-.).*, 1985, **228**, 1440–1443.
28 R. J. H. Ryan, M. Nitta, D. Borger, L. R. Zukerberg, J. A. Ferry, N. L. Harris, A. J. Iafrate, B. E. Bernstein, A. R. Sohani and L. P. Le, *PLoS One*, DOI:10.1371/journal.pone.0028585.
29 R. D. Morin *et al.*, *Nature*, 2011, **476**, 298–303.

30 A. A. Alizadeh *et al.*, *Nature*, 2000, **403**, 503–511.
31 G. Wright, B. Tan, A. Rosenwald, E. H. Hurt, A. Wiestner and L. M. Staudt, *Proc. Natl. Acad. Sci.*, 2003, **100**, 9991–9996.
32 C. P. Hans *et al.*, *Blood*, 2004, **103**, 275–283.
33 T. M. Green, K. H. Young, C. Visco, Z. Y. Xu-Monette, A. Orazi, R. S. Go, O. Nielsen, O. V. Gadeberg, T. Mourits-Andersen, M. Frederiksen, L. M. Pedersen and M. B. Møller, *J. Clin. Oncol.*, 2012, **30**, 3460–3467.
34 K. J. Savage, N. A. Johnson, S. Ben-Neriah, J. M. Connors, L. H. Sehn, P. Farinha, D. E. Horsman and R. D. Gascoyne, *Blood*, 2009, **114**, 3533–3538.
35 L. Colomo, A. Lopez-Guillermo, M. Perales, S. Rives, A. Martinez, F. Bosch, D. Colomer, B. Falini, E. Montserrat and E. Campo, *Blood*, 2003, **101**, 78–84.
36 N. A. Johnson *et al.*, *J. Clin. Oncol.*, 2012, **30**, 3452–3459.
37 J. F. R. KERR, A. H. WYLLIE and A. R. CURRIE, *Br. J. Cancer*, 1972, **26**, 239–257.
38 A. H. Wyllie, R. G. Morris, A. L. Smith and D. Dunlop, *J. Pathol.*, 1984, **142**, 67–77.
39 M. Skalka, J. Matyasova and M. Cejkova, *FEBS Lett.*, 1976, **72**, 271–274.
40 T. Yamada, H. Ohyama, Y. Kinjo and M. Watanabe, *Radiat. Res.*, 1981, **85**, 544–553.
41 M. L. Coleman, E. A. Sahai, M. Yeo, M. Bosch, A. Dewar and M. F. Olson, *Nat. Cell Biol.*, 2001, **3**, 339–345.
42 B. Verhoven, R. A. Schlegel and P. Williamson, *J. Exp. Med.*, 1995, **182**, 1597–601.
43 K. Segawa, S. Kurata, Y. Yanagihashi, T. R. Brummelkamp, F. Matsuda and S. Nagata, *Science (80-.).*, 2014, **344**, 1164–1168.
44 J. Suzuki, D. P. Denning, E. Imanishi, H. R. Horvitz and S. Nagata, *Science (80-.).*, 2013, **341**, 403–406.
45 S. J. Martin, C. P. M. Reutelingsperger, A. J. McGahon, J. A. Rader, R. C. A. A. van Schie, D. M. LaFace and D. R. Green, *J. Exp. Med.*, 1995, **182**, 1545–1556.
46 I. Vermes, C. Haanen, H. Steffens-Nakken and C. Reutelingsperger, *J. Immunol. Methods*, 1995, **184**, 39–51.
47 Y. Gavrieli, Y. Sherman and S. A. Ben-Sasson, *J. Cell Biol.*, 1992, **119**, 493–501.
48 D. L. Vaux, S. Cory and J. M. Adams, *Nature*, 1988, **335**, 440–442.
49 J. Yang, X. Liu, K. Bhalla, C. N. Kim, A. M. Ibrado, J. Cai, T. Peng, D. P. Jones and X. Wang, *Science (80-.).*, 1997, **275**, 1129–1132.
50 R. M. Kluck, E. Bossy-Wetzel, D. R. Green and D. D. Newmeyer, *Science (80-.).*, 1997, **275**, 1132–1136.
51 D. D. Newmeyer, E. Bossy-Wetzel, R. M. Kluck, B. B. Wolf, H. M. Beere and D. R. Green, *Cell Death Differ.*, 2000, **7**, 402–407.
52 P. Monaghan, D. Robertson, T. A. S. Amos, M. J. S. Dyer, D. Y. Mason and M. F. Greaves, *J. Histochem. Cytochem.*, 1992, **40**, 1819–1825.
53 E. Bossy-Wetzel, D. D. Newmeyer and D. R. Green, *EMBO (European Mol. Biol. Organ. J.*, 1998, **17**, 37-49.
54 S. W. Muchmore, M. Sattler, H. Liang, R. P. Meadows, J. E. Harlan, H. S. Yoon, D. Nettesheim, B. S. Chang, C. B. Thompson, S.-L. Wong, S.-C. Ng and S. W. Fesik, *Nature*, 1996, **381**, 335–341.
55 E. Yang, J. Zha, J. Jockel, L. H. Boise, C. B. Thompson and S. J. Korsmeyer, *Cell*, 1995, **80**, 285–291.
56 M. Zhou, Y. Li, Q. Hu, X. C. Bai, W. Huang, C. Yan, S. H. W. Scheres and Y. Shi, *Genes Dev.*, 2015, **29**, 2349–2361.
57 M. M. Hill, C. Adrain, P. J. Duriez, E. M. Creagh and S. J. Martin, *EMBO J.*, 2004, **23**, 2134–2145.
58 M. Enari, H. Sakahira, H. Yokoyama, K. Okawa, A. Iwamatsu and S. Nagata, *Nature*, 2002, **391**, 43–50.

59 F. C. Kischkel, S. Hellbardt, I. Behrmann, M. Germer, M. Pawlita, P. H. Krammer and M. E. Peter, *EMBO J.*, 1995, **14**, 5579–5588.
60 F. C. Kischkel, D. A. Lawrence, A. Chuntharapai, P. Schow, K. J. Kim and A. Ashkenazi, *Immunity*, 2000, **12**, 611–620.
61 M. Tanaka, T. Itai, M. Adachi and S. Nagata, *Nat. Med.*, 1998, **4**, 31–36.
62 A. M. Hohlbaum, S. Moe and A. Marshak-Rothstein, *J. Exp. Med.*, 2000, **191**, 1209–1220.
63 H. Matsumoto, Y. Murakami, K. Kataoka, S. Notomi, D. Mantopoulos, G. Trichonas, J. W. Miller, M. S. Gregory, B. R. Ksander, A. Marshak-Rothstein and D. G. Vavvas, *Cell Death Dis.*, 2015, **6**, 1–9.
64 L. A. Truman, C. A. Ford, M. Pasikowska, J. D. Pound, S. J. Wilkinson, I. E. Dumitriu, L. Melville, L. A. Melrose, C. A. Ogden, R. Nibbs, G. Graham, C. Combadiere and C. D. Gregory, *Blood*, 2008, **112**, 5026–5036.
65 K. Lauber, E. Bohn, S. M. Kröber, Y. Xiao, S. G. Blumenthal, R. K. Lindemann, P. Marini, C. Wiedig, A. Zobywalski, S. Baksh, Y. Xu, I. B. Autenrieth, K. Schulze-Osthoff, C. Belka, G. Stuhler and S. Wesselborg, *Cell*, 2003, **113**, 717–30.
66 D. R. Gude, S. E. Alvarez, S. W. Paugh, P. Mitra, J. Yu, R. Griffiths, S. E. Barbour, S. Milstien and S. Spiegel, *FASEB J.*, 2008, **22**, 2629–2638.
67 M. R. Elliott, F. B. Chekeni, P. C. Trampont, E. R. Lazarowski, A. Kadl, S. F. Walk, D. Park, R. I. Woodson, M. Ostankovich, P. Sharma, J. J. Lysiak, T. K. Harden, N. Leitinger and K. S. Ravichandran, *Nature*, 2009, **461**, 282–286.
68 A. Shiratsuchi, S. Osada, S. Kanazawa and Y. Nakanishi, *Biochem. Biophys. Res. Commun.*, 1998, **246**, 549–555.
69 S. Arur, U. Uche, K. Rezaul, M. Fong, V. Scranton, A. Cowan, W. Mohler and D. Han, *Dev. Cell*, 2003, **4**, 587–598.
70 S. J. Gardai, K. A. McPhillips, S. C. Frasch, W. J. Janssen, A. Starefeldt, J. E. Murphy-Ullrich, D. L. Bratton, P.-A. Oldenborg, M. Michalak and P. M. Henson, *Cell*, 2005, **123**, 321–334.
71 S. Krahling, M. K. Callahan, P. Williamson and R. A. Schlegel, *Cell Death Differ.*, 1999, **6**, 183–189.
72 R. Hanayama, M. Tanaka, K. Miwa, A. Shinohara, A. Iwamatsu and S. Nagata, *Nature*, 2002, **417**, 182–187.
73 H. A. Anderson, C. A. Maylock, J. A. Williams, C. P. Paweletz, H. Shu and E. Shacter, *Nat. Immunol.*, 2003, **4**, 87–91.
74 T. Nakano, Y. Ishimoto, J. Kishino, M. Umeda, K. Inoue, K. Nagata, K. Ohashi, K. Mizuno and H. Arita, *J. Biol. Chem.*, 1997, **272**, 29411–29414.
75 T. N. Stitt *et al.*, *Cell*, 1995, **80**, 661–670.
76 K. Nagata, K. Ohashi, T. Nakano, H. Arita, C. Zong, H. Hanafusa and K. Mizuno, *J. Biol. Chem.*, 1996, **271**, 30022–7.
77 T. D. Camenisch, B. H. Koller, H. S. Earp and G. K. Matsushima, *J. Immunol.*, 1999, **162**, 3498–503.
78 C. V. Rothlin, S. Ghosh, E. I. Zuniga, M. B. A. Oldstone and G. Lemke, *Cell*, 2007, **131**, 1124–1136.
79 P. Sen, M. A. Wallet, Z. Yi, Y. Huang, M. Henderson, C. E. Mathews, H. S. Earp, G. Matsushima, A. S. Baldwin Jr and R. M. Tisch, *Blood*, 2007, **109**, 653–660.
80 A. C. Tosello-Trampont, K. Nakada-Tsukui and K. S. Ravichandran, *J. Biol. Chem.*, 2003, **278**, 49911–49919.
81 M. Nakaya, M. Tanaka, Y. Okabe, R. Hanayama and S. Nagata, *J. Biol. Chem.*, 2006, **281**, 8836–8842.
82 A. G. Renehan, C. Booth and C. S. Potten, *BMJ*, 2001, **322**, 1536–8.

83 D. Hanahan and R. A. Weinberg, *Cell*, 2011, **144**, 646–674.
84 H. D. Ryoo, T. Gorenc and H. Steller, *Dev. Cell*, 2004, **7**, 491–501.
85 M. Hristov, W. Erl, S. Linder and P. C. Weber, *Blood*, 2004, **104**, 2761–2766.
86 T. C. Stephens, G. A. Currie and J. H. Peacock, *Br. J. Cancer*, 1978, **38**, 573–82.
87 M. S. Pavlyukov *et al.*, *Cancer Cell*, 2018, **34**, 119–135.
88 Q. Huang, F. Li, X. Liu, W. Li, W. Shi, F. Liu, B. O'Sullivan, Z. He, Y. Peng, A.-C. Tan, L. Zhou, J. Shen, G. Han, X.-J. Wang, J. Thorburn, A. Thorburn, A. Jimeno, D. Raben, J. S. Bedford and C.-Y. Li, *Nat. Med.*, 2011, **17**, 860–866.
89 C. A. Ford *et al.*, *Curr. Biol.*, 2015, **25**, 577–588.
90 P. Mao, L. Smith, W. Xie and M. Wang, *Oncol. Lett.*, 2013, **5**, 1615–1620.
91 Q. Hu, J. Peng, W. Liu, X. He, L. Cui, X. Chen, M. Yang, H. Liu, S. Liu and H. Wang, *Int. J. Clin. Exp. Pathol.*, 2014, **7**, 5057–5070.
92 C. D. Gregory, C. A. Ford and J. J. L. P. Voss, in *Advances in experimental medicine and biology*, 2016, vol. 930, pp. 51–88.
93 S. S. Dave *et al.*, *N. Engl. J. Med.*, 2004, **351**, 2159–2169.
94 R. D. Leek, C. E. Lewis, R. Whitehouse, M. Greenall, J. Clarke and A. L. Harris, *Cancer Res.*, 1996, **56**, 4625–9.
95 I. F. Lissbrant, P. Stattin, P. Wikstrom, J. E. Damber, L. Egevad and A. Bergh, *Int. J. Oncol.*, 2000, **17**, 445–496.
96 A. Nishie, M. Ono, T. Shono, J. Fukushi, M. Otsubo, H. Onoue, Y. Ito, T. Inamura, K. Ikezaki, M. Fukui, T. Iwaki and M. Kuwano, *Clin. Cancer Res.*, 1999, **5**, 1107–13.
97 E. Chargaff and R. West, *J. Biol. Chem.*, 1946, **166**, 189–197.
98 M. E. De Broe, R. J. Wiene, G. N. Logghe and F. Roels, *Clin. Chim. Acta*, 1977, **81**, 237–245.
99 B. Pan and R. M. Johnstone, *Cell*, 1983, **33**, 967–977.
100 B. T. Pan, K. Teng, C. Wu, M. Adam and R. M. Johnstone, *J. Cell Biol.*, 1985, **101**, 942–948.
101 R. M. Johnstone, M. Adam, J. R. Hammond and C. Turbide, *J. Biol. Chem.*, 1987, **262**, 9412–9420.
102 D. D. Taylor, C. G. Taylor, C. Jiang and P. H. Black, *Int. J. Cancer*, 1988, **41**, 629–635.
103 G. Raposo, H. W. Nijman, W. Stoorvogel, R. Liejendekker, C. V Harding, C. J. M. Melief and H. J. Geuze, *J. Exp. Med.*, 1996, **183**, 1161–1172.
104 S. J. Gould and G. Raposo, *J. Extracell. Vesicles*, 2013, **2**, 20389.
105 C. Théry *et al.*, *J. Extracell. Vesicles*, 2018, **7**, 1535750.
106 J. Van Deun *et al.*, *Nat. Methods*, 2017, **14**, 228–232.
107 C. Gardiner, D. Di Vizio, S. Sahoo, C. Théry, K. W. Witwer, M. Wauben and A. F. Hill, *J. Extracell. Vesicles*, 2016, **5**, 32945.
108 A. Bobrie, M. Colombo, S. Krumeich, G. Raposo and C. Thery, *J. Extracell. Vesicles*, 2012, **1**, 18397.
109 A. Cvjetkovic, J. Lötvall and C. Lässer, *J. Extracell. Vesicles*, 2014, **3**, 23111.
110 D. D. Taylor, I.-N. Chou and P. H. Black, *Biochem. Biophys. Res. Commun.*, 1983, **113**, 470–476.
111 J. Van Deun, P. Mestdagh, R. Sormunen, V. Cocquyt, K. Vermaelen, J. Vandesompele, M. Bracke, O. De Wever and A. Hendrix, *J. Extracell. Vesicles*, 2014, **3**, 24858.
112 B. J. Tauro, D. W. Greening, R. A. Mathias, H. Ji, S. Mathivanan, A. M. Scott and R. J. Simpson, *Methods*, 2012, **56**, 293–304.
113 A. N. Böing, E. van der Pol, A. E. Grootemaat, F. A. W. Coumans, A. Sturk and R. Nieuwland, *J. Extracell. Vesicles*, , DOI:10.3402/jev.v3.23430.
114 R. Cantin, J. Diou, D. Bélanger, A. M. Tremblay and C. Gilbert, *J. Immunol. Methods*, 2008, **338**, 21–30.

115 R. Vogel *et al.*, *J. Extracell. Vesicles*, 2016, **5**, 31242.
116 Z. Varga, Y. Yuana, A. E. Grootemaat, E. van der Pol, C. Gollwitzer, M. Krumrey and R. Nieuwland, *J. Extracell. Vesicles*, 2014, **3**, 23298.
117 R. Crescitelli, C. Lässer, T. G. Szabó, A. Kittel, M. Eldh, I. Dianzani, E. I. Buzás and J. Lötvall, *J. Extracell. Vesicles*, 2013, **2**, 20677.
118 E. van der Pol, F. A. W. Coumans, A. E. Grootemaat, C. Gardiner, I. L. Sargent, P. Harrison, A. Sturk, T. G. van Leeuwen and R. Nieuwland, *J. Thromb. Haemost.*, 2014, **12**, 1182–1192.
119 Y. Yuana, R. I. Koning, M. E. Kuil, P. C. N. Rensen, A. J. Koster, R. M. Bertina and S. Osanto, *J. Extracell. Vesicles*, 2013, **2**, 21494.
120 T. Kanno, T. Yamada, H. Iwabuki, H. Tanaka, S. I. Kuroda, K. Tanizawa and T. Kawai, *Anal. Biochem.*, 2002, **309**, 196–199.
121 S. Sharma, H. I. Rasool, V. Palanisamy, C. Mathisen, M. Schmidt, D. T. Wong and J. K. Gimzewski, *ACS Nano*, 2010, **4**, 1921–1926.
122 Y. Yuana, T. H. Oosterkamp, S. Bahatyrova, B. Ashcroft, P. Garcia Rodriguez, R. M. Bertina and S. Osanto, *J. Thromb. Haemost.*, 2010, **8**, 315–323.
123 J. Hardij, F. Cecchet, A. Berquand, D. Gheldof, C. Chatelain, F. Mullier, B. Chatelain and J. M. Dogné, *J. Extracell. Vesicles*, 2013, **2**, 21045.
124 P. Parisse, I. Rago, L. Ulloa Severino, F. Perissinotto, E. Ambrosetti, P. Paoletti, M. Ricci, A. P. Beltrami, D. Cesselli and L. Casalis, *Eur. Biophys. J.*, 2017, **46**, 813–820.
125 B. Whitehead, L. Wu, M. L. Hvam, H. Aslan, M. Dong, L. Dyrskjøt, M. S. Ostenfeld, S. M. Moghimi and K. A. Howard, *J. Extracell. Vesicles*, 2015, **4**, 29685.
126 F. Royo, D. Gil-Carton, E. Gonzalez, J. Mleczko, L. Palomo, M. Perez-Cormenzana, R. Mayo, C. Alonso and J. M. Falcon-Perez, *J. Extracell. Vesicles*, 2019, **8**, 1575678.
127 A. S. Lawrie, A. Albanyan, R. A. Cardigan, I. J. Mackie and P. Harrison, *Vox Sang.*, 2009, **96**, 206–212.
128 B. György, K. Módos, É. Pállinger, K. Pálóczi, M. Pásztói, P. Misják, M. A. Deli, Á. Sipos, A. Szalai, I. Voszka, A. Polgár, K. Tóth, M. Csete, G. Nagy, S. Gay, A. Falus, Á. Kittel and E. I. Buzás, *Blood*, 2011, **117**, e39–e48.
129 A. Malloy, *Mater. Today*, 2011, **14**, 170–173.
130 R. A. Dragovic, C. Gardiner, A. S. Brooks, D. S. Tannetta, D. J. P. Ferguson, P. Hole, B. Carr, C. W. G. Redman, A. L. Harris, P. J. Dobson, P. Harrison and I. L. Sargent, *Nanomedicine Nanotechnology, Biol. Med.*, 2011, **7**, 780–788.
131 C. Gardiner, Y. J. Ferreira, R. A. Dragovic, C. W. G. Redman and I. L. Sargent, *J. Extracell. Vesicles*, 2013, **2**, 19671.
132 W. Oosthuyzen, N. E. L. Sime, J. R. Ivy, E. J. Turtle, J. M. Street, J. Pound, L. E. Bath, D. J. Webb, C. D. Gregory, M. A. Bailey and J. W. Dear, *J. Physiol.*, 2013, **591**, 5833–5842.
133 V. Sokolova, A. K. Ludwig, S. Hornung, O. Rotan, P. A. Horn, M. Epple and B. Giebel, *Colloids Surfaces B Biointerfaces*, 2011, **87**, 146–150.
134 S. J. Sowerby, M. F. Broom and G. B. Petersen, *Sensors Actuators B Chem.*, 2007, **123**, 325–330.
135 G. S. Roberts, D. Kozak, W. Anderson, M. F. Broom, R. Vogel and M. Trau, *Small*, 2010, **6**, 2653–2658.
136 G. S. Roberts, S. Yu, Q. Zeng, L. C. L. Chan, W. Anderson, A. H. Colby, M. W. Grinstaff, S. Reid and R. Vogel, *Biosens. Bioelectron.*, 2012, **31**, 17–25.
137 F. A. W. Coumans, E. Van Der Pol, A. N. Bo, N. Hajji, G. Sturk, T. G. van Leeuwen and R. Nieuwland, *J. Extracell. Vesicles*, 2014, **3**, 25922.
138 H. B. Steen, *Cytom. Part A*, 2004, **57A**, 94–99.
139 W. L. Chandler, W. Yeung and J. F. Tait, *J. Thromb. Haemost.*, 2011, **9**, 1216–1224.

140 E. N. M. Nolte-'t Hoen *et al.*, *Biol. Med.*, 2012, **8**, 712–720.
141 J. P. Nolan and S. A. Stoner, *Cytom. Part A*, 2013, **83 A**, 301–305.
142 E. J. van der Vlist, E. N. M. Nolte-'t Hoen, W. Stoorvogel, G. J. A. Arkesteijn and M. H. M. Wauben, *Nat. Protoc.*, 2012, **7**, 1311–1326.
143 A. K. Enjeti, L. Lincz and M. Seldon, *Int. J. Lab. Hematol.*, 2008, **30**, 196–199.
144 A. F. Orozco and D. E. Lewis, *Cytom. Part A*, 2010, **77A**, 502–514.
145 S. E. Headland, H. R. Jones, A. S. V. D'Sa, M. Perretti and L. V. Norling, *Sci. Rep.*, 2014, **4**, 5237.
146 A. E. Morelli, A. T. Larregina, W. J. Shufesky, M. L. G. Sullivan, D. B. Stolz, G. D. Papworth, A. F. Zahorchak, A. J. Logar, Z. Wang, S. C. Watkins, L. D. Falo and A. W. Thomson, *Blood*, 2004, **104**, 3257–66.
147 Y. Takahashi, M. Nishikawa, H. Shinotsuka, Y. Matsui, S. Ohara, T. Imai and Y. Takakura, *J. Biotechnol.*, 2013, **165**, 77–84.
148 M. Morishita, Y. Takahashi, M. Nishikawa, K. Sano, K. Kato, T. Yamashita, T. Imai, H. Saji and Y. Takakura, *J. Pharm. Sci.*, 2015, **104**, 705–713.
149 D. W. Hwang, H. Choi, S. C. Jang, M. Y. Yoo, J. Y. Park, N. E. Choi, H. J. Oh, S. Ha, Y. S. Lee, J. M. Jeong, Y. S. Gho and D. S. Lee, *Sci. Rep.*, 2015, **5**, 15636.
150 T. Smyth, M. Kullberg, N. Malik, P. Smith-Jones, M. W. Graner and T. J. Anchordoquy, *J. Control. Release*, 2015, **199**, 145–155.
151 C. Grange, M. Tapparo, S. Bruno, D. Chatterjee, P. J. Quesenberry, C. Tetta and G. Camussi, *Int. J. Mol. Med.*, 2014, **33**, 1055–1063.
152 C. P. Lai, O. Mardini, M. Ericsson, S. Prabhakar, C. A. Maguire, J. W. Chen, B. A. Tannous and X. O. Breakefield, *ACS Nano*, 2014, **8**, 483–494.
153 S. C. Saunderson, A. C. Dunn, P. R. Crocker and A. D. McLellan, *Blood*, 2014, **123**, 208–216.
154 A. Caivano, I. Laurenzana, L. De Luca, F. La Rocca, V. Simeon, S. Trino, F. D'Auria, A. Traficante, M. Maietti, T. Izzo, G. D'Arena, G. Mansueto, G. Pietrantuono, L. Laurenti, P. Musto and L. Del Vecchio, *Tumor Biol.*, 2015, **36**, 9739–9752.
155 H. Julich-Haertel *et al.*, *J. Hepatol.*, 2017, **67**, 282–292.
156 M. S. Ostenfeld, S. G. Jensen, D. K. Jeppesen, L. Christensen, S. B. Thorsen, J. Stenvang, M. L. Hvam, A. Thomsen, P. Mouritzen, M. H. Rasmussen, H. J. Nielsen, T. F. Ørntoft and C. L. Andersen, *J. Extracell. Vesicles*, 2016, **5**, 31488.
157 S. M. Johnson, C. Dempsey, A. Chadwick, S. Harrison, J. Liu, Y. Di, O. J. Mcginn, M. Fiorillo, F. Sotgia, M. P. Lisanti, M. Parihar, S. Krishnan and V. Saha, *Blood*, 2016, **128**, 453–456.
158 M. A. J. van Eijndhoven *et al.*, *JCI Insight*, 2016, **1**, e89631.
159 T. Aung, B. Chapuy, D. Vogel, D. Wenzel, M. Oppermann, M. Lahmann, T. Weinhage, K. Menck, T. Hupfeld, R. Koch, L. Trumper and G. G. Wulf, *Proc. Natl. Acad. Sci.*, 2011, **108**, 15336–15341.
160 S. R. Krishnan, F. Luk, R. D. Brown, H. Suen, Y. Kwan and M. Bebawy, *Neoplasia*, 2016, **18**, 25–32.
161 T. Sequeiros, M. Rigau *et al.*, *Oncotarget*, 2017, **8**, 4960–4976.
162 K. Allenson *et al.*, *Ann. Oncol.*, 2017, **28**, 741–747.
163 L. Balaj, R. Lessard, L. Dai, Y.-J. Cho, S. L. Pomeroy, X. O. Breakefield and J. Skog, *Nat. Commun.*, 2011, **2**, 180.
164 K. Al-Nedawi, B. Meehan, J. Micallef, V. Lhotak, L. May, A. Guha and J. Rak, *Nat. Cell Biol.*, 2008, **10**, 619–24.
165 A. Zomer, C. Maynard, F. J. Verweij, A. Kamermans, R. Schäfer, E. Beerling, R. M. Schiffelers, E. de Wit, J. Berenguer, S. I. J. Ellenbroek, T. Wurdinger, D. M. Pegtel and J. van Rheenen, *Cell*, 2015, **161**, 1046–1057.

166 D. Di Vizio, J. Kim, M. H. Hager, M. Morello, W. Yang, C. J. Lafargue, L. D. True, M. A. Rubin, R. M. Adam, R. Beroukhim, F. Demichelis and M. R. Freeman, *Cancer Res.*, 2009, **69**, 5601–5609.
167 S. M. Johnson, C. Dempsey, C. Parker, A. Mironov, H. Bradley and V. Saha, *J. Extracell. Vesicles*, 2017, **6**, 1294339.
168 Q. Feng, C. Zhang, D. Lum, J. E. Druso, B. Blank, K. F. Wilson, A. Welm, M. A. Antonyak and R. A. Cerione, *Nat. Commun.*, 2017, **8**, 14450.
169 K. Al-Nedawi, B. Meehan, R. S. Kerbel, A. C. Allison and J. Rak, *Proc. Natl. Acad. Sci.*, 2009, **106**, 3794–99.
170 V. R. Minciacchi, C. Spinelli, M. Reis-Sobreiro, L. Cavallini, S. You, M. Zandian, X. Li, R. Mishra, P. Chiarugi, R. M. Adam, E. M. Posadas, G. Viglietto, M. R. Freeman, E. Cocucci, N. A. Bhowmick and D. Di Vizio, *Cancer Res.*, 2017, **77**, 2306–2317.
171 J. Paggetti, F. Haderk, M. Seiffert, B. Janji, U. Distler, W. Ammerlaan, Y. J. Kim, J. Adam, P. Lichter, G. Berchem, E. Solary and E. Moussay, *Blood*, 2015, **126**, 1106–1118.
172 V. Ciravolo, V. Huber, G. C. Ghedini, E. Venturelli, F. Bianchi, M. Campiglio, D. Morelli, A. Villa, P. Della Mina, S. Menard, P. Filipazzi, L. Rivoltini, E. Tagliabue and S. M. Pupa, *J. Cell. Physiol.*, 2012, **227**, 658–667.
173 C. S. Hong, S. Funk, L. Muller, M. Boyiadzis and T. L. Whiteside, *J. Extracell. Vesicles*, 2016, **5**, 29289.
174 L. Muller, M. Mitsuhashi, P. Simms, W. E. Gooding and T. L. Whiteside, *Sci. Rep.*, 2016, **6**, 20254.
175 D. D. Taylor and C. Gerçel-Taylor, *Br. J. Cancer*, 2005, **92**, 305–311.
176 V. Huber, S. Fais, M. Iero, L. Lugini, P. Canese, P. Squarcina, A. Zaccheddu, M. Colone, G. Arancia, M. Gentile, E. Seregni, R. Valenti, G. Ballabio, F. Belli, E. Leo, G. Parmiani and L. Rivoltini, *Gastroenterology*, 2005, **128**, 1796–804.
177 M. Baj-Krzyworzeka, R. Szatanek, K. Weglarczyk, J. Baran, B. Urbanowicz, P. Brański, M. Z. Ratajczak and M. Zembala, *Cancer Immunol. Immunother.*, 2006, **55**, 808–18.
178 K. E. Richards, A. E. Zeleniak, M. L. Fishel, J. Wu, L. E. Littlepage and R. Hill, *Oncogene*, 2017, **36**, 1770–1778.
179 P. Zheng, L. Chen, X. Yuan, Q. Luo, Y. Liu, G. Xie, Y. Ma and L. Shen, *J. Exp. Clin. Cancer Res.*, 2017, **36**, 53.
180 J. L. Hood, S. San Roman and S. A. Wickline, *Cancer Res.*, 2011, **71**, 3792–3801.
181 H. Peinado *et al.*, *Nat. Med.*, 2012, **18**, 883–91.
182 B. Costa-Silva *et al.*, *Nat. Cell Biol.*, 2015, **17**, 816–826.
183 A. Hoshino *et al.*, *Nature*, 2015, **527**, 329–35.
184 V. Muralidharan-Chari, J. Clancy, C. Plou, M. Romao, P. Chavrier, G. Raposo and C. D'Souza-Schorey, *Curr. Biol.*, 2009, **19**, 1875–85.
185 T. Wang, K. Ning, T. Lu, X. Sun, L. Jin, X. Qi, J. Jin and D. Hua, *Cancer Sci.*, 2017, **108**, 448–454.
186 E. Ferretti, C. Tripodo, G. Pagnan, C. Guarnotta, D. Marimpietri, M. V Corrias, D. Ribatti, S. Zupo, G. Fraternali-Orcioni, J. L. Ravetti, V. Pistoia and A. Corcione, *Leukemia*, 2015, **29**, 958–967.
187 C. Tucher, K. Bode, P. Schiller, L. Claßen, C. Birr, M. M. Souto-Carneiro, N. Blank, H. M. Lorenz and M. Schiller, *Front. Immunol.*, 2018, **9**, 534.
188 C. Théry, M. Boussac, P. Véron, P. Ricciardi-Castagnoli, G. Raposo, J. Garin and S. Amigorena, *J. Immunol.*, 2001, **166**, 7309–7318.
189 A. F. Orozco, C. J. Jorgez, C. Horne, D. A. Marquez-Do, M. R. Chapman, J. R. Rodgers, F. Z. Bischoff and D. E. Lewis, *Am. J. Pathol.*, 2008, **173**, 1595–1608.
190 C. Gao, R. Li, Y. Liu, L. Ma and S. Wang, *J. Trauma Acute Care Surg.*, 2012, **73**, 1152–

1160.
191 R. O. Bilyy, T. Shkandina, A. Tomin, L. E. Muñoz, S. Franz, V. Antonyuk, Y. Y. Kit, M. Zirngibl, B. G. Fürnrohr, C. Janko, K. Lauber, M. Schiller, G. Schett, R. S. Stoika and M. Herrmann, *J. Biol. Chem.*, 2012, **287**, 496–503.
192 M. Zirngibl, B. G. Fürnrohr, C. Janko, L. E. Munoz, R. E. Voll, C. D. Gregory, G. Schett and M. Herrmann, *Clin. Exp. Immunol.*, 2015, **179**, 39–49.
193 M. Ainola, P. Porola, Y. Takakubo, B. Przybyla, V. P. Kouri, T. A. Tolvanen, A. Hänninen and D. C. Nordström, *Clin. Exp. Immunol.*, 2018, **191**, 301–310.
194 A. Niessen, P. Heyder, S. Krienke, N. Blank, L.-O. Tykocinski, H.-M. Lorenz and M. Schiller, *J. Cell Sci.*, 2015, **128**, 2443–2453.
195 E. E. Torr, D. H. Gardner, L. Thomas, D. M. Goodall, A. Bielemeier, R. Willetts, H. R. Griffiths, L. J. Marshall and A. Devitt, *Cell Death Differ.*, 2012, **19**, 671–679.
196 M. L. Litvack, M. Post and N. Palaniyar, *PLoS One*, 2011, **6**, e17223.
197 L. Mutschelknaus, O. Azimzadeh, T. Heider, K. Winkler, M. Vetter, R. Kell, S. Tapio, J. Merl-Pham, S. M. Huber, L. Edalat, V. Radulović, N. Anastasov, M. J. Atkinson and S. Moertl, *Sci. Rep.*, 2017, **7**, 12423.
198 E. Smith and G. Dent, *Modern Raman Spectroscopy: A Practical Approach*, John Wiley & Sons, Ltd, 2005.
199 E. Brauchle, S. Thude, S. Y. Brucker and K. Schenke-Layland, *Sci. Rep.*, , DOI:10.1038/srep04698.
200 G. Pyrgiotakis, O. E. Kundakcioglu, K. Finton, P. M. Pardalos, K. Powers and B. M. Moudgil, *Ann. Biomed. Eng.*, 2009, **37**, 1464–1473.
201 E. Brauchle, S. Noor, E. Holtorf, C. Garbe, K. Schenke-Layland and C. Busch, *Clin. Exp. Dermatol.*, 2014, **39**, 636–645.
202 Y. Oshima, H. Shinzawa, T. Takenaka, C. Furihata and H. Sato, *J. Biomed. Opt.*, 2010, **15**, 017009.
203 S. M. Ali, F. Bonnier, A. Tfayli, H. Lambkin, K. Flynn, V. McDonagh, C. Healy, T. C. Lee, F. M. Lyng and H. J. Byrne, *J. Biomed. Opt.*, 2013, **18**, 061202.
204 N. Uzunbajakava, A. Lenferink, Y. Kraan, B. Willekens, G. Vrensen, J. Greve and C. Otto, *Biopolymers*, 2003, **72**, 1–9.
205 N. Uzunbajakava, A. Lenferink, Y. Kraan, E. Volokhina, G. Vrensen, J. Greve and C. Otto, *Biophys. J.*, 2003, **84**, 3968–3981.
206 M. Okada, N. I. Smith, A. F. Palonpon, H. Endo, S. Kawata, M. Sodeoka and K. Fujita, *Proc. Natl. Acad. Sci.*, 2012, **109**, 28–32.
207 I. Notingher, C. Green, C. Dyer, E. Perkins, N. Hopkins, C. Lindsay and L. L. Hench, *J. R. Soc. Interface*, 2004, **1**, 79–90.
208 D. A. Watson, L. O. Brown, D. F. Gaskill, M. Naivar, S. W. Graves, S. K. Doorn and J. P. Nolan, *Cytom. Part A*, 2008, **73**, 119–128.
209 R. Thurn and W. Kiefer, *Appl. Spectrosc.*, 1984, **38**, 78–83.
210 C. Xie, M. A. Dinno and Y. Li, *Opt. Lett.*, 2002, **27**, 249–251.
211 S. Casabella, P. Scully, N. Goddard and P. Gardner, *Analyst*, 2016, **141**, 689–696.
212 J. W. Chan, D. S. Taylor and D. L. Thompson, *Biopolymers*, 2009, **91**, 132–139.
213 S. Dochow, C. Krafft, U. Neugebauer, T. Bocklitz, T. Henkel, G. Mayer, J. Albert and J. Popp, *Lab Chip*, 2011, **11**, 1484–1490.
214 T. J. Moritz, D. S. Taylor, D. M. Krol, J. Fritch and J. W. Chan, *Biomed. Opt. Express*, 2010, **1**, 1138–1147.
215 H. Yao, Z. Tao, M. Ai, L. Peng, G. Wang, B. He and Y. qing Li, *Vib. Spectrosc.*, 2009, **50**, 193–197.
216 P. Mao, J. J. Wyrick, S. A. Roberts and M. J. Smerdon, *Photochem. Photobiol.*, 2017, **93**, 216–228.

217 G. J. Puppels, J. H. F. Olminkhof, G. M. J. Segers-Nolten, C. Otto, F. F. M. de Mul and J. Greve, *Exp. Cell Res.*, 1991, **195**, 361–367.
218 V. V. Pully, A. T. M. Lenferink and C. Otto, *J. Raman Spectrosc.*, 2011, **42**, 167–173.
219 E. Ó Faoláin, M. B. Hunter, J. M. Byrne, P. Kelehan, M. McNamara, H. J. Byrne and F. M. Lyng, *Vib. Spectrosc.*, 2005, **38**, 121–127.
220 B. Brozek-Pluska, J. Musial, R. Kordek, E. Bailo, T. Dieing and H. Abramczyk, *Analyst*, 2012, **137**, 3773–3780.
221 M. M. Mariani, P. Lampen, J. Popp, B. R. Wood and V. Deckert, *Analyst*, 2009, **134**, 1154–1161.
222 A. D. Meade, C. Clarke, F. Draux, G. D. Sockalingum, M. Manfait, F. M. Lyng and H. J. Byrne, *Anal. Bioanal. Chem.*, 2010, **396**, 1781–1791.
223 I. W. Schie, L. Alber, A. L. Gryshuk and J. W. Chan, *Analyst*, 2014, **139**, 2726–2733.
224 I. W. Schie and J. W. Chan, *J. Raman Spectrosc.*, 2016, **47**, 384–390.
225 I. W. Schie, R. Kiselev, C. Krafft and J. Popp, *Analyst*, 2016, **141**, 6387–6395.
226 I. Notingher, S. Verrier, S. Haque, J. M. Polak and L. L. Hench, *Biopolymers*, 2003, **72**, 230–240.
227 F. Bonnier and H. J. Byrne, *Analyst*, 2012, **137**, 322–332.
228 D. Tsikritsis, S. Richmond, P. Stewart, A. Elfick and A. Downes, *Analyst*, 2015, **140**, 5162–5168.
229 I. Notingher, G. Jell, P. L. Notingher, I. Bisson, O. Tsigkou, J. M. Polak, M. M. Stevens and L. L. Hench, *J. Mol. Struct.*, 2005, **744**–**747**, 179–185.
230 J. Gala de Pablo, F. J. Armistead, S. A. Peyman, D. Bonthron, M. Lones, S. Smith and S. D. Evans, *J. Raman Spectrosc.*, 2018, 1–10.
231 X. Li, T. Yang and S. Li, *Appl. Opt.*, 2012, **51**, 5038–5043.
232 U. Neugebauer, J. H. Clement, T. Bocklitz, C. Krafft and J. Popp, *J. Biophotonics*, 2010, **3**, 579–587.
233 U. Neugebauer, T. Bocklitz, J. H. Clement, C. Krafft and J. Popp, *Analyst*, 2010, **135**, 3178–3182.
234 A. Zoladek, F. C. Pascut, P. Patel and I. Notingher, *J. Raman Spectrosc.*, 2011, **42**, 251–258.
235 S. Hu, I. K. Morris, J. P. Singh, K. M. Smith and T. G. Spiro, *J. Am. Chem. Soc.*, 1993, **115**, 12446–12458.
236 S. Verrier, I. Notingher, J. M. Polak and L. L. Hench, *Biopolymers*, 2004, **74**, 157–162.
237 C. A. Owen, J. Selvakumaran, I. Notingher, G. Jell, L. L. Hench and M. M. Stevens, *J. Cell. Biochem.*, 2006, **99**, 178–186.
238 I. Notingher, J. Selvakumaran and L. L. Hench, *Biosens. Bioelectron.*, 2004, **20**, 780–789.
239 Y. H. Ong, M. Lim and Q. Liu, *Opt. Express*, 2012, **20**, 22158–22171.
240 D. Lin, J. Lin, Y. Wu, S. Feng, Y. Li, Y. Yu, G. Xi, H. Zeng and R. Chen, *Spectroscopy*, 2011, **25**, 23–32.
241 S. Caponi, L. Liguori, A. Giugliarelli, M. Mattarelli, A. Morresi, P. Sassi, L. Urbanelli and C. Musio, *Biophys. Chem.*, 2013, **182**, 58–63.
242 M. Fleischmann, P. J. Hendra and A. J. McQuillan, *Chem. Phys. Lett.*, 1974, **26**, 163–166.
243 M. G. Albrecht and J. A. Creighton, *J. Am. Chem. Soc.*, 1977, **99**, 5215–5217.
244 M. R. Philpott, *J. Chem. Phys.*, 1975, **62**, 1812–1817.
245 J. R. Lombardi, R. L. Birke, T. Lu and J. Xu, *J. Chem. Phys.*, 1986, **84**, 4174–4180.
246 H. Xu, J. Aizpurua, M. Käll and P. Apell, *Phys. Rev. E - Stat. Physics, Plasmas, Fluids, Relat. Interdiscip. Top.*, 2000, **62**, 4318–4324.
247 K. H. Su, Q. H. Wei, X. Zhang, J. J. Mock, D. R. Smith and S. Schultz, *Nano Lett.*, 2003,

3, 1087–1090.
248 X. Qian, S. R. Emory and S. Nie, *J. Am. Chem. Soc.*, 2012, **134**, 2000–2003.
249 G. McAnally, C. McLaughlin, R. Brown, D. C. Robson, K. Faulds, D. R. Tackley, W. E. Smith and D. Graham, *Analyst*, 2002, **127**, 838–841.
250 C. J. McHugh, F. T. Docherty, D. Graham and W. E. Smith, *Analyst*, 2004, **129**, 69–72.
251 A. Enright, L. Fruk, A. Grondin, C. J. McHugh, W. E. Smith and D. Graham, *Analyst*, 2004, **129**, 975–978.
252 A. Barhoumi, D. Zhang, F. Tam and N. J. Halas, *J. Am. Chem. Soc.*, 2008, **130**, 5523–9.
253 K. Kneipp, Y. Wang, H. Kneipp, L. T. Perelman, I. Itzkan, R. R. Dasari and M. S. Feld, *Phys. Rev. Lett.*, 1997, **78**, 1667–1670.
254 S. Nie and S. R. Emory, *Science (80-.).*, 1997, **275**, 1102–1106.
255 A. Chou, E. Jaatinen, R. Buividas, G. Seniutinas, S. Juodkazis, E. L. Izake and P. M. Fredericks, *Nanoscale*, 2012, **4**, 7419.
256 O. Alharbi, Y. Xu and R. Goodacre, *Analyst*, 2015, **140**, 5965–5970.
257 A. Jaworska, L. E. Jamieson, K. Malek, C. J. Campbell, J. Choo, S. Chlopicki and M. Baranska, *Analyst*, 2015, **140**, 2321–2329.
258 L. E. Jamieson, A. Jaworska, J. Jiang, M. Baranska, D. J. Harrison and C. J. Campbell, *Analyst*, 2015, **140**, 2330–2335.
259 S. P. Ravindranath, Y. Wang and J. Irudayaraj, *Sensors Actuators B*, 2011, **152**, 183–190.
260 D. Cam, K. Keseroglu, M. Kahraman, F. Sahin and M. Culha, *J. Raman Spectrosc.*, 2010, **41**, 484–489.
261 K. Kneipp, A. S. Haka, H. Kneipp, K. Badizadegan, N. Yoshizawa, C. Boone, K. E. Shafer-Peltier, J. T. Motz, R. R. Dasari and M. S. Feld, *App. Spectrosc.*, 2002, **56**, 150–154.
262 D. Craig, S. Mcaughtrie, J. Simpson, C. McCraw, K. Faulds and D. Graham, *Anal. Chem.*, 2014, **86**, 4775–4782.
263 S. McAughtrie, K. Lau, K. Faulds and D. Graham, *Chem. Sci.*, 2013, **4**, 3566–3572.
264 C. M. MacLaughlin, N. Mullaithilaga, G. Yang, S. Y. Ip, C. Wang and G. C. Walker, *Langmuir*, 2013, **29**, 1908–1919.
265 D. A. Watson, D. F. Gaskill, L. O. Brown, S. K. Doorn and J. P. Nolan, *Cytom. Part A*, 2009, **75**, 460–464.
266 D. S. Sebba, D. A. Watson and J. P. Nolan, *ACS Nano*, 2009, **3**, 1477–1484.
267 G. Goddard, L. O. Brown, R. Habbersett, C. I. Brady, J. C. Martin, S. W. Graves, J. P. Freyer and S. K. Doorn, *J. Am. Chem. Soc.*, 2010, **132**, 6081–6090.
268 A. Pallaoro, M. R. Hoonejani, G. B. Braun, C. D. Meinhart and M. Moskovits, *ACS Nano*, 2015, **9**, 4328–4336.
269 N. Y. Kyeong, S. M. Lee, Y. H. Ji, H. Park, M. A. Woo, M. S. Noh, S. K. Hwang, J. T. Kwon, H. Jin, Y. K. Kim, P. J. Hergenrother, H. J. Dae, Y. S. Lee and M. H. Cho, *Bioconjug. Chem.*, 2007, **18**, 1155–1162.
270 Y. Chen, X. Bai, L. Su, Z. Du, A. Shen, A. Materny and J. Hu, *Sci. Rep.*, 2016, **6**, 19173.
271 X. Jiang, Z. Jiang, T. Xu, S. Su, Y. Zhong, F. Peng, Y. Su and Y. He, *Anal. Chem.*, 2013, **85**, 2809–2816.
272 H. Zhou, Q. Wang, D. Yuan, J. Wang, Y. Huang, H. Wu, J. Jian, D. Yang, N. Huang, C. Haisch, Z. Jiang and S. Chen, *Analyst*, 2016, **141**, 4293–4298.
273 J. Zhang, X. Ma and Z. Wang, *Anal. Chem.*, 2019, **91**, 6600–6607.
274 G. Sonavane, K. Tomoda, A. Sano, H. Ohshima, H. Terada and K. Makino, *Colloids Surfaces B Biointerfaces*, 2008, **65**, 1–10.
275 G. Sonavane, K. Tomoda and K. Makino, *Colloids Surfaces B Biointerfaces*, 2008, **66**, 274–280.

276 U. Gaur, S. Kumar Sahoo, T. K. De, P. C. Ghosh, A. Maitra and P. K. Ghosh, *Int. J. Pharm.*, 2000, **202**, 1–10.
277 T. Niidome, M. Yamagata, Y. Okamoto, Y. Akiyama, H. Takahashi, T. Kawano, Y. Katayama and Y. Niidome, *J. Control. release*, 2006, **114**, 343–347.
278 C. L. Zavaleta, B. R. Smith, I. Walton, W. Doering, G. Davis, B. Shojaei, M. J. Natan and S. S. Gambhir, *Proc. Natl. Acad. Sci.*, 2009, **106**, 13511–13516.
279 K. Kumar Maiti, U. S. Dinish, A. Samanta, M. Vendrell, K. Soh, S. Park, M. Olivo and Y. Chang, *Nano Today*, 2012, **7**, 85–93.
280 U. S. Dinish, G. Balasundaram, Y.-T. Chang and M. Olivo, *Sci. Rep.*, 2014, **4**, 4075.
281 X. Niu, H. Chen, Y. Wang, W. Wang, X. Sun and L. Chen, *Appl. Mater. Interfaces*, 2014, **6**, 5152–5160.
282 P. Z. Mcveigh, R. J. Mallia, I. Veilleux and B. C. Wilson, *J. Biomed. Opt.*, 2013, **18**, 046011.
283 C. L. Zavaleta, E. Garai, J. T. C. Liu, S. Sensarn, M. J. Mandella, D. Van de Sompel, S. Friedland, J. Van Dam, C. H. Contag and S. S. Gambhir, *Proc. Natl. Acad. Sci. U. S. A.*, 2013, **110**, E2288-97.
284 E. Garai, S. Sensarn, C. L. Zavaleta, N. O. Loewke, S. Rogalla, M. J. Mandella, S. A. Felt, S. Friedland, J. T. C. Liu, S. S. Gambhir and C. H. Contag, *PLoS One*, 2015, **10**, e0123185.
285 H. Wang, R. J. Grand, A. E. Milner, R. J. Armitage, J. Gordon and C. D. Gregory, *Oncogene*, 1996, **13**, 373–9.
286 J. J. L. P. Voss, C. A. Ford, S. Petrova, L. Melville, M. Paterson, J. D. Pound, P. Holland, B. Giotti, T. C. Freeman and C. D. Gregory, *Cell Death Differ.*, 2017, **24**, 971–983.
287 A. Kauffmann, R. Gentleman and W. Huber, *Bioinformatics*, 2009, **25**, 415–6.
288 M. N. McCall, B. M. Bolstad and R. A. Irizarry, *Biostatistics*, 2010, **11**, 242–253.
289 A. Theocharidis, S. van Dongen, A. J. Enright and T. C. Freeman, *Nat. Protoc.*, 2009, **4**, 1535–1550.
290 T. C. Freeman, L. Goldovsky, M. Brosch, S. Van Dongen, P. Mazière, R. J. Grocock, S. Freilich, J. Thornton and A. J. Enright, *PLoS Comput. Biol.*, 2007, **3**, 2032–2042.
291 L. A. Truman, C. A. Ford, M. Pasikowska, J. D. Pound, S. J. Wilkinson, I. E. Dumitriu, L. Melville, L. A. Melrose, C. A. Ogden, R. Nibbs, G. Graham, C. Combadiere and C. D. Gregory, *Blood*, 2008, **112**, 5026–5036.
292 M. M. Bradford, *Anal. Biochem.*, 1976, **72**, 248–254.
293 A. Devitt, K. G. Parker, C. A. Ogden, C. Oldreive, M. F. Clay, L. A. Melville, C. O. Bellamy, A. Lacy-Hulbert, S. C. Gangloff, S. M. Goyert and C. D. Gregory, *J. Cell Biol.*, 2004, **167**, 1161–1170.
294 J. Turkevich, P. C. Stevenson and J. Hillier, *Discuss. Faraday Soc.*, 1951, **11**, 55–75.
295 C. B. Fox, R. H. Uibel and J. M. Harris, *J. Phys. Chem. B*, 2007, **111**, 11428–11436.
296 I. Tatischeff, E. Larquet, J. M. Falcon-Perez, P.-Y. Turpin and S. G. Kruglik, *J. Extracell. Vesicles*, 2012, **1**, 19179.
297 F. Lavialle, S. Deshayes, F. Gonnet, E. Larquet, S. G. Kruglik, N. Boisset, R. Daniel, A. Alfsen and I. Tatischeff, *Int. J. Pharm.*, 2009, **380**, 206–215.
298 C. Krafft, K. Wilhelm, A. Eremin, S. Nestel, N. von Bubnoff, W. Schultze-Seemann, J. Popp and I. Nazarenko, *Nanomedicine Nanotechnology, Biol. Med.*, 2017, **13**, 835–841.
299 Z. J. Smith, C. Lee, T. Rojalin, R. P. Carney, S. Hazari, A. Knudson, K. Lam, H. Saari, E. L. Ibañez, T. Viitala, T. Laaksonen, M. Yliperttula and S. Wachsmann-Hogiu, *J. Extracell. Vesicles*, 2015, **4**, 28533.
300 A. Gualerzi, S. Niada, C. Giannasi, S. Picciolini, C. Morasso, R. Vanna, V. Rossella, M. Masserini, M. Bedoni, F. Ciceri, M. E. Bernardo, A. T. Brini and F. Gramatica, *Sci. Rep.*,

2017, **7**, 9820.
301 A. Gualerzi, S. A. A. Kooijmans, S. Niada, S. Picciolini, A. T. Brini, G. Camussi and M. Bedoni, *J. Extracell. Vesicles*, 2019, **8**, 1568780.
302 R. P. Carney, S. Hazari, M. Colquhoun, D. Tran, B. Hwang, M. S. Mulligan, J. D. Bryers, E. Girda, G. S. Leiserowitz, Z. J. Smith and K. S. Lam, *Anal. Chem.*, 2017, **89**, 5357–5363.
303 D. D. Dalma-Weiszhausz, J. Warrington, E. Y. Tanimoto and C. G. Miyada, *Methods Enzymol.*, 2006, **410**, 3–28.
304 A. J. Enright and C. A. Ouzounis, *Bioinformatics*, 2001, **17**, 853–854.
305 T. Seya, J. R. Turner and J. P. Atkinson, *J. Exp. Med.*, 1986, **163**, 837–55.
306 S. Meri, B. P. Morgan, A. Davies, R. H. Daniels, M. G. Olavesen and H. Waldmannt, *Immunology*, 1990, **71**, 1–9.
307 J. Dzietczenia, T. Wróbel, G. Mazur, R. Poręba, B. Jaźwiec and K. Kuliczkowski, *Med. Oncol.*, 2010, **27**, 743–746.
308 A. Clayton, C. L. Harris, J. Court, M. D. Mason and B. P. Morgan, *Eur. J. Immunol.*, 2003, **33**, 522–531.
309 S. I. Buschow, B. W. M. van Balkom, M. Aalberts, A. J. R. Heck, M. Wauben and W. Stoorvogel, *Immunol. Cell Biol.*, 2010, **88**, 851–856.
310 J. M. Lehmann, G. Riethmüller and J. P. Johnson, *Proc. Natl. Acad. Sci. U. S. A.*, 1989, **86**, 9891–5.
311 G.-J. Wu, Q. Peng, P. Fu, S.-W. Wang, C.-F. Chiang, D. L. Dillehay and M.-W. H. Wu, *Gene*, 2004, **327**, 201–213.
312 D. Aldovini, F. Demichelis, C. Doglioni, D. Di Vizio, E. Galligioni, S. Brugnara, B. Zeni, C. Griso, C. Pegoraro, M. Zannoni, M. Gariboldi, E. Balladore, D. Mezzanzanica, S. Canevari and M. Barbareschi, *Int. J. Cancer*, 2006, **119**, 1920–1926.
313 M. F. Elshal, S. S. Khan, Y. Takahashi, M. A. Solomon and J. P. J. McCoy, *Blood*, 2005, **106**, 2923–2924.
314 M. F. Elshal, S. S. Khan, N. Raghavachari, Y. Takahashi, J. Barb, J. J. Bailey, P. J. Munson, M. A. Solomon, R. L. Danner and J. P. McCoy, *BMC Immunol.*, 2007, **8**, 29.
315 F. Cavazzini, D. Campioni, L. Ferrari, B. Buldini, M. A. Bardi, B. Michielotto, M. C. Lazzari, M. Ongari, M. Dabusti, G. Daghia, O. Sofritti, G. Basso, F. Lanza and A. Cuneo, *Cytom. Part B Clin. Cytom.*, 2016, **90**, 247–256.
316 I. Lazar, E. Clement, M. Ducoux-Petit, L. Denat, V. Soldan, S. Dauvillier, S. Balor, O. Burlet-Schiltz, L. Larue, C. Muller and L. Nieto, *Pigment Cell Melanoma Res.*, 2015, **28**, 464–475.
317 M. M. Jørgensen, R. Bæk and K. Varming, *J. Extracell. Vesicles*, 2015, **4**, 26048.
318 S. Durinck, Y. Moreau, A. Kasprzyk, S. Davis, B. De Moor, A. Brazma and W. Huber, *Bioinformatics*, 2005, **21**, 3439–3440.
319 A. Clayton, J. Court, H. Navabi, M. Adams, M. D. Mason, J. a. Hobot, G. R. Newman and B. Jasani, *J. Immunol. Methods*, 2001, **247**, 163–174.
320 J. F. Wise, Z. Berkova, R. Mathur, H. Zhu, F. K. Braun, R.-H. Tao, A. L. Sabichi, X. Ao, H. Maeng and F. Samaniego, *Blood*, 2013, **121**, 4729–39.
321 J. M. Escola, M. J. Kleijmeer, W. Stoorvogel, J. M. Griffith, O. Yoshie and H. J. Geuze, *J. Biol. Chem.*, 1998, **273**, 20121–7.
322 D. W. Voehringer, D. L. Hirschberg, J. Xiao, Q. Lu, M. Roederer, C. B. Lock, L. A. Herzenberg, L. Steinman and L. A. Herzenberg, *Proc. Natl. Acad. Sci. U. S. A.*, 2000, **97**, 2680–5.
323 M. Yunta and P. A. Lazo, *Oncogene*, 2003, **22**, 1219–1224.
324 L. Tirinato, F. Gentile, D. Di Mascolo, M. L. Coluccio, G. Das, C. Liberale, S. A. Pullano, G. Perozziello, M. Francardi, A. Accardo, F. De Angelis, P. Candeloro and E. Di

Fabrizio, *Microelectron. Eng.*, 2012, **97**, 337–340.
325 C. Lee, R. P. Carney, S. Hazari, Z. J. Smith, A. Knudson, C. S. Robertson, K. S. Lam and S. Wachsmann-Hogiu, *Nanoscale*, 2015, **7**, 9290–9297.
326 Z. Yan, S. Dutta, Z. Liu, X. Yu, N. Mesgarzadeh, F. Ji, G. Bitan and Y. Xie, *ACS Sensors*, 2019, **4**, 488–497.
327 S. Stremersch, M. Marro, B. Pinchasik, P. Baatsen, A. Hendrix, S. C. De Smedt, P. Loza-Alvarez, A. G. Skirtach, K. Raemdonck and K. Braeckmans, *Small*, 2016, **12**, 3292–3301.
328 J. Carmicheal, C. Hayashi, X. Huang, L. Liu, Y. Lu, A. Krasnoslobodtsev, A. Lushnikov, P. G. Kshirsagar, A. Patel, M. Jain, Y. L. Lyubchenko, Y. Lu, S. K. Batra and S. Kaur, *Nanomedicine Nanotechnology, Biol. Med.*, 2019, **16**, 88–96.
329 C. Lee, R. Carney, K. Lam and J. W. Chan, *J. Raman Spectrosc.*, 2017, **48**, 1771–1776.
330 J. Park, M. Hwang, B. Choi, H. Jeong, J. Jung, H. K. Kin, S. Hong, J. Park and Y. Choi, *Anal. Chem.*, 2017, **89**, 6695–6701.
331 H. Shin, H. Jeong, J. Park, S. Hong and Y. Choi, *ACS Sensors*, 2018, **3**, 2637–2643.
332 L. T. Kerr, L. Gubbins, K. Weiner Gorzel, S. Sharma, M. Kell, L. T. Kerr, L. Gubbins, K. W. Gorzel, S. Sharma, M. Kell, A. Mc Cann and B. M. Hennelly, *Proc SPIE*, 2014, **9129**, 91292Q.
333 Z. Wang, S. Zong, Y. Wang, N. Li, L. Li, J. Lu, Z. Wang, B. Chen and Y. Cui, *Nanoscale*, 2018, **10**, 9053–9062.
334 S. Zong, L. Wang, C. Chen, J. Lu, D. Zhu, Y. Zhang, Z. Wang and Y. Cui, *Anal. Methods*, 2016, **8**, 5001–5008.
335 Y.-F. Tian, C.-F. Ning, F. He, B.-C. Yin and B.-C. Ye, *Analyst*, 2018, **143**, 4915–4922.
336 T.-D. Li, R. Zhang, H. Chen, Z.-P. Huang, X. Ye, H. Wang, A.-M. Deng and J. Kong, *Chem. Sci.*, 2018, **9**, 5372–5382.
337 E. A. Kwizera, R. O'Connor, V. Vinduska, M. Williams, E. R. Butch, S. E. Snyder, X. Chen and X. Huang, *Theranostics*, 2018, **8**, 2722–2738.
338 Y. Wang, M. Salehi, M. Schütz and S. Schlücker, *Chem. Commun.*, 2014, **50**, 2711–2714.
339 S. W. Bishnoi, Y. J. Lin, M. Tibudan, Y. Huang, M. Nakaema, V. Swarup and T. A. Keiderling, *Anal. Chem.*, 2011, **83**, 4053–4060.
340 M. Manimaran and N. R. Jana, *J. Raman Spectrosc.*, 2007, **38**, 1326–1331.
341 P. Zhang, R. Zhang, M. Gao and X. Zhang, *ACS Appl. Mater. Interfaces*, 2014, **6**, 370–376.
342 H. Torul, H. Çiftçi, D. Çetin, Z. Suludere, I. H. Boyacı and U. Tamer, *Anal. Bioanal. Chem.*, 2015, **407**, 8243–8251.
343 P. K. Jain, K. S. Lee, I. H. El-Sayed and M. A. El-Sayed, *J. Phys. Chem. B*, 2006, **110**, 7238–7248.
344 W. Leng and P. J. Vikesland, *Langmuir*, 2014, **30**, 8342–8349.
345 X. Shen, C.-M. Ho and T.-S. Wong, *J. Phys. Chem. B*, 2010, **114**, 5269–5274.
346 C. Seo, D. Jang, J. Chae and S. Shin, *Sci. Rep.*, , DOI:10.1038/s41598-017-00497-x.
347 S. F. Shimobayashi, M. Tsudome and T. Kurimura, *Sci. Rep.*, , DOI:10.1038/s41598-018-35998-w.
348 K. Lee, K. Fraser, B. Ghaddar, K. Yang, E. Kim, L. Balaj, E. A. Chiocca, X. O. Breakefield, H. Lee and R. Weissleder, *ACS Nano*, 2018, **12**, 494–503.
349 J. McKiernan, M. J. Donovan, E. Margolis, A. Partin, B. Carter, G. Brown, P. Torkler, M. Noerholm, J. Skog, N. Shore, G. Andriole, I. Thompson and P. Carroll, *Eur. Urol.*, 2018, **74**, 731–738.

Appendix

Appendix 1 A full description of all of the samples used including GSE accession number and GSM sample name

GSE accession number	GSM sample name	TISSUE TYPE	SAMPLE TYPE	CELL TYPE	CELL CLASS	DISEASE STATE	IMMUNE STATUS	EBV STATUS
46062	GSM1122702_1_Bcells	WHOLE BLOOD	PBMC	PBMC	-	HEALTHY	IC	NEG
	GSM1122703_2_Bcells	WHOLE BLOOD	PBMC	PBMC	-	HEALTHY	IC	NEG
	GSM1122704_3_Bcells	WHOLE BLOOD	PBMC	PBMC	-	HEALTHY	IC	NEG
	GSM1122705_4_Bcells	WHOLE BLOOD	PBMC	PBMC	-	HEALTHY	IC	NEG
	GSM1122706_5_Bcells	WHOLE BLOOD	PBMC	PBMC	-	HEALTHY	IC	NEG
58208	GSM1403331_NOR-PBMC-01	WHOLE BLOOD	PBMC	PBMC	-	HEALTHY	IC	NEG
	GSM1403333_NOR-PBMC-03	WHOLE BLOOD	PBMC	PBMC	-	HEALTHY	IC	NEG
	GSM1403334_NOR-PBMC-04	WHOLE BLOOD	PBMC	PBMC	-	HEALTHY	IC	NEG
	GSM1403335_NOR-PBMC-05	WHOLE BLOOD	PBMC	PBMC	-	HEALTHY	IC	NEG
64028	GSM1563084_IgMIgDCD27_1	WHOLE BLOOD	PBMC	B CELL	IgM+ IgD+ CD27+	HEALTHY	IC	NEG
	GSM1563085_IgMIgDCD27_2	WHOLE BLOOD	PBMC	B CELL	IgM+ IgD+ CD27+	HEALTHY	IC	NEG
	GSM1563086_IgMIgDCD27_3	WHOLE BLOOD	PBMC	B CELL	IgM+ IgD+ CD27+	HEALTHY	IC	NEG
	GSM1563087_IgMIgDCD27_4	WHOLE BLOOD	PBMC	B CELL	IgM+ IgD+ CD27+	HEALTHY	IC	NEG
	GSM1563088_IgMIgDCD27_5	WHOLE BLOOD	PBMC	B CELL	IgM+ IgD+ CD27+	HEALTHY	IC	NEG
	GSM1563089_CSW1	WHOLE BLOOD	PBMC	B CELL	CLASS SWITCHED	HEALTHY	IC	NEG
	GSM1563090_CSW2	WHOLE BLOOD	PBMC	B CELL	CLASS SWITCHED	HEALTHY	IC	NEG
	GSM1563091_CSW3	WHOLE BLOOD	PBMC	B CELL	CLASS SWITCHED	HEALTHY	IC	NEG
	GSM1563092_CSW4	WHOLE BLOOD	PBMC	B CELL	CLASS SWITCHED	HEALTHY	IC	NEG
	GSM1563093_CSW5	WHOLE BLOOD	PBMC	B CELL	CLASS SWITCHED	HEALTHY	IC	NEG
	GSM1563094_IgMonly1	WHOLE BLOOD	PBMC	B CELL	IgM+ IgD- CD27+	HEALTHY	IC	NEG
	GSM1563095_IgMonly2	WHOLE BLOOD	PBMC	B CELL	IgM+ IgD- CD27+	HEALTHY	IC	NEG

	GSM1563096_IgMonly3	WHOLE BLOOD	PBMC	B CELL	IgM+ IgD- CD27+	HEALTHY	IC	NEG
	GSM1563098_IgMonly5	WHOLE BLOOD	PBMC	B CELL	IgM+ IgD- CD27+	HEALTHY	IC	NEG
	GSM1563099_naive1	WHOLE BLOOD	PBMC	B CELL	IgM+ IgD+ CD27-	HEALTHY	IC	NEG
	GSM1563100_naive2	WHOLE BLOOD	PBMC	B CELL	IgM+ IgD+ CD27-	HEALTHY	IC	NEG
10831	GSM273221	TONSIL	MONONUCLEAR CELLS	B CELL (GC)	CD10+	HEALTHY	IC	NEG
	GSM273227	TONSIL	MONONUCLEAR CELLS	B CELL (GC)	CD10+	HEALTHY	IC	NEG
	GSM273228	TONSIL	MONONUCLEAR CELLS	B CELL (GC)	CD10+	HEALTHY	IC	NEG
12366	GSM310429	TONSIL	MONONUCLEAR CELLS	B CELL (GC)	CD19+ CD38++ IgD-	HEALTHY	IC	NEG
	GSM310430	TONSIL	MONONUCLEAR CELLS	B CELL (GC)	CD19+ CD38++ IgD-	HEALTHY	IC	NEG
	GSM310431	TONSIL	MONONUCLEAR CELLS	B CELL (GC)	CD19+ CD38++ IgD-	HEALTHY	IC	NEG
	GSM310432	WHOLE BLOOD	PBMC	B CELL (NAIVE)	CD19+ CD27+	HEALTHY	IC	NEG
	GSM310433	WHOLE BLOOD	PBMC	B CELL (NAIVE)	CD19+ CD27+	HEALTHY	IC	NEG
	GSM310434	WHOLE BLOOD	PBMC	B CELL (NAIVE)	CD19+ CD27+	HEALTHY	IC	NEG
	GSM310435	TONSIL	MONONUCLEAR CELLS	B CELL (GC NAÏVE)	CD19+ CD38- IgD+	HEALTHY	IC	NEG
	GSM310436	TONSIL	MONONUCLEAR CELLS	B CELL (GC NAÏVE)	CD19+ CD38- IgD+	HEALTHY	IC	NEG
	GSM310437	TONSIL	MONONUCLEAR CELLS	B CELL (GC NAÏVE)	CD19+ CD38- IgD+	HEALTHY	IC	NEG
	GSM310438	WHOLE BLOOD	PBMC	B CELL (MEMORY)	CD19+ CD27-	HEALTHY	IC	NEG
	GSM310439	WHOLE BLOOD	PBMC	B CELL (MEMORY)	CD19+ CD27-	HEALTHY	IC	NEG
	GSM310440	WHOLE BLOOD	PBMC	B CELL (MEMORY)	CD19+ CD27-	HEALTHY	IC	NEG
17186	GSM422305	WHOLE BLOOD	PBMC	B CELL (NAÏVE)	CD20+ CD10- CD27-	HEALTHY	IC	NEG
	GSM422295	WHOLE BLOOD	PBMC	B CELL (NAÏVE)	CD20+ CD10- CD27-	HEALTHY	IC	NEG
	GSM422294	WHOLE BLOOD	PBMC	B CELL (NAÏVE)	CD20+ CD10- CD27+	HEALTHY	IC	NEG

	GSM422304	WHOLE BLOOD	PBMC	B CELL (MEMORY)	CD20+ CD10- CD27+	HEALTHY	IC	NEG
	GSM422296	WHOLE BLOOD	PBMC	B CELL (TRANSITIONAL)	CD20+ CD10+ CD27- CD21LO	HEALTHY	IC	NEG
	GSM422306	WHOLE BLOOD	PBMC	B CELL (TRANSITIONAL)	CD20+ CD10+ CD27- CD21LO	HEALTHY	IC	NEG
	GSM422307	WHOLE BLOOD	PBMC	B CELL (TRANSITIONAL)	CD20+ CD10+ CD27- CD21HI	HEALTHY	IC	NEG
	GSM422297	WHOLE BLOOD	PBMC	B CELL (TRANSITIONAL)	CD20+ CD10+ CD27- CD21HI	HEALTHY	IC	NEG
	GSM422299	CORD BLOOD	-	B CELL (TRANSITIONAL)	CD20+ CD10+ CD27- CD21LO	HEALTHY	IC	NEG
	GSM422302	CORD BLOOD	-	B CELL (TRANSITIONAL)	CD20+ CD10+ CD27- CD21LO	HEALTHY	IC	NEG
	GSM422300	CORD BLOOD	-	B CELL (TRANSITIONAL)	CD20+ CD10+ CD27- CD21HI	HEALTHY	IC	NEG
	GSM422303	CORD BLOOD	-	B CELL (TRANSITIONAL)	CD20+ CD10+ CD27- CD21HI	HEALTHY	IC	NEG
	GSM422301	CORD BLOOD	-	B CELL (NAÏVE)	CD20+ CD10- CD27-	HEALTHY	IC	NEG
17269	GSM432521_HD-naive-1	WHOLE BLOOD	PBMC	B CELL (NAÏVE)	CD19+ CD27- CD38+ CD21+	HEALTHY	IC	NEG
	GSM432522_HD-naive-2	WHOLE BLOOD	PBMC	B CELL (NAÏVE)	CD19+ CD27- CD38+ CD21+	HEALTHY	IC	NEG
	GSM432523_HD-naive-3	WHOLE BLOOD	PBMC	B CELL (NAÏVE)	CD19+ CD27- CD38+ CD21+	HEALTHY	IC	NEG
19599	GSM488973	BONE MARROW	-	B CELL (IMMATURE)	CD19+ CD34- CD10LO CD20++	HEALTHY	IC	NEG
	GSM488978	BONE MARROW	-	B CELL (PRE-B)	CD19+ CD34- CD10+ CD20LO	HEALTHY	IC	NEG
	GSM488979	BONE MARROW	-	B CELL (PRE-B)	CD19+ CD34- CD10+ CD20LO	HEALTHY	IC	NEG
	GSM488980	BONE MARROW	-	B CELL (PRO-B)	CD19+ CD34+ CD10+	HEALTHY	IC	NEG
	GSM488981	BONE MARROW	-	B CELL (PRO-B)	CD19+ CD34+ CD10+	HEALTHY	IC	NEG
26725	GSM658010_C106	WHOLE BLOOD	PBMC	B CELL	CD19+	HEALTHY	IC	NEG

	GSM658011_C103	WHOLE BLOOD	PBMC	B CELL	CD19+	HEALTHY	IC	NEG
	GSM658012_C107	WHOLE BLOOD	PBMC	B CELL	CD19+	HEALTHY	IC	NEG
	GSM658013_C105	WHOLE BLOOD	PBMC	B CELL	CD19+	HEALTHY	IC	NEG
	GSM658014_C104	WHOLE BLOOD	PBMC	B CELL	CD19+	HEALTHY	IC	NEG
28491	GSM705402_B_03_08_10	WHOLE BLOOD	PBMC	B CELL	CD19+	HEALTHY	IC	NEG
	GSM705403_B_05_08_10	WHOLE BLOOD	PBMC	B CELL	CD19+	HEALTHY	IC	NEG
	GSM705404_B_07_07_10	WHOLE BLOOD	PBMC	B CELL	CD19+	HEALTHY	IC	NEG
	GSM705405_B_23_07_10	WHOLE BLOOD	PBMC	B CELL	CD19+	HEALTHY	IC	NEG
	GSM705406_B_27_07_10	WHOLE BLOOD	PBMC	B CELL	CD19+	HEALTHY	IC	NEG
36907	GSM905504_CD5_1	WHOLE BLOOD	PBMC	B CELL (MATURE)	CD5+	HEALTHY	IC	NEG
	GSM905505_CD5_2	WHOLE BLOOD	PBMC	B CELL (MATURE)	CD5+	HEALTHY	IC	NEG
	GSM905506_CD5_3	WHOLE BLOOD	PBMC	B CELL (MATURE)	CD5+	HEALTHY	IC	NEG
	GSM905507_CD5_4	WHOLE BLOOD	PBMC	B CELL (MATURE)	CD5+	HEALTHY	IC	NEG
	GSM905508_CD5_5	WHOLE BLOOD	PBMC	B CELL (MATURE)	CD5+	HEALTHY	IC	NEG
	GSM905509_class_switched_1	WHOLE BLOOD	PBMC	B CELL (CLASS SWITCHED)	IgG/A+ CD27+	HEALTHY	IC	NEG
	GSM905510_class_switched_2	WHOLE BLOOD	PBMC	B CELL (CLASS SWITCHED)	IgG/A+ CD27+	HEALTHY	IC	NEG
	GSM905512_class_switched_3	WHOLE BLOOD	PBMC	B CELL (CLASS SWITCHED)	IgG/A+ CD27+	HEALTHY	IC	NEG
	GSM905514_class_switched_5	WHOLE BLOOD	PBMC	B CELL (CLASS SWITCHED)	IgG/A+ CD27+	HEALTHY	IC	NEG
	GSM905517_class_switched_6	WHOLE BLOOD	PBMC	B CELL (CLASS SWITCHED)	IgG/A+ CD27+	HEALTHY	IC	NEG
	GSM905518_class_switched_7	WHOLE BLOOD	PBMC	B CELL (CLASS SWITCHED)	IgG/A+ CD27+	HEALTHY	IC	NEG
	GSM905515_MD27_6	WHOLE BLOOD	PBMC	B CELL	IgM+ IgD+ CD27+	HEALTHY	IC	NEG
	GSM905516_MD27_7	WHOLE BLOOD	PBMC	B CELL	IgM+ IgD+ CD27+	HEALTHY	IC	NEG
	GSM905525_MD27_1	WHOLE BLOOD	PBMC	B CELL	IgM+ IgD+ CD27+	HEALTHY	IC	NEG
	GSM905526_MD27_2	WHOLE BLOOD	PBMC	B CELL	IgM+ IgD+ CD27+	HEALTHY	IC	NEG
	GSM905527_MD27_3	WHOLE BLOOD	PBMC	B CELL	IgM+ IgD+ CD27+	HEALTHY	IC	NEG

	GSM905528_MD27_4	WHOLE BLOOD	PBMC	B CELL	IgM+ IgD+ CD27+	HEALTHY	IC	NEG
	GSM905529_MD27_5	WHOLE BLOOD	PBMC	B CELL	IgM+ IgD+ CD27+	HEALTHY	IC	NEG
	GSM905519_IgM-only_1	WHOLE BLOOD	PBMC	B CELL	IgM+ IgDLO CD27+	HEALTHY	IC	NEG
	GSM905520_IgM-only_2	WHOLE BLOOD	PBMC	B CELL	IgM+ IgDLO CD27+	HEALTHY	IC	NEG
	GSM905521_IgM-only_3	WHOLE BLOOD	PBMC	B CELL	IgM+ IgDLO CD27+	HEALTHY	IC	NEG
	GSM905523_IgM-only_4	WHOLE BLOOD	PBMC	B CELL	IgM+ IgDLO CD27+	HEALTHY	IC	NEG
	GSM905524_IgM-only_5	WHOLE BLOOD	PBMC	B CELL	IgM+ IgDLO CD27+	HEALTHY	IC	NEG
	GSM905530_MGZ_1	WHOLE BLOOD	PBMC	B CELL (SPLENIC)	IgM+ CD27+ CD21HI	HEALTHY	IC	NEG
	GSM905532_MGZ_3	WHOLE BLOOD	PBMC	B CELL (SPLENIC)	IgM+ CD27+ CD21HI	HEALTHY	IC	NEG
	GSM905534_MGZ_4	WHOLE BLOOD	PBMC	B CELL (SPLENIC)	IgM+ CD27+ CD21HI	HEALTHY	IC	NEG
	GSM905535_MGZ_5	WHOLE BLOOD	PBMC	B CELL (SPLENIC)	IgM+ CD27+ CD21HI	HEALTHY	IC	NEG
	GSM905537_naive_1	WHOLE BLOOD	PBMC	B CELL (NAÏVE)	IgD+ CD27-	HEALTHY	IC	NEG
	GSM905538_naive_2	WHOLE BLOOD	PBMC	B CELL (NAÏVE)	IgD+ CD27-	HEALTHY	IC	NEG
	GSM905539_naive_3	WHOLE BLOOD	PBMC	B CELL (NAÏVE)	IgD+ CD27-	HEALTHY	IC	NEG
	GSM905540_naive_7	WHOLE BLOOD	PBMC	B CELL (NAÏVE)	IgD+ CD27-	HEALTHY	IC	NEG
	GSM905541_naive_4	WHOLE BLOOD	PBMC	B CELL (NAÏVE)	IgD+ CD27-	HEALTHY	IC	NEG
	GSM905542_naive_5	WHOLE BLOOD	PBMC	B CELL (NAÏVE)	IgD+ CD27-	HEALTHY	IC	NEG
38697	GSM947665_HSLZ_1	TONSIL	LIGHT ZONE	B CELL (GC)	CD19+ CD38+ IgD- CXCR4HI CD83LO	HEALTHY	IC	NEG
	GSM947666_HSLZ_2	TONSIL	LIGHT ZONE	B CELL (GC)	CD19+ CD38+ IgD- CXCR4HI CD83LO	HEALTHY	IC	NEG
	GSM947667_HSLZ_3	TONSIL	LIGHT ZONE	B CELL (GC)	CD19+ CD38+ IgD- CXCR4HI CD83LO	HEALTHY	IC	NEG
	GSM947668_HSLZ_4	TONSIL	LIGHT ZONE	B CELL (GC)	CD19+ CD38+ IgD- CXCR4HI CD83LO	HEALTHY	IC	NEG
	GSM947669_HSDZ_1	TONSIL	DARK ZONE	B CELL (GC)	CD19+ CD38+ IgD- CXCR4LO CD83HI	HEALTHY	IC	NEG
	GSM947670_HSDZ_2	TONSIL	DARK ZONE	B CELL (GC)	CD19+ CD38+ IgD- CXCR4LO CD83HI	HEALTHY	IC	NEG
	GSM947671_HSDZ_3	TONSIL	DARK ZONE	B CELL (GC)	CD19+ CD38+ IgD- CXCR4LO CD83HI	HEALTHY	IC	NEG

	GSM947672_HSDZ_4	TONSIL	DARK ZONE	B CELL (GC)	CD19+ CD38+ IgD- CXCR4LO CD83HI	HEALTHY	IC	NEG
39411	GSM967665_JG2004051901	WHOLE BLOOD	PBMC	B CELL	CD5+ CD19+	HEALTHY (NUTRIENT STARVED 4 HR)	IC	NEG
	GSM967666_JG2004051903	WHOLE BLOOD	PBMC	B CELL	CD5+ CD19+	HEALTHY (NUTRIENT STARVED 4 HR)	IC	NEG
	GSM967667_JG2004051905	WHOLE BLOOD	PBMC	B CELL	CD5+ CD19+	HEALTHY (NUTRIENT STARVED 4 HR)	IC	NEG
	GSM967668_JG2004051907	WHOLE BLOOD	PBMC	B CELL	CD5+ CD19+	HEALTHY (NUTRIENT STARVED 4 HR)	IC	NEG
	GSM967674_JG2004051911	WHOLE BLOOD	PBMC	B CELL	CD5+ CD19+	HEALTHY (NUTRIENT STARVED 4 HR)	IC	NEG
	GSM967675_JG2004051913	WHOLE BLOOD	PBMC	B CELL	CD5+ CD19+	HEALTHY (NUTRIENT STARVED 4 HR)	IC	NEG
	GSM967676_JG2004051915	WHOLE BLOOD	PBMC	B CELL	CD5+ CD19+	HEALTHY (NUTRIENT STARVED 4 HR)	IC	NEG
	GSM967681_JG2004060419	WHOLE BLOOD	PBMC	B CELL	CD5+ CD19+	HEALTHY (NUTRIENT STARVED 4 HR)	IC	NEG
	GSM967682_JG2004060421	WHOLE BLOOD	PBMC	B CELL	CD5+ CD19+	HEALTHY (NUTRIENT STARVED 4 HR)	IC	NEG
	GSM967683_JG2004060423	WHOLE BLOOD	PBMC	B CELL	CD5+ CD19+	HEALTHY (NUTRIENT STARVED 4 HR)	IC	NEG
	GSM967684_JG2004060425	WHOLE BLOOD	PBMC	B CELL	CD5+ CD19+	HEALTHY (NUTRIENT STARVED 4 HR)	IC	NEG
	GSM967689_JG2004070101	WHOLE BLOOD	PBMC	B CELL	CD5+ CD19+	HEALTHY (NUTRIENT STARVED 4 HR)	IC	NEG
	GSM967690_JG2004070103	WHOLE BLOOD	PBMC	B CELL	CD5+ CD19+	HEALTHY (NUTRIENT STARVED 4 HR)	IC	NEG
	GSM967691_JG2004070105	WHOLE BLOOD	PBMC	B CELL	CD5+ CD19+	HEALTHY (NUTRIENT STARVED 4 HR)	IC	NEG
	GSM967692_JG2004070107	WHOLE BLOOD	PBMC	B CELL	CD5+ CD19+	HEALTHY (NUTRIENT STARVED 4 HR)	IC	NEG
	GSM967697_JG2004070109	WHOLE BLOOD	PBMC	B CELL	CD5+ CD19+	HEALTHY (NUTRIENT STARVED 4 HR)	IC	NEG
	GSM967698_JG2004070111	WHOLE BLOOD	PBMC	B CELL	CD5+ CD19+	HEALTHY (NUTRIENT STARVED 4 HR)	IC	NEG

	GSM967699_JG2004070113	WHOLE BLOOD	PBMC	B CELL	CD5+ CD19+	HEALTHY (NUTRIENT STARVED 4 HR)	IC	NEG
	GSM967700_JG2004070115	WHOLE BLOOD	PBMC	B CELL	CD5+ CD19+	HEALTHY (NUTRIENT STARVED 4 HR)	IC	NEG
	GSM967705_JG2004070117	WHOLE BLOOD	PBMC	B CELL	CD5+ CD19+	HEALTHY (NUTRIENT STARVED 4 HR)	IC	NEG
	GSM967706_JG2004070119	WHOLE BLOOD	PBMC	B CELL	CD5+ CD19+	HEALTHY (NUTRIENT STARVED 4 HR)	IC	NEG
	GSM967707_JG2004070121	WHOLE BLOOD	PBMC	B CELL	CD5+ CD19+	HEALTHY (NUTRIENT STARVED 4 HR)	IC	NEG
	GSM967708_JG2004070123	WHOLE BLOOD	PBMC	B CELL	CD5+ CD19+	HEALTHY (NUTRIENT STARVED 4 HR)	IC	NEG
20011	GSM499734	CELL CULTURE	-	LYMPHOMA CELL LINE	NAMALWA	BURKITT	-	NEG
	GSM499735	CELL CULTURE	-	LYMPHOMA CELL LINE	SU-DHL-4	B NON-HODGKIN	-	NEG
36133	GSM886991	CELL CULTURE	-	LYMPHOMA CELL LINE	EB1	BURKITT	-	NEG
	GSM886992	CELL CULTURE	-	LYMPHOMA CELL LINE	EB2	BURKITT	-	NEG
	GSM887019	CELL CULTURE	-	LYMPHOMA CELL LINE	GA-10	BURKITT	-	NEG
	GSM886889	CELL CULTURE	-	LYMPHOMA CELL LINE	BL-41	BURKITT	-	NEG
	GSM886890	CELL CULTURE	-	LYMPHOMA CELL LINE	BL-70	BURKITT	-	NEG
	GSM886900	CELL CULTURE	-	LYMPHOMA CELL LINE	CA46	BURKITT	-	NEG
	GSM886973	CELL CULTURE	-	LYMPHOMA CELL LINE	DAUDI	BURKITT	-	NEG
	GSM887493	CELL CULTURE	-	LYMPHOMA CELL LINE	P3HR-1	BURKITT	-	NEG
	GSM887523	CELL CULTURE	-	LYMPHOMA CELL LINE	RAJI	BURKITT	-	NEG
	GSM887649	CELL CULTURE	-	LYMPHOMA CELL LINE	ST486	BURKITT	-	NEG

64085	GSM1564128_case-1	HEART (PTLD)	BIOPSY	LYMPHOMA	-	BURKITT	ID	NEG
	GSM1564129_case-2	LIVER (PTLD)	BIOPSY	LYMPHOMA	-	BURKITT	ID	NEG
	GSM1564130_case-3	KIDNEY (PTLD)	BIOPSY	LYMPHOMA	-	BURKITT	ID	POS
	GSM1564131_case-4	LIVER (PTLD)	BIOPSY	LYMPHOMA	-	BURKITT	ID	POS
	GSM1564132_case-5	HEART (PTLD)	BIOPSY	LYMPHOMA	-	BURKITT	ID	NEG
	GSM1564133_case-6	LIVER (PTLD)	BIOPSY	LYMPHOMA	-	BURKITT	ID	NEG
	GSM1564134_case-7	KIDNEY (PTLD)	BIOPSY	LYMPHOMA	-	BURKITT	ID	NEG
	GSM1564135_case-8	-	BIOPSY	LYMPHOMA	-	BURKITT	IC	NEG
	GSM1564136_case-9	-	BIOPSY	LYMPHOMA	-	BURKITT	IC	NEG
	GSM1564137_case-10	-	BIOPSY	LYMPHOMA	-	BURKITT	IC	NEG
	GSM1564138_case-11	-	BIOPSY	LYMPHOMA	-	BURKITT	IC	NEG
	GSM1564139_case-12	-	BIOPSY	LYMPHOMA	-	BURKITT	IC	NEG
38885	GSM951477_hyb10713	LYMPH NODE	BIOPSY	LYMPHOMA	-	BURKITT	IC	NEG
	GSM951478_hyb10677	LYMPH NODE	BIOPSY	LYMPHOMA	-	BURKITT	IC	NEG
	GSM951479_hyb10695	LYMPH NODE	BIOPSY	LYMPHOMA	-	BURKITT	IC	NEG
	GSM951480_hyb10731	LYMPH NODE	BIOPSY	LYMPHOMA	-	BURKITT	IC	POS
	GSM951455_hyb10733	GUT	BIOPSY	LYMPHOMA	-	BURKITT	ID	POS
26673	GSM656467	LYMPH NODE	BIOPSY	LYMPHOMA	-	BURKITT (SPORADIC)	IC	-
	GSM656452	LYMPH NODE	BIOPSY	LYMPHOMA	-	BURKITT (ENDEMIC)	IC	-
	GSM656453	LYMPH NODE	BIOPSY	LYMPHOMA	-	BURKITT (ENDEMIC)	IC	-
	GSM656454	LYMPH NODE	BIOPSY	LYMPHOMA	-	BURKITT (ENDEMIC)	IC	-
	GSM656455	LYMPH NODE	BIOPSY	LYMPHOMA	-	BURKITT (ENDEMIC)	IC	-
	GSM656456	LYMPH NODE	BIOPSY	LYMPHOMA	-	BURKITT (ENDEMIC)	IC	-
	GSM656457	LYMPH NODE	BIOPSY	LYMPHOMA	-	BURKITT (ENDEMIC)	IC	-
	GSM656458	LYMPH NODE	BIOPSY	LYMPHOMA	-	BURKITT (ENDEMIC)	IC	-
	GSM656459	LYMPH NODE	BIOPSY	LYMPHOMA	-	BURKITT (ENDEMIC)	IC	-
	GSM656460	LYMPH NODE	BIOPSY	LYMPHOMA	-	BURKITT (ENDEMIC)	IC	-
	GSM656461	LYMPH NODE	BIOPSY	LYMPHOMA	-	BURKITT (ENDEMIC)	IC	-

	GSM656462	LYMPH NODE	BIOPSY	LYMPHOMA	-	BURKITT (ENDEMIC)	IC	-
	GSM656463	LYMPH NODE	BIOPSY	LYMPHOMA	-	BURKITT (ENDEMIC)	IC	-
	GSM656465	LYMPH NODE	BIOPSY	LYMPHOMA	-	BURKITT (HIV ASSOCIATED)	ID	-
	GSM656466	LYMPH NODE	BIOPSY	LYMPHOMA	-	BURKITT (HIV ASSOCIATED)	ID	-
38885	GSM951449_hyb6595	LYMPH NODE	BIOPSY	LYMPHOMA	-	DLBCL (BURKITT LIKE)	ID	POS
	GSM951450_hyb6582	WALDEYER	BIOPSY	LYMPHOMA	-	DLBCL (BURKITT LIKE)	ID	POS
	GSM951451_hyb10696	LYMPH NODE	BIOPSY	LYMPHOMA	-	DLBCL (BURKITT LIKE)	ID	POS
	GSM951452_hyb6602	LYMPH NODE	BIOPSY	LYMPHOMA	-	DLBCL (BURKITT LIKE)	ID	POS
	GSM951453_hyb6585	LYMPH NODE	BIOPSY	LYMPHOMA	-	DLBCL (BURKITT LIKE)	ID	POS
	GSM951454_hyb6590	LYMPH NODE	BIOPSY	LYMPHOMA	-	DLBCL (BURKITT LIKE)	ID	POS
	GSM951474_hyb6589	LYMPH NODE	BIOPSY	LYMPHOMA	-	DLBCL (BURKITT LIKE)	IC	NEG
	GSM951475_hyb10725	LYMPH NODE	BIOPSY	LYMPHOMA	-	DLBCL (BURKITT LIKE)	IC	NEG
	GSM951476_hyb10686	GUT	BIOPSY	LYMPHOMA	-	DLBCL (BURKITT LIKE)	IC	NEG
36133	GSM886855	CELL CULTURE	-	LYMPHOMA CELL LINE	A3/KAW	DLBCL	-	NEG
	GSM886857	CELL CULTURE	-	LYMPHOMA CELL LINE	A4/FUK	DLBCL	-	NEG
	GSM886874	CELL CULTURE	-	LYMPHOMA CELL LINE	BCP-1		-	NEG
	GSM886931	CELL CULTURE	-	LYMPHOMA CELL LINE	CI-1	B NON-HODGKIN	-	NEG
	GSM886975	CELL CULTURE	-	LYMPHOMA CELL LINE	DB	DLBCL	-	NEG
	GSM886987	CELL CULTURE	-	LYMPHOMA CELL LINE	DOHH-2	DLBCL	-	NEG

	GSM887143	CELL CULTURE	-	LYMPHOMA CELL LINE	HT	-	-	NEG
	GSM887186	CELL CULTURE	-	LYMPHOMA CELL LINE	JM1	-	-	NEG
	GSM887289	CELL CULTURE	-	LYMPHOMA CELL LINE	MC116	-	-	NEG
	GSM887459	CELL CULTURE	-	LYMPHOMA CELL LINE	NU-DHL-1	DLBCL	-	NEG
	GSM887460	CELL CULTURE	-	LYMPHOMA CELL LINE	NU-DUL-1	-	-	NEG
	GSM887471	CELL CULTURE	-	LYMPHOMA CELL LINE	OCI-LY-19	DLBCL	-	NEG
	GSM887472	CELL CULTURE	-	LYMPHOMA CELL LINE	OCI-LY3	DLBCL	-	NEG
	GSM887514	CELL CULTURE	-	LYMPHOMA CELL LINE	PFEIFFER	DLBCL	-	NEG
	GSM887539	CELL CULTURE	-	LYMPHOMA CELL LINE	RI-1	-	-	NEG
	GSM887543	CELL CULTURE	-	LYMPHOMA CELL LINE	RL	-	-	NEG
	GSM887651	CELL CULTURE	-	LYMPHOMA CELL LINE	SU-DHL-10	DLBCL	-	NEG
	GSM887653	CELL CULTURE	-	LYMPHOMA CELL LINE	SU-DHL-4	DLBCL	-	NEG
	GSM887654	CELL CULTURE	-	LYMPHOMA CELL LINE	SU-DHL-5	DLBCL	-	NEG
	GSM887655	CELL CULTURE	-	LYMPHOMA CELL LINE	SU-DHL-6	DLBCL	-	NEG
	GSM887656	CELL CULTURE	-	LYMPHOMA CELL LINE	SU-DHL-8	DLBCL	-	NEG
	GSM887709	CELL CULTURE	-	LYMPHOMA CELL LINE	TOLEDO	DLBCL	-	NEG
	GSM887724	CELL CULTURE	-	LYMPHOMA CELL LINE	U-937	DLBCL	-	NEG
	GSM887741	CELL CULTURE	-	LYMPHOMA CELL LINE	WSU-DLCL2	DLBCL	-	NEG
38885	GSM951416_hyb10706	GUT	BIOPSY	LYMPHOMA	-	DLBCL	ID	NEG

GSM951417_hyb6597	GUT	BIOPSY	LYMPHOMA	-	DLBCL	ID	NEG
GSM951418_hyb10676	TESTIS	BIOPSY	LYMPHOMA	-	DLBCL	ID	NEG
GSM951419_hyb6554	LYMPH NODE	BIOPSY	LYMPHOMA	-	DLBCL	ID	NEG
GSM951420_hyb6566	LYMPH NODE	BIOPSY	LYMPHOMA	-	DLBCL	ID	NEG
GSM951421_hyb6569	GUT	BIOPSY	LYMPHOMA	-	DLBCL	ID	NEG
GSM951423_hyb6606	LYMPH NODE	BIOPSY	LYMPHOMA	-	DLBCL	ID	NEG
GSM951424_hyb6556	GUT	BIOPSY	LYMPHOMA	-	DLBCL	ID	NEG
GSM951425_hyb10730	LYMPH NODE	BIOPSY	LYMPHOMA	-	DLBCL	ID	NEG
GSM951426_hyb10712	LYMPH NODE	BIOPSY	LYMPHOMA	-	DLBCL	ID	POS
GSM951427_hyb10715	WALDEYER	BIOPSY	LYMPHOMA	-	DLBCL	ID	POS
GSM951428_hyb6580	LYMPH NODE	BIOPSY	LYMPHOMA	-	DLBCL	ID	POS
GSM951429_hyb10681	GUT	BIOPSY	LYMPHOMA	-	DLBCL	ID	POS
GSM951430_hyb6568	LYMPH NODE	BIOPSY	LYMPHOMA	-	DLBCL	ID	POS
GSM951431_hyb10675	WALDEYER	BIOPSY	LYMPHOMA	-	DLBCL	ID	POS
GSM951432_hyb10690	LYMPH NODE	BIOPSY	LYMPHOMA	-	DLBCL	ID	POS
GSM951433_hyb10709	WALDEYER	BIOPSY	LYMPHOMA	-	DLBCL	ID	POS
GSM951434_hyb6593	LYMPH NODE	BIOPSY	LYMPHOMA	-	DLBCL	ID	POS
GSM951435_hyb10724	LYMPH NODE	BIOPSY	LYMPHOMA	-	DLBCL	ID	POS
GSM951436_hyb6575	URINARY TRACT	BIOPSY	LYMPHOMA	-	DLBCL	ID	POS
GSM951437_hyb10703	LYMPH NODE	BIOPSY	LYMPHOMA	-	DLBCL	ID	POS
GSM951438_hyb6599	LYMPH NODE	BIOPSY	LYMPHOMA	-	DLBCL	ID	POS
GSM951439_hyb10697	LYMPH NODE	BIOPSY	LYMPHOMA	-	DLBCL	ID	POS
GSM951440_hyb6562	LYMPH NODE	BIOPSY	LYMPHOMA	-	DLBCL	ID	POS
GSM951441_hyb10727	GUT	BIOPSY	LYMPHOMA	-	DLBCL	ID	POS
GSM951442_hyb10685	BALT	BIOPSY	LYMPHOMA	-	DLBCL	ID	POS
GSM951443_hyb10688	LYMPH NODE	BIOPSY	LYMPHOMA	-	DLBCL	ID	POS
GSM951444_hyb6571	URINARY TRACT	BIOPSY	LYMPHOMA	-	DLBCL	ID	POS

GSM951445_hyb6564	LYMPH NODE	BIOPSY	LYMPHOMA	-	DLBCL	ID	POS
GSM951446_hyb10682	LYMPH NODE	BIOPSY	LYMPHOMA	-	DLBCL	ID	POS
GSM951448_hyb6579	GUT	BIOPSY	LYMPHOMA	-	DLBCL	ID	POS
GSM951456_hyb6598	LYMPH NODE	BIOPSY	LYMPHOMA	-	DLBCL	IC	NEG
GSM951457_hyb6561	LYMPH NODE	BIOPSY	LYMPHOMA	-	DLBCL	IC	NEG
GSM951458_hyb10710	LYMPH NODE	BIOPSY	LYMPHOMA	-	DLBCL	IC	NEG
GSM951459_hyb6607	MEDIASTINUM	BIOPSY	LYMPHOMA	-	DLBCL	IC	NEG
GSM951460_hyb10692	GUT	BIOPSY	LYMPHOMA	-	DLBCL	IC	NEG
GSM951461_hyb6603	LYMPH NODE	BIOPSY	LYMPHOMA	-	DLBCL	IC	NEG
GSM951462_hyb6600	LYMPH NODE	BIOPSY	LYMPHOMA	-	DLBCL	IC	NEG
GSM951463_hyb6573	LYMPH NODE	BIOPSY	LYMPHOMA	-	DLBCL	IC	NEG
GSM951464_hyb6576	LYMPH NODE	BIOPSY	LYMPHOMA	-	DLBCL	IC	NEG
GSM951465_hyb6587	LYMPH NODE	BIOPSY	LYMPHOMA	-	DLBCL	IC	NEG
GSM951466_hyb6596	EXTRACRANIAL FRONTO-PARIETAL	BIOPSY	LYMPHOMA	-	DLBCL	IC	NEG
GSM951467_hyb10683	LYMPH NODE	BIOPSY	LYMPHOMA	-	DLBCL	IC	NEG
GSM951468_hyb6563	LYMPH NODE	BIOPSY	LYMPHOMA	-	DLBCL	IC	NEG
GSM951469_hyb10728	LYMPH NODE	BIOPSY	LYMPHOMA	-	DLBCL	IC	NEG
GSM951470_hyb6581	LYMPH NODE	BIOPSY	LYMPHOMA	-	DLBCL	IC	NEG
GSM951471_hyb6570	LYMPH NODE	BIOPSY	LYMPHOMA	-	DLBCL	IC	NEG
GSM951472_hyb10719	LYMPH NODE	BIOPSY	LYMPHOMA	-	DLBCL	IC	NEG
GSM951473_hyb10714	LYMPH NODE	BIOPSY	LYMPHOMA	-	DLBCL	IC	NEG

Appendix 2 Full list of GO components used to identify potential plasma membrane proteins from the proteomics results

GO term name
adherens junction
anchored component of membrane
anchored component of plasma membrane
anchored component of synaptic vesicle membrane
apical junction complex
apical part of cell
apical plasma membrane
apicolateral plasma membrane
astrocyte projection
axolemma
axonal growth cone
azurophil granule membrane
B cell receptor complex
basal plasma membrane
basement membrane
basolateral plasma membrane
bicellular tight junction
bleb
blood microparticle
brush border membrane
cAMP-dependent protein kinase complex
CatSper complex
caveola
cell cortex
cell cortex region
cell junction
cell leading edge
cell periphery
cell projection
cell surface
cell-cell adherens junction
cell-cell contact zone
cell-cell junction
cell-substrate junction
chloride channel complex
chromaffin granule membrane
chylomicron
ciliary membrane
ciliary pocket membrane
clathrin coat
clathrin coat of coated pit

clathrin-coated vesicle
clathrin-coated vesicle membrane
clathrin-sculpted gamma-aminobutyric acid transport vesicle membrane
cleavage furrow
coated vesicle
cornified envelope
cytolytic granule
cytoplasmic ribonucleoprotein granule
cytoplasmic side of apical plasma membrane
cytoplasmic side of plasma membrane
cytoplasmic vesicle membrane
dendrite
dendritic spine
dendritic spine head
dendritic spine neck
desmosome
discoidal high-density lipoprotein particle
dystrophin-associated glycoprotein complex
endothelial microparticle
exocyst
exocytic vesicle
external side of plasma membrane
extracellular exosome
extracellular matrix
extracellular region
extracellular space
extracellular vesicle
extrinsic component of cytoplasmic side of plasma membrane
extrinsic component of external side of plasma membrane
extrinsic component of plasma membrane
fascia adherens
filopodium membrane
flotillin complex
focal adhesion
glial limiting end-foot
growth cone
hexameric IgM immunoglobulin complex
HFE-transferrin receptor complex
hydrogen:potassium-exchanging ATPase complex
immunoglobulin complex, circulating
immunological synapse
integral component of plasma membrane
integrin alpha10-beta1 complex
integrin alpha11-beta1 complex

integrin alpha1-beta1 complex
integrin alpha2-beta1 complex
integrin alpha3-beta1 complex
integrin alpha7-beta1 complex
integrin alpha8-beta1 complex
integrin complex
intercalated disc
intermediate-density lipoprotein particle
intrinsic component of the cytoplasmic side of the plasma membrane
invadopodium membrane
lamellipodium
lamellipodium membrane
lateral plasma membrane
lipopolysaccharide receptor complex
low-density lipoprotein particle
membrane coat
membrane raft
MHC class I peptide loading complex
MHC class I protein complex
MHC class Ib protein complex
MHC class II protein complex
microspike
microvillus membrane
monomeric IgA immunoglobulin complex
multivesicular body
muscle cell projection membrane
neuromuscular junction
neuron projection
neuron projection terminus
neuronal cell body membrane
pentameric IgM immunoglobulin complex
periciliary membrane compartment
phagocytic cup
photoreceptor disc membrane
photoreceptor outer segment membrane
plasma lipoprotein particle
plasma membrane
plasma membrane raft
podosome
postsynaptic density
postsynaptic membrane
presynaptic membrane
proteinaceous extracellular matrix
proximal dendrite

pseudopodium membrane
receptor complex
ruffle membrane
sarcolemma
Schwann cell microvillus
secretory dimeric IgA immunoglobulin complex
secretory IgA immunoglobulin complex
slit diaphragm
SNARE complex
sodium:potassium-exchanging ATPase complex
specific granule membrane
sperm head plasma membrane
spherical high-density lipoprotein particle
stereocilium
stereocilium tip
synaptic membrane
synaptic vesicle membrane
synaptobrevin 2-SNAP-25-syntaxin-1a complex
tertiary granule membrane
T-tubule
uropod
very-low-density lipoprotein particle
zonula adherens